XRCF Phase 1 Testing: Preliminary Results

Smithsonian Astrophysical Observatory

May 28, 1997

Contents

List of Figures

List of Tables

Preface

This document is the work of many individuals, far too many to list without the risk of leaving some out, let alone to acknowledge their efforts adequately. We'd like to mention at least the various groups that contributed to this rather Herculean effort, in no particular order: the MST HXDA team, the XRCF second floor operators, the ASC third floor staff and Calibration group, the OTG groups, MSFC Project Science, the TRW and Kodak engineers and test conductors, the XRCF staff, the MST Simulations and Analysis and MST Synchrotron groups, SAO Central Engineering, the Telescope Scientist group, and all of the others we have mistakenly omitted.

While we thank those above for their efforts, explicit blame for the contents of this document must fall upon the shoulders of its authors:

1	Introduction	R.J. Edgar, L.P. David, T.J. Gaetz, D. Jerius, D.A. Schwartz
2	Measurements of Effective Area	R.J. Edgar
3	The HSI-measured HRMA Point Spread Function	L.P. David
4	PSF-1D and PSF-2D Scans	J. Everett
5	Encircled Energy	R.J. Edgar
6	The Wings of the Point Spread Function	R.J. Edgar
7	Comparison of the Measured Effective Area and Encircled Energies to Simulations	D. Jerius
8	HRMA Ring Focus Measurements	P. Zhao, L.M. Cohen
9	Beam Uniformity	J. Everett
10	HRMA Focus Measurements and Raytrace Update	W.A. Podgorski
11	HRMA Tilts at XRCF	W.A. Podgorski
12	HRMA Off-Axis Focal Positions	W.A. Podgorski
13	Internal Decenters of the AXAF Mirrors	T.J. Gaetz
14	Rigid-Body Misalignment Parameters	T.J. Gaetz
15	HRMA Ring Focus Shutter Test	P. Zhao
16	Description of Data Organization	R.J. Edgar
	Editor	D. Jerius

Chapter 1

Introduction

This document is an interim report on the analysis of the data from Phase 1 of the calibration of the Advanced X-ray Astrophysics Facility (AXAF), which occurred between 1996 December 20 and 1997 February 11 at the X-Ray Calibration Facility (XRCF) at Marshall Space Flight Center (MSFC) in Huntsville, Alabama. The analysis of these data is still ongoing; only the first tentative conclusions are reported here.

During this test program, we ran a total of 1376 logical tests, each identified by an alphanumeric "TRW ID," assigned according to a scheme negotiated between the prime contractor, TRW, and the AXAF science community. Of these, 982 tests were done without transmission gratings, mostly for the calibration of the High Resolution Mirror Assembly (HRMA), or of the facility (such as background, beam uniformity, alignment to facility axis, etc.). The HRMA X-ray Detection System (HXDS) obtained a total of 5225 different run identifiers (runid's), which include 293,144 individual pulse-height spectra and 1486 High Speed Imager (HSI) images.

The HRMA-only tests will be described in some detail in this document. In Phase 2 of the XRCF test program, science instruments and their stand-ins were used at the focal point of the telescope. Those data are not presented here, though in many cases they bear on the same questions as the Phase 1 data.

We should perhaps emphasize that the current state of the data reduction leads to known systematic effects as large as 10% or so in some cases. We are aware of a great many of these effects, and have plans to consider most of them in the ultimate data reduction and analysis. A (partial) list of such effects can be found in Chapter 2.

Several puzzles remain to be solved. Most notable among these is the discrepancy in the effective area, discussed in Chapter 7. Raytrace simulations predict an effective area significantly higher than that which is measured by two different techniques. In most cases this discrepancy amounts to $\sim 8-10\%$, though for mirror pair 1 near its high energy cutoff, the discrepancy is even larger.

1.1 The Facility and Experimental Setup

The test setup is described in detail elsewhere (for example, in SAO (1997)), but a brief description is in order here. A set of X-ray sources is available in Building 600. These include the Electron Impact Point Source (EIPS), a Penning source, and two monochrometers which select X-ray photons emitted by rotating anode sources. These are the Double Crystal Monochrometer

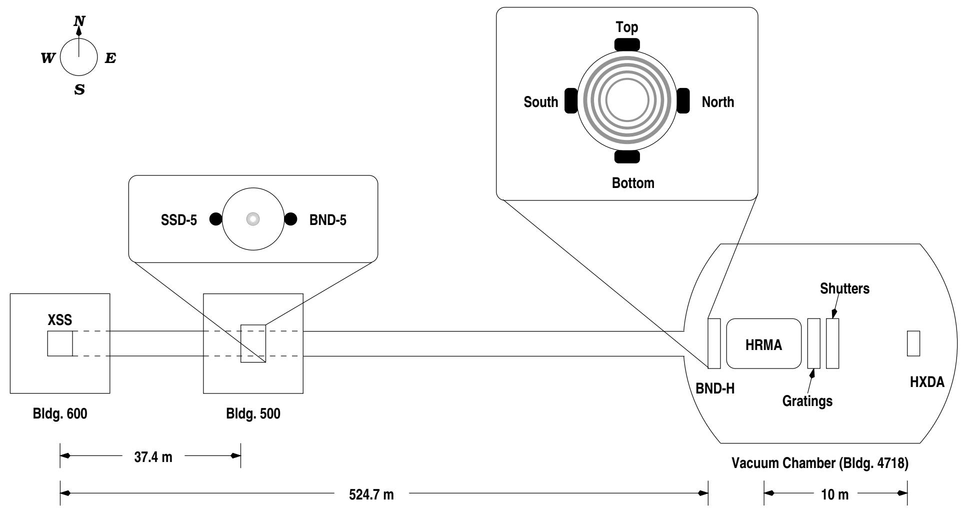

Figure 1.1: Schematic of XRCF

(DCM), and the High Resolution Erect Field Spectrometer (HIREFS).

Figure 1.1 shows the physical layout of the XRCF. Connecting Building 600 to the main instrument chamber in building 4718 at MSFC is an evacuated guide tube over 500 meters long. Approximately 38 meters down the guide tube in Building 500, but off to one side of the beam to avoid occulting it, are two beam normalization detectors (BNDs) known as the BND-500. These are a Flow Proportional Counter (FPC), fpc_5, and a solid state detector (SSD), ssd_5. The fpc_5 detector can be moved about in the beam by a pair of translation stage motors, to map the beam and test it for uniformity. The fpc_5 is closer to the source than the ssd_5. Both of the BND-500 detectors have selectable apertures.

The main instrument chamber contains a variety of equipment, including the HRMA, a set of BNDs surrounding the entrance to the HRMA, and the focal plane instrumentation, the HRMA X-ray Detector Assembly (HXDA). It also contains the flight Objective Transmission Gratings, a set of quadrant shutters (which allow each quadrant of each of the 4 constituent optic pairs of the HRMA to be exposed independently), the HRMA contamination covers, and various motors and other hardware to support operations.

The BND assembly at the HRMA entrance is known as the BND-H (Beam Normalization Detectors at the HRMA). It consists of four nearly identical flow proportional counters, whose nominal stations are adjacent to the north, bottom, south, and top quadrants of the outermost HRMA mirror shell. They are known, respectively, as fpc_hn, fpc_hb, fpc_hs, and fpc_ht. The fpc_hn detector can be moved around in front of the HRMA entrance to map the X-ray beam as it enters the HRMA. It is physically located a small distance closer to the source than the other three BND-H detectors. It can be used either with a 36 mm diameter circular aperture, in the open configuration.

The HXDA assembly at the HRMA focal point consists of two Flow Proportional Counters (FPC), one Solid State Detector (SSD), and a microchannel plate camera known as the High Speed Imager (HSI). These detectors are known respectively as fpc_x1, fpc_x2, ssd_x, and HSI. The two

Table 1.1: Facility dimensions used in data reductions

Quantity	Assumed Value
fpc_5 source distance	3835 cm
ssd_5 source distance	3861 cm
fpc_hn source distance	52430 cm
fpc_h source distance (other than fpc_hn)	52430 cm
HRMA entrance source distance (front edge of P optic)	52609 cm
fpc_h open area	32.26 cm^2

FPCs are a redundant pair. Except for an early aliveness check, all of the FPC tests actually performed were done with fpc_x2.

All of the HXDA detectors are mounted on a stack of translation stages which allow them to be placed anywhere in three dimensions in the vicinity of the telescope focus, with an accuracy of about 2 μm. They also allow the apertures for the FPCs and SSD to be selected. FPC aperture sizes range from 3 μm to 35 mm diameters; apertures smaller than 7.5 μm were rarely used.

The BNDs are exposed simultaneously with the focal plane detectors. Focal plane count rates are normalized by the photon flux density at the BNDs, leading to *aperture–relative* effective areas, in units of cm^2. These are aperture–relative since the focal plane detectors have finite size. Chapter 2 goes into more detail about the reduction efforts.

A great many facility physical dimensions are required to fully characterize the experiment for data reduction purposes. Table 1.1 lists a few of the most important dimensions, and the values they were assumed to have.

1.2 The Measurements

The objective of the test program is to validate a high-fidelity ray trace model of the HRMA, which includes a wide variety of information about the physical and engineering properties of the mirror assembly, including, for example, the effects of gravity, offloader stresses, epoxy shrinkage, surface deformations and roughness, rigid body position of the optical elements, etc. After the model is revised and validated by comparing its predictions to the XRCF data, it can then be used with considerable confidence to predict the performance of the mirrors on orbit.

Accordingly, the test program included a variety of experiments. These include measurements of encircled energy fractions *vs.* aperture size and measurements of effective area at various energies (see Figure 1.2 for a graphical summary of these tests); aperture scans of the wings of the point spread function (see Figure 1.3); measurements of the microroughness of the ends of the mirrors through encircled energy tests with the mirrors tilted to approximate the incident angles of photons from a point source at infinity (see Figure 1.4); 1- and 2-dimensional aperture scans of the point spread function (see Figure 1.5 and Chapter 4); images of the point spread function (both the inner core of the image, and with that occulted, the outer core) and images taken to constrain the internal alignment of the HRMA optics (see Figures 1.6 and 1.7); images and aperture scans at the ring focus position; various attempts to detect molecular contamination (if any); measurements of the alignment of the mirror to the facility optical axis; shutter focus measurements; and various kinds of grating tests.

Brief descriptions of the measurements follow; many of them are described more fully, including the results and the analysis done to date, in the ensuing chapters.

Focus and Tilt

The focal position and the intra-shell tilt of the mirrors can be determined by exposing, in turn, each quadrant of a mirror (or mirrors) with the quadrant shutters, and measuring the centroid of the resultant images. The offsets of the centroids allow calculation of the focus and tilts. With the HSI, this is an actual image, but with the FPC or SSD we make a 2 dimensional raster scan with a small pinhole. These measurements were typically made for each shell individually. (See Chapters 10 and 11).

Encircled Energy/Effective Area

Each of a series of pinholes is carefully centered on the image centroid. The effective area as seen by each pinhole is given by

$$A_{eff,\mathrm{pinhole}} = A_{\mathrm{BND}} \times \frac{R_{\mathrm{pinhole}}}{R_{\mathrm{BND}}}$$

where A_{BND} is the open area of the BND. R_{pinhole} is the count rate through the pinhole, and R_{BND} is the count rate seen by the BND. The pinholes typically cover $0.1''$ to $6'$ radius around the image center. Effective area measurements are a special case of the encircled energy for the largest available pinhole. (See Chapters 5 and 2.)

Point Response Function

The PRF of the mirrors was measured in two regimes. The inner core was sampled with one and two dimensional pinhole scans centered about the image centroid. The outer core was measured with the HSI by placing the inner core on specially designed masks. A one dimensional scan through the center gives the Full Width at Half Maximum measurement. Two dimensional scans can be deconvolved for ground effects to deduce the properties of the mirror in orbit. (See Chapters 3 and 4.)

Wing Scan

The far outer wings of the PRF are measured via a one-dimensional scan with a relatively large pinhole. These measurements are generally made using one quadrant of one mirror; the direction of the scan was in the plane of the incident and reflected ray at the midpoint of the quadrant. Typical scans are $20''$ to $35'$ from the image center. During many scans the HRMA was tilted so that the grazing angle of the photons from the XSS with respect to the mirror would be more similar to that on orbit. (See Chapter 6.)

Ring Focus

The ring focus describes a position on the optical axis of the HRMA where spherical aberration due to a finite-distance source causes the rays from the front and back of the mirrors to cross, giving a minimum thickness ring which is ideal for analyzing 1g mechanical effects on the ground calibration. HSI images were taken at the ring focus position, which for the HRMA is 65.2 mm in front of the finite distance focal point. (See Chapter 8.)

Background

Runs were made with the gate valve from the source chamber closed, so that there were no X-rays from the source. Setup of the detectors was identical to a subsequent series of measurements with a given X-ray source.

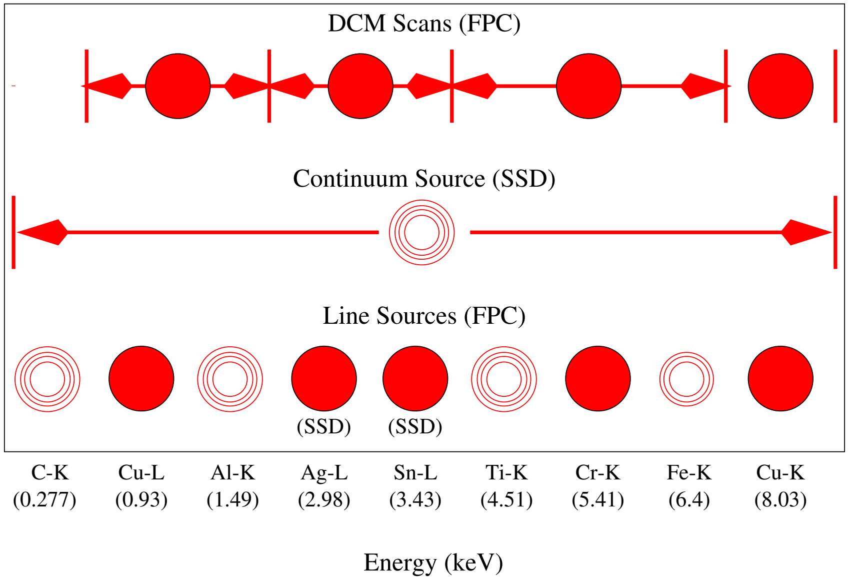

Figure 1.2: The on-axis encircled energy/effective area tests where performed using 3 complementary methods: 1) Line sources with the FPC (bottom row), a continuum source (i.e, the carbon anode run at a high voltage) with the SSD (middle row), and the DCM with the FPC (top row). Filled circles indicate tests that were done with the full HRMA, while open circles indicate tests that were done with single shells (e.g., 4 concentric circles indicate that the test was done for each shell separately).

Beam Uniformity

Two dimensional scans made with the BNDs at the HRMA and at at Bldg. 500. These scans approximated coverage of the region of space occupied by the HRMA, and by the fixed bnd detectors. (See Chapter 9.)

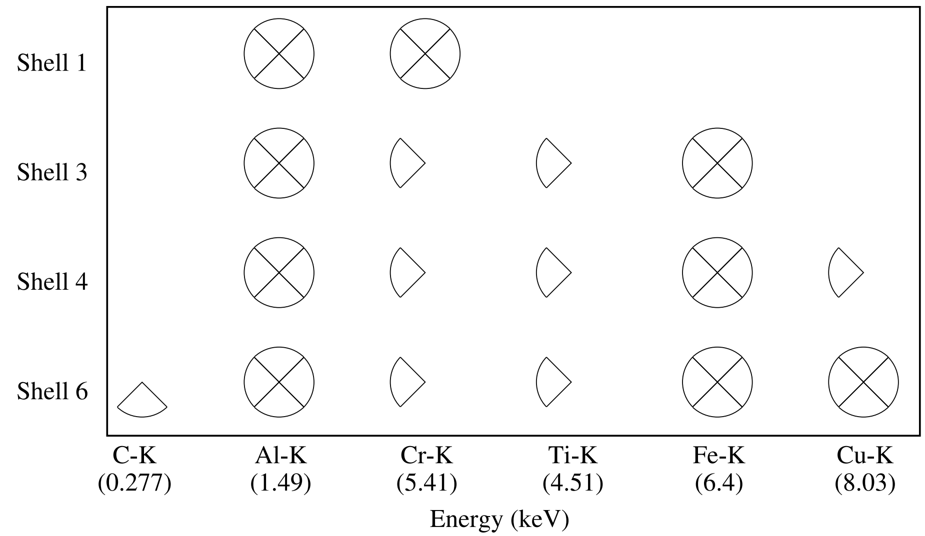

Figure 1.3: All wing scans were performed with only one quadrant of one shell open. This figure shows the wing scan measurements that were performed during Phase 1 as a function of energy, shell, and quadrant. The south quadrant is on the left and the north quadrant is on the right.

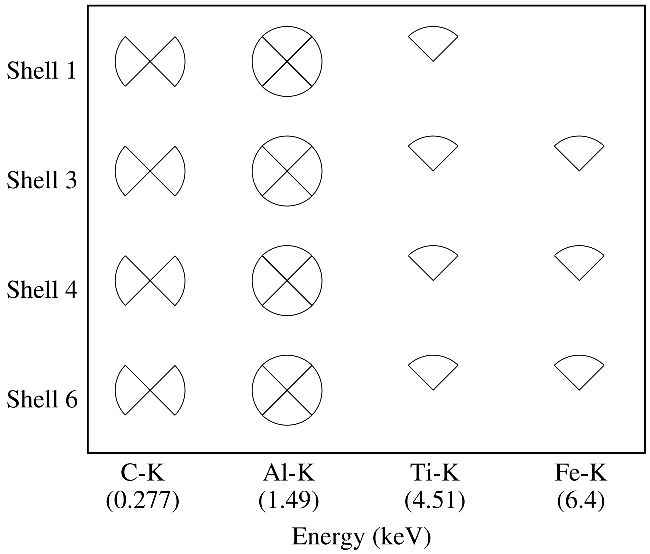

Figure 1.4: Mirror ends survey measurements completed during Phase 1 as a function energy, shell, and quadrant. The south quadrant is on the left and the north quadrant is on the right.

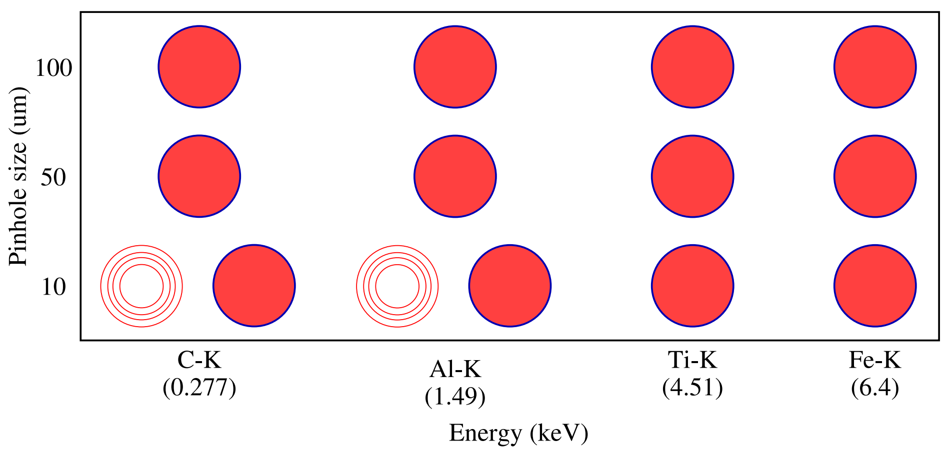

Figure 1.5: 2-D pinhole scans performed during Phase 1 as a function of energy and pinhole diameter. Filled circles indicate tests that were done with the full HRMA, while open circles indicate tests that were done with single shells.

1.2. The Measurements

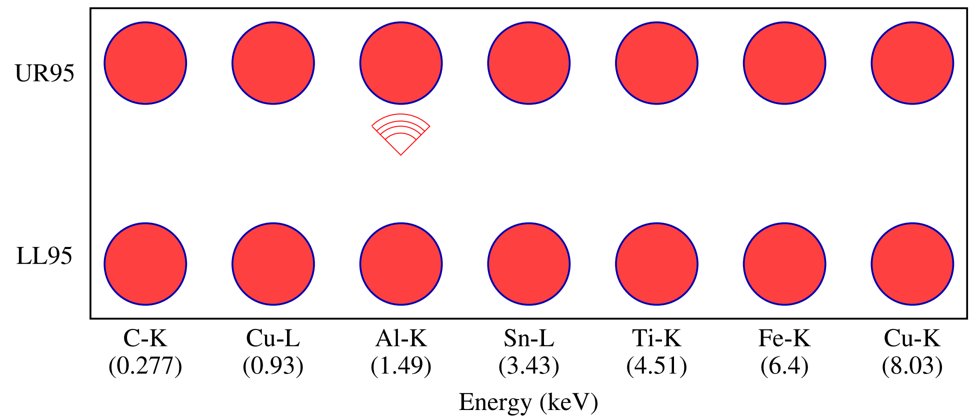

Figure 1.6: PSF Outer core measurements performed during Phase 1 with the HSI. The HSI has two cusps which can block out the centroid of the image. One is on the upper right of the detector (UR95) and one is on the lower left (LL95). The pie slice at Al-Ka indicates images that were obtained with only the top shutter open for individual shells.

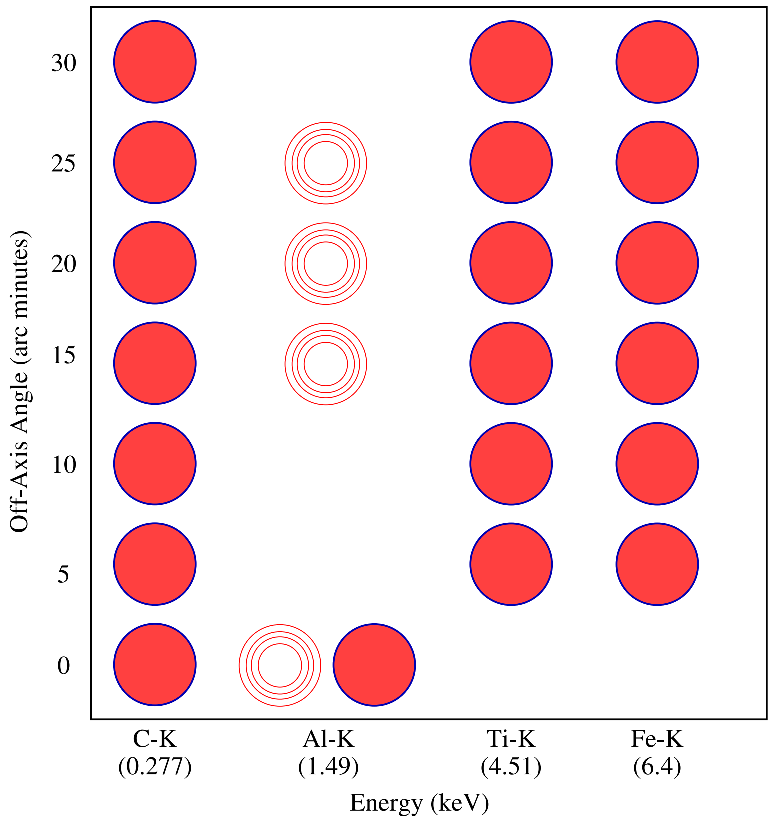

Figure 1.7: HSI images obtained during Phase 1 as a function of energy and angle off-axis. Filled circles indicate tests that were done with the full HRMA, while open circles indicate tests that were done with single shells.

1.3 The Simulations

Because there isn't time in the lifetimes of the members of the team to completely calibrate or characterize every facet of the HRMA, the measurements are augmented by a highly detailed mechanical and optical ray-trace model of the HRMA. The XRCF measurements are used to refine and correct the *ab initio* and semi-empirical components which make it up.

The MST simulation is composed of the following components (which describe model `xrcf_SAO1G+HDOS_HDOS-scat-970220_03`):

- a monochromatic point source at the XRCF distance of 527279 mm to the front side of the CAP.
- Iridium optical constants derived from the Henke data (Henke et al., 1993) below 2 keV, and from the data released by the MST Synchrotron group on 23 December 1996 for the P6 flat.
- Rigid-body Optic positions and tilts as discussed in Chapters 10, 14 and 13.
- Mirror deformations:
  - Low order surface map data from HDOS.
  - Estimates of the 2nd and 3rd order distortions from HATS data.
  - Epoxy cure shrinkage effects for 2 weeks after pump-down.
  - Distortion due to horizontal orientation in 1g.
  - Modifications to cone-angle to give correct focal positions as determined from XRCF measurements (see Chapter 10).
- Surface micro-roughness scattering derived from high order HDOS surface map data (20 February 1997 distillation)
- Apertures, Collimators, Baffles (Central Aperture Plate (CAP), fore and aft structures, and P6 Ghost baffle) modeled as annuli with rectangular obstructing struts (where appropriate). All plates are 100% opaque, and are of zero thickness, except for the CAP, which is given the as-measured thickness

One major deficiency of this model is that the X-ray source is modeled as a point source, rather than as an extended object. Since the source varied in size (up to $\sim 0.2''$), the simulations are uniformly "peakier" in the core than the measurements.

In comparisons to the measurements we make no attempt to model the detectors; instead we rely upon the spectral analysis to determine effective areas free of detector artifacts. All simulation results described in this document are derived from this model, unless otherwise noted.

1.4 Coordinate Systems

In this section we summarize the relations between various coordinate systems of interest; these include:

Tower:	HRMA Alignment Test System Tower at EKC (HATS measurements)
`DPSAOsac`:	Double-pass raytraces to simulate HATS measurements
`SAOsac`:	standard raytraces (*e.g.*, XRCF conditions)
XRCF:	coordinate system at the XRCF test facility
HRMA:	HRMA-based coordinate system aligned with the standard AXAF coordinate directions

Figure 1.8 illustrates the different coordinate systems. Note that the XRCF coordinates differ from the standard HRMA/AXAF coordinate system by a flip of 180° about the X_{HRMA} axis, while the `DPSAOsac` coordinates differ from the standard `SAOsac` coordinates by a flip of 180° about the X_{SAOsac} axis (the Y_{HRMA} axis). Note also that we are primarily concerned here with the directions of the coordinate axes rather than the location of the coordinate origin.

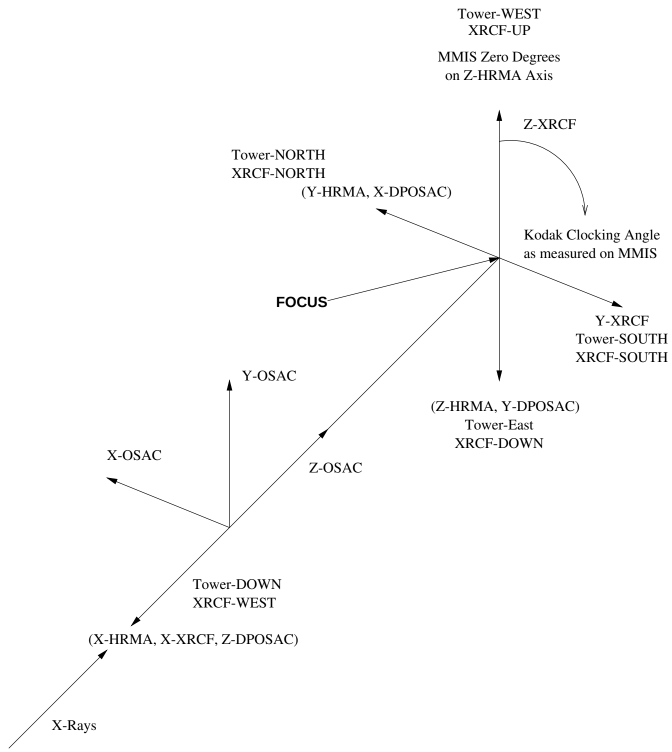

Figure 1.8: Relations between HATS tower, XRCF, and `SAOsac` coordinates

The SAO/MST raytrace system, `SAOsac`, specifies rigid-body positioning in terms of the location and orientation of the body-center of the optic. The body-center "tilt" coordinates are `azmis` and `elmis`, where

`azmis`: positive rotation about an axis parallel to the `SAOsac` Y axis; positive rotation is right-hand-rule rotation with angle increasing from the $+Z$ axis towards the $+X$ axis. (X' axis is the new X axis after `azmis` rotation; Z' axis is the new Z axis after `azmis` rotation).

`elmis`: negative rotation about an axis parallel to `SAOsac` X' axis; positive rotation is right-hand-rule with angle increasing from the $+Y$ axis towards the $+Z'$ axis. Positive `elmis` rotation takes $+Z'$ axis towards the $+Y$ axis.

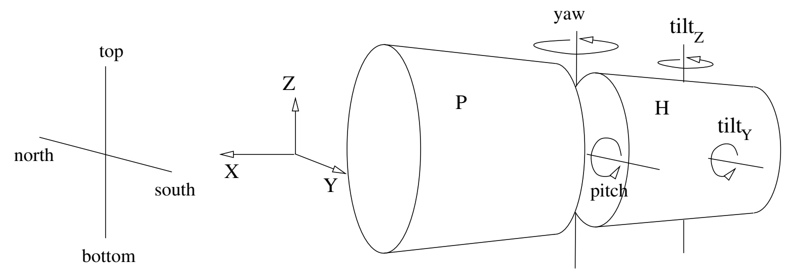

Figure 1.9: Schematic of XRCF coordinate and rotation conventions

For completeness, the corresponding conventions for mirror element rotations in the HRMA and XRCF coordinates are

θ_Y: positive rotation about an axis parallel to the `HRMA` $+Y$ axis; positive rotation is right-hand-rule rotation with angle increasing from the $+Z$ axis towards the $+X$ axis.

θ_Z: positive rotation about an axis parallel to the `HRMA` $+Z$ axis; positive rotation is right-hand-rule rotation with angle increasing from the $+X$ axis towards the $+Y$ axis.

and

$tilt_Y$: positive rotation about an axis parallel to the `XRCF` $+Y$ axis; positive rotation is right-hand-rule rotation with angle increasing from the $+Z$ axis towards the $+X$ axis.

$tilt_Z$: positive rotation about an axis parallel to the `XRCF` $+Z$ axis; positive rotation is right-hand-rule rotation with angle increasing from the $+X$ axis towards the $+Y$ axis.

At the XRCF, the orientation of the HRMA as a whole was specified by *pitch* and *yaw*:

pitch: positive rotation about an axis parallel to the `XRCF` $+Y$ axis. Positive rotation is right-hand-rule rotation with angle increasing from the $+Z$ axis towards the $+X$ axis.

yaw: positive rotation about an axis parallel to the `XRCF` $+Z$ axis. Positive rotation is right-hand-rule rotation with angle increasing from the $+X$ axis towards the $+Y$ axis.

The raytrace simulations are always performed in the appropriate `SAOsac` coordinate system; the orientation of the HRMA relative to the source is given by *bundle_el* and *bundle_az*, the direction *from* the source *towards* HRMA. The relation between *pitch*, *yaw*, *bundle_el*, and *bundle_az* are summarized in Table 1.2.

Table 1.2: Relations between coordinate systems

$$
\begin{array}{lllll}
+bundle\_el_{SAOsac} & = & -bundle\_el_{DPSAOsac} & = & -pitch \\
+bundle\_az_{SAOsac} & = & -bundle\_az_{DPSAOsac} & = & -yaw
\end{array}
$$

The relations between coordinate directions are summarized in Table 1.3.

Table 1.3: Relations between coordinate systems

$$
\begin{array}{lllllllll}
+Y_{XRCF} & = & -Y_{HRMA} & = & -X_{SAOsac} & = & -X_{DPSAOsac} & & \\
+Z_{XRCF} & = & -Z_{HRMA} & = & +Y_{SAOsac} & = & -Y_{DPSAOsac} & & \\
+X_{XRCF} & = & +X_{HRMA} & = & -Z_{SAOsac} & = & +Z_{DPSAOsac} & & \\
+tilt_Y & = & -\theta_Y & = & +elmis_{SAOsac} & = & +elmis_{DPSAOsac} & = & +pitch \\
+tilt_Z & = & -\theta_Z & = & +azmis_{SAOsac} & = & -azmis_{DPSAOsac} & = & +yaw
\end{array}
$$

1.4. Coordinate Systems

Chapter 2

Measurements of Effective Area

In this section we describe the measurements of the HRMA effective area, their reductions, and the results.

There are two broad classes of effective area experiments done in XRCF Phase 1. These were [1] using the electron impact point source (EIPS) with the focal plane flow proportional counter (fpc_x2), at selected spectral lines; and [2] using the EIPS with a graphite anode, a beryllium filter, a high voltage of 15 kV, (all of which produce a quasi-continuum spectrum) with the focal plane solid state detector (ssd_x).

The data reduction and analysis for the two types of experiments (called "line" and "continuum" for conciseness) proceed in rather different fashions. The line measurements were processed at SAO by the MST Simulations and Analysis group, while the continuum measurements were reduced by the Project Science group at MSFC.

2.1 A Description of the Line Measurements

During Phase 1 at the XRCF, the HRMA effective area was measured at numerous spectral lines. The source used was the electron impact point source (EIPS). The anode selected, in concert with the high voltage used in the source, dictates the spectrum, both line and continuum, emitted by the source. Much of the continuum flux is absorbed by a filter placed between the source and the beam-line (and hence all the detectors). This filter is chosen in such a way as to have an optical depth of 2 or 4 at the line in question, and so it is much thicker at slightly higher energies where it has an absorption edge.

Most of the effective area experiments were in fact encircled energy (EE) measurements, in which the total effective area enclosed by a variety of circular apertures in the focal plane is measured. The aperture diameters range from $5\,\mu$m to 35mm.

As mentioned in Chapter 1, the BND detectors are used to measure the photon flux density at the HRMA entrance, which is determined by dividing the count rate from each detector by the open area of its aperture (corrected for mesh transmission), and averaging the results.

This is then divided into the count rate from the focal plane detector, giving a quantity which has units of cm^2, known as the effective area. The quantity of interest here is the total effective area into the 2π steradians downstream from the HRMA. We have measured the effective area out to an aperture diameter of 35mm, and scanned the wings of the point spread function beyond that, to distances up to 115mm from the image core. These "wing scans" will be discussed in Chapter 6.

In addition to the encircled energy measurements, the Grating Team put into the test plan a series of effective area measurements without gratings in the optical system. These were done with 1mm apertures, at a wide variety of EIPS energies, in general with either the full HRMA, or with the outer two (1 and 3) or inner two (4 and 6) mirror shells. We have analyzed these data in the same way as the EE data.

There are also a series of effective area tests done with the Double Crystal Monochrometer (DCM). The reduction and analysis of these data will be difficult; they are complicated by both a weak signal (low signal-to-noise ratio) and poor beam uniformity (factor of two scatter among the various detector positions in the beam map). We will not comment further on these data here.

2.2 Reduction of the Line Measurements

The outputs of the HXDS (HRMA X-ray Detector System; the assemblage of detectors described above) equipment, for spectral detectors, consists of a pulse-height spectrum for each of the detectors (focal plane plus BNDs), and various derived products based on region-of-interest sums over spectral channels. These are converted into FITS files compatible with the XSPEC X-ray spectral analysis program.

The resulting FITS files are fit to a model which includes the source properties (spectral lines plus a Kramer continuum model, of the form $(E_{max} - E)/E$), the X-ray filter properties, and the detector properties. This model, known as JMKmod (Tsiang, 1997) is based on the discussion of proportional counter physics in Jahoda and McCammon (1988), generalized to include solid state detectors. We use a unit diagonal response matrix in XSPEC with this software, allowing us to control all the features of the detector model within our own software, and to adjust detector parameters as well as source parameters to fit the observed spectra.

There are in excess of 50 parameters to be set in this model, but the vast majority of them can be set from values obtained from the facility data or experiment design. We then fit the remaining 3 to 6 parameters interactively, once for each type of detector for each source setup. The interesting parameters here are the ones that describe the flux in the spectral line in question (including escape peaks, partial charge-collection "shelf" features in the spectrum, pileup, and other detector effects). Also allowed to float freely in most fits is the relative flux of the continuum and the line.

There are numerous effects to be accounted for in such a procedure. Here is a list of those we have done only approximately, with an estimated bias or error at the few percent level for each. They are discussed one by one below.

- The fits are done by minimizing the χ^2 statistic.
- No background subtraction is done.
- No correction is made for the mesh in the focal plane FPC window.
- Deadtime is estimated by the detector software, and we use this estimate.
- We have assumed that the quantum efficiency of all of the flow proportional counter detectors is identical.
- We assume the EIPS beam is uniform at the HRMA entrance, and estimate the flux by a straight average of the four BND-H detectors.

In cases where there are few counts per channel, the χ^2 statistic, with its built-in assumptions of Gaussian distributed errors, is both inappropriate and biased (Bevington and Robinson, 1992). A more appropriate statistic, based on maximum likelihood arguments and the Poisson distribution is discussed by Cash (1979), and Nousek and Shue (1989). This statistic is implemented within

XSPEC, and only technical details of learning how to use the errors it generates prevent us from using it exclusively. We have verified that in cases with many counts per channel this C-statistic produces comparable results to the conventional χ^2 method.

For the Encircled Energy experiments, the count rates are orders of magnitude above background in every case. Therefore, for these cases, background subtraction or modeling will not be a significant effect. For wing scan spectra, however, this will be important. In those cases, because of poor statistics in the background spectra, we elected to fit a function (often a power law plus Gaussian combination) to the background spectrum, and then use this function (with no free parameters) as a component in fitting the X-Ray spectra. This decision was driven in part by a feature of XSPEC which makes use of the C-statistic (see previous paragraph) incompatible with background subtraction. It also eliminates the need to deal with channels which, due to statistical fluctuations, would have a negative count rate if background subtraction were done.

The FPC detectors have a mesh of 100 μm wires on 2mm centers to support their plastic windows against the pressure differential. For the BND detectors, which are uniformly illuminated, we have reduced the working area by the fraction of the geometrical area obscured by this mesh. For the focal plane detector, a focused, on-axis image will fit within a single mesh cell, and an effort was made to place the focused image at the center of such a mesh cell. Mesh obscuration is thought to be small in most cases. Proper accounting for this effect will ultimately be done by a ray trace simulation of the mirrors and FPCs.

The ratio of the quantum efficiencies of the detectors should come into the effective area. We have assumed that the detectors are identical, and so that this ratio is unity. Eventually the details of window thicknesses and counter body dimensions will need to be accounted for. We estimate this effect to be at the level of a few percent or below, except possibly at very low energies (*i.e.* the Be and B K-α lines). Ultimately the detectors will each be calibrated at BESSY, and absolute quantum efficiency calibrations will be used.

Detector dead time is estimated by the detector operating software using a Gedke-Hale technique, and we adopt this estimate (which is recorded in each raw spectral file header). An electronic pulser input was included in nearly all spectra, and a comparison of pulses injected to pulses detected will allow a more accurate dead time correction. We believe this effect is of the order of a percent.

The EIPS appears to present a beam of X-Rays which is uniform at the 2% level or better at the HRMA entrance. Extensive beam mapping efforts were undertaken, and a sampling of these data are presented in Chapter 9.

2.3 Line Measurement Results

In Table 2.1 we give measured encircled energies for the largest aperture used in each experiment. Also given are the mirror shells used, and the energy of the spectral line.

The EE measurements were made shell-by-shell at the K-α lines of C, Al, Ti and Fe, and with the full HRMA at Cu L, Ag L, Sn L, Cr K, and Cu K. The Sn L spectrum is of sufficient complexity that results from that test will not be reported here. The Ag L tests were done with the `ssd_x` at the focal point, and so we normalized them to the `ssd_5` beam normalization detector. Since the largest `ssd_x` aperture is 2mm instead of 35mm, we present the results of the Ag L tests in Table 2.2.

Errors quoted are the formal errors derived from XSPEC parameter estimation. A more careful approach would be to derive confidence intervals for the line strength, and propagate them through the calculations. An additional term, added in quadrature, is included to account for the RMS variation among the BND detectors when calculating the X-Ray flux at the HRMA entrance. In

Table 2.1: Measured Line Encircled Energies, 35mm aperture

Energy [keV]	Shell	$A_{\rm eff}$ [cm^2]
0.277	1	317.46 ±14.24
0.277	3	203.06 ± 9.38
0.277	4	169.21 ± 7.66
0.277	6	93.68 ± 3.80
0.930	All	750.14 ±38.27
1.486	1	296.30 ± 5.09
1.486	3	197.27 ± 1.80
1.486	4	161.25 ± 1.73
1.486	6	91.76 ± 1.11
4.510	1	99.54 ± 1.54
4.510	3	110.84 ± 1.59
4.510	4	102.65 ± 1.99
4.510	6	67.62 ± 1.05
5.410	All	312.56 ± 7.14
6.400	3	58.32 ± 1.98
6.400	4	82.70 ± 3.17
6.400	6	64.58 ± 2.14
8.030	All	77.97 ± 1.92

many cases, this term dominates the error. In such cases, understanding the beam uniformity data and the variation in sensitivity among the BND detectors (and as a function of energy) will allow reduction of the size of the error bars.

2.4 Reduction of the Continuum Measurements

Much of the work reported in this section was done by Allyn Tennant of the Project Science group at MSFC.

The continuum spectrum was obtained by placing a graphite anode into the EIPS, setting the source high voltage to 15 kV, and using a beryllium filter. This results in a spectrum which is close to a Kramer continuum spectrum, with weak lines from residual heavy elements which contaminate the graphite anode. We fit the spectrum in the vicinity of the lines with a combination of a continuum and Gaussian line profiles, and used the centroids to obtain a relation between photon energy and detector pulse-height channel. This relation is quite linear, but with a small zero-point offset.

After adjusting the mapping between channel number and energy for both the `ssd_x` and `ssd_5` spectra, they were divided, and scaled by geometrical factors (`ssd_5` aperture area, and ratio of source distances squared) to form an effective area, at all energies from about 1 keV upwards, at SSD resolution. The result is an effective area curve which allows us to interpolate between the FPC line measurements, and to independently check the accuracy of that method.

The largest pinhole available for these continuum EE measurements is 2mm in diameter, so for some optics and at some energies, there may be substantial (up to about 10%) amounts of the power scattered beyond the largest aperture used. These measurements were done on a shell-by-shell basis. For information only, we have summed these curves. *The reader should be aware that this procedure introduces errors,* and may not be representative of the HRMA performance as a whole, since the various mirror shells do not come to a focus at the same physical point. Thus the curve presented here is not exactly what would be observed through a 2mm aperture exposed to the full HRMA.

The resulting effective area curve shows a small bump near the Ge edges around 1.25keV. We are uncertain of the cause, but the effect is real in the sense that it is clearly visible in the raw data. The SSD quantum efficiency falls rapidly below 1keV, and so the data in this energy regime should not be trusted. The data used here were taken on 1997 January 13 with a 2μs shaping time constant. There are additional data taken with a 10μs time constant, which will have an effect on the energy resolution of the detectors.

In Figure 2.1 we plot both the continuum measurements of the effective area, and the line measurements. In order to make the measurements comparable, we have used the largest pinhole available in the continuum measurements (2mm), and the same size pinhole from the line measurements. (Thus the effective areas reported here are somewhat less than the ones in Table 2.1, which used a 35mm aperture.) Five curves are plotted, one for each shell plus the sum. When the line measurements were done shell-by-shell, they are plotted that way; those done for the full HRMA are plotted near the full HRMA curve.

In Table 2.2 we give the line measurements of the effective area in each case plotted in Figure 2.1, along with an interpolation of the continuum measurement at the same energy. All these data were taken with 2mm apertures. Carbon points have been omitted from the table since the continuum data do not exist for this low energy. Note that the line measurements are between 88% and 99% of the continuum measurements. A notably large discrepancy occurs for shell 1 at Ti K; otherwise the size of the disagreement generally increases with energy. Causes for these discrepancies are under investigation, but may include

- Inaccurate source distances for the various detectors (for instance, the continuum ssd_5 fluxes were extrapolated to the BND-H position, while the line fpc_h fluxes were corrected to the front of the HRMA glass; this, however, is only a 0.8% effect);
- Systematic differences in sensitivity among the BND-H detectors, which are known to change with energy;
- Unknown details of the quantum efficiency of the fpc_x2 detector;
- Systematics of the spectral fits;
- Differences between the ssd_x and ssd_5 quantum efficiency and spatial uniformities;
- Steeply falling spectra convolved with a finite SSD resolution.

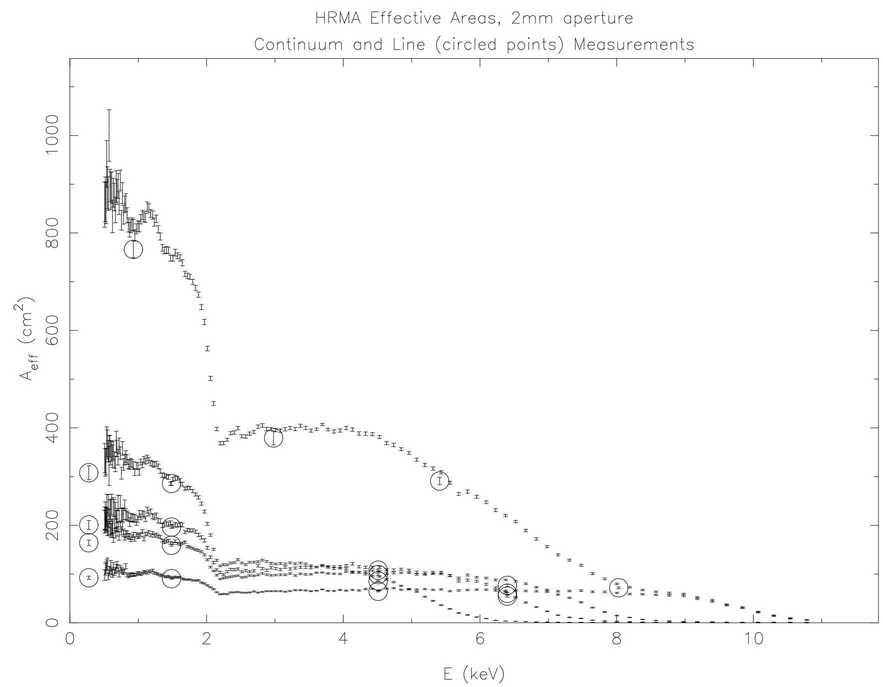

Figure 2.1: Line and Continuum measurements of the Effective Area. Circled points are line measurements. Continuum HRMA values are derived from the individual shells, which were measured at their best-focus axial locations. Note that the full-HRMA curve is obtained by summing the individual shells, and is presented for reference only. An actual measurement with a 2 mm pinhole would yield somewhat different results.

Table 2.2: Measured line and continuum encircled energies using 2mm apertures, and the line/continuum measurement ratio.

Energy [keV]	Shell	A_{eff}^{line} [cm^2]	A_{eff}^{cont} [cm^2]	Ratio
0.9297	All	766.27 ±17.0	815.70 ±12.5	0.939
1.486	1	285.94 ±3.54	288.80 ±3.77	0.990
1.486	3	196.49 ±2.55	202.62 ±3.92	0.969
1.486	4	159.13 ±1.75	163.60 ±2.40	0.972
1.486	6	90.57 ±1.27	93.19 ±1.53	0.971
2.98	All	379.35 ±14.2	396.35 ±3.42	0.957
4.51	1	85.69 ±1.38	95.33 ±1.31	0.898
4.51	3	107.99 ±1.79	114.21 ±2.01	0.945
4.51	4	99.04 ±2.07	105.65 ±1.43	0.937
4.51	6	64.67 ±1.26	67.37 ±1.01	0.959
5.41	All	290.86 ±7.73	310.40 ±3.26	0.937
6.4	3	54.73 ±1.76	60.94 ±1.40	0.898
6.4	4	76.86 ±2.59	87.70 ±1.51	0.876
6.4	6	60.45 ±2.09	66.04 ±1.21	0.915
8.03	All	71.81 ±1.77	78.88 ±1.51	0.910

Chapter 3

The HSI-measured HRMA Point Spread Function

The High Speed Imager (HSI) was used during Phase 1 of the XRCF calibration to measure both the inner and outer core of the HRMA Point Spread Function (PSF). The inner core tests were executed by focusing the beam on the center of the HSI and running the sources at fairly low fluxes to minimize the effects of gain saturation in the HSI pores. These measurements typically produced good photon statistics out to radii of approximately 0.5-1.0mm from the image centroids. The outer core measurements were carried out in two steps. First, an HSI image was taken slightly off one of the cusps in the HSI mask at a fairly low source flux (with the 4MFP filter in place). Second, the HSI was moved so that the beam would be centered on the cusp, the 4 MFP filter was removed from the source, and a long exposure was taken at a higher source flux. The image centroid in the longer HSI exposure on the cusp is then determined by calculating the centroid in the short off-cusp image and using the stage logs to determine the subsequent motion of the HSI. These outer core measurements produced good photon statistics out to radii of approximately 10mm from the image centroids. In this section I will present a preliminary analysis of the on-axis HSI images.

3.1 PSF/Inner Core Measurements

There are only a few HSI PSF/Inner Core measurements on-axis. Figure 3.1 shows the HRMA PSF at C-Kα at the HRMA ensemble focus. The HSI data was first degapped and background subtracted. The background rate was determined from the HSI exposure taken during the source change to the carbon anode. The PSF was determined by calculating the net counts in concentric annuli about the image centroid. The widths of the annuli vary from 1 pixel near the image centroid to 100 pixels near the edge of the detector. This was required to obtain good photon statistics in the outer portions of the image. The surface brightness plots in this chapter all have an arbitrary normalization. Figure 3.1 shows that the PSF clearly has an easily distinguishable core (radius of approximately 150 μm) and power-law component. The wings of the PSF can be characterized by a fairly steep power-law with $\Sigma \propto r^{-2.8}$.

Using a similar analysis, the PSF for each shell at Al-Kα was determined from the HSI images (see Figures 3.2 and 3.3). Figure 3.2 shows that shells 1, 3, and 4 have very similar PSFs, with a FWHM of approximately 35 μm. This includes the mirror resolution, the broadening of the image

due to the finite source size, and the intrinsic spatial resolution of the HSI (FWHM $\approx$ 20 μm). Due to the structure in the HSI image of shell 6, the image centroid is displaced by approximately 20 μm from the peak surface brightness (see Figure 3.2). The FWHM of shell 6 (which is somewhat meaningless due to its highly structured core) is significantly greater than the three larger shells and is approximately 100 μm. Figure 3.3 shows that the core region of the PSF has approximately the same extent for all four shells, and that the slope of the surface brightness in the wings of the PSF is consistent, within the photon statistics, for each shell.

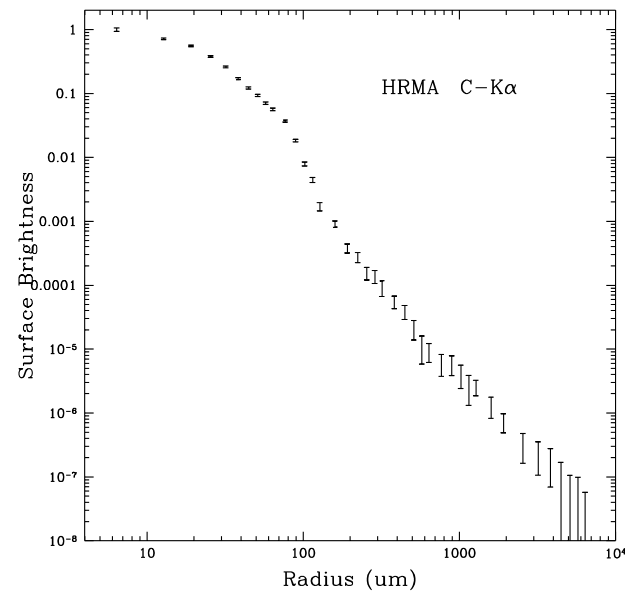

Figure 3.1: HRMA PSF at C-Kα

3.2 PSF/Outer Core Measurements

Most of the HSI PSF/Outer Core tests were done with the full HRMA ensemble. The data analysis is identical to that for the inner core measurements, except in how the image centroid is determined. Figure 3.4 compares the PSF/Outer Core measurements for a broad range of EIPS energies (C-Kα, Al-Kα, Ti-Kα, Fe-Kα, and Cu-Kα). There are several features evident in the surface brightness plots shown in Figure 3.4. At high energies (Fe-Kα, and Cu-Kα) there appears to be a steepening in the slope of the PSF at 1-2 mm. The opposite change in slope is evident at Al-Kα. Overall, the range in power-law indices in the surface brightness profile varies from -2.8 to -2.2. However, these results are highly preliminary. There are many concerns in any analysis of HSI data. In particular, the QE of uncoated microchannel plates is known to be highly angle dependent. To further investigate this effect, we have run several simulations and found that the mean incident photon angle only varies by 2-3 ° over the HSI for in-focus images. This should not produce a significant effect in the data analysis presented here. Another concern is the spatial linearity of the

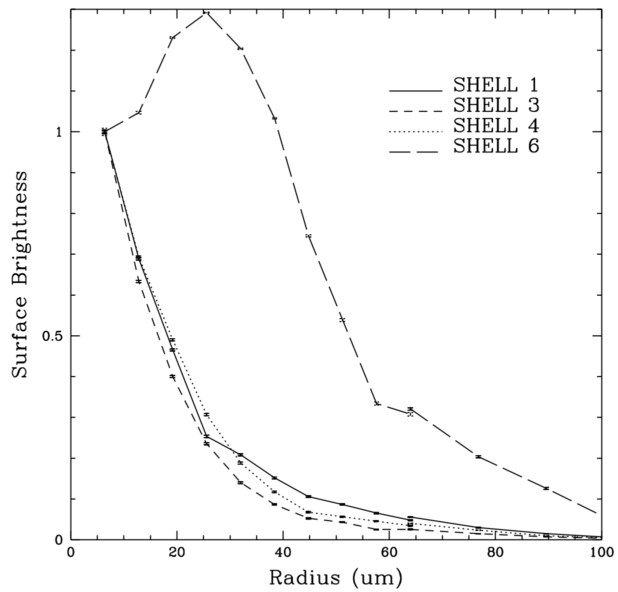

Figure 3.2: Comparison of the PSF for each shell at Al-Kα

HSI on large scales. The breaks in the surface brightness profiles could reflect spatial nonlinearity in the detector. All of this work still needs to be compared to the FPC encircled energy tests to check for consistency. Such a comparison will help determine what effects are detector related.

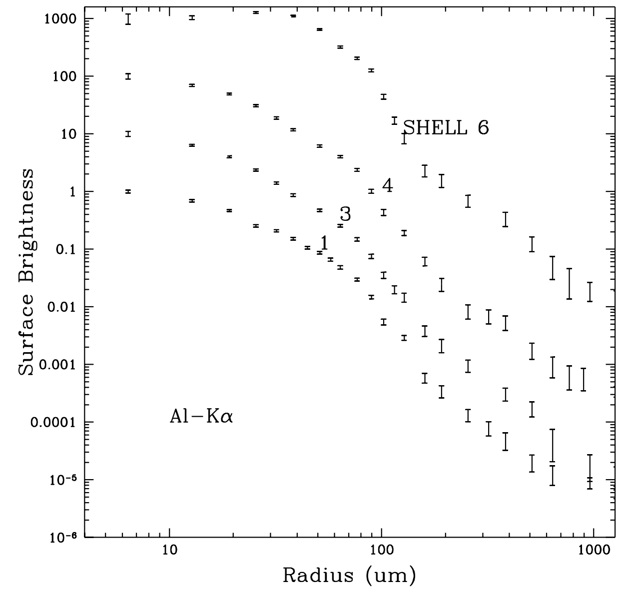

Figure 3.3: Comparison of the PSF for each shell at Al-Kα

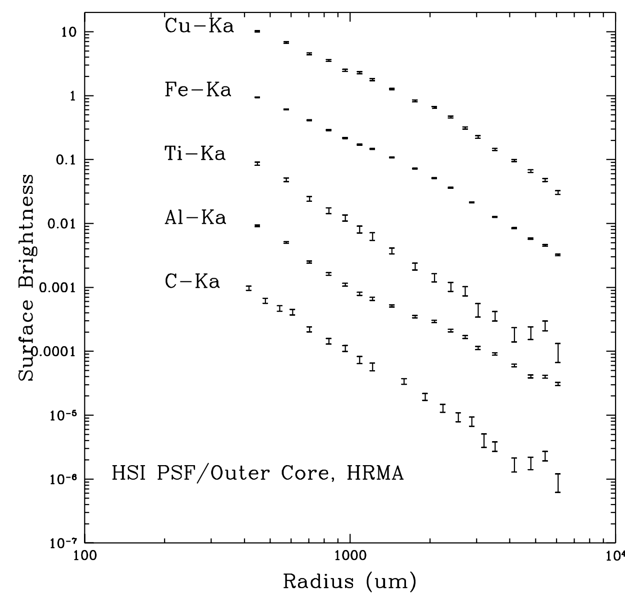

Figure 3.4: Comparison of the PSF/Outer Core tests at a range of energies

Chapter 4

PSF-1D and PSF-2D Scans

In this chapter, we examine the Point Spread Function (PSF) of the HRMA through both one-dimensional and two-dimensional pinholes scans (PSF-1D and PSD-2D scans, respectively), as measured with the Flow Proportional Counters (FPCs) during Phase 1. We will also compare those tests to simulated pinhole scans using the MST `SAOsac` simulator.

4.1 PSF-1D Scans

The PSF-1D scans are executed by a focal plane FPC (fpc_x2) which is moved horizontally through the center of the focused X-ray beam (as found in preceding `beam-center` tests) and then vertically through the same center. The FPC was fitted with a $5\,\mu$m diameter aperture and was usually stepped by $2\,\mu$m between collects for a total of 81 measurements taken on each axis (yielding one measurement at the center of the focused X-ray beam, and 40 measurements to each side). However, some tests were taken with only 33 measurements in each direction, with the FPC stepping by $3\,\mu$m each time.

We have concentrated our early efforts on understanding the PSF-1D scans taken with the EIPS Al-Kα source near the beginning of Phase 1. These scans, which were the only PSF-1D scans taken on a shell by shell basis, are summarized in Table 4.1.

Table 4.1: Analyzed PSF-1D Scans

Shell	Axis	TRW ID	Run ID	Date	Day [GMT]
1	Y	D-IXF-P1-1.001	107290	Jan 03, 1997	003
	Z	D-IXF-P1-1.002	107292	Jan 03, 1997	003
3	Y	C-IXF-P1-1.003	106768	Dec 21, 1996	356
	Z	C-IXF-P1-1.004	106769	Dec 21, 1996	356
4	Y	D-IXF-P1-11.005a	107937	Jan 08, 1997	008
	Z	D-IXF-P1-11.006	107938	Jan 08, 1997	008
6	Y	D-IXF-P1-11.007	107941	Jan 08, 1997	008
	Z	D-IXF-P1-11.008	107942	Jan 08, 1997	008

For each test, we converted the HXDS output files to FITS files, and fit them in XSPEC using the JMKmod model (Tsiang, 1997) of the FPC detectors. This fitting was done in the same manner

as the data reduction for the Effective Area measurements; for more details on the fitting process and systematic effects inherent in its use, see Chapter 2.

In addition to the analysis of the FPC measurements, these tests have been modeled with the MST `SAOsac` simulator. The measurements were simulated at Al-Kα, and were done in the same manner as the XRCF tests: we started with a `beam-center`, followed by horizontal and vertical scans centered upon the determined peak. Shells 1, 2, and 3 had 81 point scans, with a $5\,\mu$m aperture stepped by $2\,\mu$m, while Shell 6 had 33 point scans with a $5\,\mu$m aperture stepped by $3\,\mu$m. During the tests that were taken on IRIG day 008 (scans of Shells 4 and 6), the HRMA's on-axis configuration was actually $-1'$ off-axis in yaw (Texter, 1997). Our simulations for those shells take this into account. (Note that we do not present data for the scans through Shell 6, as the beam centering routines did not converge on a center, and were aborted. These problems can be understood by looking at the PSF-2D scan for Shell 6 (Figure 4.13)).

Both measurements and simulations are displayed as effective areas. The data were shifted to place the A_{eff} peak of both the simulated and XRCF data at a position of zero. Figures 4.1 through 4.6 show both the actual XRCF data and the simulated measurements.

Listed in Table 4.2 are the Full-Width at Half-Maximum (FWHM) results for the shell by shell scans with the Al-Kα anode. For each shell, the FWHM was calculated by first fitting a spline to find the peak of the data, and then finding the width of the plot at half of that maximum by linear interpolation along both sides of the peak. Errors in A_{eff} (determined by the XSPEC fitting algorithm) were propagated through both the spline equation and the linear interpolation equation (assuming an error of $\pm 1\,\mu$m in the positioning of the motor stage) to derive the final error in the FWHM. The horizontal (Y) measurements are more indicative of the on-orbit performance.

Table 4.2: FWHM derived from PSF-1D scans

Shell	Axis	TRW ID	Run ID	FWHM [μm]	
				Measured	Simulated
1	Y	D-IXF-P1-1.001	107290	12.79 ± 1.10	6.27 ± 0.13
	Z	D-IXF-P1-1.002	107292	16.61 ± 1.07	8.25 ± 0.08
3	Y	C-IXF-P1-1.003	106768	12.47 ± 1.35	6.43 ± 0.04
	Z	C-IXF-P1-1.004	106769	21.23 ± 1.33	6.82 ± 0.06
4	Y	D-IXF-P1-11.005a	107937	18.39 ± 1.33	15.60 ± 0.24
	Z	D-IXF-P1-11.006	107938	20.67 ± 1.24	20.65 ± 0.16

The most apparent feature in the comparisons between our simulations and test results is the difference in peak height, which appears greatest for Shells 1 and 3, where the simulated peaks are approximately 160% and 210% higher, respectively, than the actual test peaks. This difference could be caused by a failure in the actual `beam-center` measurements to arrive at an accurate center for these tests, and thus these PSF-1D scans may have been offset from the peak. Another reason that might account for at least part of this difference is that the simulator works only with a point source, and so perhaps we are seeing effects due at least partly to the extended nature of the real EIPS source. It should be noted, however, that the simulations do reproduce the wings of the scan fairly well in many cases, the only exception being the Shell 3 vertical scan.

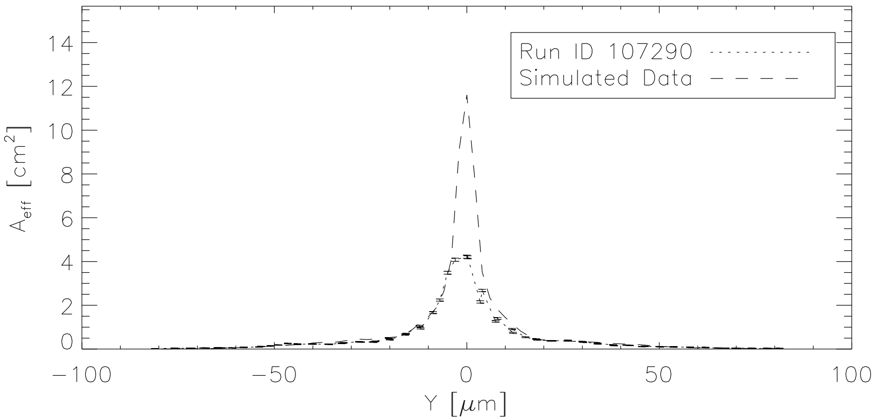

Figure 4.1: Horizontal PSF-1D Scan for Shell 1 vs. Simulation

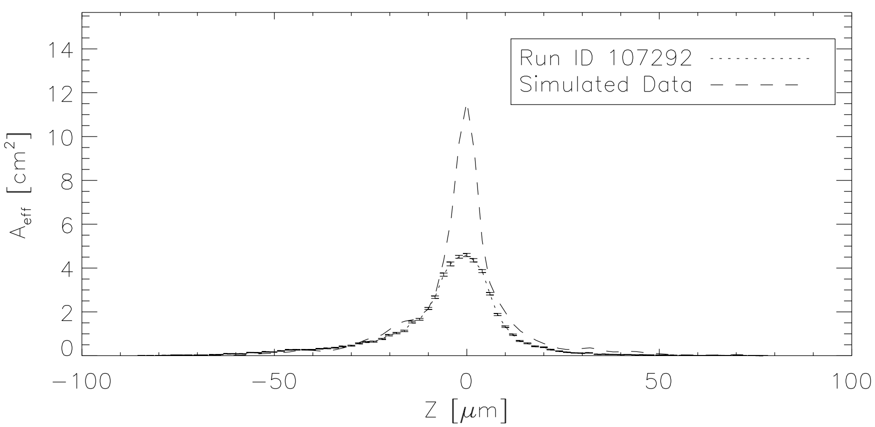

Figure 4.2: Vertical PSF-1D Scan for Shell 1 vs. Simulation

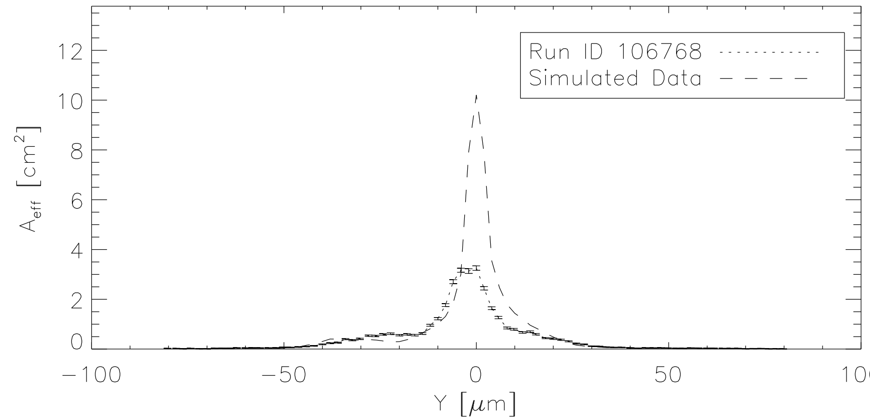

Figure 4.3: Horizontal PSF-1D Scan for Shell 3 vs. Simulation

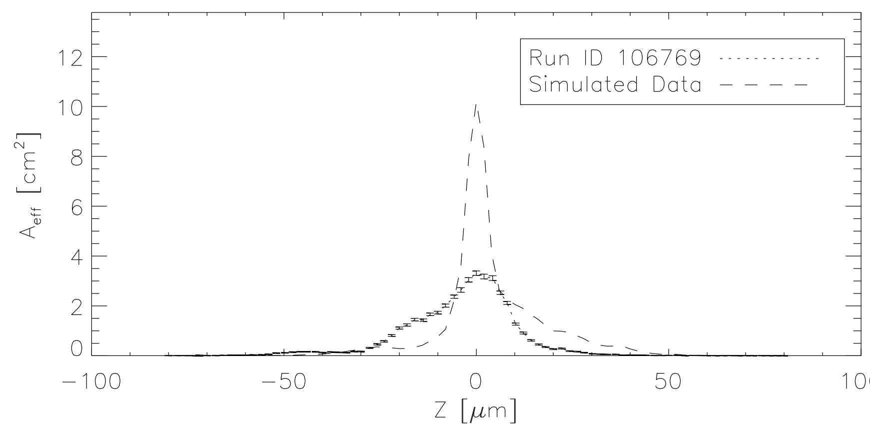

Figure 4.4: Vertical PSF-1D Scan for Shell 3 vs. Simulation

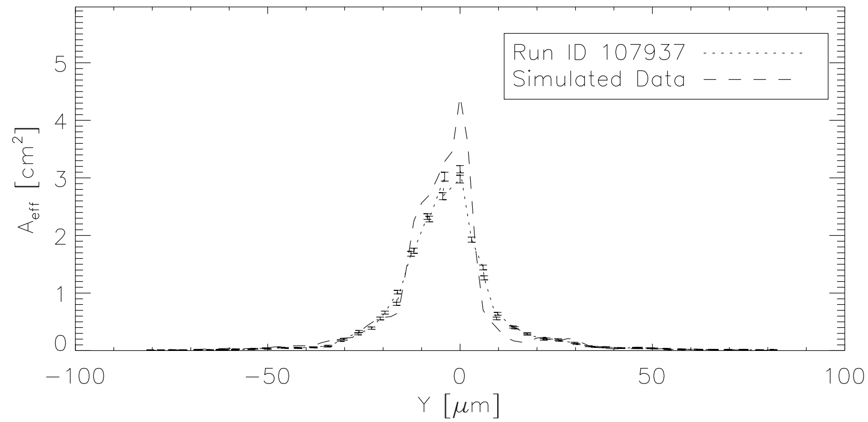

Figure 4.5: Horizontal PSF-1D Scan for Shell 4 vs. Simulation. Note that this has yaw $= -1'$.

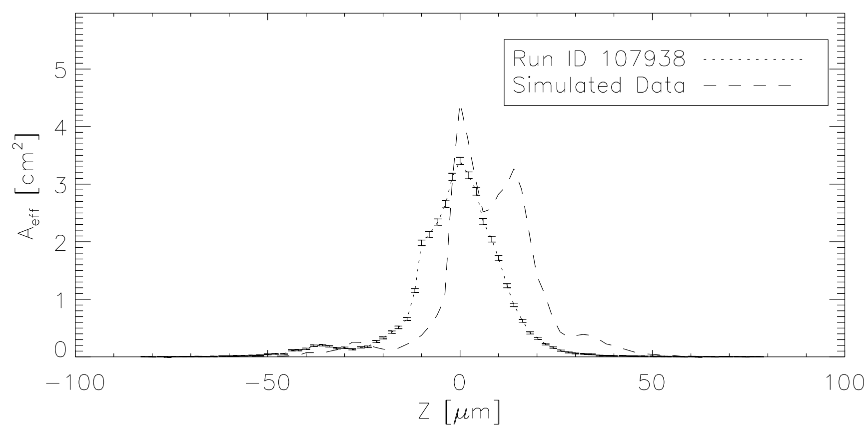

Figure 4.6: Vertical PSF-1D Scan for Shell 4 vs. Simulation. Note that this has yaw $= -1'$.

4.2 PSF-2D Scans

4.2.1 Shell by Shell PSF-2D Scans and Model Comparisons

One problem apparent with the PSF-1D scan is that if the center of the beam was not found accurately, slices through the image will not sample the PSF's core. Also, it would, of course, be much more informative to look at how the PSF varies over the entire focal plane, rather than just along two axes across it. To answer these concerns, two dimensional PSF (PSF-2D) scans were taken at XRCF.

The PSF-2D tests were executed by first finding the center of the beam (using `beam-center`) and then sampling over a 19 by 19 grid around that center with a 10 μm pinhole. These 19 by 19 scans are the highest resolution 2D scans that we have of the Point Spread Function. Other, successive PSF-2D scans used larger apertures over a larger area, but we have chosen to concentrate initially on the high resolution 19 by 19 scans.

The last set of these PSF-2D tests were shell by shell runs with the Al-Kα EIPS anode, and are listed in Table 4.3. Each of these tests was analyzed by simply taking the HXDS "`.sum`" files (which contain the total counts found in a specified Region of Interest (ROI) and the live time, which we use to get an estimate of the detected flux) for `fpc_x2` and the BND "North" detector and taking the ratio of the two count rates to derive a normalized flux at the focal plane. Due to imprecise motor motion and logging for the small step sizes used with the focal plane detector, the resultant set of stage locations is not a regular grid, and the raw data are thus not easily plotted. To get surface plots of the PSF-2D scans, linear interpolation was used to derive the values on a regular coordinate grid. The peak of the scan was then defined to be the center of the plot, with the coordinate axes shifted to have the origin located at the peak.

Table 4.3: Analyzed PSF-2D Scans

Shell	TRW ID	Run ID
1	E-IXF-P2-1.001	111481
3	E-IXF-P2-1.002	111477
4	E-IXF-P2-1.003	111479
6	E-IXF-P2-1.004	111483,111485

All tests were taken on Feb 8, 1997 (IRIG day 039)

Along with the surface plots of the XRCF data, we have also run simulations of those PSF-2D scans, using the model `xrcf_SAO1G+HDOS_HDOS-scat-970220_03` at Al-Kα. Again, the simulations were done in exactly the same manner as the measurements: starting out with `beam-center`, and then sampling with a 10 μm pinhole around that center in a 19 by 19 grid. As with the PSF-1D scans, the simulated detected counts were then divided by the input flux density to determine the simulated A_{eff}. The axes of the coordinate grid were also translated to set the peak value at the center of the plot. The comparisons of these simulations of the shell by shell PSF-2D scans to the actual tests are shown in Figures 4.7 through 4.14.

The most striking difference is that the simulated peaks are again somewhat higher than the peaks found in the actual test data: Shells 1, 3, and 4 differ by approximately 60%, 40%, and 25%. While large, these differences are remarkably better than the PSF-1D percentage differences for Shells 1 and 3, while Shell 4 has approximately the same percent difference as before. Of course, there is still much work to be done to resolve the differences between the test data and the simulations, but it seems that the PSF-2D scans do give us a better look at the image core than

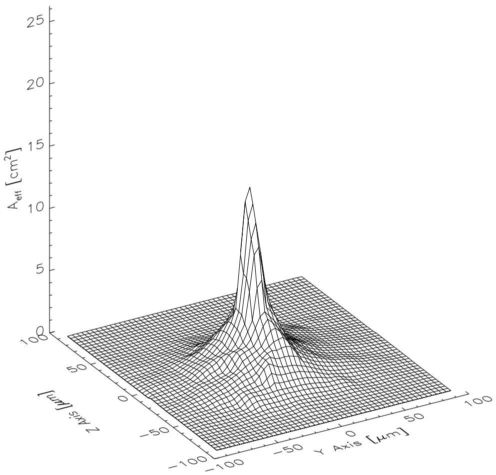

Figure 4.7: FPC PSF-2D Scan at Al-Kα for Shell 1

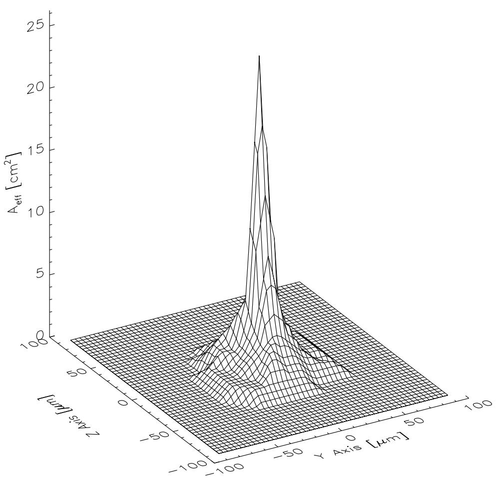

Figure 4.8: PSF-2D Simulated Scan at Al-Kα for Shell 1

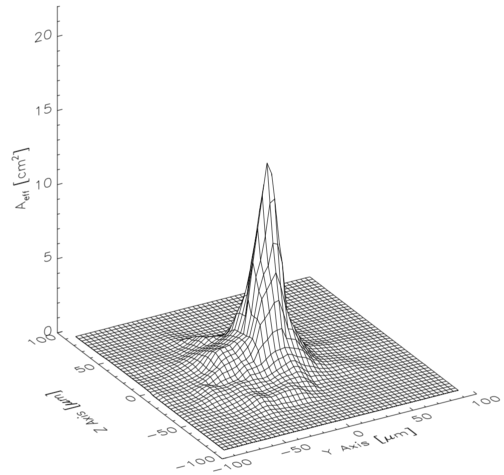

Figure 4.9: FPC PSF-2D Scan at Al-Kα for Shell 3

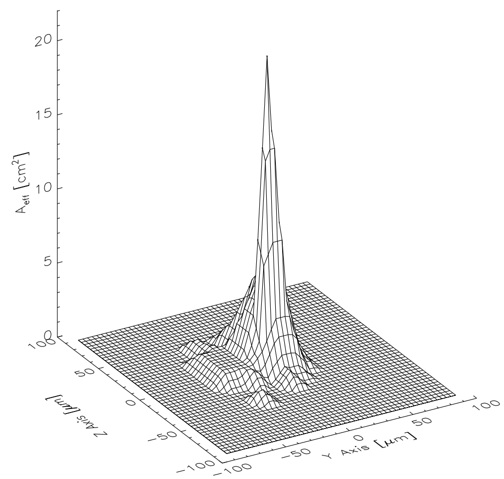

Figure 4.10: PSF-2D Simulated Scan at Al-Kα for Shell 3

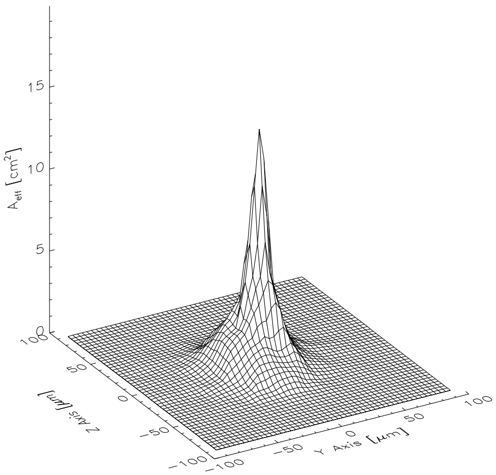

Figure 4.11: FPC PSF-2D Scan at Al-Kα for Shell 4

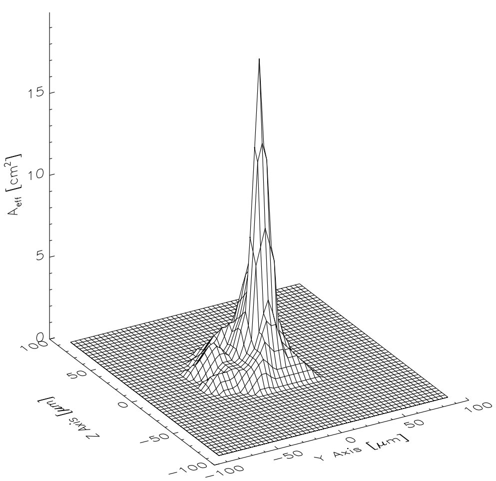

Figure 4.12: PSF-2D Simulated Scan at Al-Kα for Shell 4

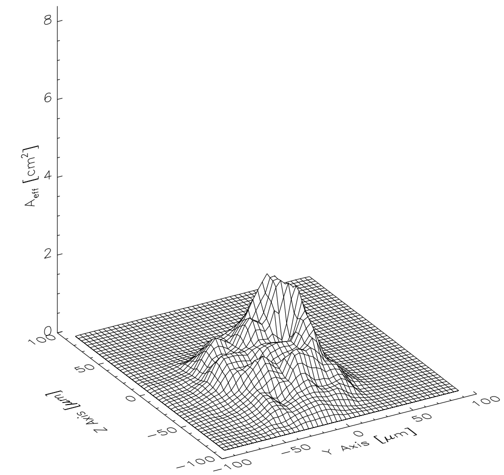

Figure 4.13: FPC PSF-2D Scan at Al-Kα for Shell 6

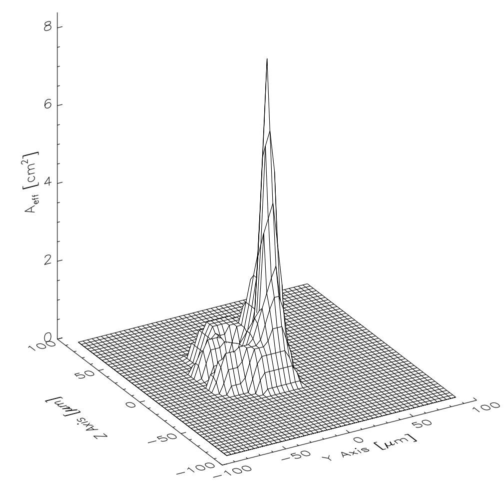

Figure 4.14: PSF-2D Simulated Scan at Al-Kα for Shell 6

the PSF-1D scans did for Shells 1 and 3, in that their peak heights are much greater. This again hints that perhaps the `beam-center` routines carried out before the analyzed PSF-1D scans were not entirely successful in finding the center of the beam: only Shell 4 seems to have had an accurate center. Additionally, since the simulations do not include the extended nature of the X-ray source, they will be much "peakier" than the real data. Shell 6 remains a problem, due to the extended nature of its image.

4.2.2 HRMA Ensemble PSF-2D Scan

Another 19 by 19 scan that has been analyzed is a much earlier scan of the HRMA Ensemble PSF at Al-Kα. This PSF-2D scan was Run ID 106772 (TRW ID C-IXF-P2-2.001) taken on December 21, 1996, with the Al-Kα anode. This test was analyzed more extensively than the rest, utilizing the JMKmod FPC model and XSPEC fitting to derive A_{eff} for each measurement, which were then plotted together in the same manner as the previous measurements (see Figures 4.15 to 4.16).

4.2.3 FWHM Calculations from PSF-2D Scans

Since it seems very possible that few of the PSF-1D scans actually sampled the core of the Point Spread Function, it is much more informative to look at the FWHM calculated from the PSF-2D scans. This was done by simply finding the peak in each PSF-2D scan, and then sampling along the horizontal and vertical axes through that peak to simulate a PSF-1D scan. It must be noted, however, that the PSF-2D scans were executed using a 10 μm pinhole on an FPC stepped by 10 μm, whereas the earlier PSF-1D scans were run using a 5 μm pinhole on an FPC stepped by 2 to 3 μm.

Comparison plots of the horizontal and vertical scans through both the test data and simulated data are shown in Figures 4.17 through 4.26. Again, the difference in height is very apparent, but is not as great as the differences seen in the the PSF-1D scans, as mentioned before. In fact, for Shell 4, the simulated A_{eff} measurements match very well with the real test results. And, again, we see that the simulations match the wings of the PSF fairly well. Shell 6 remains a problem due to its very extended image.

Analyzing these portions of the PSF-2D scans in the same way that we did the earlier PSF-1D scans, we can find the FWHM for each shell. The results of that analysis are shown in Table 4.4. The HRMA Ensemble is performing at the half-arcsecond level, as are all of the individual mirror shells, with the exception of Shell 6, with only slightly degraded performance. The horizontal (Y) measurements are more indicative of the on-orbit performance.

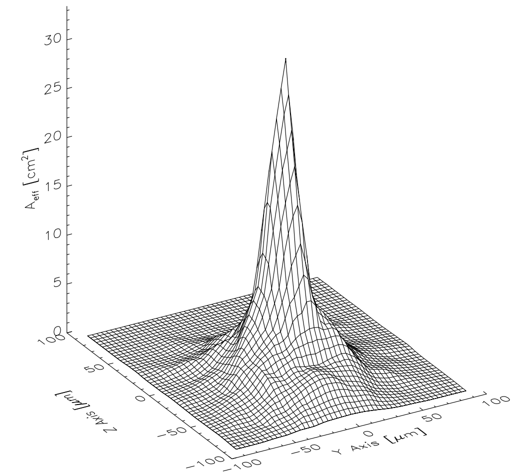

Figure 4.15: FPC PSF-2D Scan at Al-Kα for HRMA Ensemble

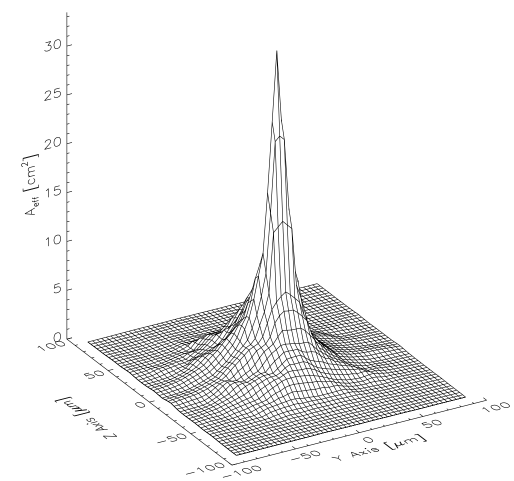

Figure 4.16: PSF-2D Simulated Scan at Al-Kα for HRMA Ensemble

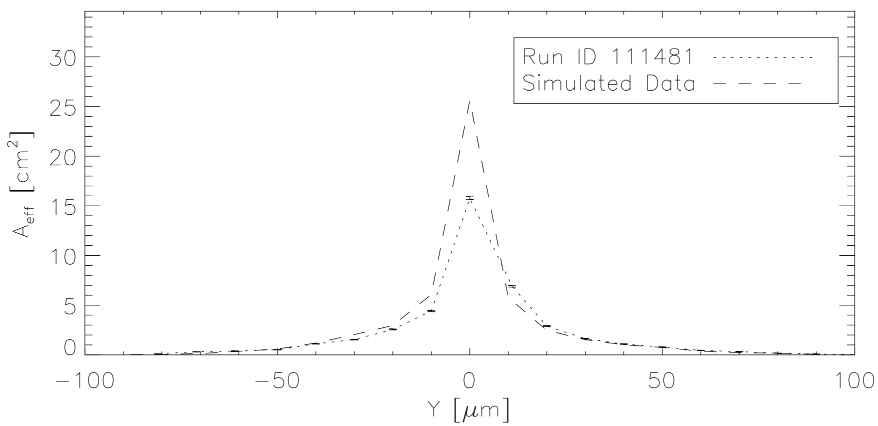

Figure 4.17: Horizontal slice through PSF-2D Scan for Shell 1 vs. Simulation

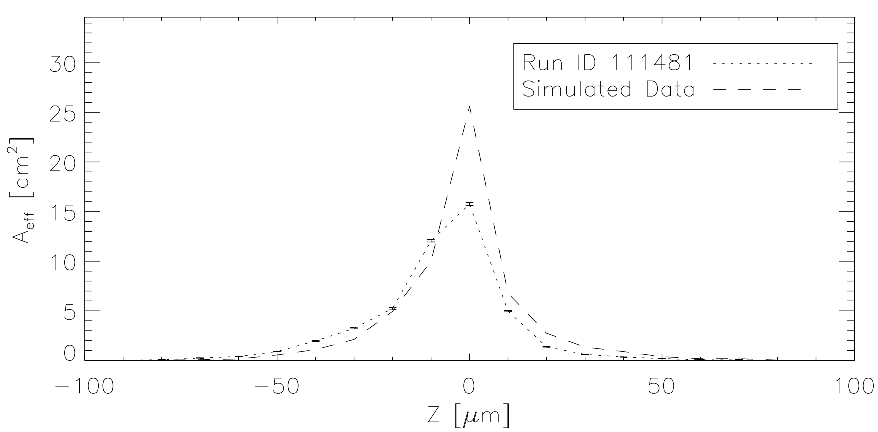

Figure 4.18: Vertical slice through PSF-2D Scan for Shell 1 vs. Simulation

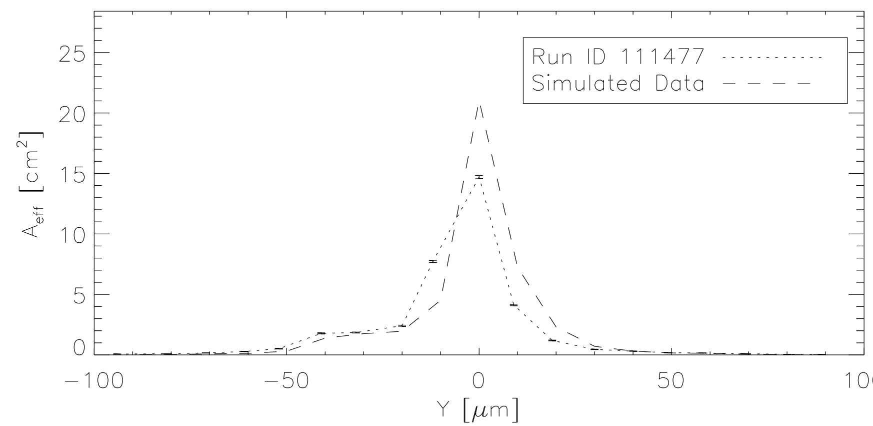

Figure 4.19: Horizontal slice through PSF-2D Scan for Shell 3 vs. Simulation

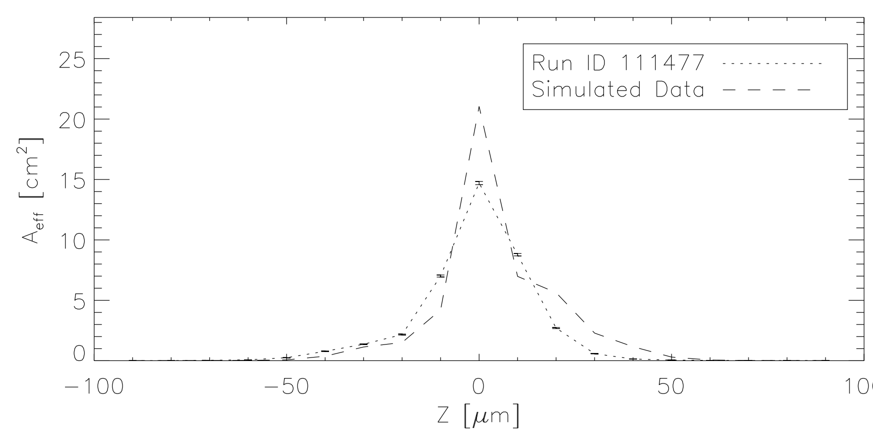

Figure 4.20: Vertical slice through PSF-2D Scan for Shell 3 vs. Simulation

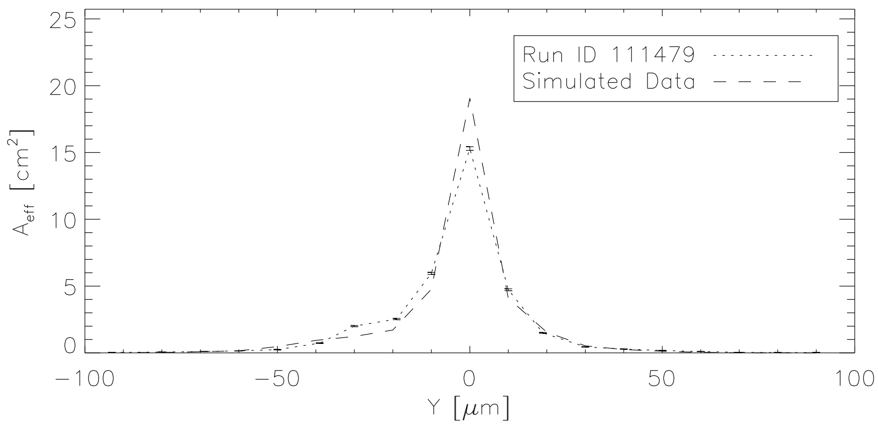

Figure 4.21: Horizontal slice through PSF-2D Scan for Shell 4 vs. Simulation

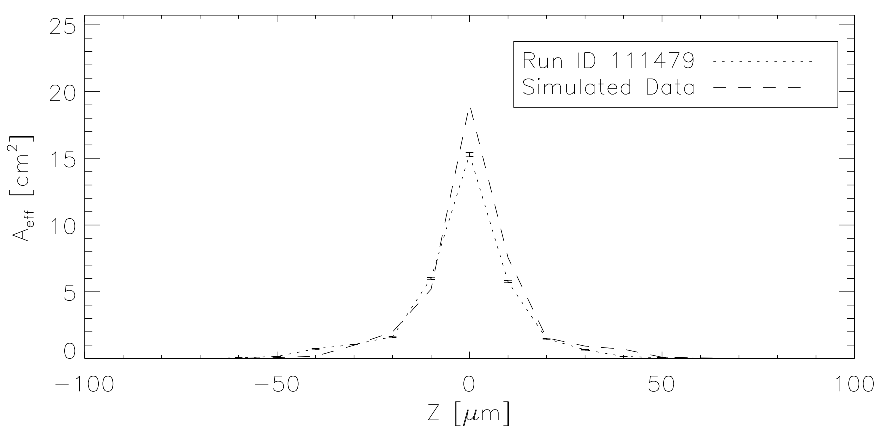

Figure 4.22: Vertical slice through PSF-2D Scan for Shell 4 vs. Simulation

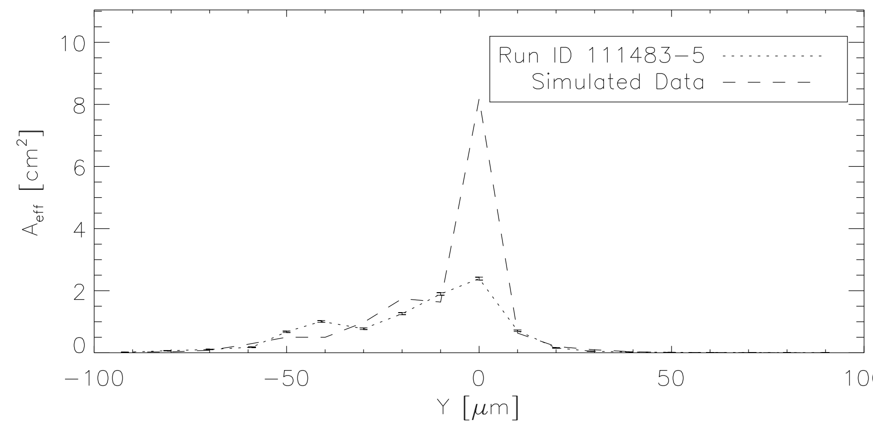

Figure 4.23: Horizontal slice through PSF-2D Scan for Shell 6 vs. Simulation
.

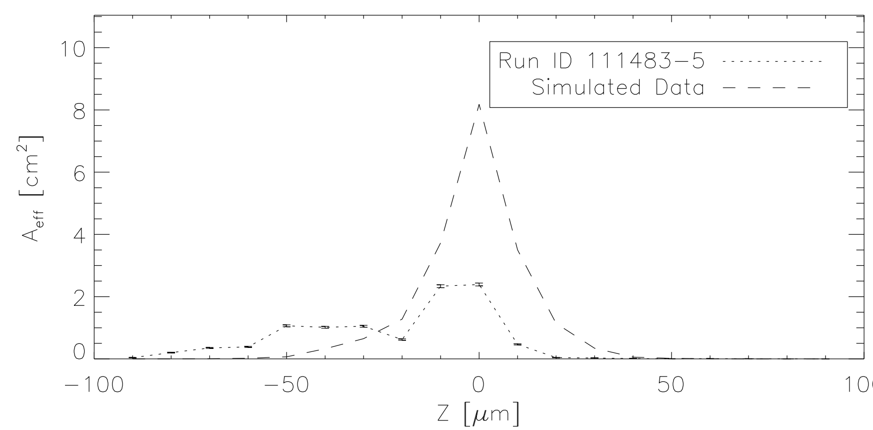

Figure 4.24: Vertical slice through PSF-2D Scan for Shell 6 vs. Simulation

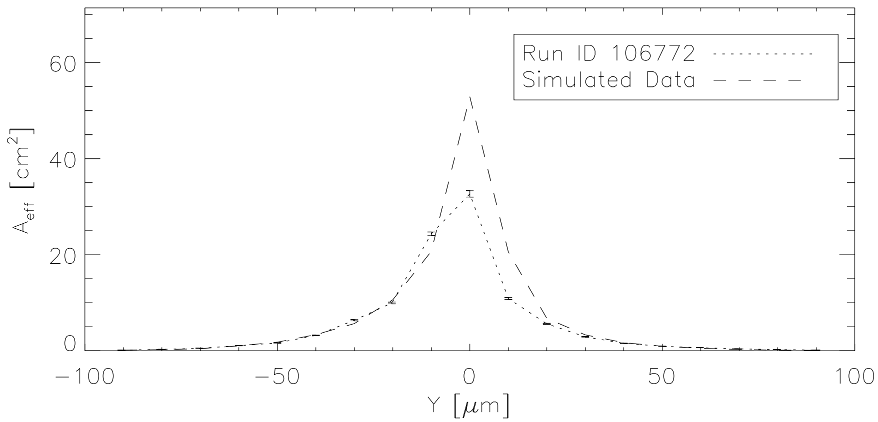

Figure 4.25: Horizontal slice through PSF-2D Scan for HRMA Ensemble vs. Simulation

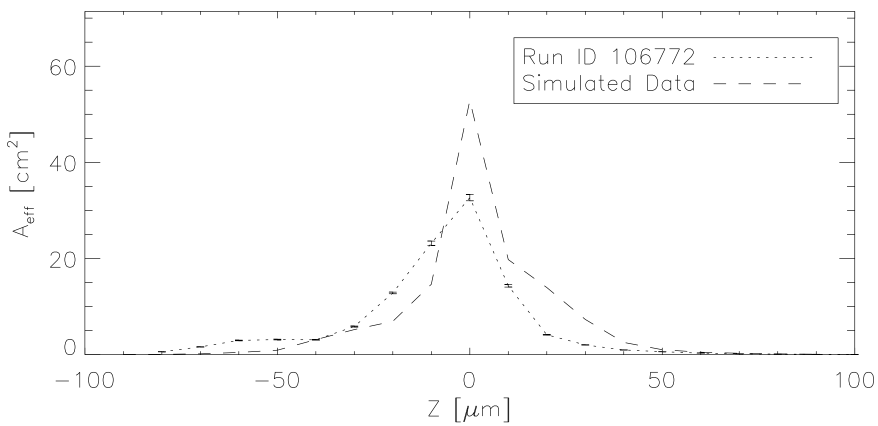

Figure 4.26: Vertical slice through PSF-2D Scan for HRMA Ensemble vs. Simulation

Table 4.4: FWHM derived from PSF-2D scans

Shell	Axis	TRW ID	FWHM [μm]	
			Measured	Simulated
1	Y	E-IXF-P2-1.001	16.61 ± 1.19	13.01 ± 0.06
	Z		22.81 ± 1.11	14.98 ± 0.09
3	Y	E-IXF-P2-1.002	18.21 ± 1.29	13.96 ± 0.09
	Z		21.85 ± 1.27	13.72 ± 0.08
4	Y	E-IXF-P2-1.003	15.41 ± 1.15	13.03 ± 0.07
	Z		16.25 ± 1.19	15.13 ± 0.11
6	Y	E-IXF-P2-1.004	27.47 ± 1.53	11.66 ± 0.09
	Z		21.00 ± 1.11	17.93 ± 0.16
HRMA Ensemble	Y	C-IXF-P2-2.001	22.64 ± 1.14	16.41 ± 0.05
	Z		25.29 ± 1.24	14.89 ± 0.06

Chapter 5

Encircled Energy

In this chapter we present a set of encircled energy curves, measured at various energies and for various mirror combinations.

The experiments and data reductions were described in Chapter 2. We present here plots of the effective area captured within a circular aperture centered on the focused image, as functions of the aperture diameter.

Some of the experiments were done one shell at a time, on axis, at the C K-α, Al K-α, Ti K-α, and Fe K-α lines. Also done on-axis were full-HRMA measurements at the Cu L-α, Cr K-α, and Cu K-α lines. In addition, there were "ends survey" tests done, in which one quadrant of a single mirror shell was exposed, and the HRMA tilted in pitch or yaw to simulate an infinite source distance. This illuminates a larger fraction of the length of the optic, and allows one to search for effects of larger surface roughness near the ends of the optic.

A few encircled energy tests were done with the solid state detectors, both with the continuum source (EIPS with graphite target, 15 kV, and a beryllium target), and with selected lines such as Ag and Sn L-α. The analysis of these data lag behind the simpler FPC spectra, and are not reported here.

The natural units for the measured points in an encircled energy experiment are cm^2, since the measured quantity is the effective area, integrated over the aperture. There are occasional points where, due to experimental error, the error bars are large and the points lie off the trend line. In most cases these points are within the calculated error bar of the trend line, so few real excursions exist. Those excursions which are real are cases in which the aperture was not properly centered on the image, and so the flux measured in the pinhole is less than it should have been. These points should be ignored.

Current ray trace models do not yet incorporate an accurate image of the source's spatial structure, and so are not comparable to the data. The source is believed to subtend an angle of $0.2''$ or so as seen from the HRMA, and so the core of the image is somewhat more diffuse than the point-source ray trace models predict. The normalization of the curves are also somewhat discrepant. This effect is discussed elsewhere in this document, in the chapters on effective areas (Chapter 2 and Chapter 7). However, except for the inner core of the image, the shapes of the encircled energy curves match the simulations quite closely. Detailed comparisons are made in chapter Chapter 7.

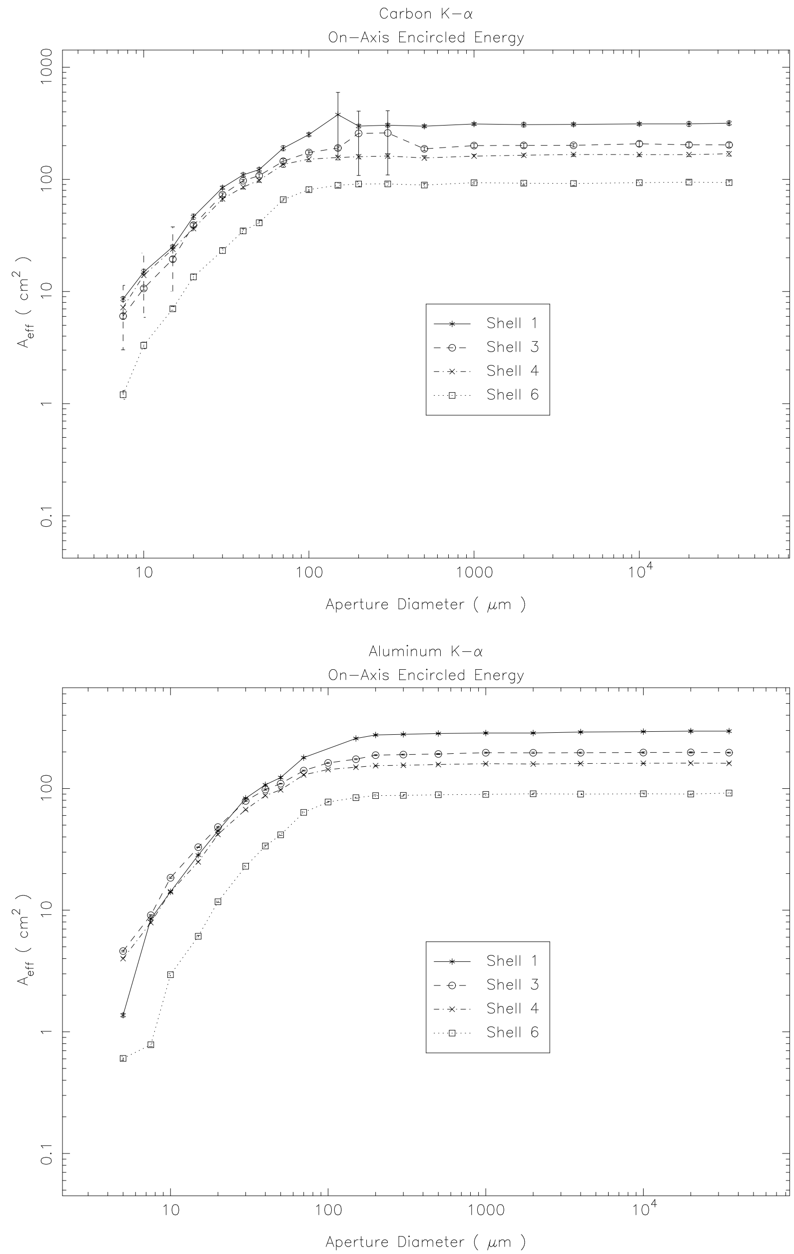

Figure 5.1: On-axis Carbon and Aluminum K-α Encircled Energy

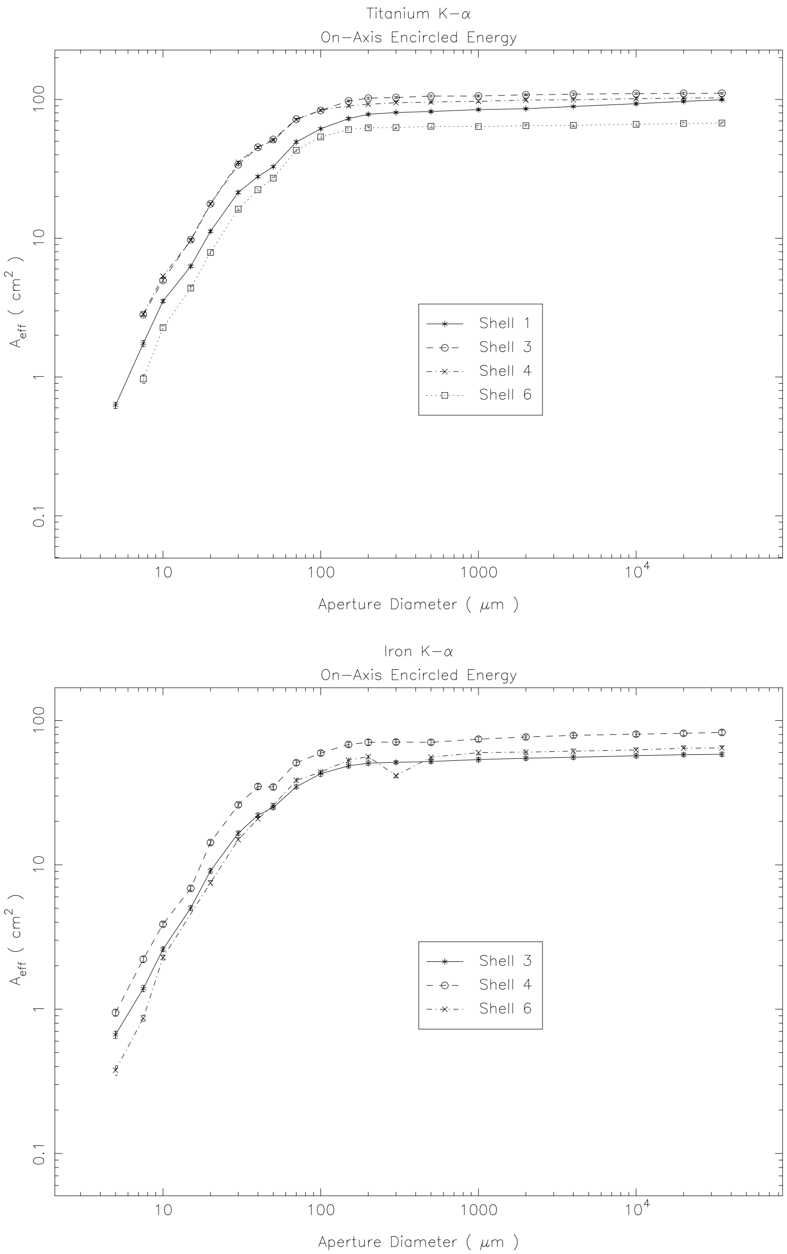

Figure 5.2: On-axis Titanium and Iron K-α Encircled Energy

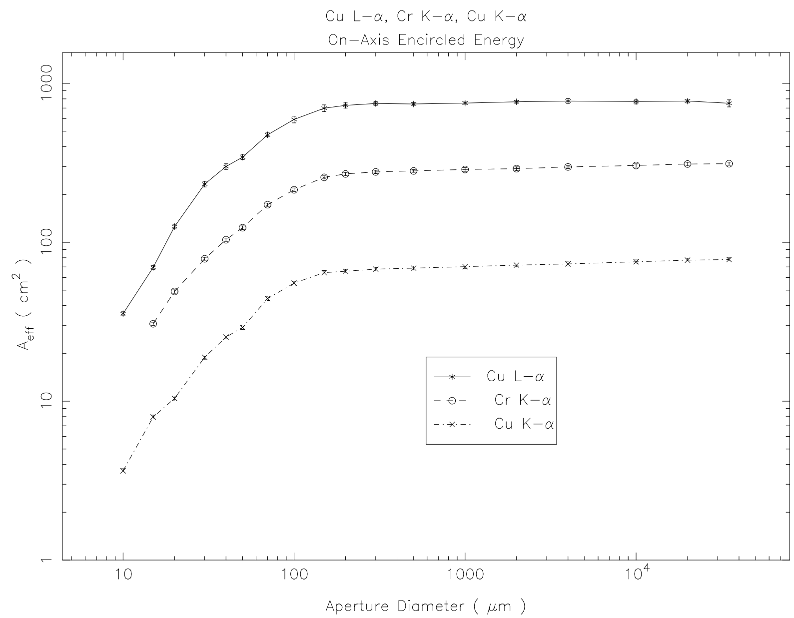

Figure 5.3: On-axis Full-HRMA Copper L- and K-α and Chromium K-α Encircled Energy

Chapter 6

The Wings of the Point Spread Function

In this chapter we describe the measurements of the HRMA point spread function wings, their reductions, and the results.

6.1 The X-ray Wing Scan Experiments and Data Reduction

The wing scan experiments consist of a series of aperture exposures, in a linear pattern, with the center exposure placed on the core of the point spread function. In order to expose as much of the optic as is possible given the finite source distance at XRCF, the tests are done one quadrant at a time, and the mirror assembly is pitched or yawed a few minutes of arc such that the diverging rays from the source strike the mirror approximately parallel to the mirror assembly axis of rotational symmetry (closer to on-orbit, infinite source conditions).

The analysis of these data can provide two properties of the mirror: First, they allow the measurement of the RMS surface roughness of the mirrors, and a diagnosis of the amount of dust on the optics (if any). Second, by simply looking at the surface brightness as a function of off-axis angle, we can extrapolate the wings of the point spread function to discover how much of the effective area falls outside of the largest pinhole used in the Encircled Energy tests. This allows us to correct the measured effective areas at selected energies for scattering beyond the largest aperture used.

Data reduction is done in much the same way as outlined in Chapter 2 for effective area measurements. However, the wings of the point spread function are very faint. This creates two effects which must be accounted for here, which were insignificant in most other experiments.

First, the count rates in most bins do not exceed background levels by a very large factor. Inspecting the pulse-height spectra by eye often shows a noise spike increasing to low pulse-heights, a lump near where the line belongs, and an otherwise flat or slowly changing background with pulse height. Escape peaks, where appropriate, sometimes show above background and sometimes do not. We have accounted for background by finding a nearly contemporaneous background test, where available, and fitting a function (often a broad Gaussian with a power law increasing towards low pulse heights) to the background data. This function is then included without free parameters in the fits to the wing scan data. We have selected this approach for two reasons: first, that the statistical precision of the background spectra is often inadequate to do background subtraction without risking substantial numbers of channels with negative count rates to be fit; and secondly, the use of the C-statistic in XSPEC (see next paragraph) is incompatible with background subtraction.

Secondly, in faint spectra like those considered here, the assumption of Gaussian statistics which underlies the χ^2 formalism is incorrect. Cash (1979) and Nousek and Shue (1989) have discussed an alternative approach, based on maximum likelihood methods and explicitly including Poisson statistics, which gives unbiased parameter estimates even in the limit of few counts per bin. For this report, we have not used this statistic, known as the C-statistic, for purely technical reasons having to do with the programming interface between the interactive XSPEC program and the batch-oriented fitting scripts used for the data reduction. We expect to correct this for the final analysis of these data.

6.2 Analysis of the Reduced Data

We follow closely the approach used in the VETA-I analysis (O'Dell et al., 1992). It is shown there how to convert measured count rates into the power spectral density (PSD) of the surface, $2W_1$, and the offset from the image core into a spatial frequency, f. The equation used is based on (7) from O'Dell et al. (1992):

$$2W_1(f) \approx \frac{f\psi(\theta)\lambda^4}{16\pi\sin^4\alpha},$$

where $f = \theta\sin\alpha/\lambda$ is the spatial frequency, θ is the off-axis angle, α is the mean graze angle for the mirror shell, λ is the wavelength, and $\psi(\theta)$ is the surface brightness, normalized to the effective area as measured (see Chapter 2) using the largest (35 mm) pinhole, and scaled by a factor of $2 \times 88/360$ to account for the fact that these experiments are done one quadrant at a time. (In the limit of purely in-plane scattering, *i.e.* the scattering is done in the same plane as the optical axis, each individual quadrant of the image is illuminated by two opposing mirror quadrants. As the quadrant shutters admit 88° per quadrant, each contributes a fraction of scattered photons to the wings of the point spread function in a given quarter of the focal plane equivalent to 88/360.)

It should be the case that $\int_{2\pi}\psi\, d\Omega = 1$; for now we are ignoring signal that falls outside the 35 mm pinhole in the EE tests in this normalization. As discussed below, this is at worst a 4% effect, and usually much smaller.

It should be emphasized that the PSD thus calculated is *per surface*.

We then plot (Figures 6.1 and 6.2) this approximation to $2W_1$ as a function of f for all energies available for a given optic quadrant. We present also, in Figure 6.3 for comparison, similar plots derived from optical measurements of the surface roughness. Note that the X-ray points fall systematically above the optical PSD. This effect is under investigation. We discuss the derivation of these optical PSDs below.

6.3 HDOS metrology measurements

The HRMA mirror surface metrology measurements were performed (at the Hughes Danbury Optical Systems, Inc. (HDOS) in Danbury, CT) for each shell after it was polished but before being coated. The instruments used were the CIDS (Circularity and Inner Diameter Station), the PMS (Precision Metrology Station), and the MPMI or WYKO (Micro Phase Measuring Interferometer, a slightly modified WYKO Corporation instrument). The CIDS was used to determine circularity and the inner diameters of the HRMA shells. The PMS was used to measure along a meridian. With these two instruments, HDOS essentially measured both the 'hoops' and 'staves' of each barrel, and thus mapped the entire surface. Finally, microroughness was sampled on each mirror using the WYKO.

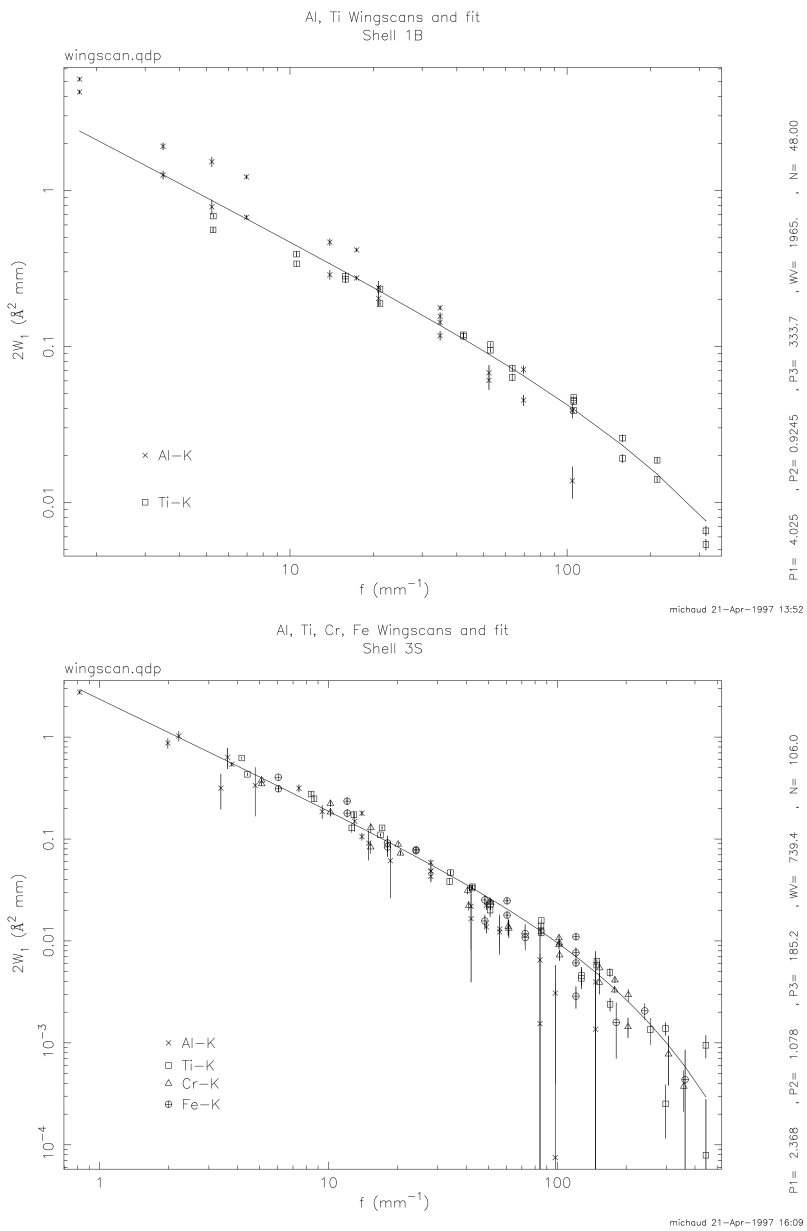

Figure 6.1: "$2W_1$" *vs.* f plot for Wingscans for Shells 1B and 3S, with power law fit.

6.3. HDOS metrology measurements

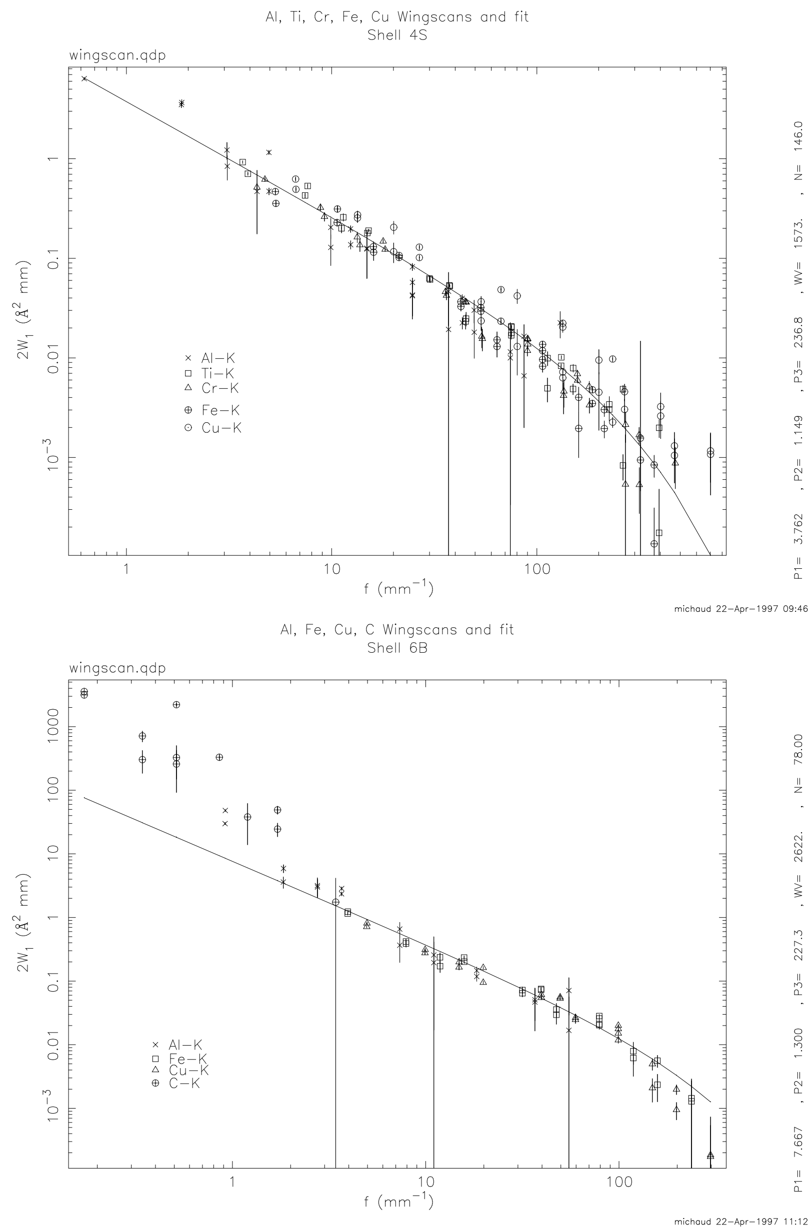

Figure 6.2: "$2W_1$" *vs.* f plot for Wingscans for Shells 4S and 6B, with power law fit. Note that the carbon points lie above the trend for the other energies; this may be evidence of dust contamination.

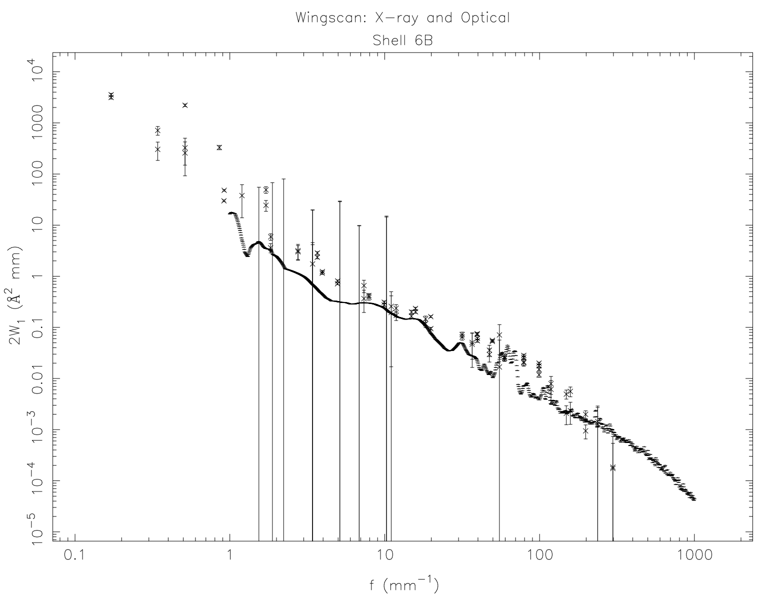

Figure 6.3: $2W_1$ *vs.*f plot for Wingscans for Shell 6B, with the optically measured surface PSD overplotted.

6.4 PSDs from the HDOS metrology measurements

The primary data used for PSDs to produce the scattering tables were HDOS map files for low frequency errors and HDOS WYKO files for higher frequency errors.

The map files represent a combination of PMS axial scan data and CIDS circularity data. Each of these files had solid body translations and rotations removed and was then divided into two complementary maps by passing the data through a filter; the low pass portions were combined with the calculated mount induced distortions, fit with spline functions, and used deterministically in the ray-tracing. The high frequency portions were combined with the WYKO data and treated statistically. The standard HDOS filter was used for the separation; the parameters were such that the transition between low and high frequency passbands occurred from 0.02 to 0.03 mm^{-1}.

The WYKO data with each magnification (x1.5, x10, and x40) were combined into mean PSD files, and these files were used with the program `foldw1` (which is similar to the HDOS program `eegraz`) to calculate scattering distributions. The calculation was based on the scattering theory by Beckmann and Spizzichino (1963). These scattering distributions were used by a post–processing program to calculate image distributions. The PSD files do not agree perfectly in the overlap regions, so a linear weighting was used in the overlap regions such that the weight given to the lower frequency file would decrease from 1.0 to 0.0 while the weight given to the high frequency file would increase from 0.0 to 1.0. The frequency intervals are, in units of mm^{-1}, 0.000 to 0.226, 0.226 to 0.5, 0.5 to 1.5, 1.5 to 2.0, 2.0 to 5.0, 5.0 to 10.0, and 10.0 to 1000.0.

Because the mirror surface roughness is worse near the end of each mirror, the PSDs were

calculated for different sections (ranging from 5 to 12 sections) for each shell, with a center section covering about 80% of the mirror surface and end sections covering the rest.

6.5 Results

To date we have analyzed data for four of the sixteen mirror quadrants: 6B (the bottom quadrant of the innermost mirror pair); 4S (south quadrant of Shell 4); 3S (south quadrant of Shell 3); and 1B (bottom quadrant of the outermost mirror shell). Below we show plots of these PSDs.

One effect we have included only approximately pertains to the fact that in these tests a surface brightness profile which is dropping quickly with distance from the core of the PSF is being sampled with pinholes which in some cases have diameters as large as their off-axis distances. Thus a spatially rapidly changing function of off-axis angle is being sampled with a very large aperture, and one obtains the flux, not at the center of the pinhole, but at some other position nearer the core of the image. This effect can be corrected for, if one presumes that the surface brightness profile obeys a power law: $\psi = \psi_0 \theta^{-\gamma}$. Here θ, the off-axis angle, is essentially the ratio of the off-axis distance r to the HRMA focal length. One then integrates this profile over the aperture, and obtains, in general, the confluent hypergeometric function ${}_2F_1(\frac{\gamma}{2}, \frac{\gamma}{2}, 2; \frac{a^2}{r^2})$, where a is the aperture radius, and r is the off-axis distance. In the case $\gamma = 2$, this reduces to a simple function. For this analysis, we have assumed that $\gamma = 2$. Fits to the surface brightness profiles show that in fact γ lies between 2.1 and 2.5 for most cases, so a small correction will be necessary in the next iteration of this data analysis.

If one fits a function to the data and integrates over specified limits in f, one obtains a mean-square surface roughness, σ^2 (O'Dell et al., 1992). In most cases, there is evidence of a turndown for large f, so a power law with exponential cutoff was fit to the data in each case. We obtain only bad fits, in part because we include both sides of the wing scan, *i.e.* both scattering toward and away from the mirror surface. We do this to obtain some sort of "average" wing profile, allowing the fitting function to decide on the relative weights of the two points at each f. The fitting function is integrated from 1 to 1000 inverse millimeters. We include these preliminary values in Table 6.1. Note that these surface roughness values are somewhat higher than those obtained optically with the WYKO instrument. The discrepancy is under investigation.

Shell	σ^2 (Å^2)
1B	26.11
3S	9.13
4S	12.84
6B	19.09

Table 6.1: Mean square surface roughnesses for four HRMA quadrants, integrating the fitted PSD from 1 to 1000 inverse millimeters.

Note in Figure 6.2 that in the one case where we have carbon K-α wing scan data (Shell 6B), there is some evidence that the carbon points are systematically higher than those taken at higher energies. If this trend holds up under further scrutiny, it represents evidence for dust contamination of that mirror quadrant. However, wing scans were done for carbon for this shell both parallel to the axis of the exposed quadrant (vertically in this case), and perpendicular (horizontally). One expects that surface roughness scattering is primarily in the plane of the reflection (so that it would be distributed vertically for a bottom mirror quadrant), while dust scattering is more nearly isotropic.

Thus the lack of significant detection in the horizontal scan is evidence *against* the presence of significant dust on the mirror surface.

We have also fit functions of the form $\psi = \psi_0\theta^{-\gamma}e^{-\theta/\theta_0}$ to the surface brightness profiles. The integral over solid angle of this function, from the radius of the largest pinhole used in the encircled energy (EE) tests out to $\pi/2$ gives the additional effective area which was missed by the EE test. This can be used to correct the estimates of the effective area of the HRMA at selected energies (where wing scan data exist). Such integrals show that the fraction of the power inside the 35 mm pinhole which falls outside of it is less than about 4% for all cases in which wing scan data have been fit. That is to say that the effective areas reported elsewhere in this report could be corrected upwards by up to 4%. In general, the correction is much less at low energies (*e.g.* 0.4% at Al for Shell 3).

In order to show the consistency of the data, we have plotted in Figure 6.4 the surface brightness profile measured in two different ways, for the one case where this is feasible. In Chapter 5 we discuss encircled energy tests. These tests give a measurement of the surface brightness integrated out to the radius of the aperture, so numerically differentiating the effective area *vs.* radius curve gives us the surface brightness. This was then scaled by a factor of $2 \times 88/360$ as above to account for the fact that the wing scans are done one quadrant at a time. We also plot the surface brightness (unnormalized) as measured in the wing scan experiment. The case of Ti K-α for Shell 1 is unique in that the encircled energy curve is both steep enough in the outer parts, and well enough measured, that the numerical derivative can be computed with finite error bars. Other cases examined showed the wing scan data at a level not inconsistent with the encircled energy data, but due to the large error bars on the latter, no stronger conclusions can be drawn.

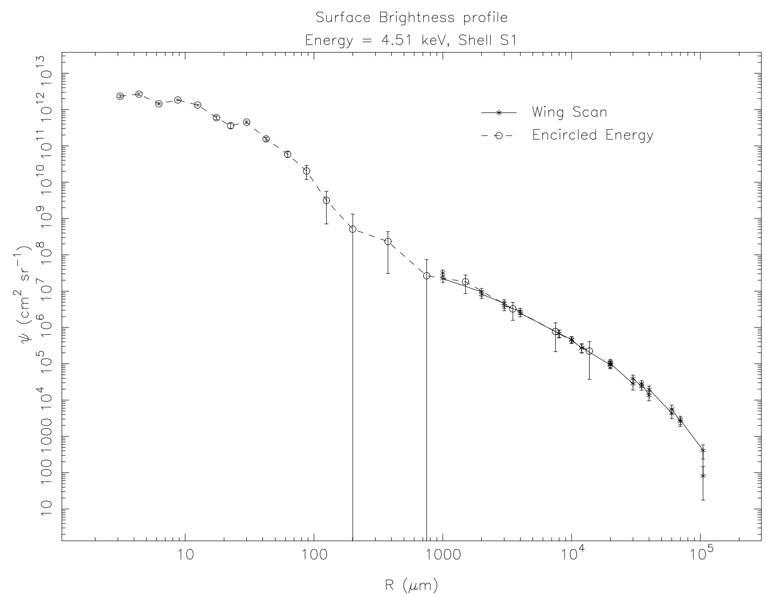

Figure 6.4: Surface Brightness *vs.* Radius for Shell 1S at Ti K-α. This is a composite plot based on both wing scan data and an encircled energy test.

Chapter 7

Comparison of the Measured Effective Area and Encircled Energies to Simulations

Chapter 2 presented the measured SSD and FPC effective areas, while Chapter 5 presented measured encircled energy data. Here we discuss how these data compare to the MST simulations, and what might explain the differences.

7.1 Comparison of Effective Area data to simulations

Figures 7.1 and 7.2 present the ratio of MST's current HRMA model of the 2mm pinhole effective area to the measured data from the SSD (from A. Tennant) for each of the shells. Data for the HRMA are in Table 7.1 (we have not generated simulations for as many energies for the HRMA). The simulations overestimate the effective area above 1.5keV and underestimate it below that energy. Deviations tend to increase with energy, up to the critical energy for the shell (where the shell's grazing angle is larger than the reflectance critical angle), where they decrease. Shell 1 exhibits the largest deviation.

Comparisons of the simulations to the FPC measurements are shown in Figure 7.3; the data are presented in Table 7.2. Again, the simulations over-estimate the effective area compared to the measurements.

7.1.1 Possible Sources of the Discrepancies

In order to isolate which part of the simulation is the prime target for the deviations, we have undertaken a series of studies on our own and in conjunction with R. Elsner of AXAF Project

Table 7.1: SSD 2mm HRMA Effective Areas *vs.* Simulations

Energy	A_{eff}		Simul. / FPC
[keV]	SSD	Simulation	
0.930	815.709 ± 12.456	767.339 ± 0.760	0.941 ± 0.014
2.984	396.209 ± 3.412	426.200 ± 0.426	1.076 ± 0.009
5.415	310.093 ± 3.264	341.692 ± 0.348	1.102 ± 0.012
8.048	78.246 ± 1.512	85.904 ± 0.089	1.098 ± 0.021

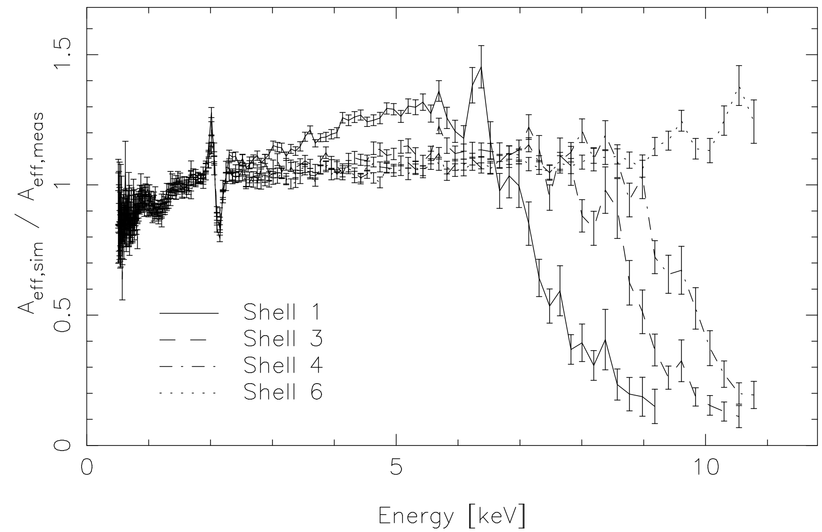

Figure 7.1: Comparison of SSD Measured Effective Area to Simulations. The zig-zag artifact near 2 keV results from the SSD's averaging of flux across the Ir edge; this effect is not in the simulations.

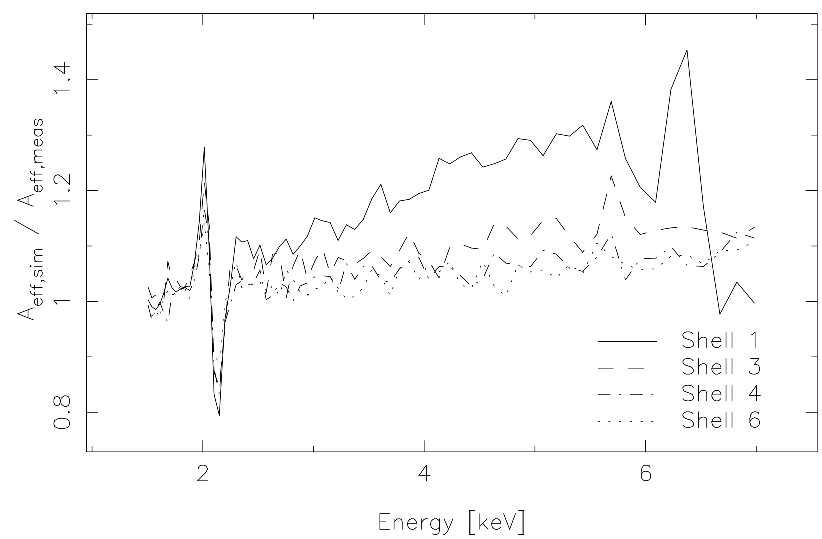

Figure 7.2: Comparison of SSD Measured Effective Area to Simulations. A magnified version of Figure 7.1, illustrating the comparison at energies less than the shells' cutoff energies.

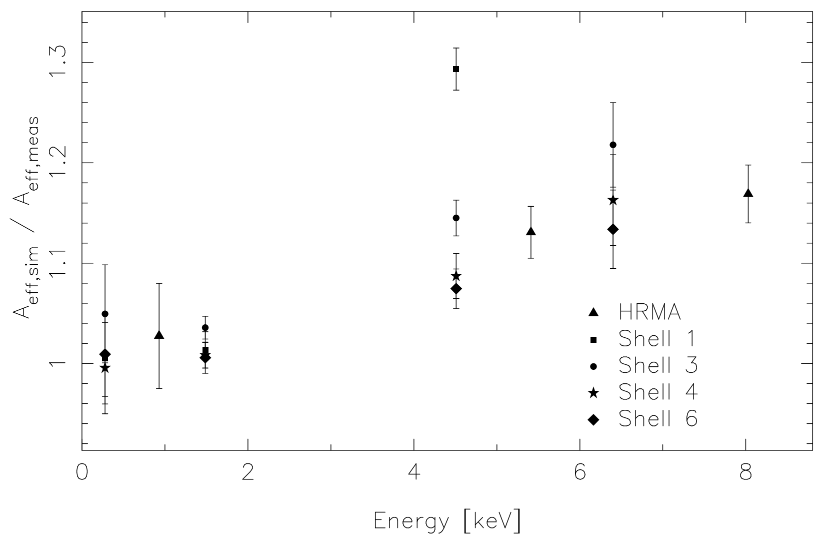

Figure 7.3: FPC 35mm Effective Areas *vs.* Simulations

Table 7.2: FPC 35mm Effective Areas *vs.* Simulations

Shell	Energy [keV]	A_{eff} FPC	A_{eff} Simulation	Simul. / FPC
1	0.277	317.465 ± 14.241	319.014 ± 1.537	1.005 ± 0.045
1	1.486	296.303 ± 5.087	300.307 ± 1.448	1.014 ± 0.018
1	4.510	99.545 ± 1.538	128.762 ± 0.623	1.294 ± 0.021
3	0.277	203.063 ± 9.381	213.095 ± 1.294	1.049 ± 0.049
3	1.486	197.270 ± 1.797	204.316 ± 1.241	1.036 ± 0.011
3	4.510	110.841 ± 1.588	126.914 ± 0.771	1.145 ± 0.018
3	6.400	58.317 ± 1.983	71.026 ± 0.432	1.218 ± 0.042
4	0.277	169.214 ± 7.655	168.442 ± 1.167	0.995 ± 0.046
4	1.486	161.249 ± 1.729	162.555 ± 1.126	1.008 ± 0.013
4	4.510	102.650 ± 1.993	111.587 ± 0.774	1.087 ± 0.022
4	6.400	82.705 ± 3.170	96.166 ± 0.667	1.163 ± 0.045
6	0.277	93.682 ± 3.800	94.539 ± 0.898	1.009 ± 0.042
6	1.486	91.756 ± 1.112	92.279 ± 0.877	1.006 ± 0.015
6	4.510	67.619 ± 1.050	72.662 ± 0.691	1.075 ± 0.020
6	6.400	64.576 ± 2.144	73.213 ± 0.697	1.134 ± 0.039
HRMA	0.930	750.143 ± 38.270	770.777 ± 0.762	1.028 ± 0.052
HRMA	5.410	312.559 ± 7.136	353.429 ± 0.350	1.131 ± 0.026
HRMA	8.030	77.971 ± 1.923	91.143 ± 0.090	1.169 ± 0.029

Science. There are four areas where the errors in the simulations could lead to energy dependent errors:

- shifted obstructions
- optical constants / reflectance model
- surface micro-roughness scattering
- optical axis mis-alignment

Shifted Obstructions

Lateral (i.e., perpendicular to the optical axis) shifts of one of the support structures will affect the inner mirrors differently than the outer ones. To ensure that our apertures, baffles, and what not are correctly positioned, we compared analytical estimations of the geometric area with ray traces. In order to make the former both tractable and believable, we used ideal optics, no deformations, with a source at an infinite distance. Given the as-built dimensions of the apertures, analytical derivations of the obstructed geometric area for our simple aperture models is straightforward. The results, shown in Table 7.3, indicate that the apertures are correctly placed in the simulations.

Table 7.3: Comparison of Analytical to Raytraced Geometric Area

Shell	Geometric Area [cm^2] Analytical	Raytrace	% Diff.
1	443.746	442.921	0.186
3	283.241	282.745	0.175
4	218.379	218.110	0.123
6	116.731	116.793	-0.053

Optical Constants

As mentioned in §1.3, we use both Henke (Henke et al., 1993) and MST Synchrotron program derived optical constants. Previous work by the Synchrotron team has shown that their work, while different in the details from Henke constants at the same energy, does not exhibit a large enough deviation to account for the effective area discrepancies.

The effective area results presented here use a simplified model of the optics' surfaces, namely a semi-infinite layer of iridium. We have begun incorporating a multi-layer reflectivity model into our simulations; Figure 7.4 presents our initial calculations of the ratio of the multi-layer effective areas to the those derived from the mono-layer calculation. There are significant differences at energies beyond the shells' critical angles, primarily for Shell 1, but very little at lower energies. Note that while the relative amplitude shown in Figure 7.4 is large, its absolute contribution is small, as there is little reflectivity at higher energies.

The reduction of the synchrotron reflectivity measurements requires a model incorporating a surface roughness parameter, which is a different approach than that used in the raytrace simulations' handling of surface roughness. While the synchrotron analyses should be result in optical constants which are independent of the surface roughness model, we are undertaking studies to determine the sensitivity of the synchrotron reduction algorithms to the surface roughness.

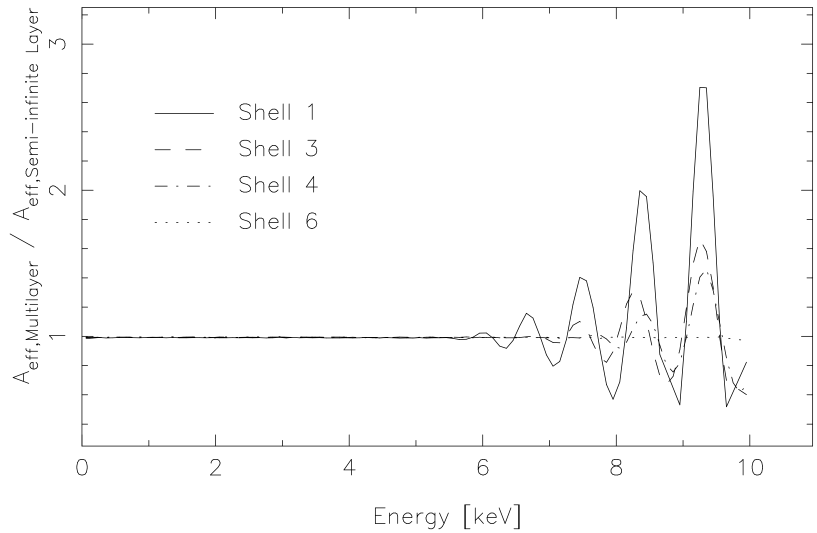

Figure 7.4: Effect of Multi-layer *vs.* Semi-Infinite Layer on Effective Areas

Surface Micro-roughness Scattering

As a diagnostic, Figures 7.5 to 7.8 show the ratio of measurements at various energies and pinhole sizes to simulations of these measurements. Energy and aperture size related differences may indicate that the models are not correctly reflecting the mirror scattering. The decrease in difference between the measurements and the models as pinhole diameters increase implies that the models predict less scattering than the what the data show. Indeed, Figure 6.3 indicates that surface roughness as derived from the XRCF data seems to be higher than that predicted from the HDOS PSD measurements.

Optical Axis Misalignment

Any tilt of the HRMA relative to the source will produce changes in the measured effective area, in an energy dependent fashion. Figure 7.9 illustrates the effects of a $1'$ tilt in yaw upon the effective area. At most it is several percentage points.

7.1.2 Cross-checks of the Model

A cross-check of the MST model was performed by comparing its predicted 2π effective areas against that of R. Elsner's (MSFC Project Science) model. Simulations were run for the following scenarios:

- on-orbit, perfect optics, no scatter, no baffles
- on-orbit, perfect optics, no scatter, baffles
- XRCF, no scatter, baffles

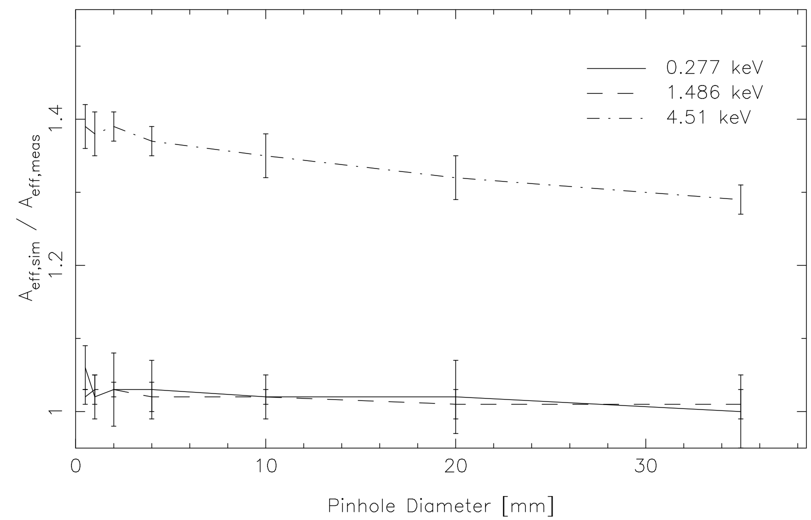

Figure 7.5: Shell 1 FPC Effective Areas *vs.* Simulations

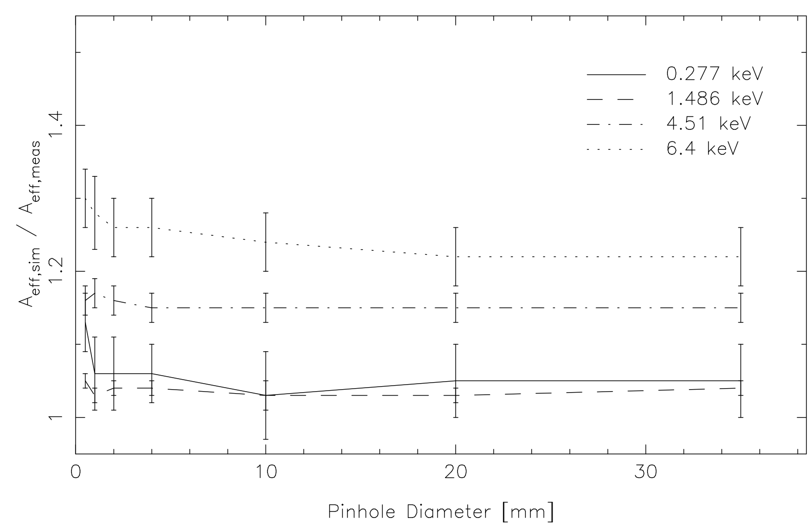

Figure 7.6: Shell 3 FPC Effective Areas *vs.* Simulations

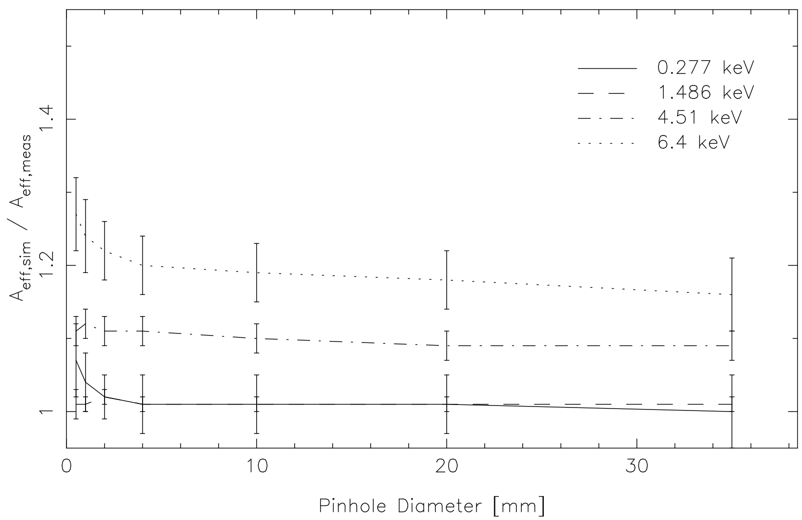

Figure 7.7: Shell 4 FPC Effective Areas *vs.* Simulations

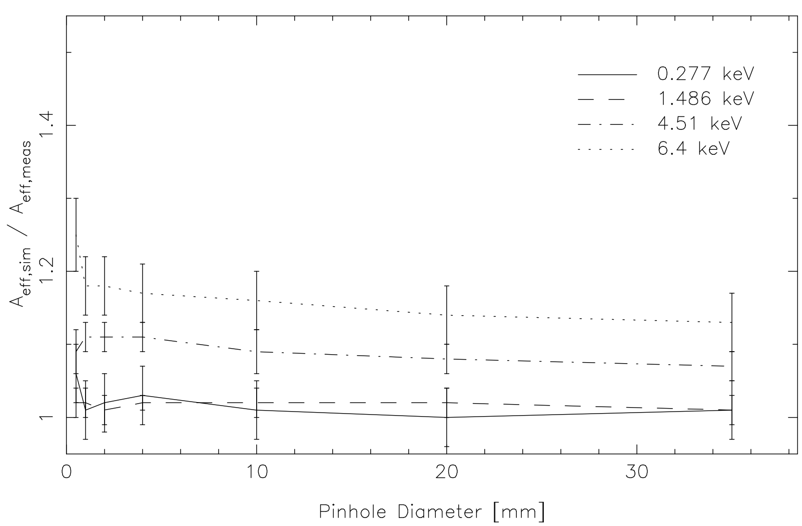

Figure 7.8: Shell 6 FPC Effective Areas *vs.* Simulations

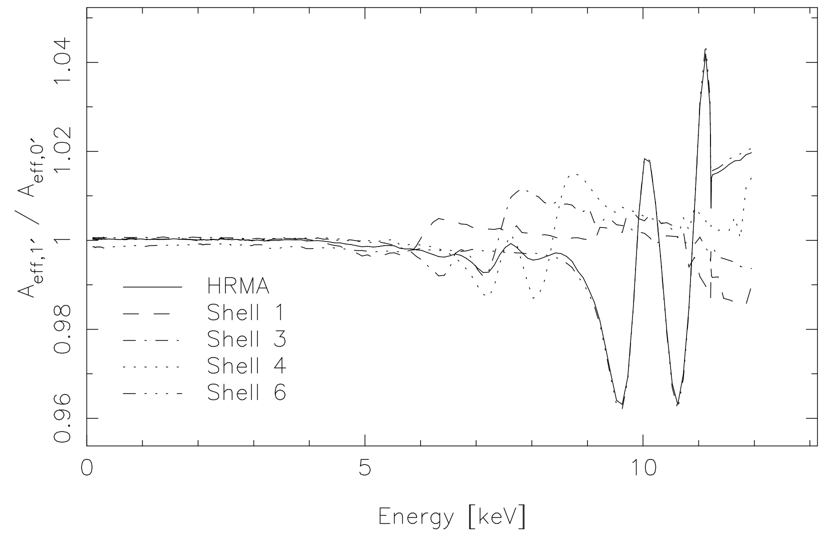

Figure 7.9: Sensitivity of the Effective Area due to a $1'$ tilt in HRMA yaw

at 0.277, 1.49, 6.4 and 8.03 keV. As noted, in all cases we did not include scattering. Our results agree to within a couple of percent. (The MST models were an earlier version which did not included the XRCF-deduced decenter). The comparison indicates that we cannot be grossly wrong in the positioning of the optics or the obstructions. Since Elsner's models used Henke optical constants exclusively, this implies that the synchrotron derived optical constants that we use above 2 keV cannot be substantially wrong.

7.1.3 Conclusion

While we have not yet found a single "smoking gun" which might explain the differences between the measured and simulated effective areas, there are a number of areas where the simulations may be improved, each of which may reduce the difference by a few percent. Additionally, there are many systematic uncertainties in the measurements which are still being accounted for (quantum efficiency differences between the BND's, uncertainties in distance, etc.).

7.2 Comparison of Encircled Energy Measurements to Simulations

Figures 7.10 to 7.14 show comparisons of the measured FPC encircled energies to the simulations. In general the agreement is quite good. The inner cores disagree in part because the simulations treat the XSS as a point source. Additionally, the smaller pinholes were not reliably centered.

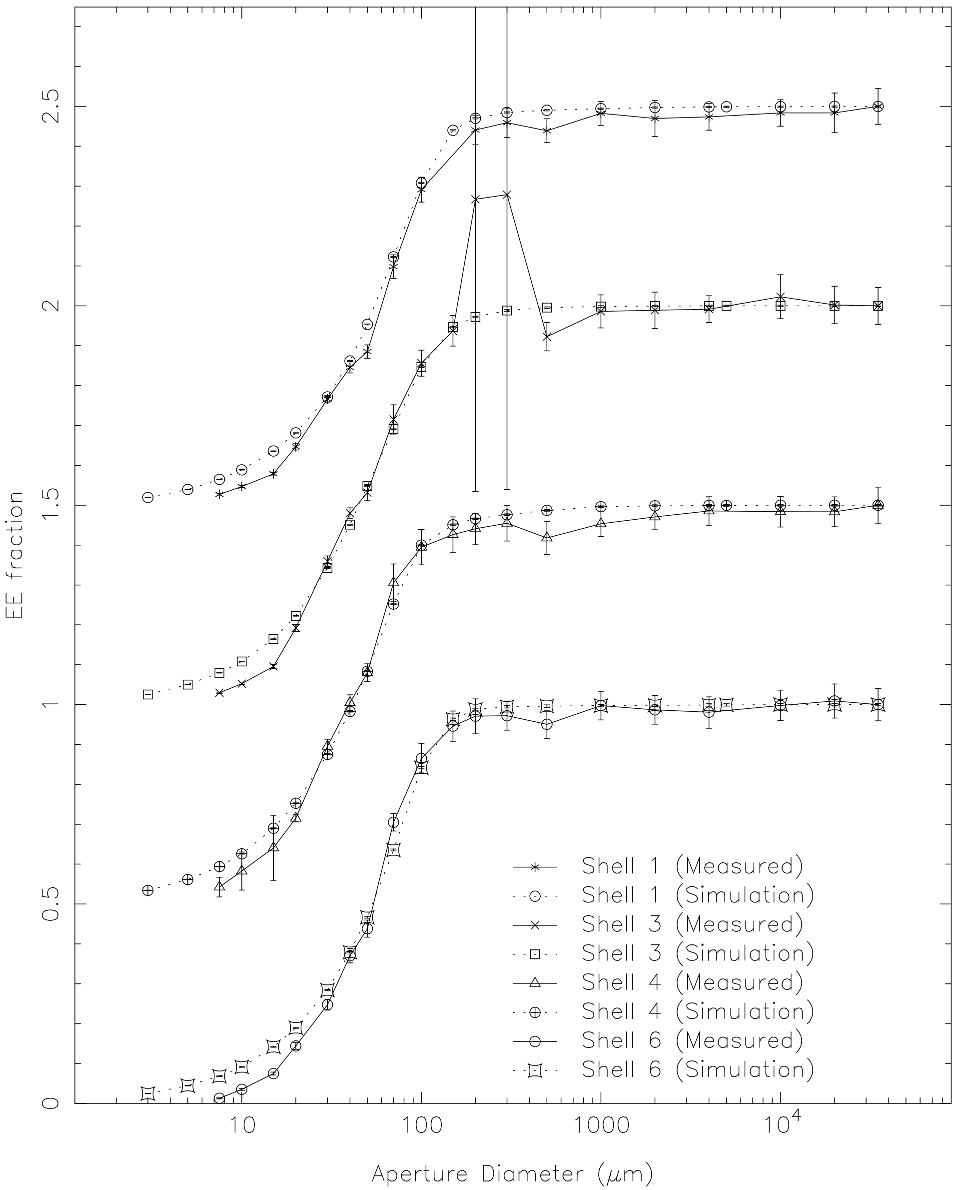

Figure 7.10: Encircled Energy Fractions at 0.277 keV. The values for Shells 1–3 have been shifted upwards for clarity.

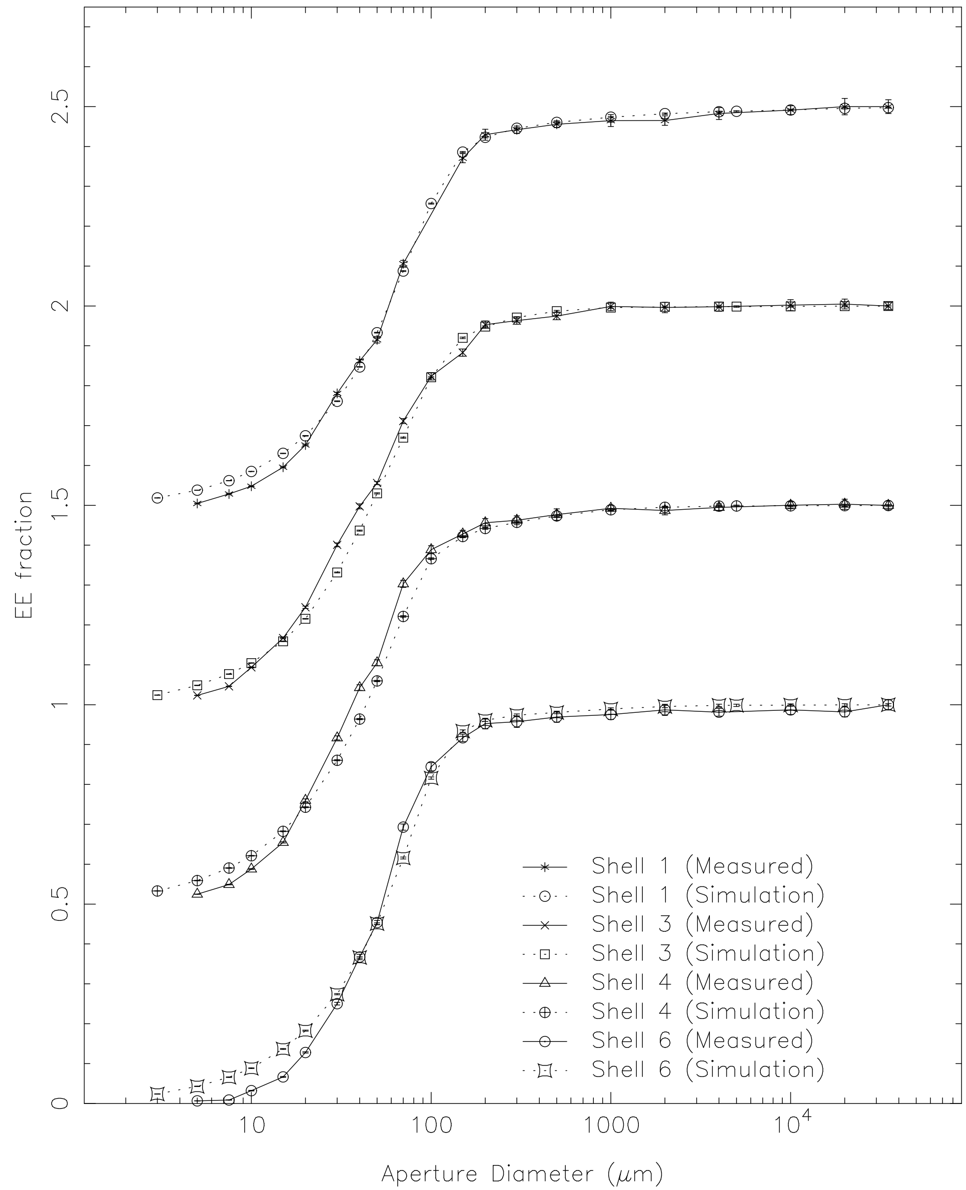

Figure 7.11: Encircled Energy Fractions at 1.486 keV. The values for Shells 1–3 have been shifted upwards for clarity.

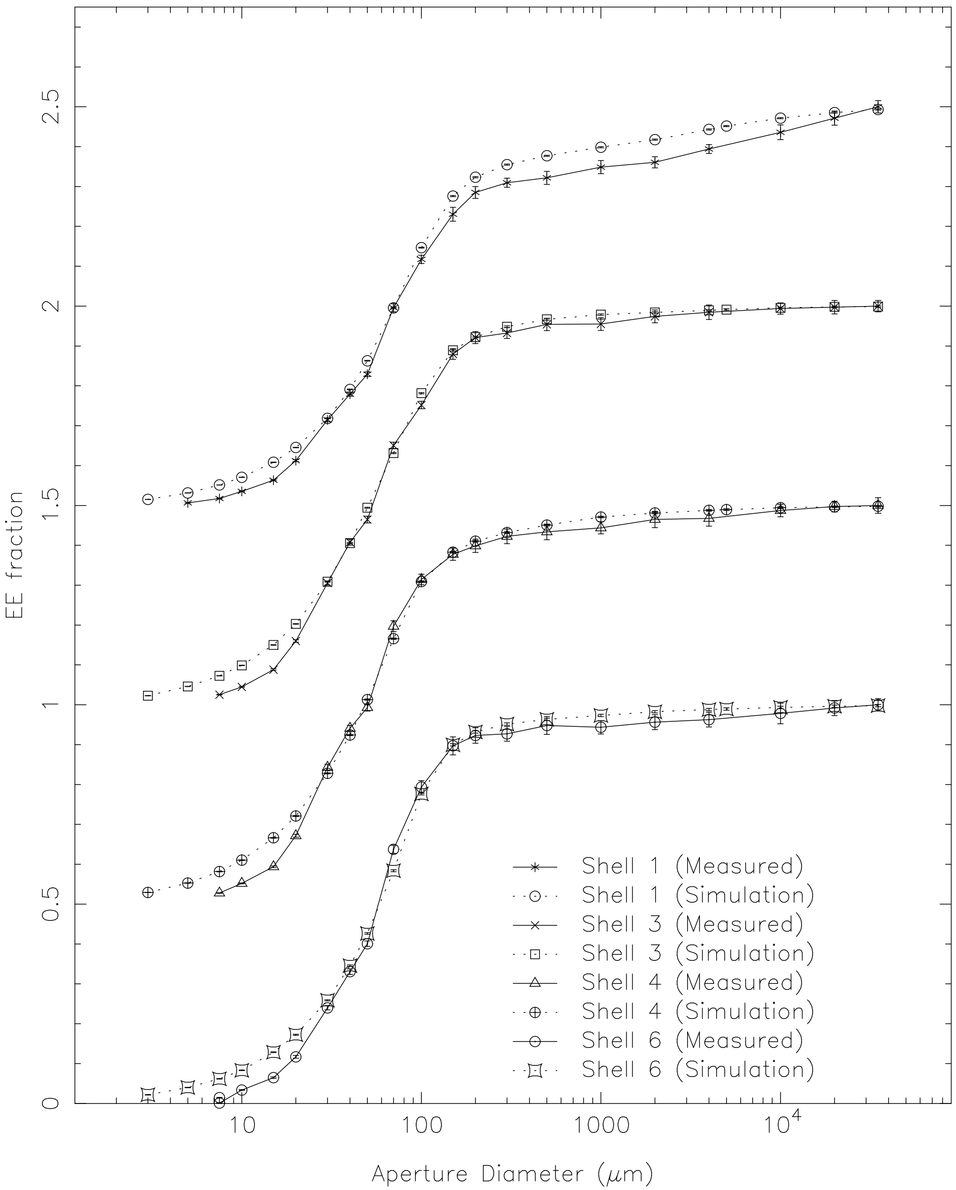

Figure 7.12: Encircled Energy Fractions at 4.51 keV. The values for Shells 1–3 have been shifted upwards for clarity.

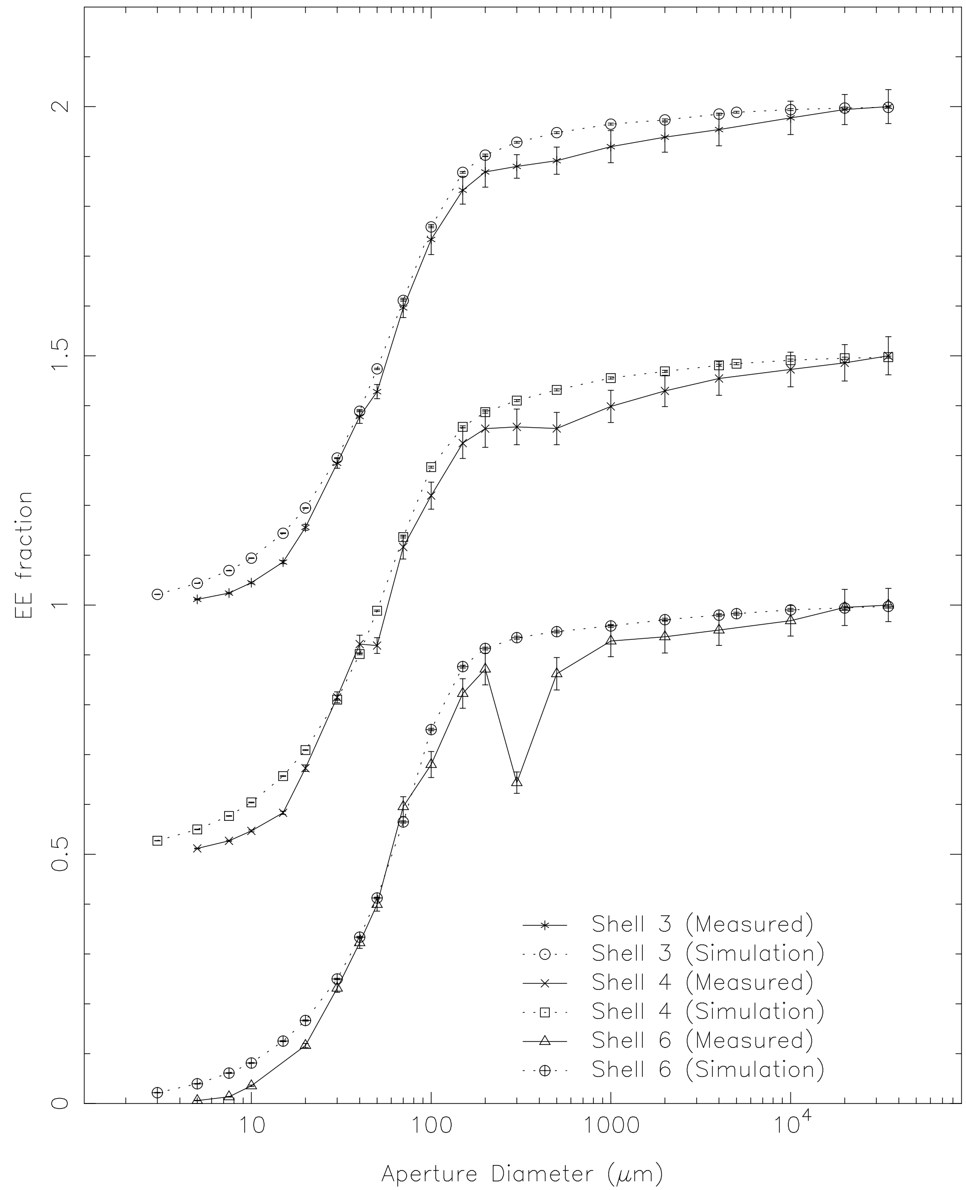

Figure 7.13: Encircled Energy Fractions at 6.4 keV. The values for Shells 3 and 4 have been shifted upwards for clarity.

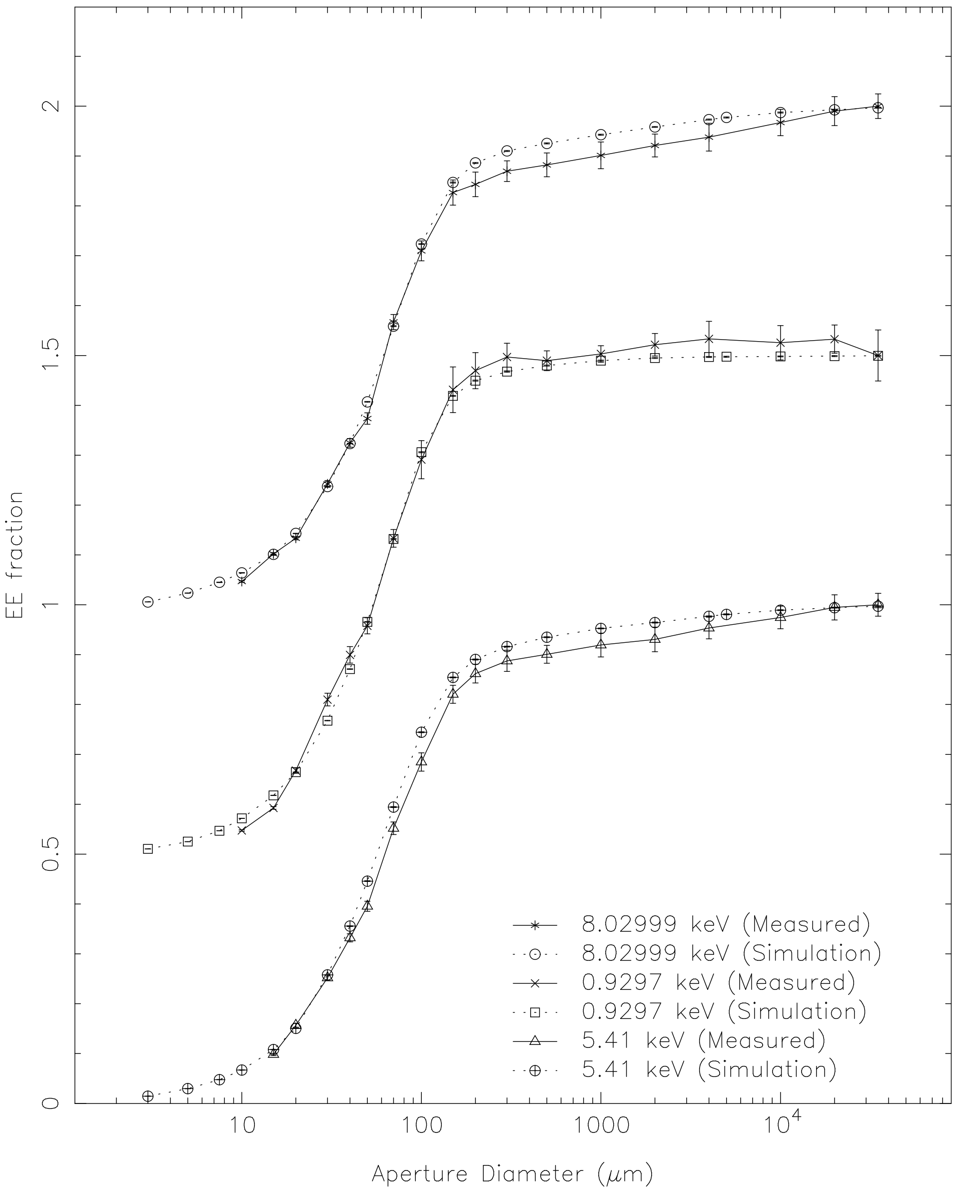

Figure 7.14: HRMA Encircled Energy Fractions. The values for higher energies have been shifted upwards for clarity.

Chapter 8

HRMA Ring Focus Measurements

8.1 Introduction

The AXAF mirror (HRMA) ring focus measurements were made with an HSI (High Speed Imager, a microchannel plate) X-ray detector. The ring focus is a sharply focused ring formed by X-rays before they reach the HRMA focal plane (Griner et al., 1985; Zissa and Korsch, 1986). It is caused by spherical aberrations due to the finite source distance at the XRCF. There are four rings, one for each of the four shells of the HRMA.

The ring focus measurements reveal aspects of the test system distortions and the mirror surface figures which are difficult or impossible to detect in the focal plane. The measurement results show periodic modulations of the ring width which were caused by gravity and strain in the epoxy bonds that are part of the mechanical support system. The strongest component of the modulation has 12-fold symmetry, because these distortions were exerted on the mirror through the 12 flexures which support each mirror shell. Five ring focus HSI images were taken with different sources during Phase 1. By examining the small changes in the ring width, temporal effects, such as changes in epoxy strain, may be diagnosed.

The HRMA ring focus measurements were planned as a result of successful similar measurements done with the VETA-I (Verification Engineering Test Article I) in 1991, as described in Zhao et al. (1993). The data analysis here is also based on similar efforts described in that paper.

In this chapter we discuss the preliminary assessment of the ring focus measurement results, ring focus model, the epoxy strain issue and its effect on the HRMA on-orbit performance. In §8.2 we describe the ring focus measurements and the data obtained. In §8.3 we discuss the data analysis. In §8.4 we show the measurement results with figures. In §8.5 we describe the ring focus models and their each elements. In §8.6 we compare the data with the models. Finally, in §8.7 we summarize the ring focus measurements and our current assessment to the HRMA mirror deformation.

8.2 Measurements and Data

Based on raytrace simulations, the ring focus plane was calculated to be 65.2 mm towards the HRMA from the focal plane (or 10209.3 mm from the datum A – front surface of the CAP (Central Aperture Plate)). Five long exposure (1800 seconds) HSI images were taken with the detector in this plane (see Table 8.1). There was a repress (the test vacuum chamber was repressurized and opened) between the first and the second ring focus measurements, and another repress between the

Table 8.1: HRMA Ring Focus Measurement Data

Date (GMT)	Run ID	TRW ID	Source	Defocus [mm]	Integration time (seconds)
961223	106856	C-IXH-RF-1.005	Al-K	65.2	1800
970110	108185	D-IXH-RF-1.003	Fe-K	65.2	1800
970115	108944	D-IXH-RF-1.002	C-K	65.2	1800
970124	110004	D-IXH-RF-1.005	Al-K	65.2	1800
970210	111804	E-IXH-RF-1.007	Al-K	65.2	1800

fourth and the fifth measurements. Work was done on the HRMA alignment mechanism (actuators) during both repress cycles.

Figures 8.1 – 8.5 show these five HSI images. Four rings in each figure are X-ray images from the four mirror shells of the HRMA. The images shown are as seen from the mirror towards the HSI – top is the top, bottom is the bottom, left is the north and right is the south of the XRCF. The 12 gaps around the rings are the images of the supporting struts in the apertures and collimators.[1] A scale bar at the bottom of each figure shows the size of 1 mm or $20.2''$. At the 65.2 mm defocus, the mean radii of the four rings are 3.88 mm, 3.10 mm, 2.73 mm, and 2.05 mm, respectively.

The right (south) sides of the images are brighter than the left. This is because the HSI quantum efficiency is a function of incident angle, and the HSI pores were tilted about 6 degrees towards the south (looking from the top, the front (facing the HRMA) ends of the pores were towards the south).[2]

Near the 12 gaps of each ring, the ring width bulges out. This is primarily due to the gravity effect around the 12 mirror holders at those locations, which we will discuss later. In Figure 8.2, the ring 1 (the largest ring) image is very faint. This is because it is an Fe-K (6.4 keV) source image. At this energy, the critical angle of reflection from Ir is $45.3'$, while mirror P1 has a mean grazing angle of about $55.1'$ at the XRCF. It is beyond the critical angle, so there is not much reflection at 6.4 keV from the Shell 1. (The same is true for on-orbit operation, where Shell 1 has a mean grazing angle of $51.3'$.)

8.3 Data Analysis

The HSI image data were digitized to a qpoe format in a 4096×4096 readout array with a pixel size of $(6.45\,\mu\mathrm{m})^2$. Each image collected 1–2 million photons. Before the data analysis, the HSI images were carefully evaluated. One of the processes is called degap. The HSI readout is a crossed grid charge detector, which consists of two orthogonal planes of wires electrically separated from each other. These two wire plates are located behind the microchannel plate stack to collect the charge. The electron charge cloud has a core/halo type of structure and spreads over several wires. A fine position algorithm was developed to determine the centroid of the charge cloud to a small fraction of the wire spacing. An artifact due to this algorithm is 16 vertical and 16 horizontal gaps left in the raw images (Chappell and Murray, 1989). The degap process restores the image so that

[1] From the 12 gap positions, it was found that the orientation of the HSI was slightly misaligned with respect to the HRMA (the HSI was rotated 0.7° clockwise, so the HRMA images appeared on the HSI were rotated 0.7° counterclockwise). This misalignment was considered in the data analysis.

[2] From the ring focus data, the relative HSI quantum efficiency curve can be obtained since the X-ray incident angle can be very precisely determined and varies around the ring. This study will be presented elsewhere because it is beyond the scope of this report.

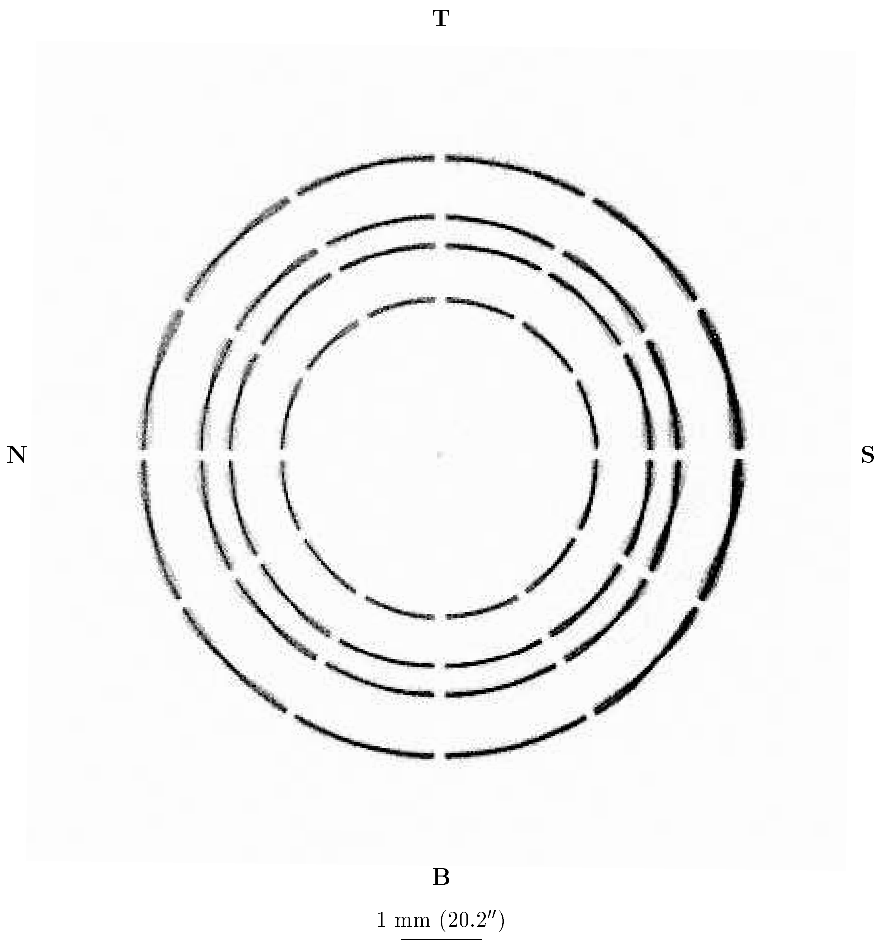

Figure 8.1: The HRMA ring focus image. Source: Al-K; Defocus: 65.2 mm; Date: 96/12/23; Run ID: 106856; TRW ID: C-IXH-RF-1.005.

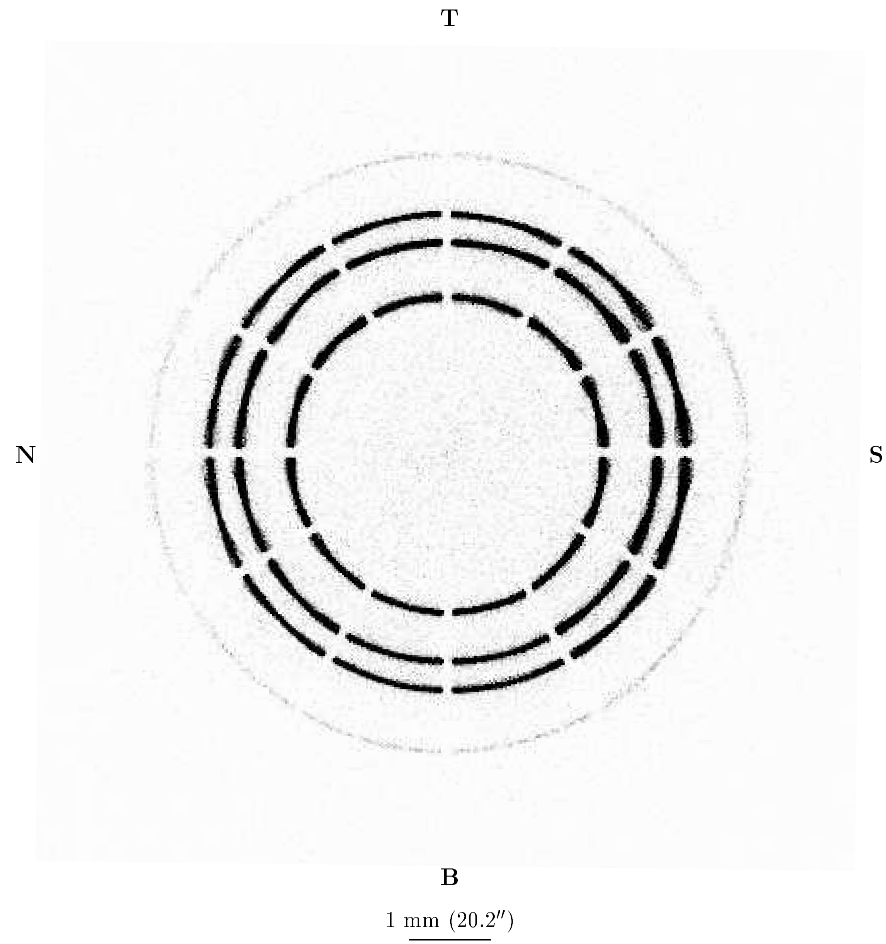

Figure 8.2: The HRMA ring focus image. Source: Fe-K; Defocus: 65.2 mm; Date: 97/01/10; Run ID: 108185; TRW ID: D-IXH-RF-1.003.

T

N

S

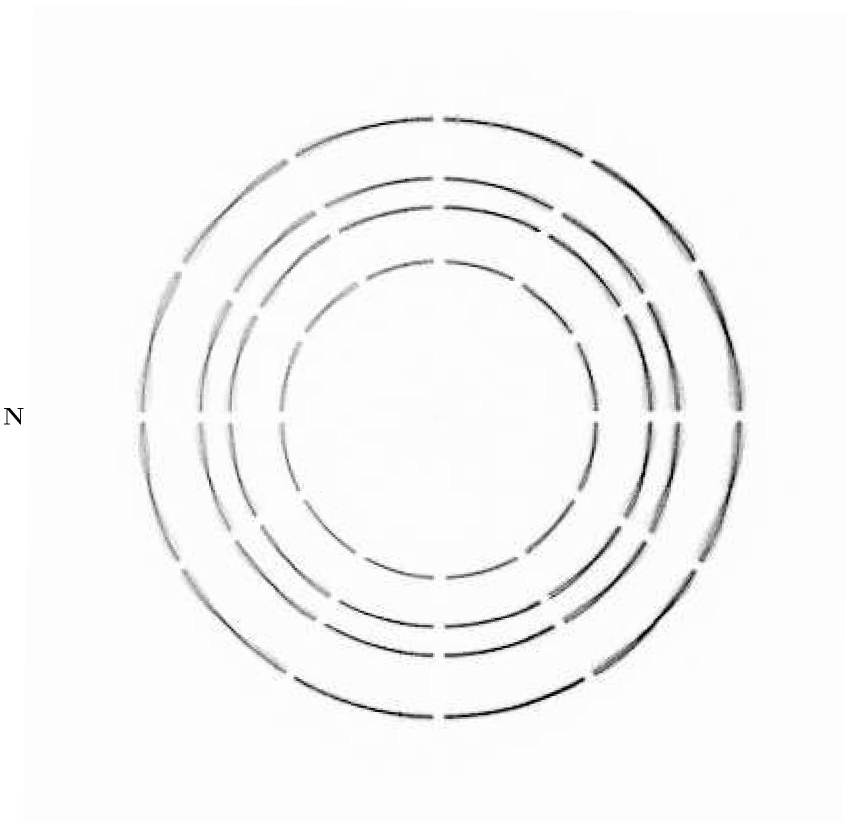

B

1 mm (20.2″)

Figure 8.3: The HRMA ring focus image. Source: C-K; Defocus: 65.2 mm; Date: 97/01/15; Run ID: 108944; TRW ID: D-IXH-RF-1.002.

T

N

S

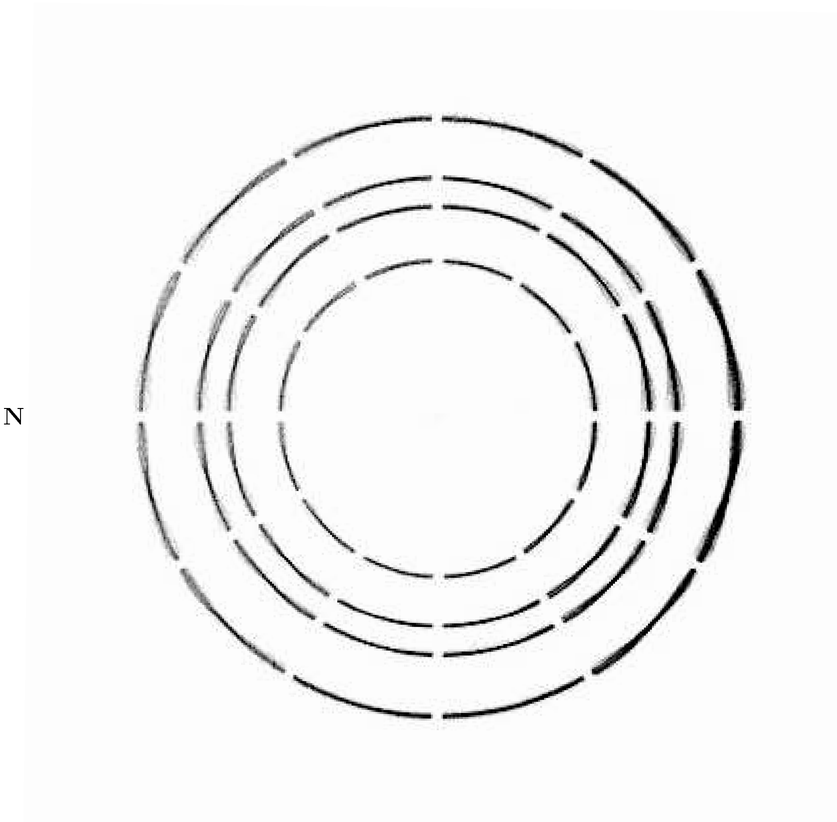

B

1 mm (20.2″)

Figure 8.4: The HRMA ring focus image. Source: Al-K; Defocus: 65.2 mm; Date: 97/01/24; Run ID: 110004; TRW ID: D-IXH-RF-1.005.

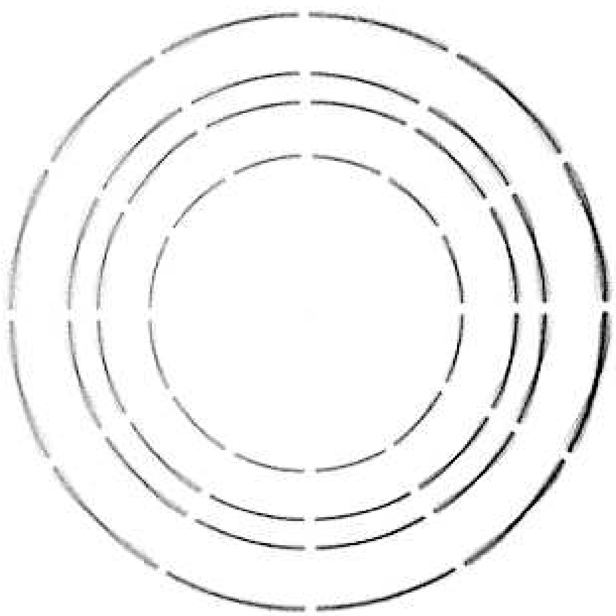

Figure 8.5: The HRMA ring focus image. Source: Al-K; Defocus: 65.2 mm; Date: 97/02/10; Run ID: 111804; TRW ID: E-IXH-RF-1.007.

each pixel appears at its actual location. By examining the final images, the residual gaps or pixel overlaps were less than one pixel wide.

Each degapped ring image was then divided into annuli and pie sectors, using IRAF (Image Reduction and Analysis Facility). In the vicinity of the ring, each annulus was chosen to be one pixel (6.45 μm) wide. Each sector was chosen to be 2° wide, which gives adequate statistical errors and azimuthal resolution. Photon counts in each cell of the annulus-sector grid were tabulated. Radial profiles across each ring for each azimuthal angle were then plotted. Figures 8.6 – 8.9 show some selected ring profiles. For most parts of the ring, the radial profiles are single peaked. Near the 12 gaps (except the top and the bottom gap), the radial profiles are double, even triple peaked. This is due to the fact that the mirror was slightly bent at the 12 holding points because of gravity effect (see §8.5).

The ring width RMS and FWHM, and mean radius were calculated for each radial profile. There are a large number of scattered photons in each image. Because a photon far away from the ring can carry large statistical weight, the above calculations are meaningless without clipping. Therefore, a window of 320 μm was set around each ring in order to perform the calculations. Inside this window, focused photons were strongly dominant over the scattered photons. All the photons outside this window, where scattered photons were dominant, were ignored.

The ring width RMS was chosen to represent the ring width because it carries a better statistical value than the FWHM. The ring radii showed large effects from the HSI plate scale non-uniformity, which is not well known.

8.4 Results

For each of the five images, the ring width RMS variation of each ring was plotted as a function of the azimuthal angle. Figures 8.10 – 8.13 show the ring width RMS variations for image 110004. The top panels show the data points with error bars (the RMS is calculated from the 180 profiles but with the data falling into the 12 gaps removed) as a function of the azimuthal angle, where 0° is at the top of the ring; 90° is to the south; 180° is at the bottom; and −90° is to the north. A modulation with a 30° period is clearly shown in this figure. Each middle panel is a spline fit of the data. Each bottom panel is the Fourier transformation of the data, plotted as the modulation power vs. the frequency in one circumference. The modulation has dominant frequencies of 2 (180° period), 12 (30° period) and their higher harmonics.

Figures 8.14 – 8.17 are the summary figures for the HRMA ring focus measurements. They show the ring width RMS variations and their Fourier transforms for all four rings from all five measurements. The five ring focus measurements were made from the beginning of the HRMA phase 1 calibration to the end of the phase 1. The purpose is to see if there were any changes in the ring structure, especially the 12 fold symmetry, in order to determine the change in the epoxy strain.

Rings with the Fe-K source (the dotted curve) have wider width, because Fe-K has higher energy (6.4 keV), therefore more scattering which make a wider ring width. The width of ring 1 for Fe-K is especially wide and noisy (it goes off scale). This is because there were not many photons in ring 1 as mentioned before (see Figure 8.2). For Shells 3, 4 and 6, Fe-K rings have wider width but basically match the profiles from other sources.

Data taken with Al-K and C-K source have enough counts and less scattering. They are used to do the comparison for the epoxy strain effect.

All the curves have 12 dominant split peaks at 30° multiples. They are primarily due to the gravity, and possibly also thermal, and epoxy strain effects. Since each shell was held at 12 rather

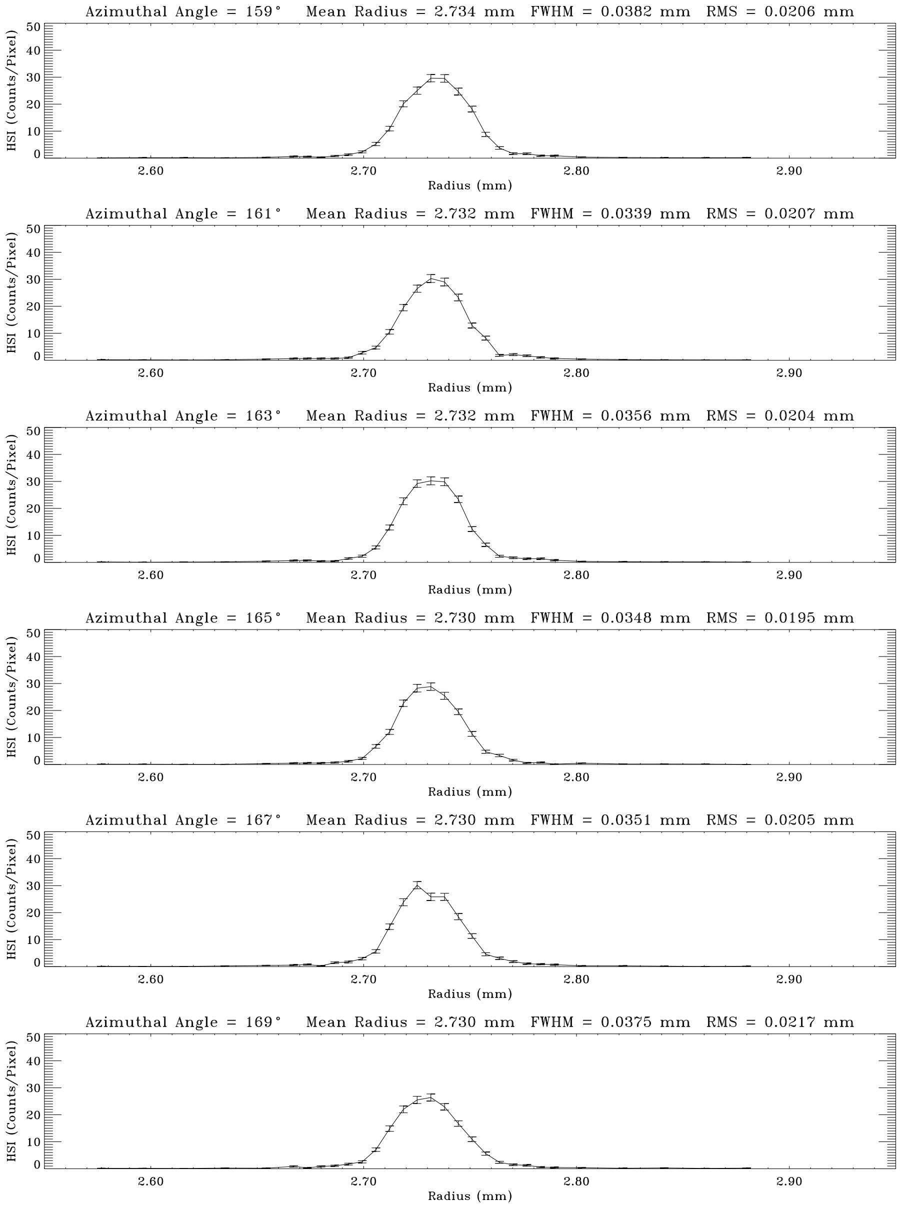

Figure 8.6: Selected profiles from ring 4. Source: Al-K; Defocus: 65.2 mm; Date: 97/01/24; Run ID: 110004; TRW ID: D-IXH-RF-1.005.

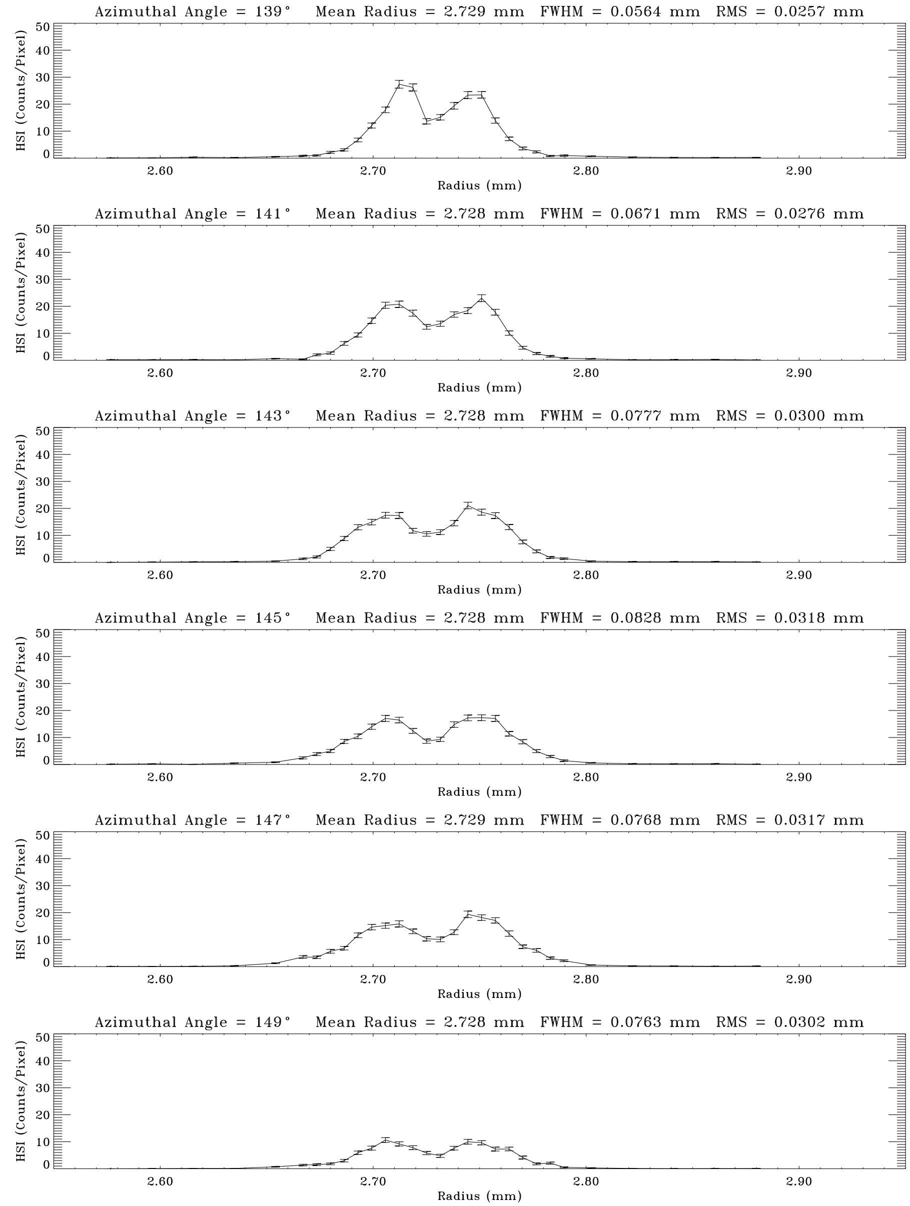

Figure 8.7: Selected profiles from ring 4. Source: Al-K; Defocus: 65.2 mm; Date: 97/01/24; Run ID: 110004; TRW ID: D-IXH-RF-1.005.

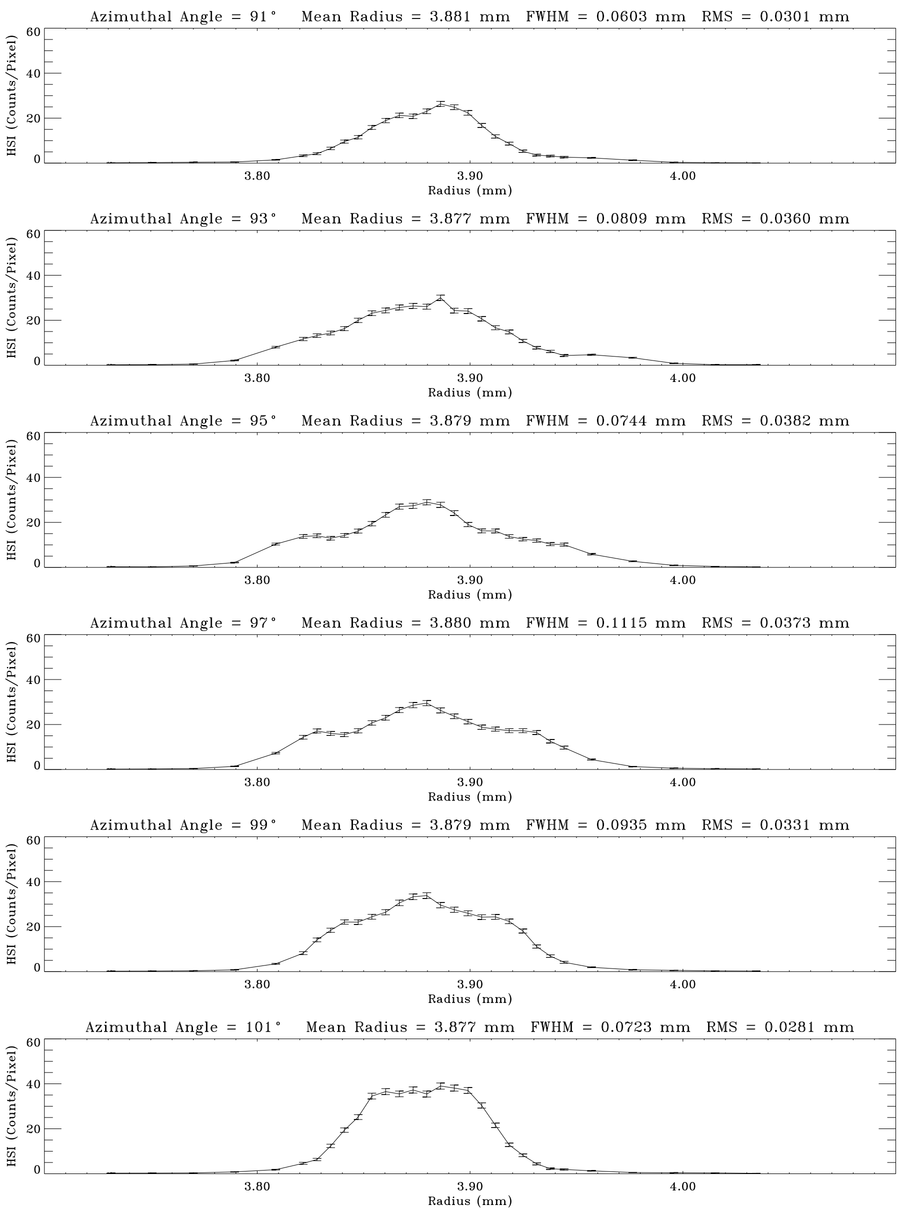

Figure 8.8: Selected profiles from ring 1. Source: Al-K; Defocus: 65.2 mm; Date: 97/01/24; Run ID: 110004; TRW ID: D-IXH-RF-1.005.

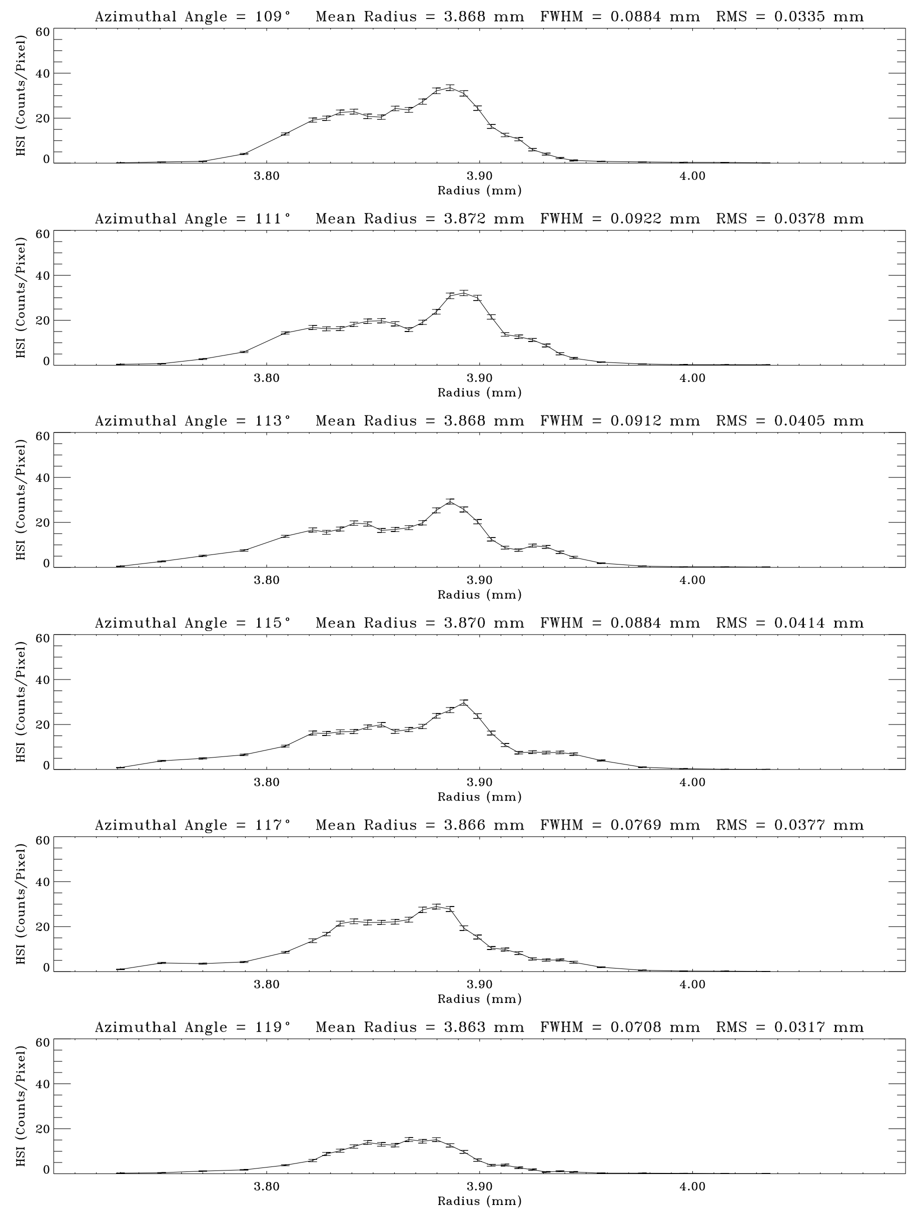

Figure 8.9: Selected profiles from ring 1. Source: Al-K; Defocus: 65.2 mm; Date: 97/01/24; Run ID: 110004; TRW ID: D-IXH-RF-1.005.

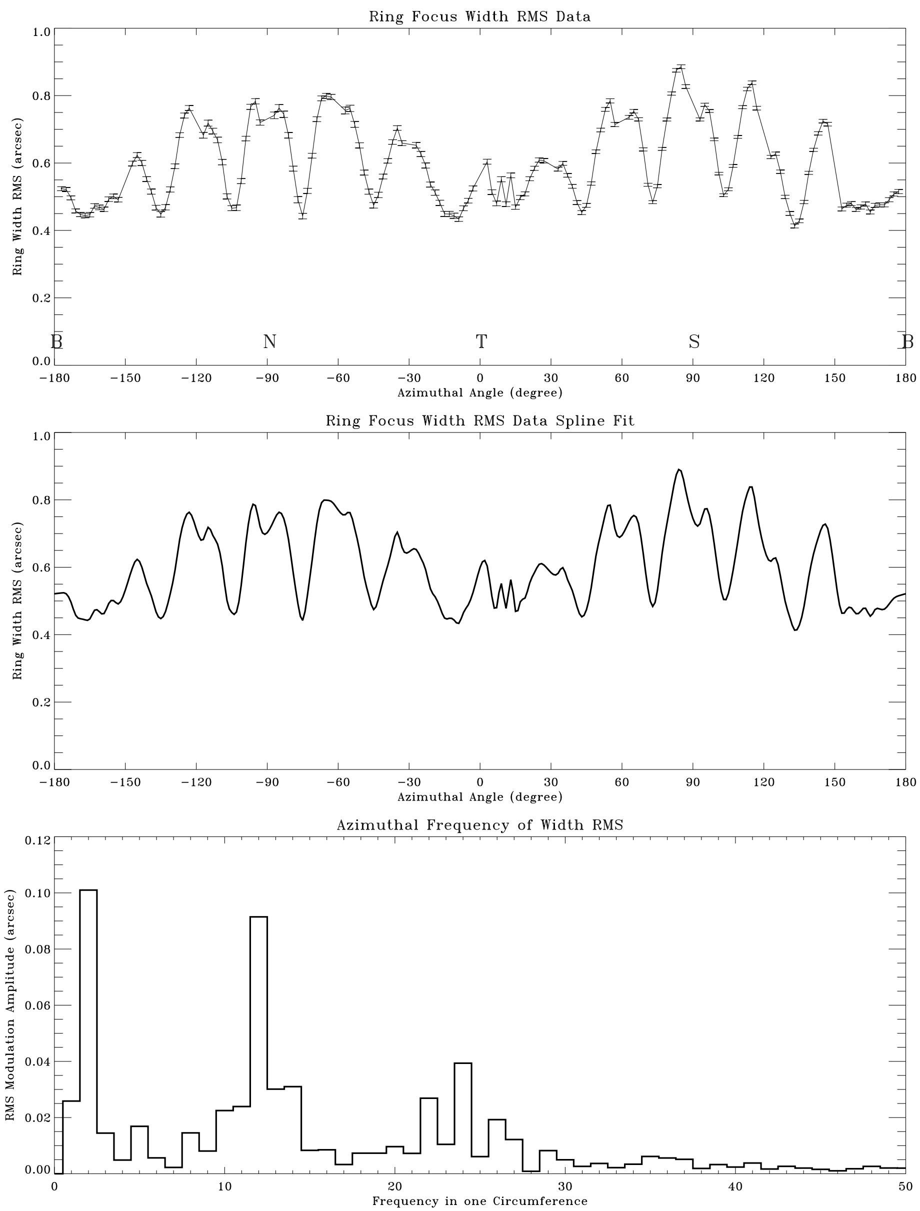

Figure 8.10: The Ring width RMS from ring 1. Source: Al-K; Defocus: 65.2 mm; Date: 97/01/24; Run ID: 110004; TRW ID: D-IXH-RF-1.005.

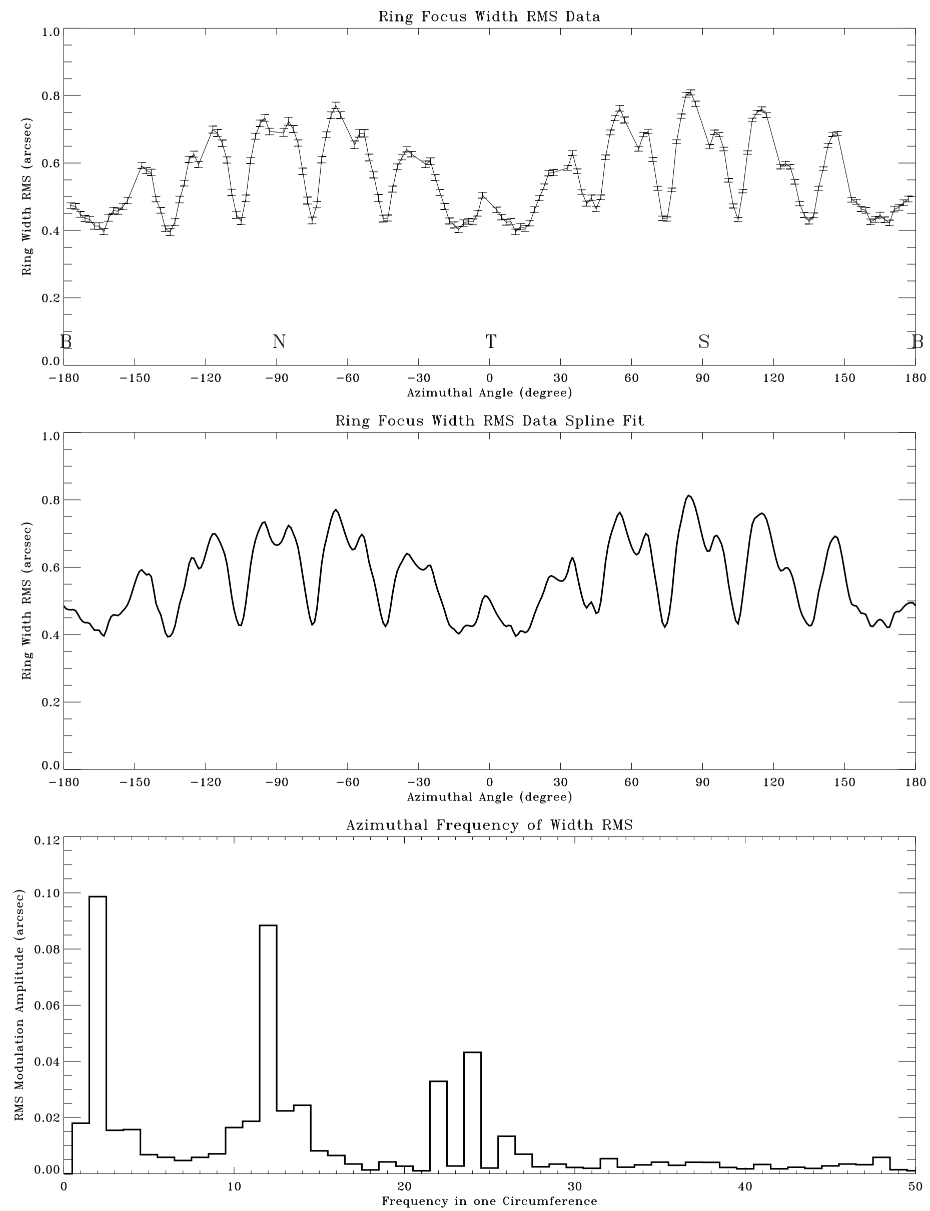

Figure 8.11: The Ring width RMS from ring 3. Source: Al-K; Defocus: 65.2 mm; Date: 97/01/24; Run ID: 110004; TRW ID: D-IXH-RF-1.005.

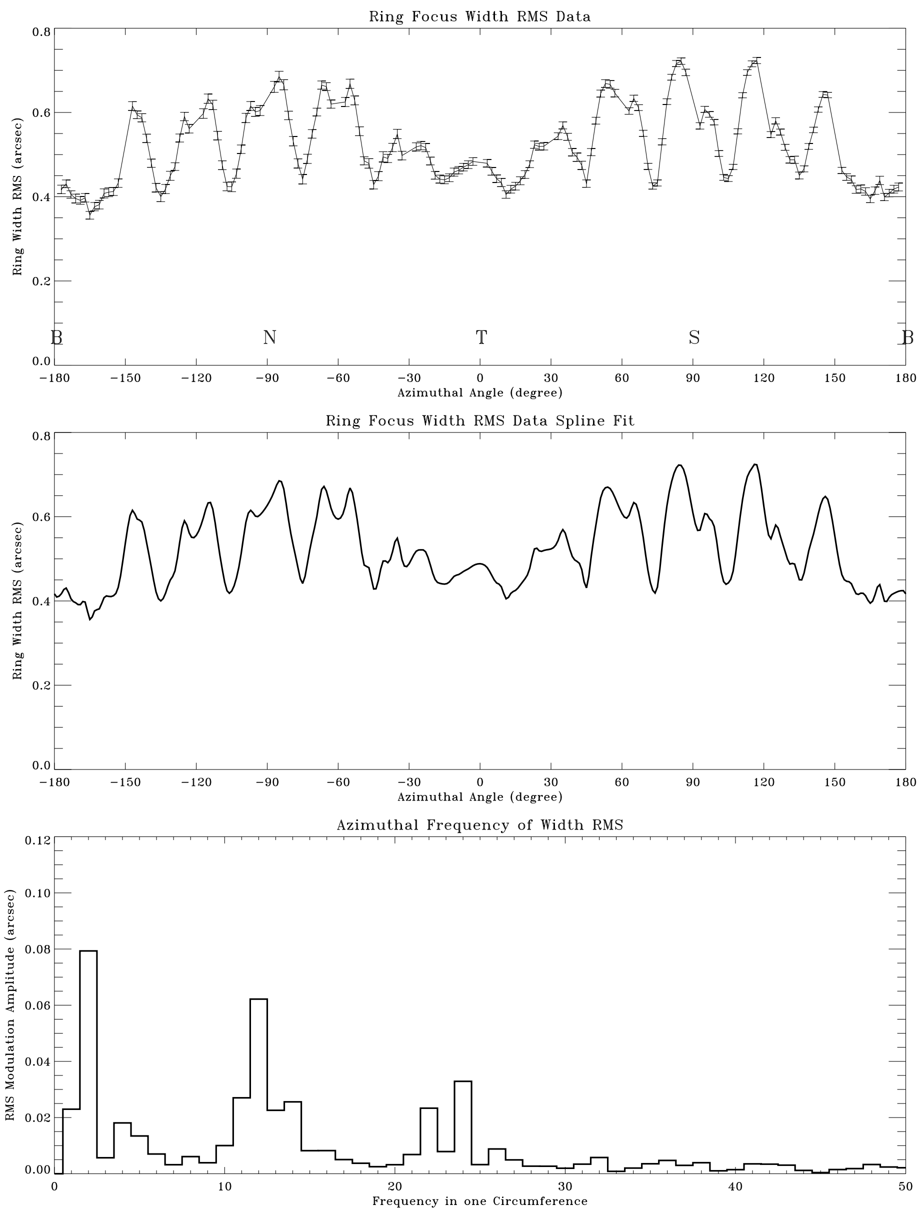

Figure 8.12: The Ring width RMS from ring 4. Source: Al-K; Defocus: 65.2 mm; Date: 97/01/24; Run ID: 110004; TRW ID: D-IXH-RF-1.005.

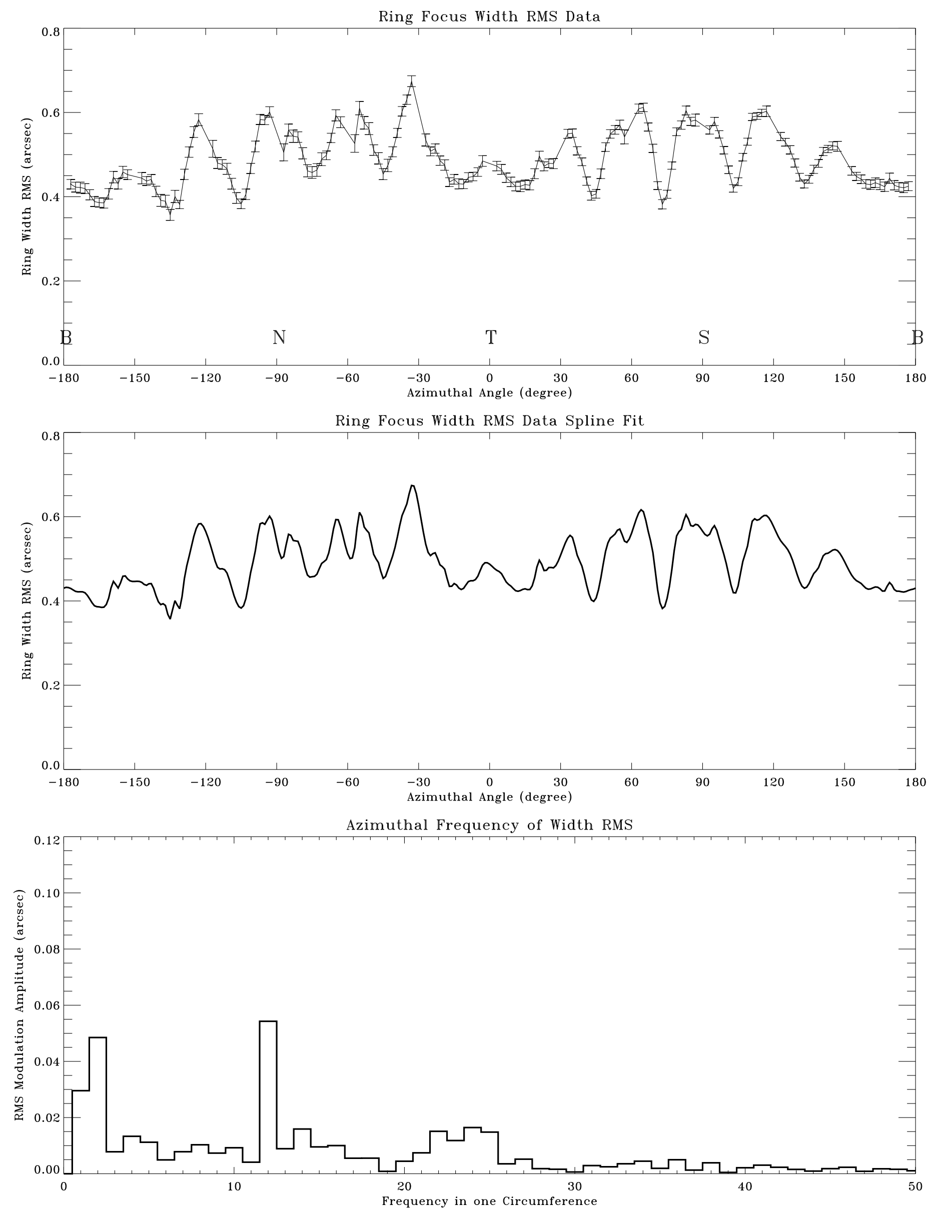

Figure 8.13: The Ring width RMS from ring 6. Source: Al-K; Defocus: 65.2 mm; Date: 97/01/24; Run ID: 110004; TRW ID: D-IXH-RF-1.005.

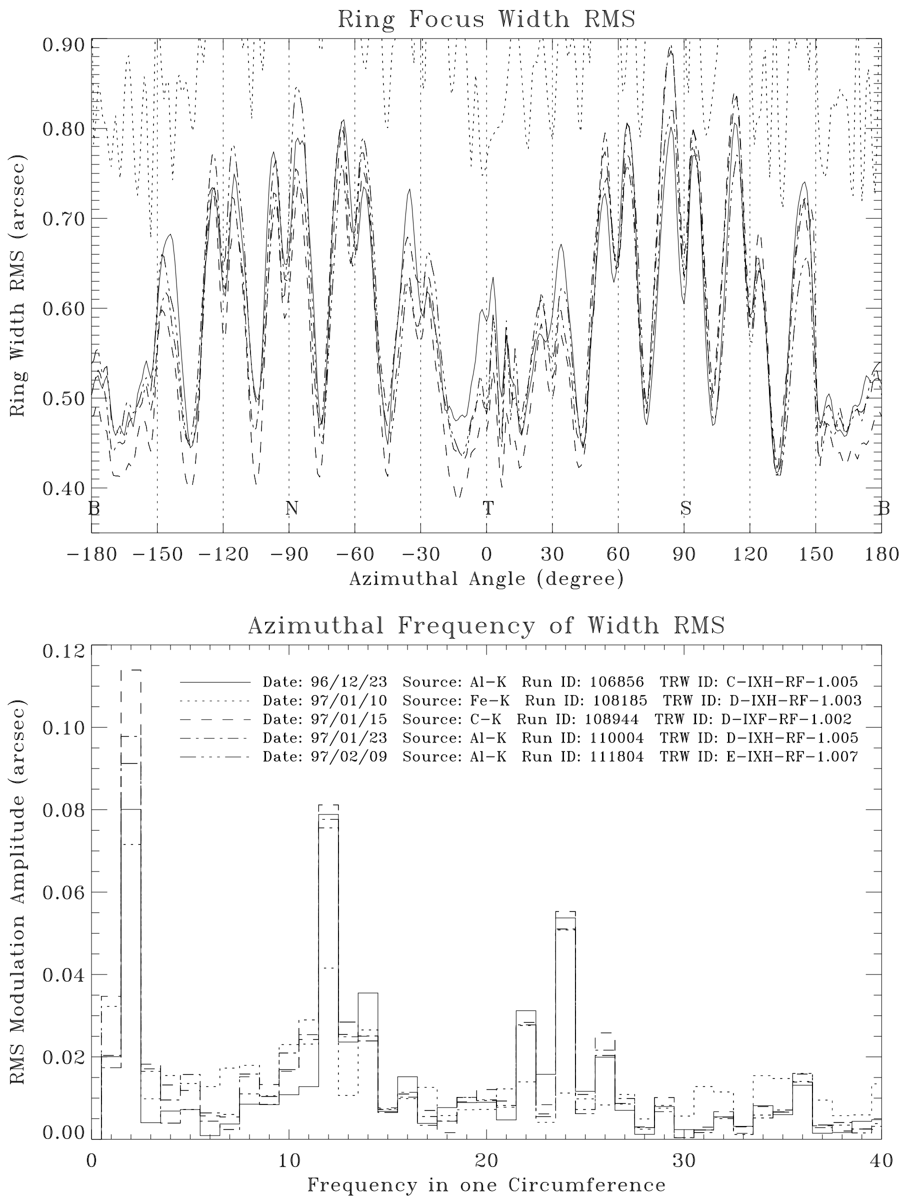

Figure 8.14: The Ring width RMS of ring 1, from all five ring focus measurements.

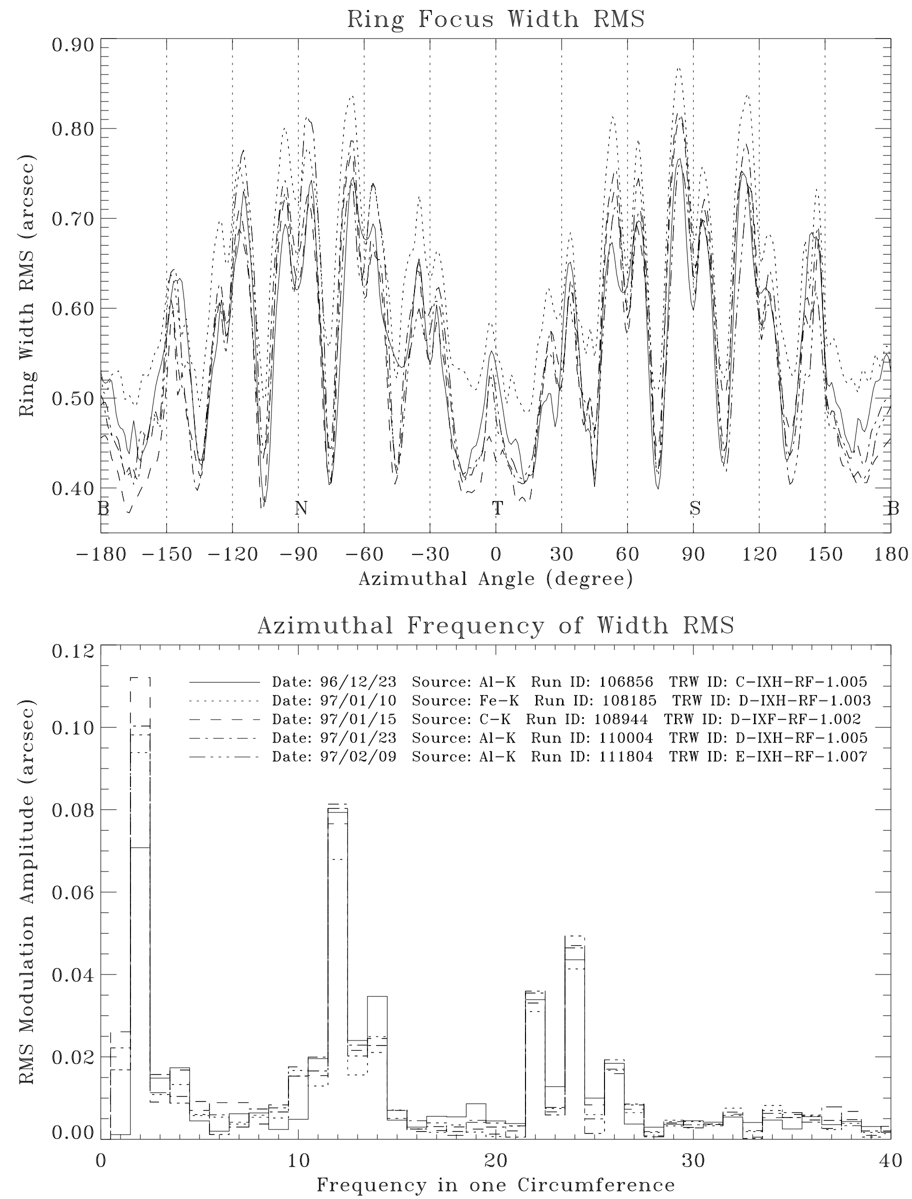

Figure 8.15: The Ring width RMS of ring 3, from all five ring focus measurements.

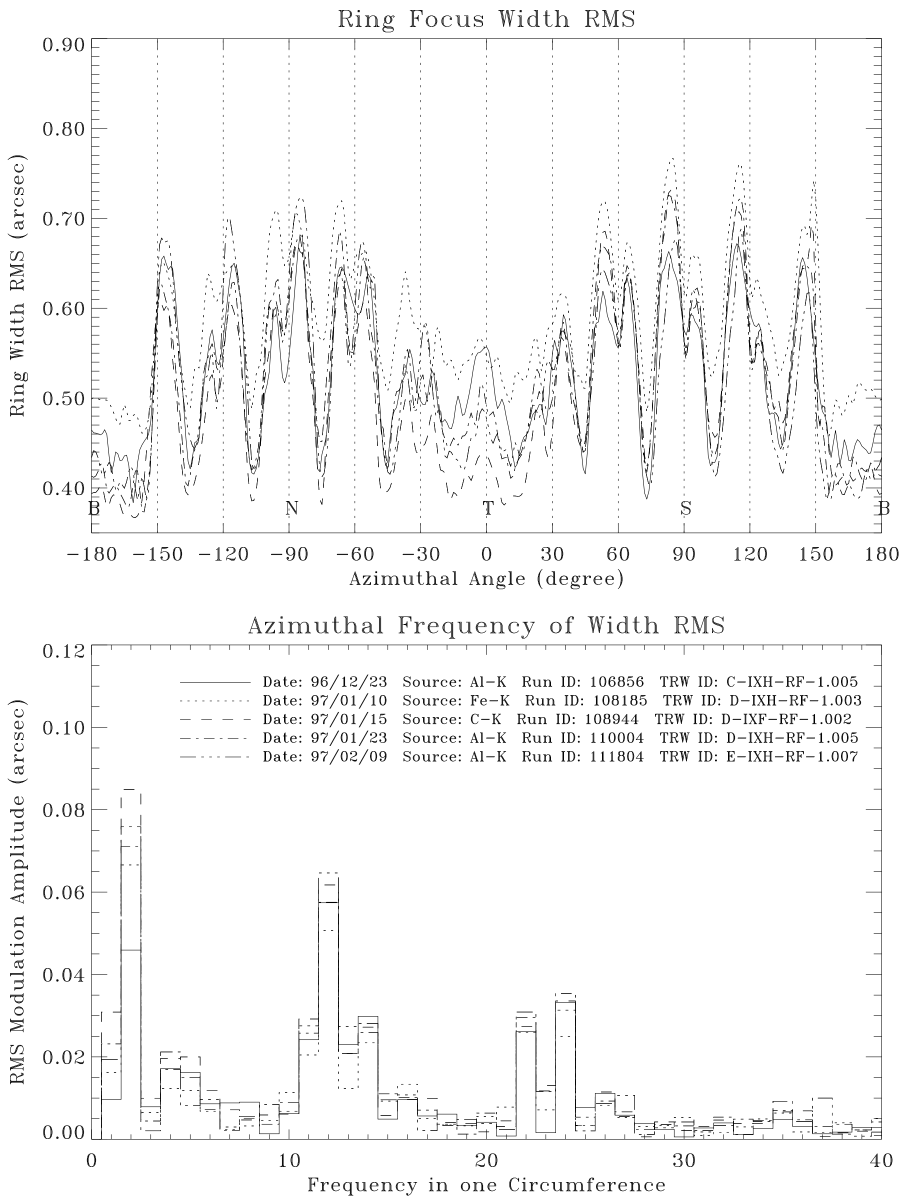

Figure 8.16: The Ring width RMS of ring 4, from all five ring focus measurements.

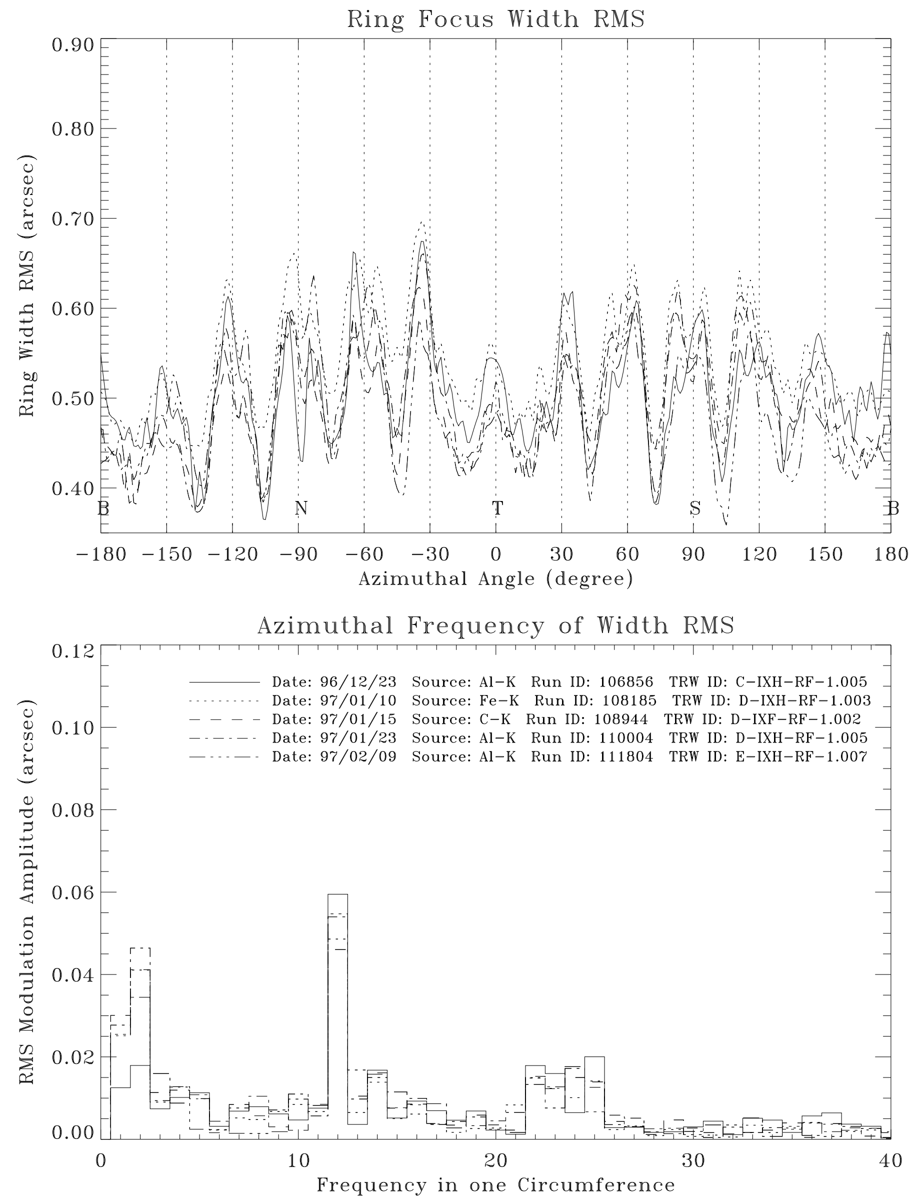

Figure 8.17: The Ring width RMS of ring 6, from all five ring focus measurements.

small areas (the largest shells were epoxy bonded to 2 inch diameter Invar pads), gravity caused local distortions at those 12 locations. The distortions along the sides of the mirror were more severe than at the top or bottom. These local distortions would cause higher harmonics of the 12-fold symmetry (i.e. 24 fold) and also a 2-fold symmetry due to the fact that the amplitude of the side distortions are much larger than that from the top and bottom. The 2-fold symmetry is slightly upset because the epoxy gaps are not uniform at each of the 12 bonds.

8.5 Ring Focus Models

To understand the results of the HRMA ring focus measurements, we developed ring focus models. The ring focus models are computer generated images by ray-tracing to simulate the X-rays passing through the HRMA mirror and the test system. All the details such as the mirror surface roughness scattering and the HSI detector response were also simulated. The analysis used for the real data was also applied to the model images. As an example, Figure 8.18 is a HRMA model ring focus image with all the elements considered and the epoxy strain set at −0.5% (an inward bump of 0.5% of the epoxy thickness at the bonding points, see below).

The ring focus models include the following elements:

1. HRMA mirror surface map from HDOS.
2. HRMA mirror assembly errors as measured by EKC.
3. HRMA decenter and tilt as measured during the calibration.
4. Gravity (1-g) distortions modeled by SAO.
5. Epoxy strain distortions modeled by SAO.
6. Thermal effects.
7. Finite source distance.
8. HRMA apertures and their supporting struts.
9. HRMA mirror surface reflectivity and roughness scattering.
10. HSI detector resolution.

The finite size of the source was not included.

The HRMA mirror surface (low frequency) map are from the Hughes Danbury Optical Systems, Inc. (HDOS) metrology measurements. The HRMA mirror assembly errors were measured by the Eastman Kodak Company (EKC) when assembling the HRMA. Because mirror shells were made slightly different from ideal shells, they had to be bonded slightly different from the design positions in order to obtain the best on-orbit parfocalization. The HRMA decenter and tilt (H shells with respect to P shells) errors were measured and analyzed during the calibration (Chapter 13 and Gaetz et al., 1997).

The SAO 1-g model is a full 360 degree Finite Element Analysis (FEA) model. Twelve tangential flexures support each optic. In a 1-g vertical field, the model indicates that the flexures at the sides of the optic each support about 17% of the optic's weight, the flexures 30° above and below the sides support about 12% of the optic's weight and the flexures 60° above and below the sides support about 4% of the optic's weight. The flexures at the top and bottom support essentially no weight because of their flexibility. The flexures that are more highly loaded cause the optic to twist more about the optical axis (a so-called circumferential slope). At the side locations (±90°), the gravity causes a large slope change on the optic across the centerline of the flexure such that optic above the ±90° was pushed in while below the ±90° was pulled out. The peak-to-valley distortion (±85° to ±95°) was about 0.37 μm. Therefore there are inward dimples centered at around ±85° and

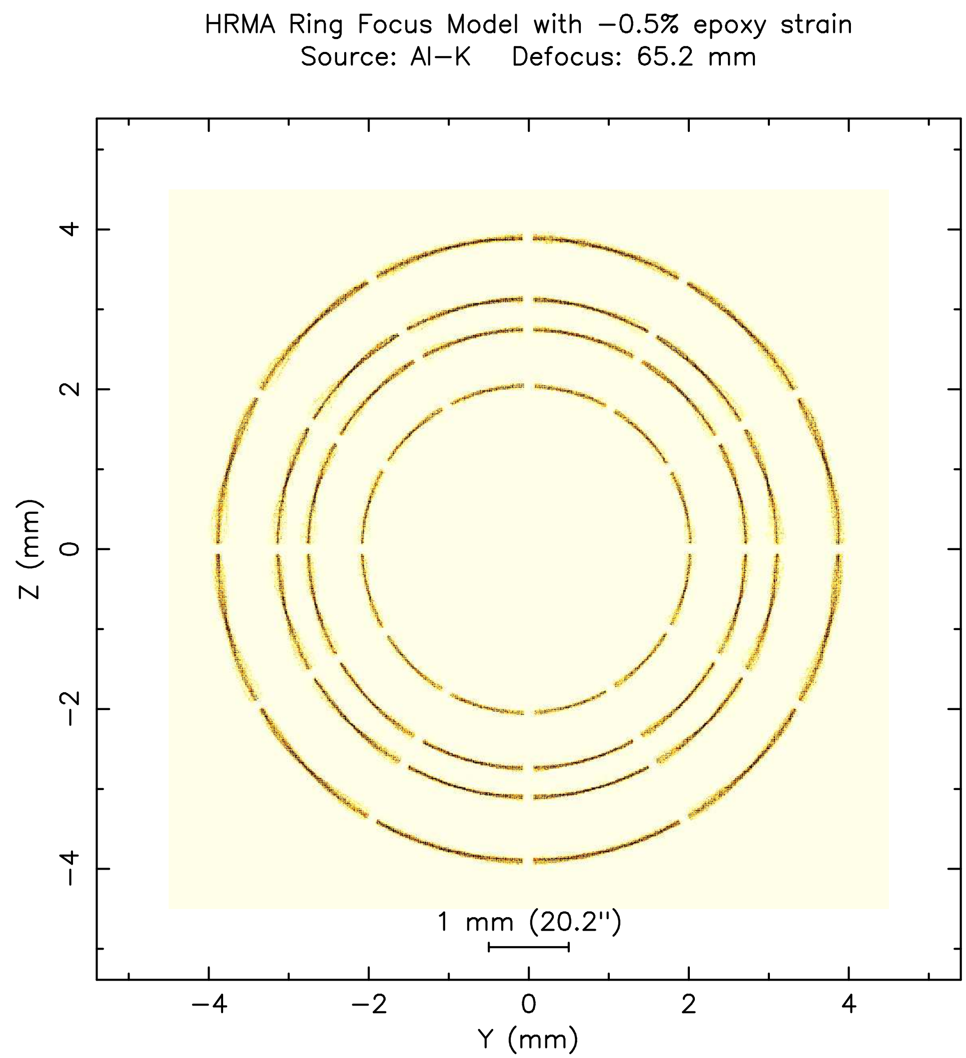

Figure 8.18: The HRMA ring focus model with -0.5% epoxy strain. Source: Al-K; Defocus: 65.2 mm

outward dimples centered at around ±95°. At 30° above and below the side locations, the slope change is about 1/2 of that which occurs at the side locations. At 60° above and below, the slope change is about 1/6 of that at the sides. At the top and bottom of the optic, there is essentially no slope change as there is no twisting effect by the gravity. (A more detailed analysis of the SAO 1-g model can be found in Cohen 1997.)

The epoxy strain was measured on test flats at the EKC. The results show two kinds of effects: (1) The in-plane cure shrinkage of about 0.075% and "through-the-thickness" (TTT, through the 0.0075" nominal thickness direction) shrinkage of about 2% took place within a few days after bonding; (2) Long term epoxy strains of order 1% due to moisture gain and loss in the epoxy, −1% (inward bump) in the fully dried condition and +1% (outward bump) in the fully moist. For effect (1), we assume that about 1 week after each optic is bonded there are 12 outward bumps. Those outward bumps were due to the large (−2%) TTT strain which causes the optic to be pulled outward while the flexure is pulled inward. The magnitude of this outward bump is the equivalent to an epoxy moisture strain of about +0.32%. For effect (2), the epoxy strain will change based on the moisture. The time constant for this effect is on the order of months. (A more detailed analysis of the epoxy strain effects can be found in Cohen 1997.)

For the thermal effects, a uniform temperature change of 11.1°F is equivalent to an epoxy strain of 1%. The optics were bonded at the EKC at an average temperature of 69.83°F, whereas the temperatures during the ring focus measurements were 69.79±0.05°F. This small temperature change is negligible (equivalent to an epoxy strain of 0.0036%).

The finite source distance in the model is 527.27904 meters from the CAP datum A (front of the CAP). The geometries of the HRMA apertures and their supporting struts are well defined.

The mirror reflectivity was calculated using the optical constant obtained by Henke (0.1–2 keV) (Henke et al., 1993) and synchrotron measurements (2–12 keV) by SAO (Graessle et al., 1997). The mirror surface roughness data from the HDOS WYKO measurements were used with a program `foldw1` to calculate scattering distributions. The calculation was based on the scattering theory in Beckmann and Spizzichino (1963).

The HSI detector has a spatial resolution of 14 μm (FWHM) and read out pixel size of 6.45 μm.

Of all the elements mentioned above, the 1-g and epoxy strain are the two central issues for the modeling. Although gravity is constant, epoxy strain can change. That is why we make several measurements during the calibration to determine the epoxy strain change. However, the gravity effect is very strong and the epoxy strain exhibits only a very small effect on the ring focus RMS width where the gravity effect dominates.

Figure 8.19 shows the model of ring 1 with the Al-K source and all of the model elements except for gravity and epoxy strain. The ring width RMS is about 0.5″, with a random noise of the order of 0.1″. This "noisy" ring width is due to the actual mirror surface imperfections as measured at the HDOS. (For an ideal mirror, the ring width RMS should be 0.01″ with no noise.) As seen from its Fourier transform, there is no noticeable modulation to the general "noisy" shape (the largest term is only 0.015″). This indicates that there is no significant "structure" in the mirror.

Figure 8.20 shows the model of ring 1 with the 1-g effect but still without any epoxy strain. The ring width RMS displays significant split peaks at 30° multiples, except at the top and bottom of the ring. This is the gravity twisting effect at the optic holding points as expected. Notice the base line of this curve is still at about 0.5″ which is set by the mirror surface figure (imperfection). Its Fourier transform shows dominant 12 fold symmetry and higher harmonics due to the 12 split peaks, as well 2 fold symmetry due to the fact that the peaks are much larger at the sides than at the top and bottom.

Figure 8.21 shows the model of ring 1 with the epoxy strain effects. The top panel shows the

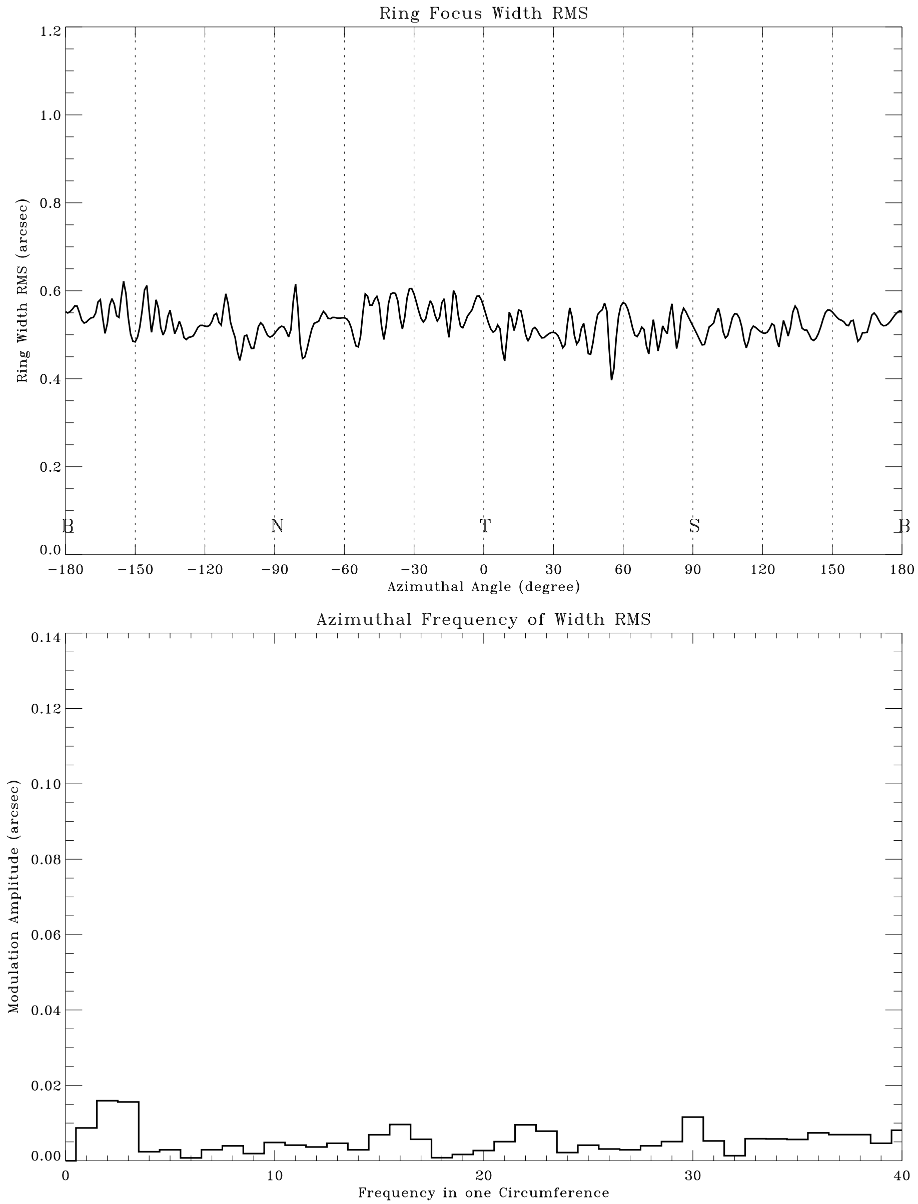

Figure 8.19: HRMA ring focus model: Ring 1, Al-K source, no gravity, no epoxy strain.

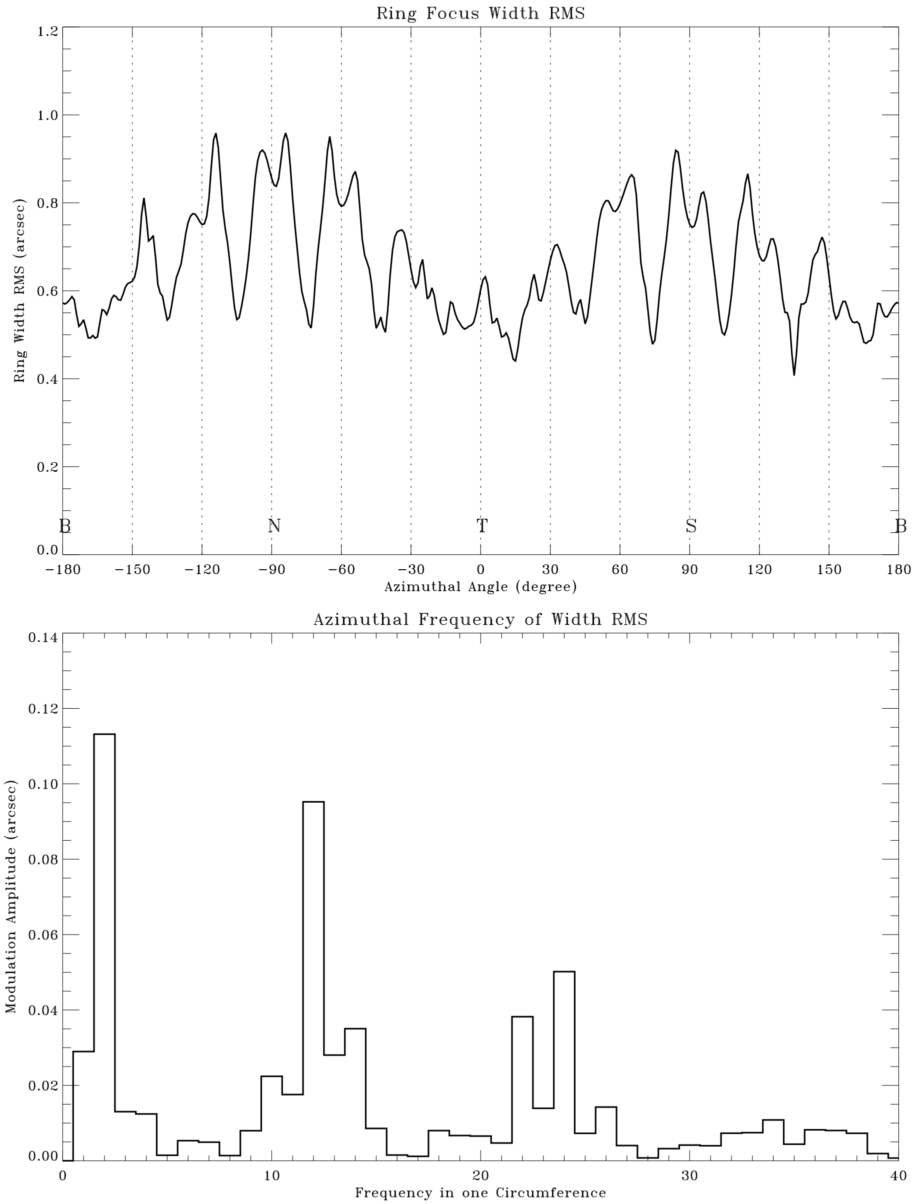

Figure 8.20: HRMA ring focus model: Ring 1, Al-K source, with gravity, no epoxy strain.

mirror with (−2%) TTT initial epoxy cure plus the long term epoxy strains from 1% (fully moist condition) to −1% (fully dried condition). The solid line is the 0.0% moist, i.e. no long term epoxy strain. When the moisture increases, the epoxy strain would enforce an outward bump at each supporting point. This bump would increase the outward dimple below each supporting point due to the gravity twist, and decrease the inward dimple above each supporting point due to the gravity twist. When the moisture decrease, the epoxy strain would enforce an inward bump at each supporting point, and the effect is reversed. This epoxy strain effect is shown clearly in the Figure 8.21: When the moisture increases (0.5% and 1.0% moist), the peaks 5°outside the 30° multiples (below the supporting points) increase while the the peaks 5° inside the 30° multiples (above the supporting points) decrease. When moisture decreases (-0.5% and -1.0% moist), the inside peaks increase while the outside peaks decrease.

As we can see, the effect of epoxy strain change is very dramatic at this 1% level. The actual data (Figures 8.14 – 8.17) show little noticeable effect like this. Therefore we conclude that the epoxy strain change must be significantly less than 1%.

8.6 Comparison of Data with the Model

To see if there were any changes in the ring structure, we compare the ring focus data taken on the first date with that of the last date.

Figures 8.22 – 8.25 show the ring width RMS from date 96/12/23 and 97/02/10. They were both taken with the Al-K source. The top panels show the two RMS curves. There are small changes. For most of the double peaks, especially on the left (north), the inside peaks increased while the outside peaks decreased. As analyzed in the previous section, this indicates the possibility of an inward bump at the flexures due to the moisture decrease in the epoxy. However, this change is not very consistent. On the right side of ring 1, there is very little change. Peaks at 150° from all four rings and some peaks on the right side of ring 3 seem have the opposite change (i.e. inside peaks decreased while outside peaks increased).

The second panels show the Fourier transforms of the above two curves. The third panels show the differences of the two RMS curves (RMS of 97/02/10 minus RMS of 96/12/23). The bottom panels show the Fourier transform of the difference. In general, the changes in the RMS width are very small – only in the 0.1″ level.

The small change in the ring focus could be due to the temperature, gravity or the epoxy strain. The temperature during the measurements, as mentioned earlier, was very constant and very close to the HRMA assembling temperature and its effect is negligible. The gravity could cause the small change if the HRMA support conditions were changed from the first to the last date of the measurements. This is possible as the test vacuum chamber was opened twice and work was done on the HRMA actuators during both repress cycles. However, at this time, we do not have enough convincing data and information to model this scenario. Supposing that the change was purely due to the epoxy strain, which is the most likely case, we can give a estimate of the change based on our model.

Figure 8.26 shows the model for ring 1 with the epoxy strain of −2% TTT plus 0.0% and −0.3% moist. The four panels show the same curves as shown in Figure 8.22 and with the same scale. Comparing Figure 8.26 with Figure 8.22, we see many similarities and also differences:

1. The width RMS curve of both data and model have the same base line of about 0.5″. This indicates that the model for the mirror surface figure is correct.

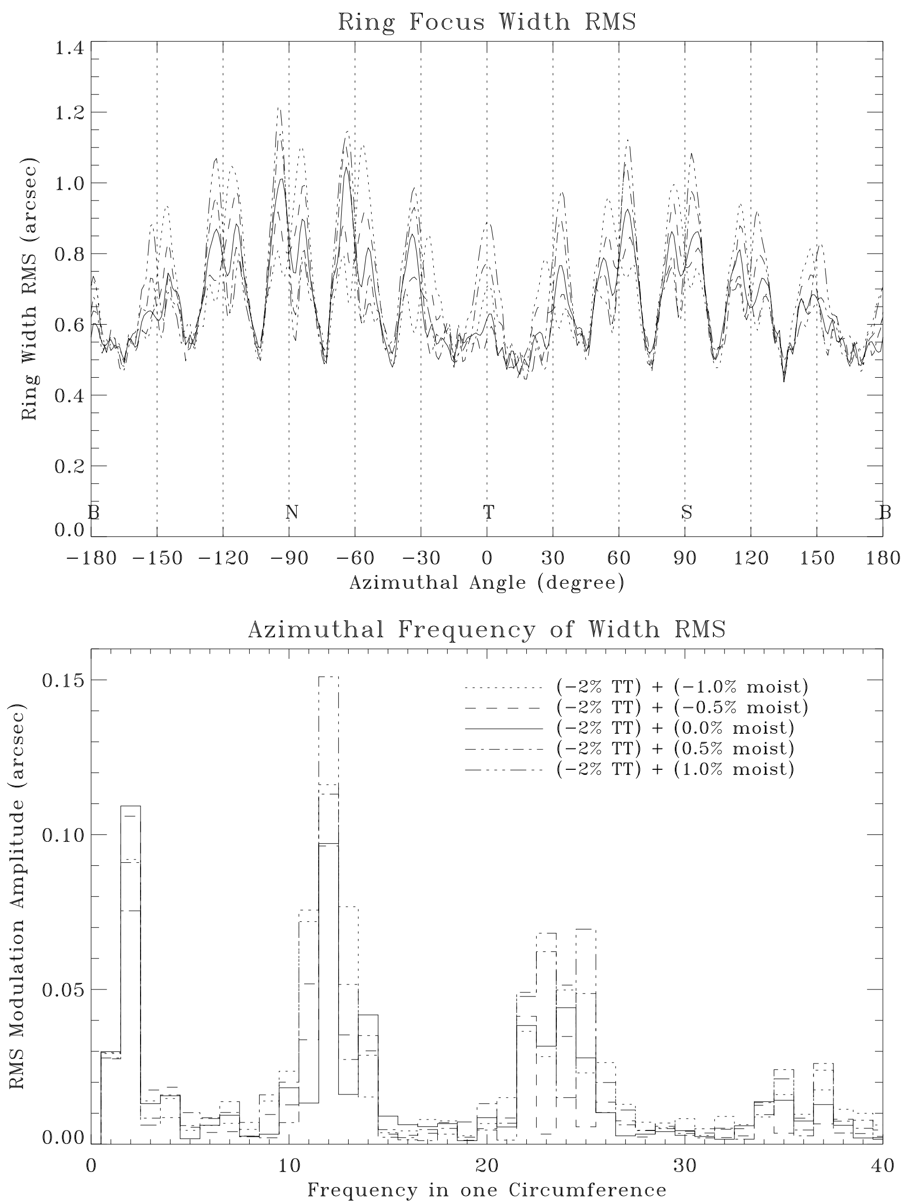

Figure 8.21: HRMA ring focus model: Ring 1, Al-K source, with gravity and epoxy strain change.

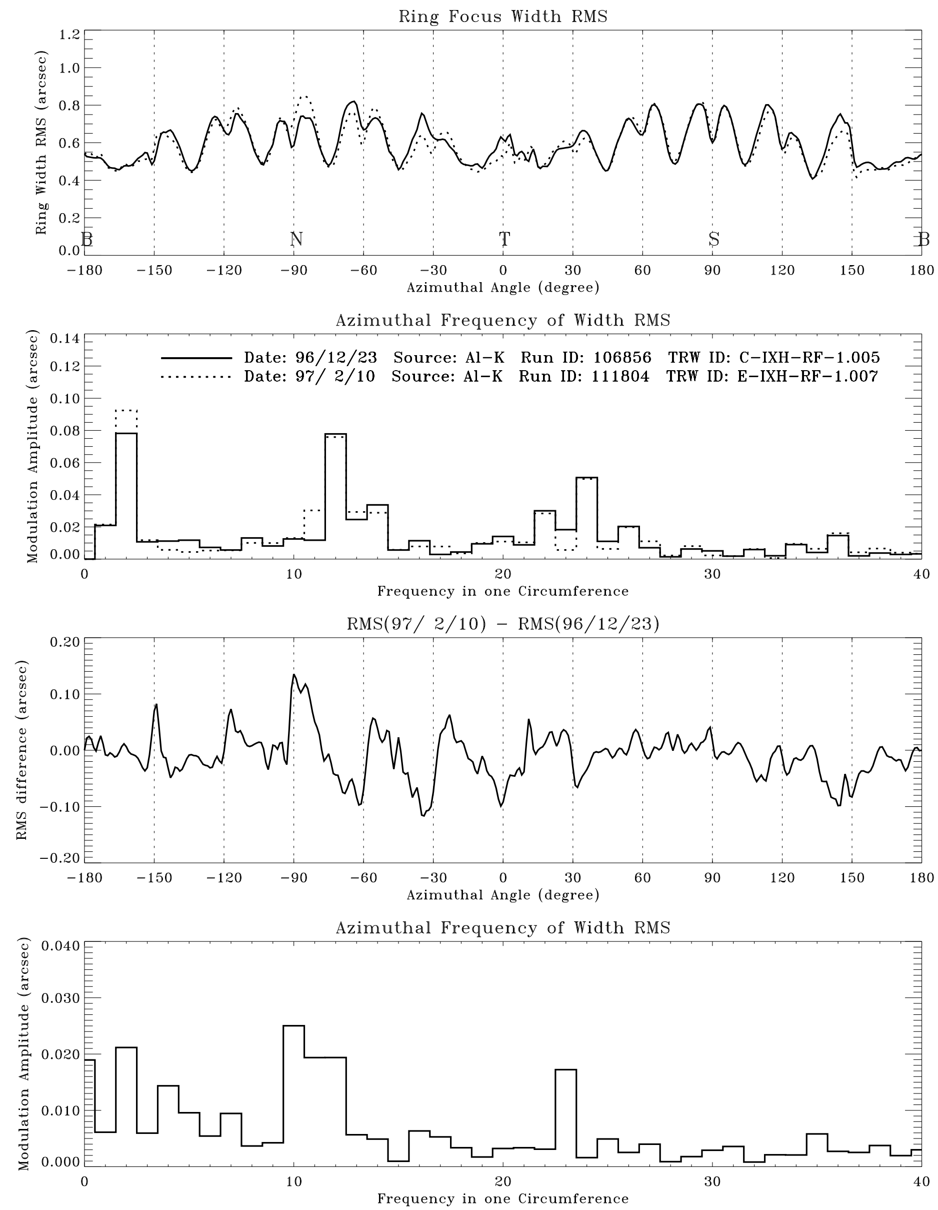

Figure 8.22: HRMA ring focus Data: Ring 1, Al-K source, data of 96/12/23 and 97/02/10 and their difference.

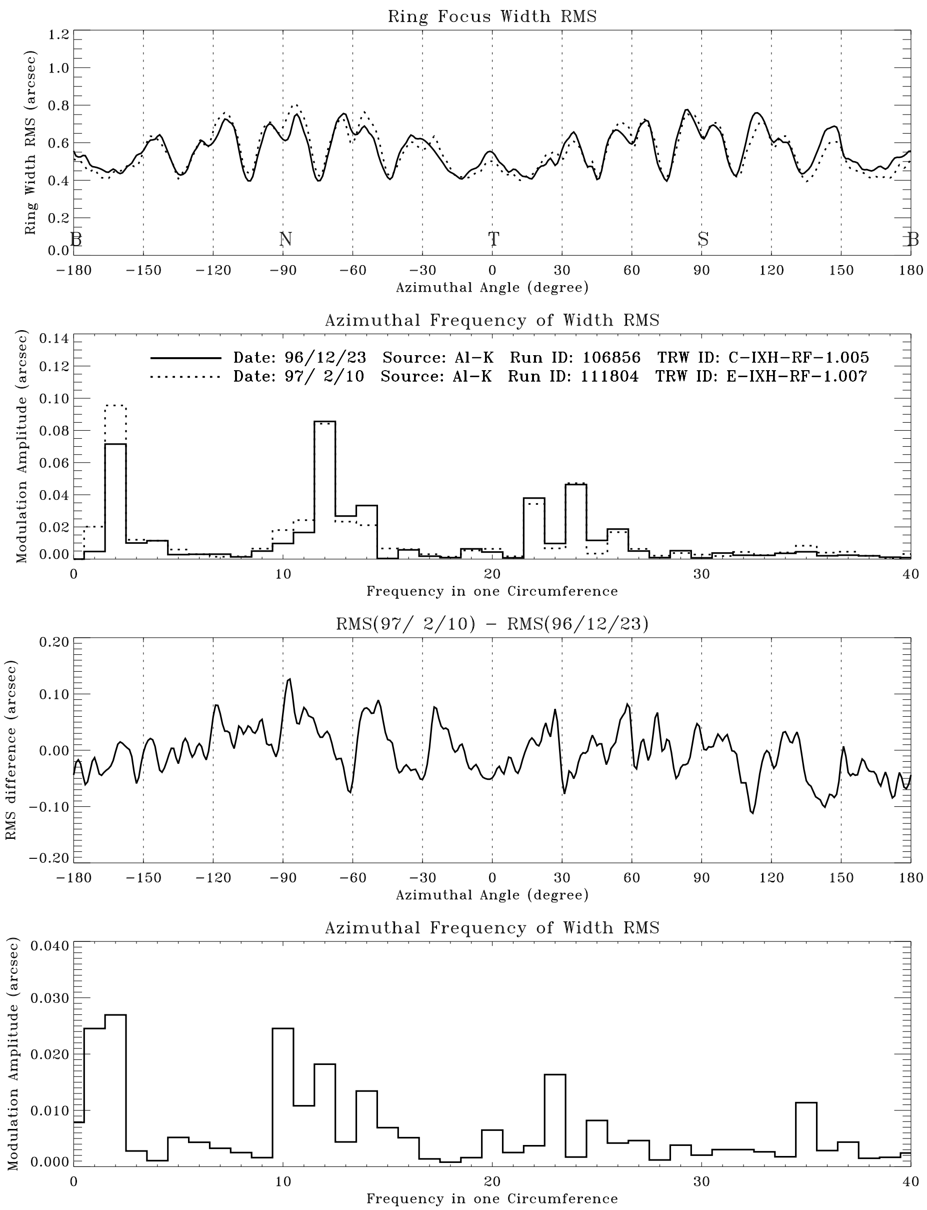

Figure 8.23: HRMA ring focus Data: Ring 3, Al-K source, data of 96/12/23 and 97/02/10 and their difference.

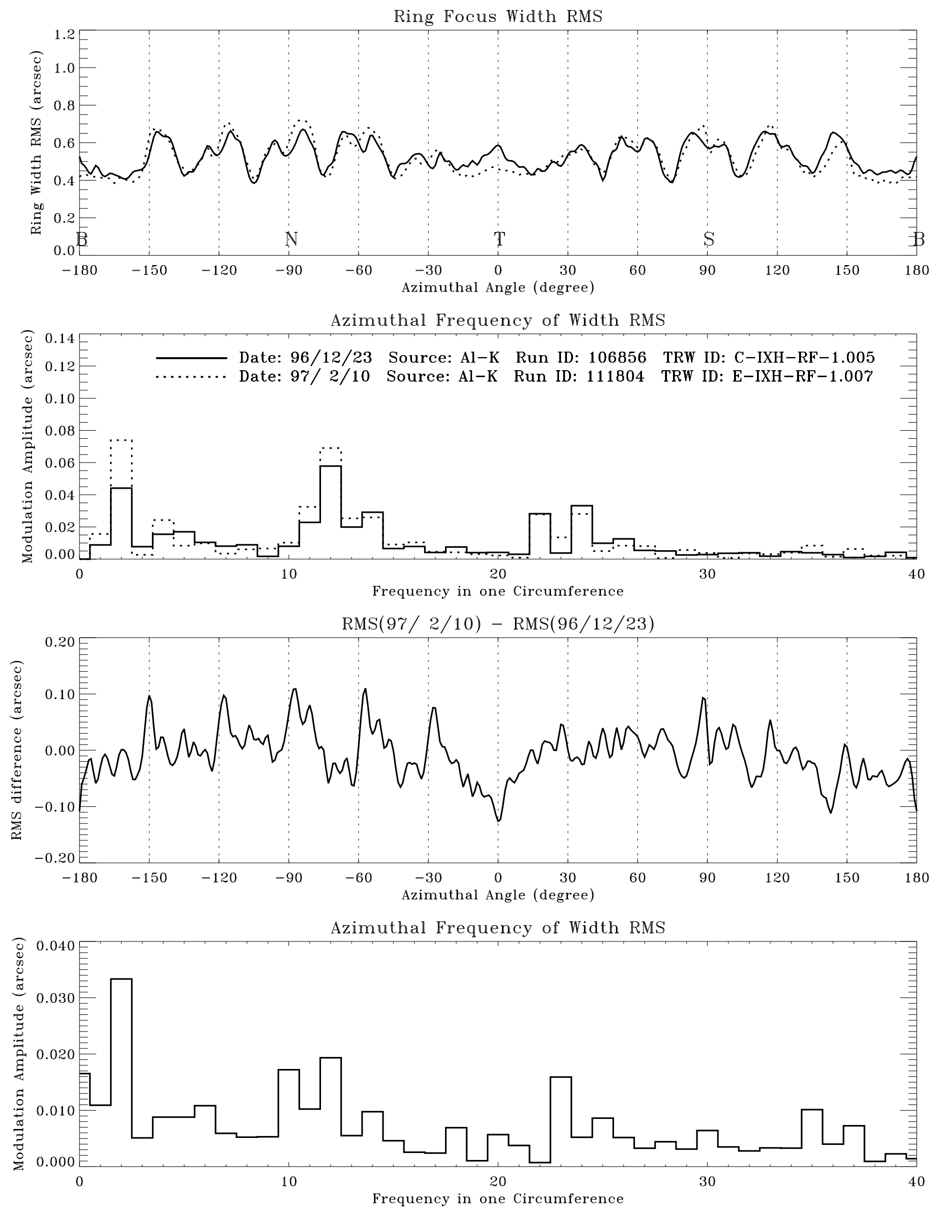

Figure 8.24: HRMA ring focus Data: Ring 4, Al-K source, data of 96/12/23 and 97/02/10 and their difference.

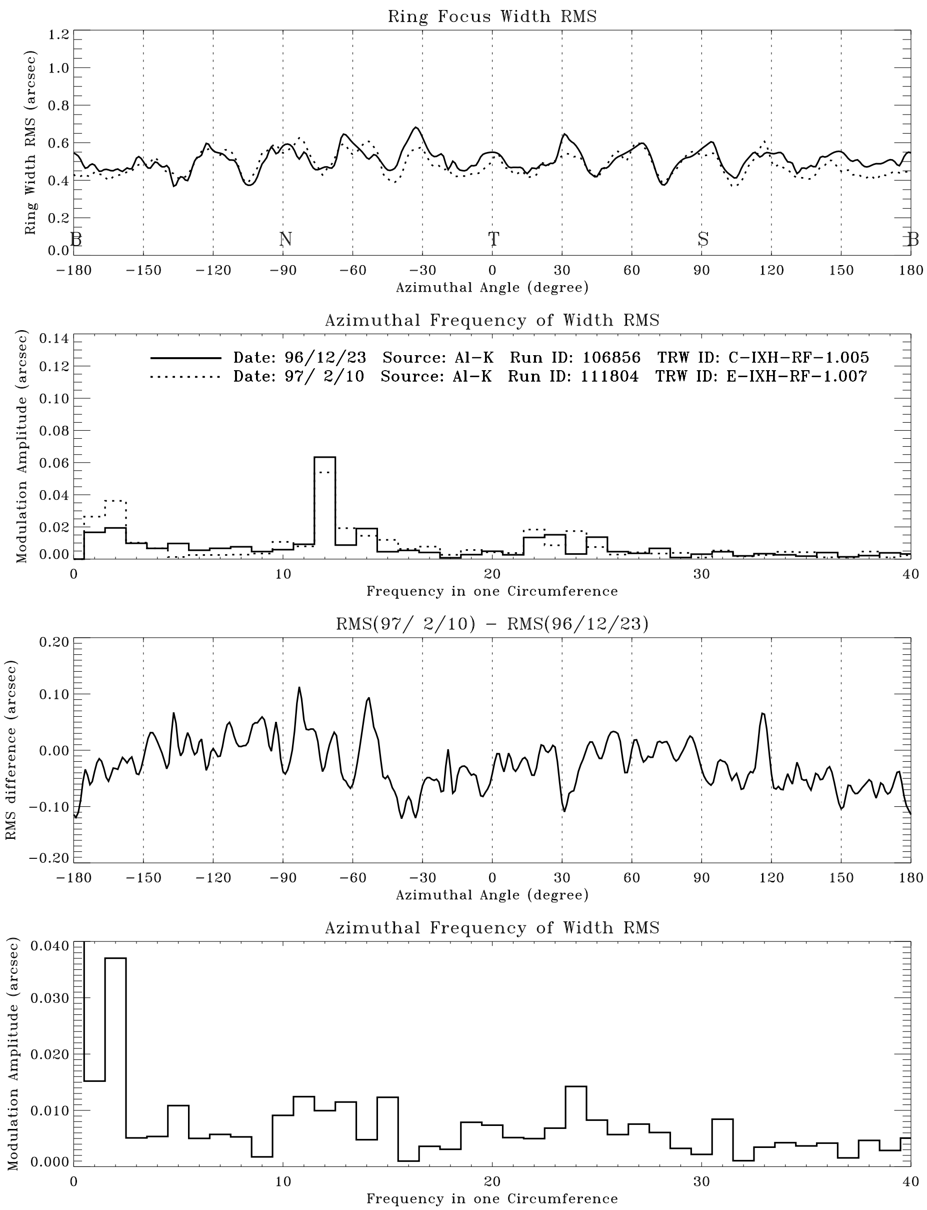

Figure 8.25: HRMA ring focus Data: Ring 6, Al-K source, data of 96/12/23 and 97/02/10 and their difference.

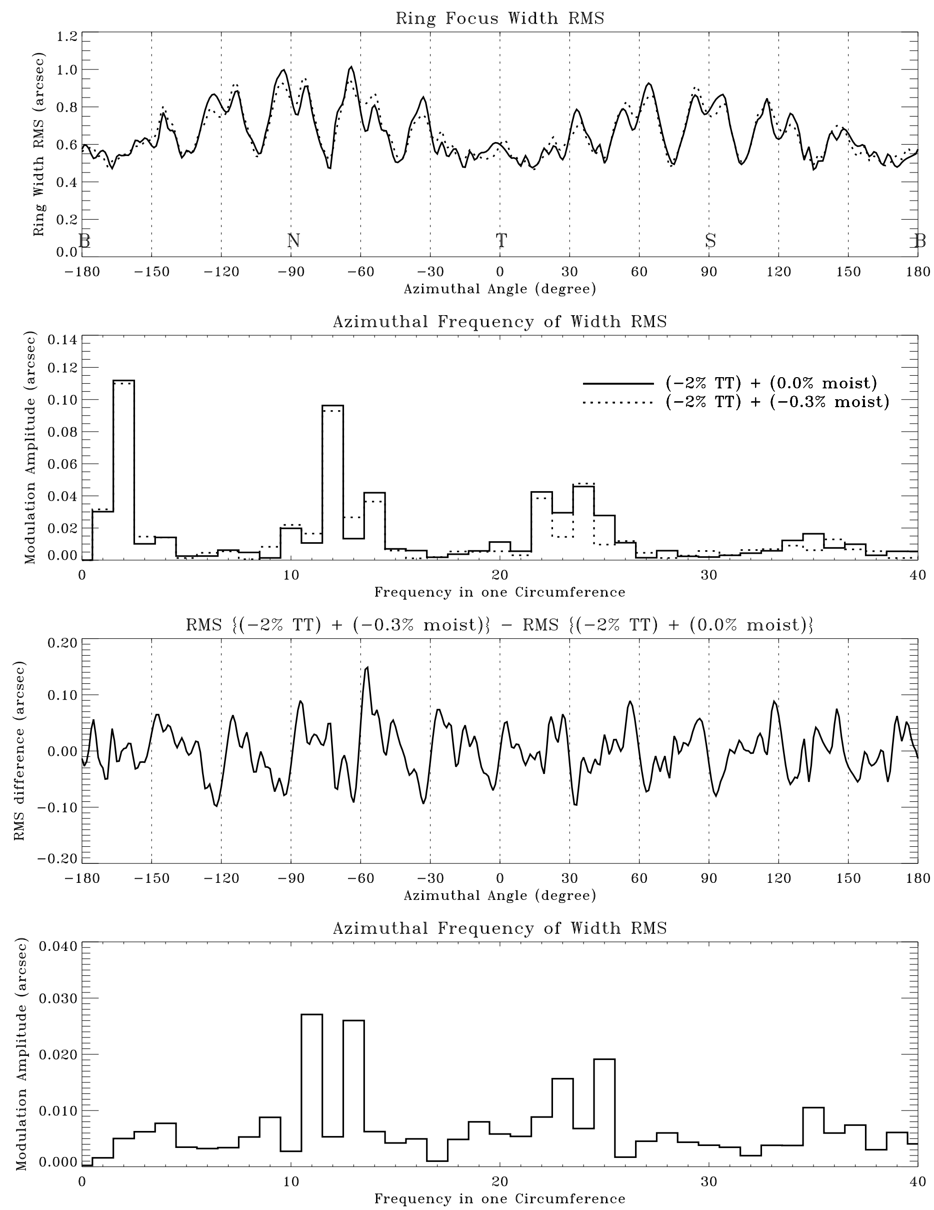

Figure 8.26: HRMA ring focus model: Ring 1, Al-K source, epoxy strain with 0.0% and -0.3% moist and their difference.

2. Both curves have 12 dominate split peaks at the 30°multiples. They both have 2, 12 and 24 fold symmetries. This indicates that the 1-g model is right.

3. The model has larger modulation amplitude than that of the data. This indicates that we have not chosen the correct amount of epoxy strain for the model.

4. The model show the inside peaks increase and outside peaks decrease on both sides of the curve due to the epoxy moisture loss, while the data only shows this effect on the left side (-180°to 0°). At this time, we do not yet have a good explanation for this. It could be due to the HRMA loading condition changed during the test. It could also be due to the epoxy moisture condition was not uniform to begin with.

5. The RMS difference curves show similar structures between the data and the model. Only the data has smaller amplitude on the right side (0° to 180°). Their Fourier transforms also have similar and different peaks. These indicate that our model for the epoxy strain change is still not perfect.

8.7 Summary

The HRMA ring focus measurements were made with the HSI detector during the HRMA calibration. From 96/12/23 to 97/02/10, five HSI images were taken. The data show the RMS ring width has 12 dominate split peaks around the center line of the 12 mirror holding flexures. The ring focus model was generated using the raytrace, considering all the factors from the mirror surface figure to the XRCF test environment.

In general, the model and the data have fairly good agreement. Effects of mirror surface figure, assembly errors, decenter and tilt, finite source, gravity etc. are clearly shown in the model and agree with the data. The change in the epoxy strain (the only thing we can actually measure) is quite small (significantly less than 1%). The strong 1-g effect masked the epoxy strain effect therefore we can not, at this time, determine accurately the epoxy strain effect and its change. The small epoxy strain change could be caused by most of the moisture loss in the epoxy bond occurred before the beginning of ring focus measurements, due to the HRMA vacuum exposure and dry nitrogen purge used after the final assembly. The small change observed during the calibration interval would lead us to expect a limited change between the calibration and flight performance. Even in a worst case, it is unlikely the epoxy strain effect on-orbit will be more than 0.5% due to moisture loss. A raytracing calculation with the 1-g effect removed shows that this case will degrade the AXAF performance by no more than 5% from a one arc second diameter encircled energy for mirror pair 1. The observed change of the ring focus data from other shells is less than that observed from Shell 1, and hence the total effect should be less than 5% loss for the whole HRMA.

At the time of this report is written, this study is still underway. An HRC ring focus image taken two months after the last HSI data is still yet to be analyzed. More detailed modeling is still to be made. We will provide a more detailed report and the HRMA performance prediction once this study is complete.

Chapter 9

Beam Uniformity

This chapter contains an overview of the Beam Uniformity (BU) measurements taken at XRCF and an analysis of BU data from Phase 1 testing.

9.1 Beam Uniformity Tests

After each source and filter change at XRCF, a Beam Uniformity (BU) scan was taken to determine if the beam was, in any way, non-uniform at the entrance aperture of the HRMA. The possibility of beam non-uniformity is important not only to tests that examine the response of different parts of the mirrors (such as shutter tests or Ring Focus measurements) but also to the use of the Flow Proportional Counters (FPCs) in front of the HRMA for flux normalization: if there is a spatial non-uniformity in the beam, it is no longer strictly valid to find the flux at the face of the HRMA by averaging the flux detected in the four FPCs. One must employ a beam uniformity map to determine the actual flux.

There were two different types of BU scans taken: one was executed at the face of the HRMA with the "North" Beam Normalization Detector (one of the FPCs at the face of the HRMA; known as fpc_hn for Beam Normalization Detector at the HRMA, North). This detector carried out a 40 point scan with four points at the positions of the fpc_h detectors, and the rest closely following the circumferences of the mirror shells. One can see this pattern in a plot from our analysis code, shown in Figure 9.1. fpc_hn had a 36 mm diameter hole defining its aperture fo these scans.

The second type of BU test was a seven point scan done with the FPC in Building 500, about 38 meters from the source building, and about 460 meters in front of the HRMA. These were fairly simple scans where two of the points coincided with the home positions of the fpc_5 and ssd_5 detectors with the other five in the middle of the X-ray beam. An example of the five point main X-ray beam scan is shown in Figure 9.2. The fpc_5 used either the 4, 12, or 36 mm aperture for these scans.

9.2 Beam Uniformity Analysis

For each BU test, the HXDS system writes .sum files which contain counts from each of the detectors (determined by a sum of all of the counts in a specified Region of Interest, or ROI) as well as live time information. An IDL program has been developed that reads in the .sum files for the fpc_h and fpc_5 detectors, calculates the flux, and then calculates a normalized flux. For the

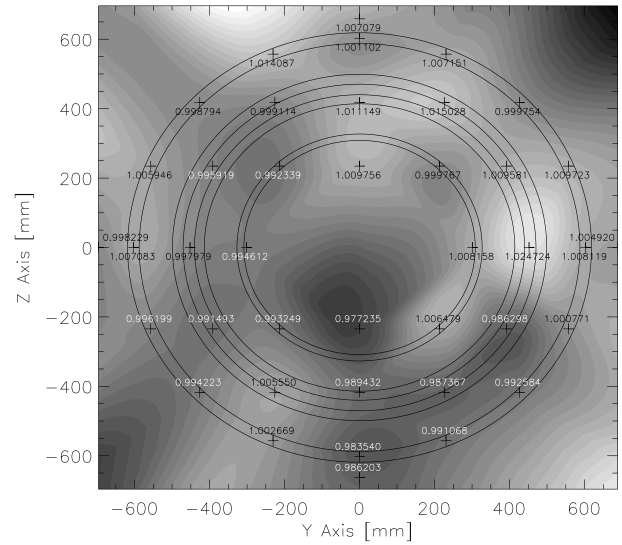

Figure 9.1: fpc_hn Scan Pattern with Smoothed Fit to Normalized Count Rates. The data was taken for MST Run ID 108363 (TRW ID D-BND-BU-2.038) on January 11, 1997 with the C-Kα EIPS anode. The concentric annuli represent the positions of the HRMA.

fpc_h tests, that normalized flux is derived by first taking the ratio of the fpc_h count rate to the fpc_5 count rate. The average of that normalized count rate is then calculated, and divided back into the normalized count rate. Uncertainties are derived using Poisson statistics.

For the fpc_5 data, a second set of count rates is not available, so the program simply averages all of the fpc_5 count rates, and then divides the average into the count rates to derive a normalized count rate. As above, uncertainties are derived using Poisson statistics.

The program then projects the detector scan points back to the location of the HRMA and produces either a smoothed surface over the data points or a fit to the data, depending on user input. The interpolation scheme works by first tiling the coordinate grid with triangles whose vertices are data points. Next, the program uses a fifth order polynomial to interpolate between the data points and extrapolate outside of the data (Akima, 1978). This produces a smooth surface that the program then uses to map out the flux as a function of mean mirror radius and azimuth. This method produces a map that very closely follows the data points, and was used initially as the basis for all of our BU analysis. An representative example of part of the output of this mode of the program is shown in Figures 9.1 and 9.2.

For fitting, the simplest function we can fit to the data is a simple constant. We might hope that this constant would be the best fit, thus showing that the beam is indeed uniform within statistical uncertainty. We can compare that constant to fits of other functions that we might believe to be physically valid. For the Electron Impact Point Source (EIPS) and the Penning Source, the

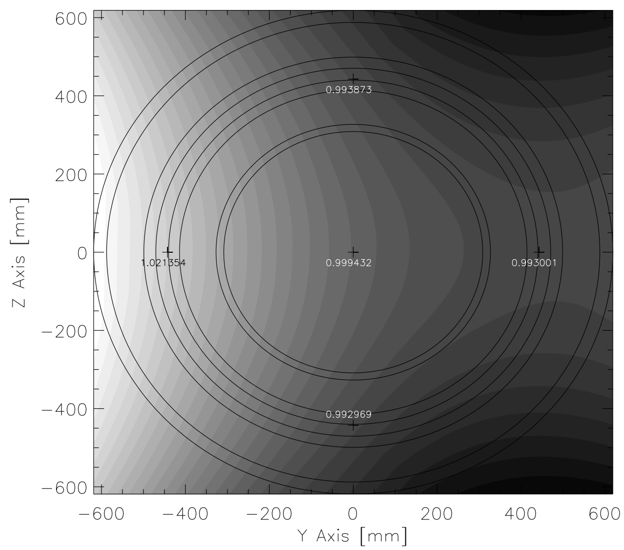

Figure 9.2: fpc_5 Scan Pattern with Smoothed Fit to Normalized Count Rates. The data in this figure is from MST Run ID 106698 (TRW ID C-BND-BU-2.035) taken on December 20th, 1996 with the Al-Kα EIPS source.

variations we might expect to see come mostly from some variation in the thickness of the filter in front of the source, which we might model with a simple slanted plane (in XRCF coordinates):

$$(Normalized\ Count\ Rate)_i = a + by_i + cz_i$$

This equation fits much of the EIPS data fairly well, yielding a χ^2_ν close to 1. The program then plots the fit as a function of mean mirror shell radius and azimuth, and also plots the data points that are close to that mirror shell, for comparison. Results for MST Run ID 108363 (TRW ID D-BND-BU-2.038, taken on January 11, 1997 with the C-Kα EIPS anode) are shown below in Figures 9.3 through 9.5. The fits shown in those figures show a maximum variation of the fit of only 1.9 percent. This is actually very common for the BU maps: most fits vary only as much as 1 to 2 percent (an exception is MST Run ID 110147), and the maximum variation is usually found over the outermost shell, as one might expect.

For the Double-Crystal Monochrometer (DCM) Source and especially the High Resolution Erect Field Spectrometer (HIREFS) Sources, however, elements in the path of the X-ray beam might induce more non-uniformity in the horizontal direction, so we can introduce an additional term to attempt to fit that variation with the following equation:

$$(Normalized\ Count\ Rate)_i = a + by_i + cy_i^2 + dz_i$$

The fits shown in Figures 9.6 through 9.8 (the results from MST Run ID 109842, which was TRW ID D-BND-BU-3.008, taken on January 22, 1997 with the DCM source at 4.51 keV) also

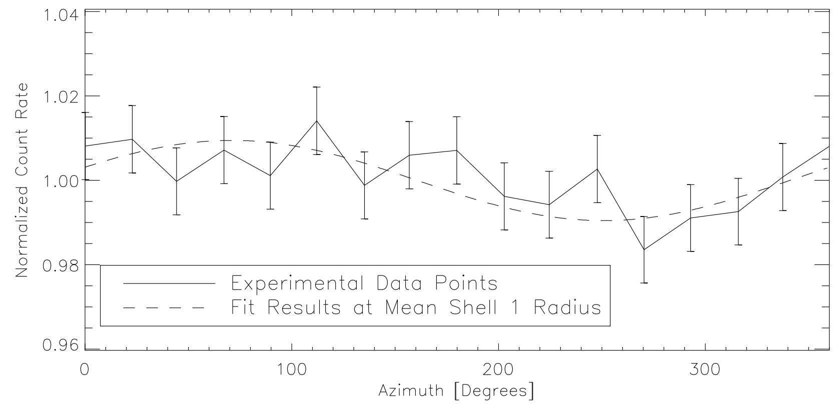

Figure 9.3: Variation in fit and data points as a function of azimuth for mirror Shell 1. The data is from MST Run ID 108363 (TRW ID D-BND-BU-2.038), which was taken on January 11, 1997 with the C-Kα EIPS anode.

show a maximum amplitude of only 1.6 percent, which is again consistent with the other Phase 1 fpc_h DCM BU scans.

The question still remains, however, of whether those equations actually fit the data any better (within statistical uncertainties) than a simple constant. We can apply the F test to determine whether the addition of the extra parameters in the above equations actually yields a better fit (Bevington and Robinson, 1992, pg. 208-209). While for about half of the analyzed BU tests, the F test shows that the added parameters fit no better than a constant (to within statistical uncertainty), the other half of the tests do have F values outside of the 1% confidence level, indicating that our functional forms yield a significantly better fit than a simple constant. All of the BU tests that we have analyzed are listed in Table 9.2, and the data that were significantly better fit with our functional forms are indicated there. We will continue to analyze the BU data to see if there are any other cases of some significant beam non-uniformity. Still, almost all beam non-uniformity effects seem to be at or below the 2% level (with the notable exception of Run ID 110147). Please note, however, that there remain Phase 1 BU tests not in Table 9.2 that did not have acceptable fits to the simple models presented above (did not have χ^2_ν close to unity) . Work continues on those tests, and the results will be posted to the BU WWW page (at URL `http://hea-www.harvard.edu/asclocal/cal/beam_uniform/bumap.html`), when finished.

9.3 Future Directions

Further work will entail fitting the FPC data within XSPEC and using the resultant fluxes instead of the .sum files we are using now. Also, work will continue on the analysis of all of the BU tests from other phases as well as those Phase 1 BU tests not listed in Table 9.2 (those which were not acceptably fit). Again, all results will be posted to the BU web site.

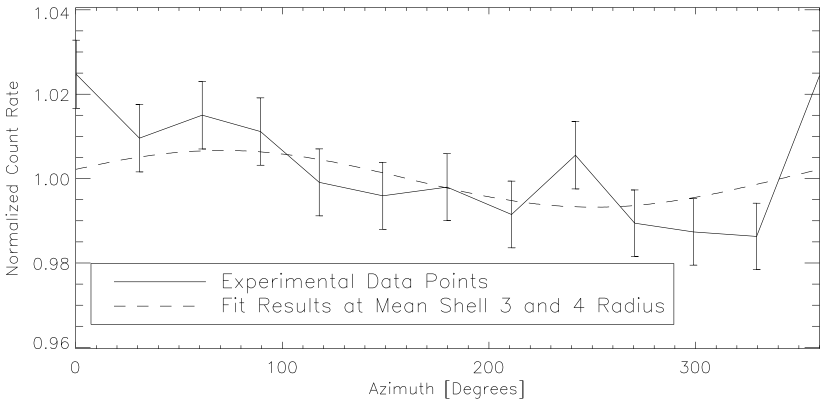

Figure 9.4: Variation in fit and data points as a function of azimuth for mirror Shells 3 and 4. The data is from MST Run ID 108363 (TRW ID D-BND-BU-2.038), which was taken on January 11, 1997 with the C-Kα EIPS anode.

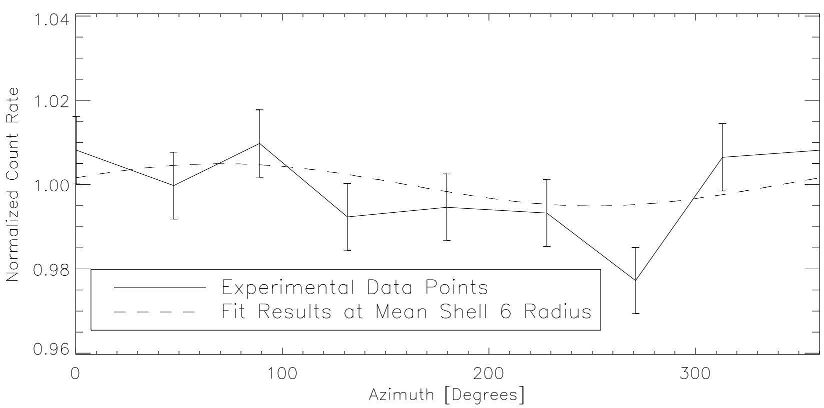

Figure 9.5: Variation in fit and data points as a function of azimuth for mirror Shell 6. The data is from MST Run ID 108363 (TRW ID D-BND-BU-2.038), which was taken on January 11, 1997 with the C-Kα EIPS anode.

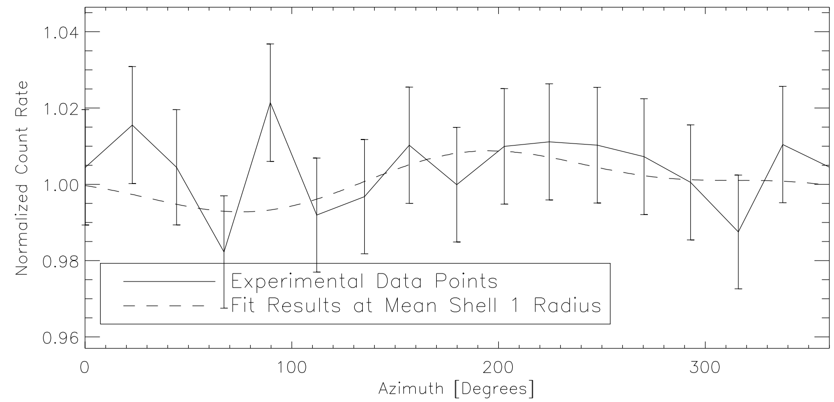

Figure 9.6: Variation in fit and data points as a function of azimuth for mirror Shell 1. The data is from MST Run ID 109842 (TRW ID D-BND-BU-3.008), which was taken on January 22, 1997 with the DCM source at 4.51 keV.

9.4 Acknowledgments

Thanks to Mark Freeman, who started this program long ago, to Jeremy Drake and Diab Jerius, who helped me push it further, and to Deron Pease for throwing megabytes of data through it.

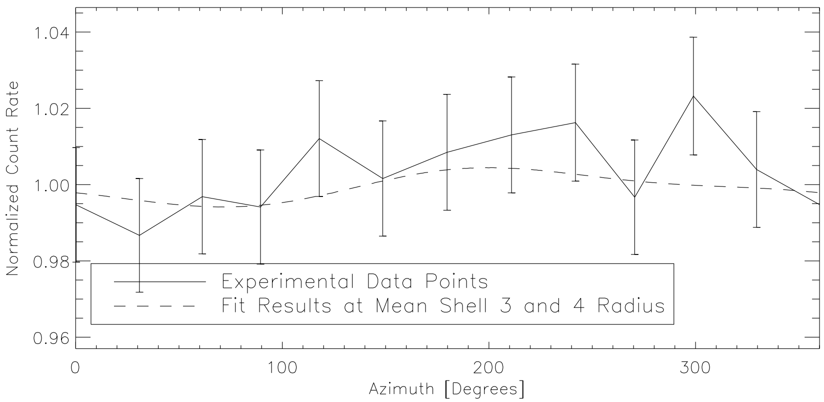

Figure 9.7: Variation in fit and data points as a function of azimuth for mirror Shells 3 and 4. The data is from MST Run ID 109842 (TRW ID D-BND-BU-3.008), which was taken on January 22, 1997 with the DCM source at 4.51 keV.

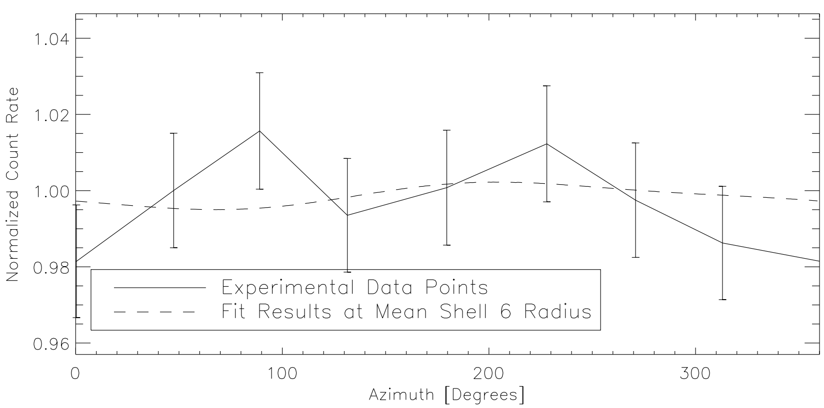

Figure 9.8: Variation in fit and data points as a function of azimuth for mirror Shell 6. The data is from MST Run ID 109842 (TRW ID D-BND-BU-3.008), which was taken on January 22, 1997 with the DCM source at 4.51 keV.

Table 9.1: Analyzed Phase 1 Beam Uniformity Tests. Any Phase 1 BU tests that are not included in this test list has not been fit acceptably, yet. Work will continue on those BU tests.

TRW ID	MST Run ID	Date	Source	Energy [keV]
C-BND-BU-2.036	106699,106701	Dec 20, 1996	EIPS	1.49
C-BND-BU-60.010	106802	Dec 22, 1996	EIPS	0.28
C-BND-BU-60.008	106826	Dec 22, 1996	EIPS	1.49
D-BND-BU-2.028	108095	Jan 9, 1997	EIPS	6.40
D-BND-BU-2.038	108363	Jan 11, 1997	EIPS	0.28
D-BND-BU-2.030	109102	Jan 15, 1997	EIPS	4.51
D-BND-BU-3.008	109842	Jan 22, 1997	DCM	4.51
D-BND-BU-3.004	109853	Jan 22, 1997	DCM	1.60
D-BND-BU-2.018	110147	Jan 25, 1997	EIPS	2.29
E-BND-BU-2.028	110798	Jan 31, 1997	EIPS	6.40
E-BND-BU-2.030	110958	Feb 2, 1997	EIPS	4.51
E-BND-BU-2.016	111172	Feb 4, 1997	EIPS	2.98

Table 9.2: Fit Results for analyzed BU tests with acceptable χ^2_ν. Any Phase 1 BU tests that are not included in this test list has not been fit acceptably, yet. Also listed is the maximum variation of the fit over the entrance aperture to the HRMA.

TRW ID	χ^2_ν	Fit Parameters	Error in Parameters	Max Variation [Percent]	Functional Form Fits Better?
C-BND-BU-2.036	1.88	$a = 1.00$ $b = -1.15 \times 10^{-5}$ $c = -3.78 \times 10^{-6}$	1.17×10^{-3} 3.17×10^{-6} 3.17×10^{-6}	1.5	Yes
C-BND-BU-60.010	1.00	$a = 1.00$ $b = -5.52 \times 10^{-6}$ $c = 6.95 \times 10^{-6}$	3.33×10^{-3} 9.01×10^{-6} 9.00×10^{-6}	1.1	No
C-BND-BU-60.008	1.94	$a = 1.00$ $b = -9.38 \times 10^{-6}$ $c = -8.46 \times 10^{-6}$	1.18×10^{-3} 3.19×10^{-6} 3.20×10^{-6}	1.5	Yes
D-BND-BU-2.028	1.97	$a = 1.00$ $b = -7.19 \times 10^{-6}$ $c = 7.45 \times 10^{-6}$	1.97×10^{-3} 5.37×10^{-6} 5.30×10^{-6}	1.3	No
D-BND-BU-2.038	1.02	$a = 1.00$ $b = 5.18 \times 10^{-6}$ $c = 1.49 \times 10^{-5}$	1.26×10^{-3} 3.41×10^{-6} 3.43×10^{-6}	1.9	Yes
D-BND-BU-2.030	0.85	$a = 1.00$ $b = -2.90 \times 10^{-6}$ $c = -2.81 \times 10^{-6}$	2.42×10^{-3} 6.56×10^{-6} 6.57×10^{-6}	0.5	No
D-BND-BU-3.008	0.85	$a = 9.98 \times 10^{-1}$ $b = -6.85 \times 10^{-6}$ $c = 1.68 \times 10^{-8}$ $d = -7.44 \times 10^{-6}$	3.39×10^{-3} 6.46×10^{-6} 1.77×10^{-8} 6.44×10^{-6}	1.6	No
D-BND-BU-3.004	0.28	$a = 1.00$ $b = 1.55 \times 10^{-5}$ $c = -6.39 \times 10^{-9}$ $d = 2.64 \times 10^{-6}$	3.36×10^{-3} 6.38×10^{-6} 1.76×10^{-8} 6.38×10^{-6}	1.9	Yes
D-BND-BU-2.018	3.83	$a = 1.00$ $b = -4.32 \times 10^{-5}$ $c = -2.65 \times 10^{-5}$	1.24×10^{-3} 3.33×10^{-6} 3.36×10^{-6}	6.1	Yes
E-BND-BU-2.028	1.46	$a = 1.00$ $b = -1.83 \times 10^{-6}$ $c = 2.00 \times 10^{-6}$	2.05×10^{-3} 5.53×10^{-6} 5.54×10^{-6}	0.3	No
E-BND-BU-2.030	0.58	$a = 1.00$ $b = 6.72 \times 10^{-6}$ $c = 5.83 \times 10^{-6}$	1.33×10^{-3} 3.59×10^{-6} 3.59×10^{-6}	1.0	Yes
E-BND-BU-2.016	1.12	$a = 1.00$ $b = 1.75 \times 10^{-6}$ $c = 1.63 \times 10^{-6}$	1.49×10^{-3} 4.03×10^{-6} 4.05×10^{-6}	0.3	No

Chapter 10

HRMA Focus Measurements and Raytrace Update

10.1 HRMA Focus Measurements at XRCF

Two dimensional HXDS FPC pinhole scans were made on a shell-by-shell and quadrant-by-quadrant basis on three separate occasions during the Phase 1 HRMA XRCF testing period. These scans were used to calculate the best focus position of each of the four HRMA shells as well as the relative P-H tilts. We have analyzed these data and updated our raytrace model of the HRMA to include the XRCF measured focus results. We have not yet incorporated the XRCF measured intra-shell mirror tilts. In this section we describe these measurements and the subsequent analysis.

Centroids determined from a shell's quadrant images yield four pairs of coordinate values. From these, two focus estimates may be constructed:

$$\Delta_{Y,i} = 0.995 \frac{\pi}{4\sqrt{2}} \frac{F}{R_i} (Y_{i,N} - Y_{i,S})$$
$$\Delta_{Z,i} = 0.995 \frac{\pi}{4\sqrt{2}} \frac{F}{R_i} (Z_{i,T} - Z_{i,B})$$

where $\Delta_{Y,Z}$ are the focus error estimates; R_i is the nodal radius for the mirror pair, and F is the distance from the mirror node to the (finite conjugate) focus. (The 0.995 factor accounts for the fact that the quadrants are really only 88°.) A disagreement between these two focus error estimates may be indicative of astigmatism, either intrinsic to the optic or resulting from 1g distortions. In addition, two alignment estimators can be formed:

$$tilt_{Y,i} = 0.978 \frac{\pi}{4F'_i} (Y_{i,N} + Y_{i,S} - Y_{i,T} - Y_{i,B})$$
$$tilt_{Z,i} = 0.978 \frac{\pi}{4F'_i} (Z_{i,N} + Z_{i,S} - Z_{i,T} - Z_{i,B})$$

where F'_i is the distance from the body center of the H optic to the *far focus* of the H. (The 0.978 factor is a correction for 88° quadrants.)

The HRMA focus data from the three measurement sets performed are summarized in Figure 10.1. Five groups of data are shown, the four individual shells and the complete HRMA. For

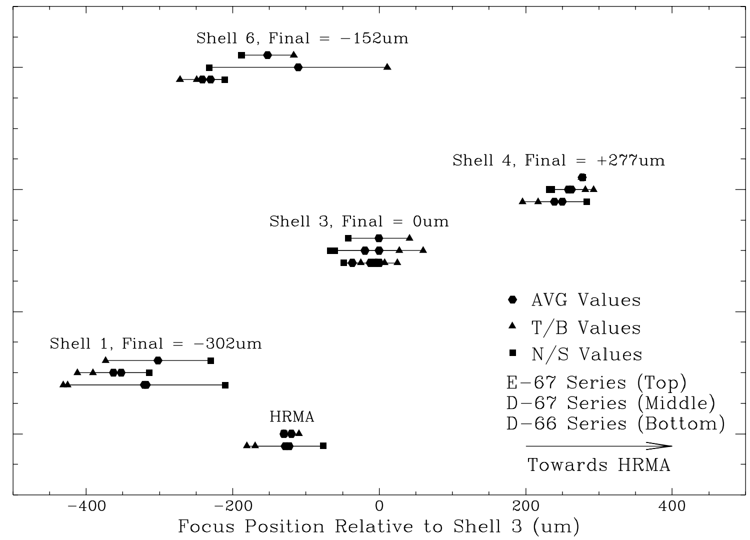

Figure 10.1: HRMA Focus Data: Focal positions are shown in μm relative to the Shell 3 focus. A positive difference represents a focus position closer to the HRMA than the Shell 3 focus (this is the XRCF sign convention and *not* that of `SAOsac`). The data are taken from three series of tests, and are shown stacked – the legend describes the stacking order. Note that there were no HRMA tests in series E-67.

the four HRMA shells three data lines are shown, representing the initial (D-66 series), intermediate (D-67 series), and final (E-67 series) data. The focus of a shell may be calculated from either the *top* and *bottom* quadrants or the *north* and *south* quadrants. The average of these two foci was used as the shell focus position. The difference between the T/B focus and the N/S focus may be due to either astigmatism in the mirrors or to measurement error (a certain amount of separation is also induced by the 1G test environment).

The best dataset was E-67, the last one taken; more was known about the shell image qualities beforehand and more time was allocated to capture all of the flux from each quadrant of each shell, compared to the earlier data. The relative foci from these measurements are shown in Table 10.1. Positive numbers represent focus positions closer to the HRMA, or shorter overall focal lengths.

Table 10.1: Best Estimate of XRCF Measured Focus of Shells, relative to Shell 3

Shell	F_N - F_3 (μm)
1	−302
3	0
4	+277
6	−152

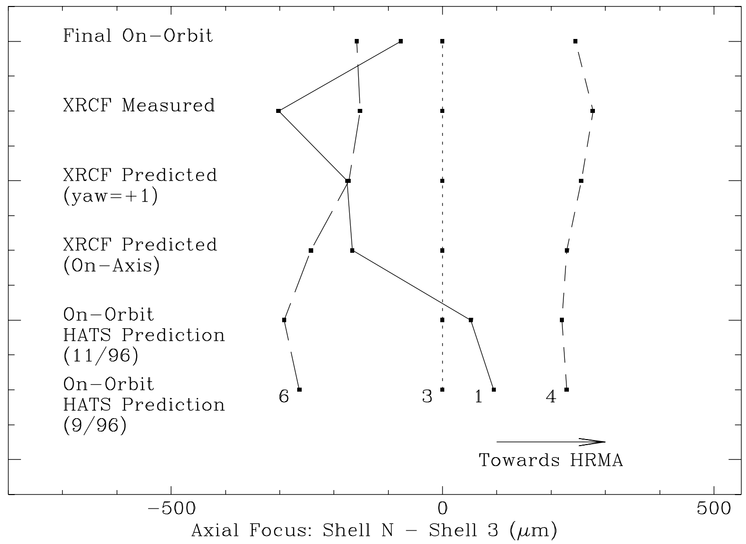

Figure 10.2: HRMA Focus History

In Figure 10.2 the XRCF measured focus data are compared with various focus predictions for both the on-orbit (infinite source distance, no gravity) and XRCF (finite source distance, 1G) conditions. Six different cases are shown, presented vertically with the focus values of each shell connected by lines. The bottom two cases represent the pre-calibration predictions of *on-orbit* focus from the Kodak HATS data. The bottom set of data is from the September 1996 testing, after all alignments but prior to HRMA final assembly. The next set up represents data from Kodak's November 96 HRMA Acceptance Test Procedure (ATP), after HRMA final assembly at Kodak and just prior to shipment to XRCF. Both sets of data show that the foci of the shells span about 500 μm, with the ordering of the foci as (6 – 3 – 1 – 4) in order of *decreasing* focal lengths.

The middle two cases shown in Figure 10.2 represent pre-calibration predictions of XRCF focus from the November 1996 Kodak test data, for HRMA yaw angles of both zero and one arc minute. Table 10.2 presents a comparison of predictions of the on-orbit and XRCF focal distances, relative to the P side of the HRMA CAP. The overall change in focal distance is about 195mm (longer at XRCF). However, the most interesting feature shown is that the Shell 1 focal distance increases much more (about 250 μm) than that of the other 3 shells. In Figure 10.2 this feature is shown clearly as the Shell 1 focus moves from a position between 3 and 4, for the on-orbit case, to a position further away from the HRMA, now between 6 and 3. This behavior was initially considered to be an anomaly and possibly a mistake, since raytrace studies using the *ideal* HRMA optic prescriptions and spacings did *not* give this result. However, when the as-built P1 and H1 surface prescriptions and mirror axial spacings are used this feature is seen (this result has been confirmed by Dave Zissa and Paul Glenn).

The "XRCF measured" case in Figure 10.2 shows what is considered to be the best estimate from XRCF testing of the shell-to-shell relative focus. This is from the data in Table 10.1, discussed

Table 10.2: Comparison of pre-XRCF Predictions of On-orbit and XRCF HRMA foci

	Focus relative to P side of CAP(mm)			
Shell	$F_{\rm XRCF}$	$F_{\rm On-Orbit}$	ΔF	$\Delta F - \Delta F_{\rm Shell3}$
1	10274.9145004675	10079.6696878001	195.2461	0.2949
3	10274.7304206266	10079.779404296	194.9512	0.0000
4	10274.3675449462	10079.4606206727	194.9062	−0.0449
6	10274.7562744271	10079.7697370664	194.9863	0.0352

above. We see that there is is a discrepancy of about 200 μm in the position of the Shell 1 focus at XRCF as compared with the predictions based on Kodak optical test data. At XRCF, Shell 1 had the longest focal distance, a result which was consistent over all of the testing. In discussion with L. Van Speybroeck (AXAF Telescope Scientist), we decided that the XRCF data was most likely more accurate than the Kodak optical test data, and that we should use this data as the basis for our HRMA model. The process of incorporating the XRCF data into our raytrace model is discussed below. The end result is shown as the top case in Figure 10.2. This assumption makes the predicted HRMA performance somewhat better, as the span of the foci is a bit smaller. It is now baselined in SAO's HRMA raytrace model.

10.2 Update of SAO HRMA Raytrace Model from XRCF Focus Data

In the pre-calibration SAO baseline mirror definition file, `EKCHDOS04`, the shell relative foci were set equal to those measured in the Kodak optical tests. This was done by adjusting the CAP-to-H mirror spacing so that the relative foci as determined by raytracing were equal to that measured in the optical tests. In the updated, post-calibration, SAO baseline, derived from XRCF testing, the CAP-to-mirror spacings are set to the values measured at Kodak for both P and H mirrors, and the relative foci were adjusted by making slight changes to the average cone angles of the mirrors. These cone angles were adjusted until the raytraced foci, at the XRCF finite source distance, were close to the XRCF measured relative foci. The shell 3 focus was left unchanged, and the foci of the other shells were adjusted relative to that of shell 3. The as-measured mirror data (from Kodak and HDOS) are given in Table 10.3. The data in Table 10.3 were used in the updated mirror definition file, `EKCHDOS06`.

Alteration of the cone angles was done by adding an additional "deformation" to the optics described by a Fourier-Legendre polynomial with three Legendre terms and no Fourier terms. The only non-zero term, the l_1 term, is equal to -0.001mm for the P optics and $+0.001$mm for the H optics (two term L-F files would have sufficed for this application). A single numerical scaling factor for these deformations was determined for each shell, and was used for both the P and H optics. The value of these multipliers was determined by trial-and-error by running tests with the full XRCF raytrace model including the `EKCHDOS06` mirror database :

Shell	Multiplier
1	0.0872
3	0.0
4	0.0150
6	0.0461

Table 10.3: As Measured Optic lengths and distances

Shell	L_P (mm)	L_H (mm)	CAP (mm)	P-CAP (in)	H-CAP (in)	ZC_P (mm)	ZC_H (mm)
1	842.2150	842.1920	49.911	0.2153	0.3940	-426.5761	481.0146
3	842.2080	842.1970	49.911	0.6144	0.3905	-436.7098	480.9282
4	842.2080	842.2250	49.911	0.7580	0.3860	-440.3572	480.8279
6	842.2090	842.2000	49.911	0.9440	0.3230	-445.0821	479.2152

L_P Length of P Mirror
L_H Length of H Mirror
CAP Thickness of CAP
P-CAP Distance from P side of CAP to P mirror
H-CAP Distance from H side of CAP to H mirror
ZC_P Z co-ordinate of center of P mirror in SAO raytrace co-ordinates
ZC_H Z co-ordinate of center of H mirror in SAO raytrace co-ordinates

Table 10.4: Final Mirror Focal Positions at XRCF and on orbit

	XRCF			On Orbit	
	Raytrace		Meas.	Raytrace	
Shell	F_N (mm)	-(F_N - F_3) (μm)	F_N - F_3 (μm)	F_N (mm)	-(F_N - F_3) (μm)
1	10275.0342	-305	-302	10079.8359	-77
3	10274.7295	0	0	10079.7588	0
4	10274.4551	274	277	10079.5137	245
6	10274.8730	-144	-152	10079.9170	-158

The resultant deformations are summed with the other mirror distortions to create the final mirror maps.

In Table 10.4, raytrace results using these offset files plus the new `EKCHDOS06` mirror database are given for both the XRCF and on-orbit cases, plus the measured XRCF relative foci (repeated for convenience from Table 10.1. The raytraced F_N are measured relative to the P side of the CAP in the raytrace (`SAOsac`) coordinate system. The foci relative to Shell 3 are presented in the XRCF coordinate system (recall from Figure 1.8 that the `SAOsac` Z optical axis coordinate is flipped with respect to the XRCF X coordinate). A positive relative focus again indicates a focus value closer to the HRMA. The results from the on-orbit raytrace (the last column in Table 10.4) are also plotted as "Final On-Orbit" in Figure 10.2.

Test data are given in Tables 10.5 through 10.7.

Table 10.5: Test Data for HRMA Focus Tests: D-66 Series

Date	TRW Test ID	Shell	PrimeX [μm]	δF_y [μm]	δF_z [μm]	Yaw [′]	Pitch [′]
01/02/97	D-IXF-P2-66.001	3	−32566	180.8	178.7	0	0
01/02/97	D-IXF-P2-66.002						
01/02/97	D-IXF-P2-66.003						
01/02/97	D-IXF-P2-66.004						
01/02/97	D-IXF-P2-66.005	3	−32566	180.8	166.8	0	0
01/02/97	D-IXF-P2-66.002						
01/02/97	D-IXF-P2-66.003						
01/02/97	D-IXF-P2-66.004						
01/02/97	D-IXF-P2-66.026	3	−32804	−15.0	−39.1	0	0
01/02/97	D-IXF-P2-66.027						
01/02/97	D-IXF-P2-66.028						
01/02/97	D-IXF-P2-66.029						
01/02/97	D-IXF-P2-66.030	3	−32804	−15.0	−88.8	0	0
01/02/97	D-IXF-P2-66.027						
01/02/97	D-IXF-P2-66.028						
01/02/97	D-IXF-P2-66.029						
01/02/97	D-IXF-P2-66.006	4	−32563	−106.0	−18.7	0	0
01/02/97	D-IXF-P2-66.007						
01/03/97	D-IXF-P2-66.008						
01/03/97	D-IXF-P2-66.009						
01/03/97	D-IXF-P2-66.010	4	−32563	−106.0	−40.0	0	0
01/03/97	D-IXF-P2-66.007						
01/03/97	D-IXF-P2-66.008						
01/03/97	D-IXF-P2-66.009						
01/03/97	D-IXF-P2-66.011	6	−33060	−108.9	−47.9	0	0
01/03/97	D-IXF-P2-66.012						
01/03/97	D-IXF-P2-66.013						
01/03/97	D-IXF-P2-66.014						
01/03/97	D-IXF-P2-66.015	6	−33060	−108.9	−70.7	0	0
01/03/97	D-IXF-P2-66.012						
01/03/97	D-IXF-P2-66.013						
01/03/97	D-IXF-P2-66.014						
01/03/97	D-IXF-P2-66.016	1	−32962	−11.5	209.2	0	0
01/03/97	D-IXF-P2-66.017						
01/03/97	D-IXF-P2-66.018						
01/03/97	D-IXF-P2-66.019						
01/03/97	D-IXF-P2-66.020	1	−32962	−11.5	203.2	0	0
01/03/97	D-IXF-P2-66.017						
01/03/97	D-IXF-P2-66.018						
01/03/97	D-IXF-P2-66.019						

Table 10.5: Test Data for HRMA Focus Tests: D-66 Series, continued

Date	TRW Test ID	Shell	PrimeX [μm]	δF_y [μm]	δF_z [μm]	Yaw [′]	Pitch [′]
01/03/97	D-IXF-P2-66.021	1346	−32866	−49.4	54.7	0	0
01/03/97	D-IXF-P2-66.022						
01/03/97	D-IXF-P2-66.023						
01/03/97	D-IXF-P2-66.024						
01/03/97	D-IXF-P2-66.025	1346	−32866	−49.4	43.2	0	0
01/03/97	D-IXF-P2-66.022						
01/03/97	D-IXF-P2-66.023						
01/03/97	D-IXF-P2-66.024						

Table 10.6: Test Data for HRMA Focus Tests: D-67 Series

Date	TRW Test ID	Shell	PrimeX [μm]	δF_y [μm]	δF_z [μm]	Yaw [′]	Pitch [′]
01/05/97	D-IXF-P2-67.001	3	−32782	41.5	−52.6	−1	0
01/05/97	D-IXF-P2-67.002						
01/05/97	D-IXF-P2-67.003						
01/05/97	D-IXF-P2-67.004						
01/05/97	D-IXF-P2-67.005	3	−32776	41.5	−79.0	−1	0
01/05/97	D-IXF-P2-67.002						
01/05/97	D-IXF-P2-67.003						
01/05/97	D-IXF-P2-67.004						
01/05/97	D-IXF-P2-67.006	4	−32499	22.9	−23.1	−1	0
01/05/97	D-IXF-P2-67.007						
01/05/97	D-IXF-P2-67.008						
01/05/97	D-IXF-P2-67.009						
01/05/97	D-IXF-P2-67.010	4	−32502	22.9	−37.9	−1	0
01/05/97	D-IXF-P2-67.007						
01/05/97	D-IXF-P2-67.008						
01/05/97	D-IXF-P2-67.009						
01/05/97	D-IXF-P2-67.011	6	−32984	5.3	−238.1	−1	0
01/05/97	D-IXF-P2-67.012						
01/06/97	D-IXF-P2-67.013						
01/06/97	D-IXF-P2-67.014						
01/06/97	D-IXF-P2-67.015	6	−32984	5.3	−238.1	−1	0
01/06/97	D-IXF-P2-67.012						
01/06/97	D-IXF-P2-67.013						
01/06/97	D-IXF-P2-67.014						
01/06/97	D-IXF-P2-67.016	1	−33058	12.9	111.1	−1	0
01/06/97	D-IXF-P2-67.017						
01/06/97	D-IXF-P2-67.018						
01/06/97	D-IXF-P2-67.019						
01/06/97	D-IXF-P2-67.020	1	−33058	12.9	89.9	−1	0
01/06/97	D-IXF-P2-67.017						
01/06/97	D-IXF-P2-67.018						
01/06/97	D-IXF-P2-67.019						
01/06/97	D-IXF-P2-67.021	1346	−32861	26.3	26.0	−1	0
01/06/97	D-IXF-P2-67.022						
01/06/97	D-IXF-P2-67.023						
01/06/97	D-IXF-P2-67.024						
01/06/97	D-IXF-P2-67.025	1346	−32861	26.0	5.6	−1	0
01/06/97	D-IXF-P2-67.022						
01/06/97	D-IXF-P2-67.023						
01/06/97	D-IXF-P2-67.024						

Table 10.7: Test Data for HRMA Focus Tests: E-67 (Final) Series

Date	TRW Test ID	Shell	PrimeX [μm]	δF_y [μm]	δF_z [μm]	Yaw [′]	Pitch [′]
02/07/97	E-IXF-P2-67.001	3	−32562	−282.03	−365.2	0	0
02/07/97	E-IXF-P2-67.002						
02/07/97	E-IXF-P2-67.003						
02/07/97	E-IXF-P2-67.004						
02/07/97	E-IXF-P2-67.006	4	−31970	−9.64	−8.2	0	0
02/07/97	E-IXF-P2-67.007						
02/07/97	E-IXF-P2-67.008						
02/07/97	E-IXF-P2-67.009						
02/07/97	E-IXF-P2-67.011	6	−32341	85.09	13.6	0	0
02/07/97	E-IXF-P2-67.012						
02/07/97	E-IXF-P2-67.013						
02/07/97	E-IXF-P2-67.014						
02/07/97	E-IXF-P2-67.016	1	−32589	−120.6	22.6	0	0
02/07/97	E-IXF-P2-67.017						
02/07/97	E-IXF-P2-67.018						
02/07/97	E-IXF-P2-67.019						

10.3 Updated deformation and sum files

In `SAOsac` terminology Legendre-Fourier DFR "offset" files were created to describe the deformation to the optics which provides the required change in optic cone angle:

`p`N`_off.DFR` (where $N = 1, 3, 4, 6$):

```
P  Deformation                                                   3    0
   0.00000E+00   -1.00000E-03    0.00000E+00
```

`h`N`_off.DFR` (where $N = 1, 3, 4, 6$):

```
H  Deformation                                                   3    0
   0.00000E+00    1.00000E-03    0.00000E+00
```

So-called "sum" files direct the summation of the various distortions and their magnitudes (i.e. the scaling factor mentioned above). The Shell 1 files look like this:

`p1_xrcf_sum_off.files` :

```
p1_xrcf_sum_off.SPL 422 288
/proj/axaf/Syseng/models/hrma-xrcf/xrcf_2wks/p1_xrcf_sum.SPL 1.000 0.000
p1_off.DFR 0.0872 0.000
```

`h1_xrcf_sum_off.files` :

```
h1_xrcf_sum_off.SPL 422 288
/proj/axaf/Syseng/models/hrma-xrcf/xrcf_2wks/h1_xrcf_sum.SPL 1.000 0.000
h1_off.DFR 0.0872 0.000
```

The "sum" files have names of the form *xn*`_xrcf_sum_off.SPL` where $x = \{p, h\}$ and $n = \{1, 3, 4, 6\}$.

All of these files are located in

`/proj/axaf/Syseng/models/hrma-xrcf/xrcf_2wks_offset/`

on the CfA Central Engineering and High Energy Astrophysics LANs.

Chapter 11

HRMA Tilts at XRCF

In this section we discuss HRMA rigid body misalignments (relative P-H tilt and decenter). Data is presented from the optical alignments at Kodak, from the XRCF calibration and from various analyses.

Relative rigid body misalignments of the P to H optics in either decenter or tilt cause a comatic image distortion in the focal plane. This distortion is a "coma circle" in which the position of the rays in the coma circle moves around the circle twice as the input ray bundle (to the shell) varies once around the shell input aperture. Figure 11.1 illustrates this. The coma circle diameter in the focal plane is related to the P-H decenter and tilt angle as follows:

	1″ P-H tilt	1 mm P-H decenter
Coma circle radius (″)	1	10
Coma circle radius (μm)	48.5	488

11.1 Coordinate Systems and tilt angles

Since tilt and decenter both produce coma in the image plane we will interpret this coma as a tilt of the H optic relative to the P optic. Three different coordinate systems and sets of tilt angles have been used (see also §1.4 and Figure 1.8):

- HRMA Coordinates (θ_Y, θ_Z)
- `SAOsac` Raytrace Coordinates (*azmis*, *elmis*)
- XRCF Coordinates ($tilt_Y$, $tilt_Z$)

The tilt angles are interpreted as a rotation of the H optic about a given coordinate axis, relative to the perfectly aligned P optic. The rotation axes are as follows (again see Figure 1.8);

Coordinates	H Angle	Rotation axis
HRMA	θ_Y	+Y-HRMA
	θ_Z	+Z-HRMA
SAOSAC	*azmis*	+Y-OSAC
	elmis	−X-OSAC
XRCF	$tilt_Y$	+Y-XRCF
	$tilt_Z$	+Z-XRCF

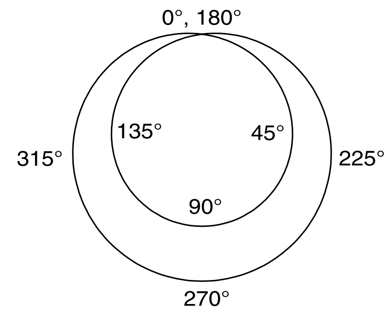

Figure 11.1: Schematic of coma circle (2θ) image distortion. The limaçon is the pattern of the photons at the focal surface. The angles refer to the azimuth of the optic at which the photons were reflected.

Tilt angle relationships:

$$\begin{aligned} azmis &= -\theta_Z = +tilt_Z \\ elmis &= -\theta_Y = +tilt_Y \end{aligned}$$

Table 11.1 provides a summary of relative tilt angles (H with respect to P) for various conditions. The four HRMA shells are given with the two tilt angles per shell. These angles are shown in terms of the XRCF angles, $tilt_Y$ and $tilt_Z$. The tilt angles as measured at Kodak by the HATS (in the final ATP measurements) are shown in line 1. In lines 2 and 3 the XRCF 1G *corrections* to the tilt angles are given for both SAO's FEA model and EKC's FEA model. Note that the corrections are about XRCF Y only, Y being the horizontal axis at XRCF. Lines 4 through 9 present various raytrace predictions of the tilt angles, based on various HRMA models and using a simulated quad shutter tilt calculation. The cases are defined as follows:

EKCHDOS04 Based on Kodak test data of 9/96 with *no* decenter, full XRCF mirror maps (SAO)

EKCHDOS04_low Based on Kodak test data of 9/96 with *no* decenter, mirror map includes only 3 term Legendre fit of surface (no 1G)

EKCHDOS04_low_off Based on Kodak test data of 9/96 with *no* decenter, mirror map includes only 3 term Legendre fit of surface (no 1G), HRMA pointed 1′ off-axis in azimuth

EKCHDOS05 Based on Kodak ATP test data of 11/96 with XRCF measured decenter, full XRCF mirror maps (SAO), axial spacing as in `EKCHDOS04`

EKCHDOS05_low Based on Kodak ATP test data of 11/96 with XRCF measured decenter, mirror map includes only 3 term Legendre fit of surface (no 1G)

EKCHDOS06 Based on Kodak ATP test data of 11/96 with XRCF measured decenter, full XRCF mirror maps (SAO), axial spacing derived from XRCF measurements

EKCHDOS06_off Based on Kodak ATP test data of 11/96 with XRCF measured decenter, full XRCF mirror maps (SAO), axial spacing derived from XRCF measurements, HRMA pointed 1′ off-axis in azimuth

Table 11.1: HRMA Tilt Angles

	Model	Shell 1 Y [″]	Shell 1 Z [″]	Shell 3 Y [″]	Shell 3 Z [″]	Shell 4 Y [″]	Shell 4 Z [″]	Shell 6 Y [″]	Shell 6 Z [″]
1	Kodak ATP HATS	0.03	−0.09	−0.02	0.07	0.00	0.06	−0.03	0.32
2	XRCF 1G Corr(SAO)	−0.24	0.00	−0.08	0.00	−0.12	0.00	−0.12	0.00
3	XRCF 1G Corr(EKC)	−0.23	0.00	−0.18	0.00	−0.21	0.00	−0.33	0.00
4	EKCHDOS04	−0.19	−0.15	−0.08	0.03	−0.13	0.07	−0.29	0.27
5	EKCHDOS04_low	0.04	−0.11	−0.03	0.06	0.00	0.05	−0.09	0.27
6	EKCHDOS04_low_off	0.04	0.04	−0.03	0.23	0.00	0.23	−0.09	0.47
7	EKCHDOS05	−0.01	−0.03	0.13	0.11	0.05	0.15	−0.05	0.38
8	EKCHDOS05_low	0.20	0.00	0.18	0.14	0.17	0.13	0.15	0.39
9	EKCHDOS06	−0.01	−0.03	0.13	0.11	0.04	0.15	−0.05	0.38
10	EKCHDOS06_off	−0.01	0.12	0.12	0.29	0.05	0.34	−0.05	0.58
11	Measured 1/5-6/97†	−0.15	−0.14	−0.05	−0.06	−0.04	−0.08	−0.44	0.18
12	Measured 1/5-6/97	−0.17	−0.14	−0.07	−0.05	−0.05	−0.07		
13	Measured 2/7-8/97	−0.14	−0.02	−0.05	0.12	−0.04	0.04	−0.43	0.36
14	Kodak ATP+SAO XRCF	−0.21	−0.09	−0.10	0.07	−0.12	0.06	−0.15	0.32
15	Kodak ATP+EKC XRCF	−0.20	−0.09	−0.20	0.07	−0.12	0.06	−0.36	0.32

†XRCF tilts measured 1′ off-axis in azimuth

Lines 11, 12 and 13 give the measured XRCF tilt angles for 3 different cases, using the quad shutter calculations. Lines 11 and 12 present data from tests on 1/5/97 and 1/6/97, when the HRMA was 1′off-axis in azimuth. The data in line 11 is the initial baseline tilt data from these tests. The data in line 12 is repeatability data in which the *top* quadrant was re-measured and used in conjunction with the initial data from the other three quadrants. The data in lines 11 and 12 should be the same. The data in line 13 is from the last series of focus/tilt measurements in Phase 1 (at Al Kα), taken on 2/7/97 and 2/8/97. An important difference between this data and the data taken in early January is that the HRMA was on-axis for the February data, but was +1′ off-axis in azimuth when the January data was taken.

Lines 14 and 15 give the arithmetic sums of the Kodak ATP tilt angles plus the XRCF 1G tilts for the SAO model (line 14) and the EKC model (line 15).

11.2 Tilt Measurements

Examination of the measured tilt data in Table 11.1 (lines 11 - 13) shows excellent agreement for all of the $tilt_Y$ measurements, with a span of only 0.03″ over all shells for the three sets of data. There are larger differences between the January and February data in $tilt_Z$, however. The February data show, for all four shells, numerically larger values of $tilt_Z$, the differences ranging from about 0.10″ to 0.20″. This discrepancy is due to the difference in HRMA alignment, specifically the 1′ azimuth off-axis angle. Simulations show the same trend in tilt angles as the HRMA azimuth is varied. Comparison of raytrace cases `EKCHDOS04_low` *vs.* `EKCHDOS04_low_off` and `EKCHDOS06` *vs.* `EKCHDOS06_off` show that the $tilt_Z$ angles do increase as the HRMA azimuth is increased, by about the same amounts as seen in the measurements. In Table 11.2 the 1/5-6/97 data has been adjusted for the off-axis azimuth effect, line B, and compared with the 2/7-8/97 data, line C. The agreement is excellent, and we will therefore use the tilt values measured in 2/97 as our reference

Table 11.2: Summary of HRMA Tilt Angles

	Model	Shell 1 Y [″]	Shell 1 Z [″]	Shell 3 Y [″]	Shell 3 Z [″]	Shell 4 Y [″]	Shell 4 Z [″]	Shell 6 Y [″]	Shell 6 Z [″]
A	Offaxis Az delta	0.00	0.15	-0.01	0.18	0.01	0.19	0.00	0.20
B	1/5-6/97 + Az delta	-0.15	0.01	-0.05	0.12	-0.04	0.11	-0.44	0.38
C	Measured 2/7-8/97	-0.14	-0.02	-0.05	0.12	-0.04	0.04	-0.43	0.36
D	EKCHDOS06	-0.01	-0.03	0.13	0.11	0.04	0.15	-0.05	0.38
E	(Data - Model)	-0.13	0.01	-0.18	0.01	-0.08	-0.11	-0.38	-0.02

measurement, with the HRMA at an on-axis condition.

11.3 Comparison with models

The raytrace simulation denoted as `EKCHDOS06` represents our best model of the HRMA at the XRCF to date. Calculations of tilt angles were made from it using the `wedge` program to simulate the quadrant shutters, in conjunction with the HXDS shutter focus algorithm. A comparison of the modeled tilts with measured tilts may be seen by comparison of lines C and D in Table 11.2. The differences in modeled vs. measured tilts are given in line E of Table 11.2. The differences in $tilt_Z$ are smaller than in $tilt_Y$. These differences may indicate a lack of accuracy in the XRCF 1G modeling of rigid body tilts, since only $tilt_Y$ is affected by gravity in XRCF testing, and it has the larger differences.

11.4 Future work

We plan to investigate the 1G models of the HRMA with respect to tilt to try to determine if there are modeling issues which may affect the tilts. If not, then we will “tune” the 1G models to the XRCF measured data, so that the modeled tilts are close to the measured tilts. This procedure is based on the assumption that the tilt data from the Kodak HATS tests is correct, as well as the XRCF data, and that the most likely source of error is the 1G model. This conclusion is supported by the agreement seen in the $tilt_Z$ values, which are not affected by gravity. One important result which follows from this assumption is that shell 6 will have significantly better performance on-orbit that at XRCF, since a large fraction of the $tilt_Y$ seen at XRCF is gravity induced. This assumption will be checked by examination of on-orbit image properties at high energies.

11.5 Quad shutter tilt data from XRCF tests

11.5.1 Shell 1

Runid	Date	TRW ID	Shell / Quad	Center [μm] Y	Z
107656	01/06/97	D-IXF-P2-67.016	1T	-307159.66	10676.87
107657	01/06/97	D-IXF-P2-67.017	1N	-307147.69	10683.71
107659	01/06/97	D-IXF-P2-67.018	1B	-307152.50	10665.15
107660	01/06/97	D-IXF-P2-67.019	1S	-307146.31	10677.72

Y Tilt = -0.153014
Z Tilt = -0.143143

107663	01/06/97	D-IXF-P2-67.020	1T	-307159.59	10674.64
107657	01/06/97	D-IXF-P2-67.017	1N	-307147.69	10683.71
107659	01/06/97	D-IXF-P2-67.018	1B	-307152.50	10665.15
107660	01/06/97	D-IXF-P2-67.019	1S	-307146.31	10677.72

Y Tilt = -0.170591
Z Tilt = -0.143143

111470	02/07/97	E-IXF-P2-67.016	1T	-307110.59	10624.46
111471	02/07/97	E-IXF-P2-67.017	1N	-307102.25	10630.90
111474	02/07/97	E-IXF-P2-67.018	1B	-307109.31	10622.07
111475	02/07/97	E-IXF-P2-67.019	1S	-307115.00	10633.48

Y Tilt = -0.140715
Z Tilt = -0.0209302

11.5.2 Shell 3

Runid	Date	TRW ID	Shell / Quad	Center [μm] Y	Z
107637	01/05/97	D-IXF-P2-67.001	3T	-307167.59	10676.34
107638	01/05/97	D-IXF-P2-67.002	3N	-307156.75	10688.66
107639	01/05/97	D-IXF-P2-67.003	3B	-307150.00	10680.82
107640	01/05/97	D-IXF-P2-67.004	3S	-307153.22	10674.62

Y Tilt = -0.0482356
Z Tilt = -0.0603847

107641	01/05/97	D-IXF-P2-67.005	3T	-307166.53	10674.11
107638	01/05/97	D-IXF-P2-67.002	3N	-307156.75	10688.66
107639	01/05/97	D-IXF-P2-67.003	3B	-307150.00	10680.82
107640	01/05/97	D-IXF-P2-67.004	3S	-307153.22	10674.62

Y Tilt = -0.0658127
Z Tilt = -0.0517239

111451	02/07/97	E-IXF-P2-67.001	3T	-307116.59	10613.04
111452	02/07/97	E-IXF-P2-67.002	3N	-307110.19	10634.03
111453	02/07/97	E-IXF-P2-67.003	3B	-307112.28	10644.09
111454+7†	02/07/97	E-IXF-P2-67.004	3S	-307134.19	10629.06

†This run included an extra 1D scan

Y Tilt = -0.0469876
Z Tilt = 0.122213

11.5.3 Shell 4

Runid	Date	TRW ID	Shell / Quad	Center [μm] Y	Z
107642	01/05/97	D-IXF-P2-67.006	4T	-307163.59	10677.85
107644	01/05/97	D-IXF-P2-67.007	4N	-307153.69	10685.39
107645	01/05/97	D-IXF-P2-67.008	4B	-307152.19	10679.59
107646	01/05/97	D-IXF-P2-67.009	4S	-307151.97	10677.10

Y Tilt = -0.0397929
Z Tilt = -0.0798714

107647	01/05/97	D-IXF-P2-67.010	4T	-307162.38	10676.75
107644	01/05/97	D-IXF-P2-67.007	4N	-307153.69	10685.39
107645	01/05/97	D-IXF-P2-67.008	4B	-307152.19	10679.59
107646	01/05/97	D-IXF-P2-67.009	4S	-307151.97	10677.10

Y Tilt = -0.0484686
Z Tilt = -0.0702483

111458	02/07/97	E-IXF-P2-67.006	4T	-307114.69	10629.45
111459	02/07/97	E-IXF-P2-67.007	4N	-307119.09	10630.60
111460	02/07/97	E-IXF-P2-67.008	4B	-307119.66	10630.07
111461	02/07/97	E-IXF-P2-67.009	4S	-307119.84	10634.37

Y Tilt = -0.0429504
Z Tilt = 0.0358459

11.5.4 Shell 6

Runid	Date	TRW ID	Shell / Quad	Center [μm] Y	Z
107655	01/05/97	D-IXF-P2-67.015	6T	-307157.16	10641.41
107652	01/05/97	D-IXF-P2-67.012	6N	-307162.00	10681.58
107653	01/06/97	D-IXF-P2-67.013	6B	-307143.06	10654.70
107654	01/06/97	D-IXF-P2-67.014	6S	-307161.69	10669.99

Y Tilt = -0.43721
Z Tilt = 0.184763

111462	02/07/97	E-IXF-P2-67.011	6T	-307109.50	10600.10
111463	02/07/97	E-IXF-P2-67.012	6N	-307136.59	10626.19
111466	02/07/97	E-IXF-P2-67.013	6B	-307113.44	10599.34
111467	02/07/97	E-IXF-P2-67.014	6S	-307131.88	10628.12

Y Tilt = -0.432541
Z Tilt = 0.359181

Chapter 12

HRMA Off-Axis Focal Positions

For off-axis angles the optimum focal surface of the HRMA is closer to the HRMA than that for on-axis. This displacement depends on both off-axis angle and shell. A raytrace simulation of the offset of the best off-axis focus from the best on-axis focus was made using SAO's XRCF HRMA model (model `xrcf_SAO1G+HDOS_HDOS-scat-old_02`, which does not implement the XRCF-determined decenter). This data is presented in Table 12.1.

Table 12.1: Offset from on-axis focus (mm), + towards HRMA

Angle [']	System	Shell 1	Shell 3	Shell 4	Shell 6
0	0.0000	0.0000	0.0000	0.0000	0.0000
5	1.4384	1.0905	1.5921	2.0559	3.6470
10	5.6211	4.0979	6.2833	8.0436	14.0232
15	12.1095	9.0284	13.6771	17.4109	30.3917
20	20.6847	15.5253	23.6882	30.2079	54.1046
25	31.1065	23.6816	36.0489	46.4008	85.0136
30	44.7368	34.0254	51.7845	66.5531	122.6774

A series of tests was run on 1/30/97 and 1/31/97 to measure the best focus using the HSI and the quad shutter focus procedure. The starting point (in PrimeX) for each measurement was the on-axis best focus, as determined by the quad shutter focus procedure using the FPC. The FPC facility optical axis (FOA) in place during this test series is listed in Table 12.2.

Since Table 12.2 is determined for the HXDS FPC's, the PrimeX offset between the HSI and `fpc_x2` (20 μm aperture) must be added to the PrimeX values in the table to obtain the initial PrimeX values for the HSI. At the time of these tests the PrimeX value carried for the 20 μm aperture for `fpc_x2` was -43500 μm. The PrimeX value carried for the HSI was -46475 μm, so 2975 μm must be subtracted from the PrimeX values in Table 12.2 to yield the on-axis best focus values for the HSI. These values are listed in Table 12.3.

Table 12.2: HXDS FOA Values During Off-Axis Tests

IRIG	Shell	Prime X	Prime Y	PCAZ
030102900000	all	−32679	−307153	10543
030102901000	1	−32912	−307153	10543
030102901000	3	−32561	−307153	10543
030102902000	4	−32292	−307153	10543
030102903000	6	−32664	−307153	10543

Table 12.3: HSI PrimeX Values for Best On-Axis Focus

Shell	PrimeX_{00} [mm]
HRMA	−35.6540
1	−35.8870
3	−35.5360
4	−35.2670
6	−35.6390

The measured data from the 20 tests (some with 2 iterations) are listed in Table 12.4. The data given are:

TRW ID	Test ID
RunID	One of 4 RunID's from the Quad shutter test
θ	Off-axis angle
ϕ	Clocking of the off-axis angle relative to XRCF-Y (see Figure 1.8).
Shell	HRMA shell number
PrimeX	Initial PrimeX stage position during test
ΔX	Change in PrimeX for best focus from HSI measurement and shutter focus calculation
$\delta \mathrm{F}_{\mathrm{meas}}$	$\mathrm{PrimeX}/1000 - \Delta X/1000 - \mathrm{PrimeX}_{00}$
$\delta \mathrm{F}_{\mathrm{sim}}$	Simulated shift in focal position from the on-axis focal position
$\Delta \mathrm{F}$	$\delta \mathrm{F}_{\mathrm{meas}} - \delta \mathrm{F}_{\mathrm{sim}}$

$\delta \mathrm{F}_{\mathrm{meas}}$ and $\delta \mathrm{F}_{\mathrm{sim}}$ are plotted in Figure 12.1.

Table 12.4: Off-Axis Focus Test Data

TRW ID	RunID	θ [′]	ϕ [°]	Shell	PrimeX [μm]	ΔX [μm]	δF_{meas} [mm]	δF_{sim} [mm]	ΔF [mm]
E-IXH-SF-15.001	110553	5	135	All	−34215.08	−613	2.0519	1.4384	0.6135
E-IXH-SF-15.001	110560	5	135	All	−33603.14	49	2.0019	1.4384	0.5635
E-IXH-SF-15.002	110561	5	135	1	−34860.02	−450	1.4770	1.0905	0.3865
E-IXH-SF-15.002	110568	5	135	1	−34408.06	−9	1.4879	1.0905	0.3974
E-IXH-SF-15.003	110569	5	135	3	−33942.11	−412	2.0059	1.5921	0.4138
E-IXH-SF-15.003	110577	5	135	3	−33528.65	10	1.9973	1.5921	0.4052
E-IXH-SF-15.004	110578	5	135	4	−33209.18	−384	2.4418	2.0559	0.3859
E-IXH-SF-15.004	110585	5	135	4	−32823.22	−4	2.4478	2.0559	0.3919
E-IXH-SF-15.005	110586	5	135	6	−31990.30	−407	4.0557	3.6470	0.4087
E-IXH-SF-15.005	110593	5	135	6	−31579.34	788	3.2717	3.6470	-0.3753
E-IXH-SF-15.006	110595	10	0	All	−30030.50	−35	5.6585	5.6211	0.0374
E-IXH-SF-15.006	110603	10	0	All	−29995.50	−7	5.6655	5.6211	0.0444
E-IXH-SF-15.007	110607	10	0	1	−31786.82	186	3.9142	4.0979	-0.1837
E-IXH-SF-15.007	110611	10	0	1	−31972.80	50	3.8642	4.0979	-0.2337
E-IXH-SF-15.008	110618	10	0	3	−29252.07	487	5.7969	6.2833	-0.4864
E-IXH-SF-15.008	110619	10	0	3	−29739.53	44	5.7525	6.2833	-0.5308
E-IXH-SF-15.009	110623	10	0	4	−27221.28	726	7.3197	8.0436	-0.7239
E-IXH-SF-15.009	110630	10	0	4	−27949.21	−59	7.3768	8.0436	-0.6668
E-IXH-SF-15.010	110631	10	0	6	−21614.34	1160	12.8647	14.0232	-1.1585
E-IXH-SF-15.010	110638	10	0	6	−22775.72	−195	13.0583	14.0232	-0.9649
E-IXH-SF-15.011	110640	15	135	All	−23542.15	315	11.7968	12.1095	-0.3127
E-IXH-SF-15.011	110647	15	135	All	−23858.61	38	11.7574	12.1095	-0.3521
E-IXH-SF-15.012	110648	15	135	1	−26923.31	845	8.1187	9.0284	-0.9097
E-IXH-SF-15.012	110655	15	135	1	−27770.22	−34	8.1508	9.0284	-0.8776
E-IXH-SF-15.013	110656	15	135	3	−21857.31	898	12.7807	13.6771	-0.8964
E-IXH-SF-15.014	110660	15	135	4	−17854.21	791	16.6218	17.4109	-0.7891
E-IXH-SF-15.015	110664	15	135	6	−5245.48	−329	30.7225	30.3917	0.3308
E-IXH-SF-15.016	110670	25	135	All	−4546.05	−1058	32.1660	31.1065	1.0595
E-IXH-SF-15.016	110677	25	135	All	−3487.15	−32	32.1988	31.1065	1.0923
E-IXH-SF-15.017	110678	25	135	1	−12202.78	−1143	24.8272	23.6816	1.1456
E-IXH-SF-15.018	110682	25	135	3	514.45	578	35.4725	36.0489	-0.5765
E-IXH-SF-15.019	110688	25	135	4	11135.89	1060	45.3429	46.4008	-1.0579
E-IXH-SF-15.020	110692	25	135	6	49377.06	587	84.4291	85.0136	-0.5845

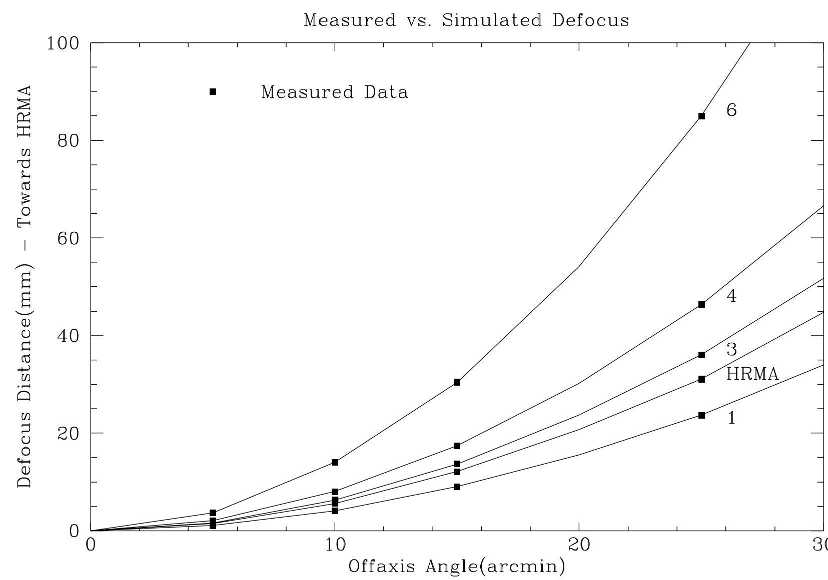

Figure 12.1: Measured vs. Simulated Off-Axis Focus Data

Chapter 13

Internal Tilt-Compensated Coma-Free Decenter of the AXAF mirrors

This chapter discusses the investigation and analysis of one of the major "minor mysteries" encountered during Phase 1 testing at XRCF. The first two sections (§13.1 and §13.2) provide a brief description of the investigation which led to the discovery of the "tilt-compensated" (*i.e.*, *coma-free*) decenters between the P and H optics in the HRMA. Although the decenter was first detected in quadrant flux balance measurements, detailed off-axis X-ray images led to a much more powerful approach to determining the decenter values. The detailed morphology of the X-ray images is discussed in §13.3. The measurements of the tilt-compensated decenters are described in §13.4. Finally, in §13.5 some suggestions are made for future investigation.

13.1 Quadrant Shutter Flux Balance

During the attempts to assess the relation between the HRMA optical axis and the FOA, a series of quad-shutter flux balance experiments were performed. These tests were part of an attempt to measure the misalignment of the HRMA optical axis relative to the Facility Optical Axis (FOA) by the variation in the amount of flux detected through individual mirror quadrants. For example, as the HRMA pitch is changed, one would expect the relationship between the fluxes from the Top and Bottom quadrants to change. The "2nd Floor" scientists at XRCF noted anomalies which were difficult to explain: an asymmetry of 6 or 7% between the Shell 6 top and bottom shutter fluxes (and correspondingly smaller asymmetries for the larger shells) even though other evidence suggested that HRMA axis alignment to the FOA in pitch was really rather close.

Various suggestions were considered. The effects of vignetting by various baffles and obstructions were investigated, but in each case the required decenters were too large to be plausible (*e.g.*, decenters of the precollimator by several millimeters), the size of the effect was too small, or the effect did not fit the observed trends very well. Tests at ring focus exonerated the shutter assembly itself (see Chapter 15). Finally it was suggested by that an internal relative decenter between the P and H optic might explain the anomalies. Preliminary raytrace investigations showed that a pure decenter of several hundred μm could affect the flux balance in the way observed. Because such large decenters would have been immediately noticed in the optical coma measurements (Chapter 14), it was postulated that a coma-free combination of decenter plus tilt ("tilt-compensated decenter") was responsible. In the case of an H optic, this motion is a rigid-body rotation of the H optic

about its far focus; the coma from the tilt component of the motion exactly cancels the coma produced by the decenter component. Further raytraces showed that the decenter component of the tilt-compensated decenter accounted for most of the flux balance anomaly; although the tilt compensation is needed to account for the observed coma, the tilt compensation modified the flux balance discrepencies by $\lesssim$10%.)

C. Atkinson (EKC) reviewed the assembly procedure and came up with a scenario whereby an initial decenter could have been introduced between P6 and the optical axis and which would naturally lead to each of the mirror pairs having approximately the same tilt-compensated decenters; tolerances are such that a relative decenter of a few hundred μm are possible.

Noise and systematic errors made it difficult to obtain good values of the decenters from the flux balance differences alone.

13.2 Off-Axis X-ray Images

Off-axis HSI images for the whole HRMA were taken at a number of off-axis angles and energies (see Table 13.1). These off-axis images showed a peculiar pincushion-like cuspy feature in the core and this proved to be the breakthrough needed for understanding the P to H decenters. Preliminary raytrace studies confirmed that a P to H decenter of several hundred μm could generate pincushion-like cusps in off-axis images qualitatively similar to those observed. The off-axis images established tilt-compensated decenter as the most likely explanation for the flux balance results; any explanation in terms of obscuration or vignetting would fail to account for the distinctive characteristic features in the off-axis X-ray images.

Considerable effort was expended in attempting to deduce the optic decenters from the available full-HRMA images at different energies; T. Gaetz (SAO) determined that two mirror pairs (at least) exhibited a tilt-compensated decenter, probably of about the same magnitude and direction, but the complexity of four overlapping images made it very difficult to make further progress. (Even the identification between pincushion and responsible mirror shell was problematic; some of the tentative identifications proved to be incorrect.)

In order to diagnose the P to H decenters which seemed to be implied by the quadrant flux balance data and the full-HRMA off-axis images, a series of off-axis images for individual mirror pairs was requested and obtained. These images were all at Al-Kα (see Table 13.2) and are plotted in Figures 13.1, 13.2, and 13.3.

Systematic raytrace investigations were undertaken to understand the effect of tilt-compensated decenter on off-axis images (T.Gaetz, SAO); as a result of these studies, a scheme was developed for deriving the decenter parameters based on detailed measurements of image features. The results of these studies and the resulting tilt-compensated decenter parameters as assessed from the X-ray images are described below.

13.3 Morphology of the Off-axis X-ray Images

The off-axis images taken at XRCF show two distinctive features: a pair of overlapping large, approximately oval lobes, and a small pincushion-like caustic in the core. This section discusses the morphology of these features and their dependence on decenter magnitude and direction relative to the off-axis source direction.

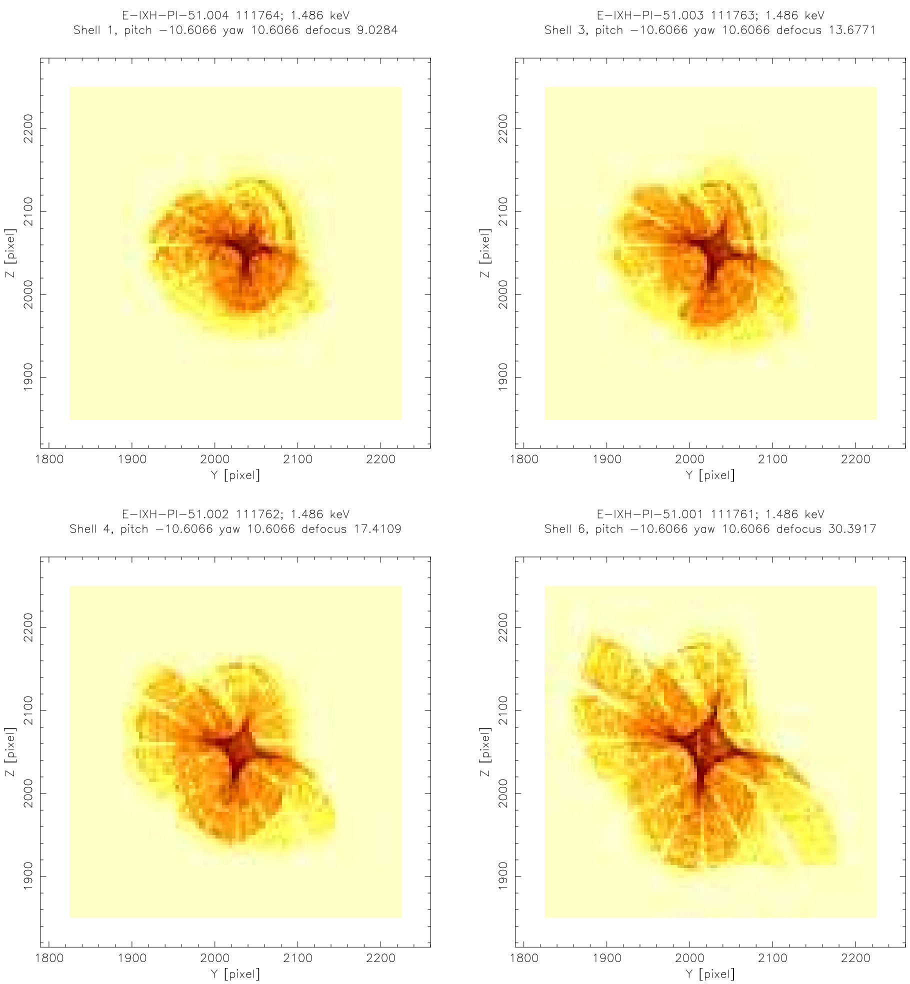

Figure 13.1: Off-axis images for individual shells; pitch = $-10.61'$, yaw = $10.61'$. Pixel width $6.43\,\mu$m; binned to 4×4 pixels. Two large overlapping lobes and a dense central pincushion can be seen; the light lanes are shadows of the CAP struts. The concentric ridges in the large lobes result from low-frequency surface errors on the mirrors. (X-ray data; logarithmic stretch)

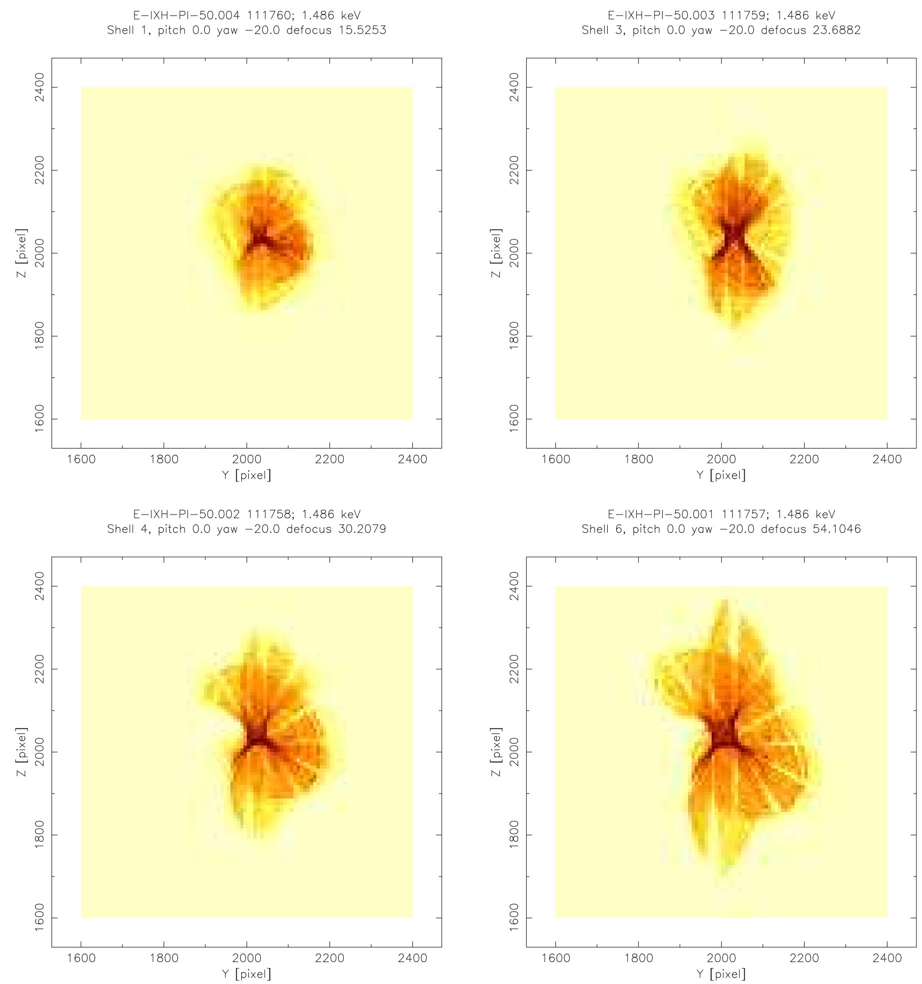

Figure 13.2: Off-axis images for individual shells; pitch = $0'$, yaw = $-20'$. Pixel width $6.43\,\mu$m; binned to 8×8 pixels. Two large overlapping lobes and a dense central pincushion can be seen; the light lanes are shadows of the CAP struts. The concentric ridges in the large lobes result from low-frequency surface errors on the mirrors. (X-ray data; logarithmic stretch)

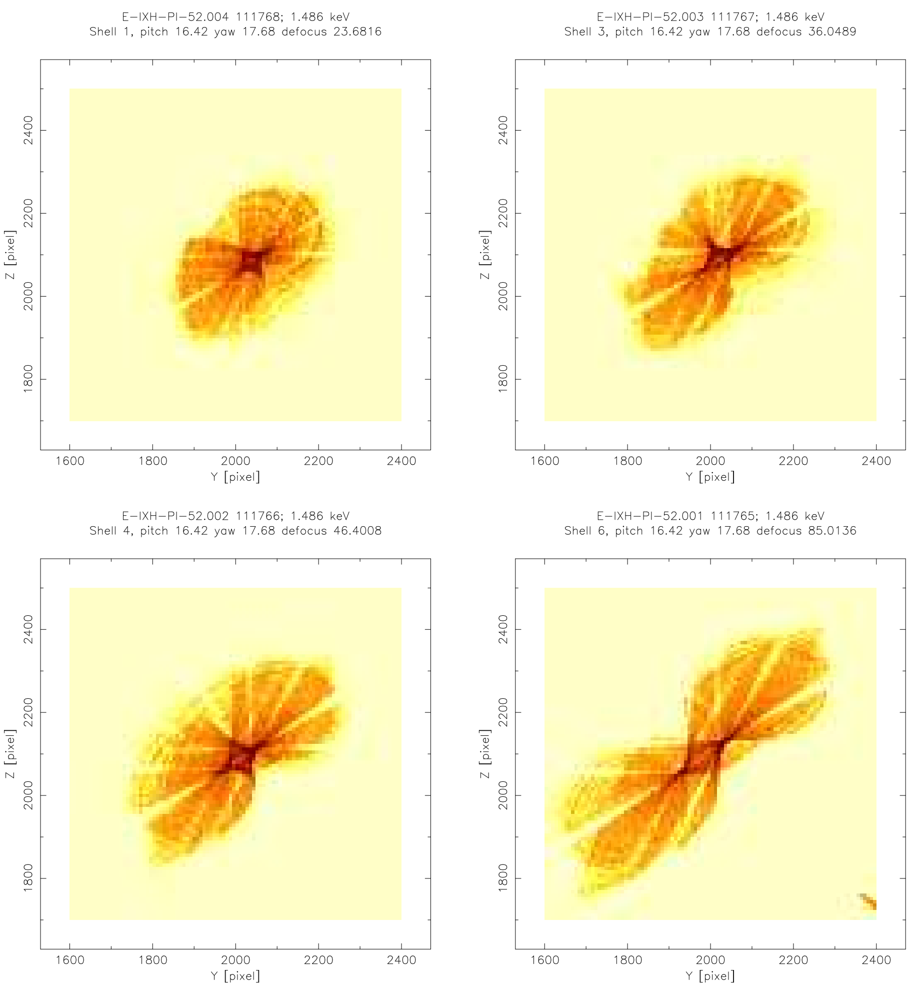

Figure 13.3: Off-axis images for individual shells; pitch = $16.42'$, yaw = $17.68'$. Pixel width $6.43\,\mu$m; binned to 8×8 pixels. Two large overlapping lobes and a dense central pincushion can be seen; the light lanes are shadows of the CAP struts. The concentric ridges in the large lobes result from low-frequency surface errors on the mirrors. (X-ray data; logarithmic stretch)

Table 13.1: Phase 1 Off-Axis Images (Full HRMA)

TRW ID	RunID	Energy	Shell	pitch	yaw	defocus
E-IXH-PI-6.001	110594	0.277	HRMA	−3.54	3.54	1.4384
E-IXH-PI-7.002	110639	0.277	HRMA	0	−10	5.6211
E-IXH-PI-6.003	110668	0.277	HRMA	−10.61	10.61	12.1095
E-IXH-PI-7.004	110669	0.277	HRMA	0	−20	20.6847
E-IXH-PI-6.005	110700	0.277	HRMA	−17.68	17.68	31.1065
E-IXH-PI-6.006	110701	0.277	HRMA	−21.21	21.21	44.7368
E-IXH-PI-12.004	110887	6.4	HRMA	0	−20	20.6847
E-IXH-PI-12.002	110888	6.4	HRMA	0	−10	5.6211
E-IXH-PI-11.001	110889	6.4	HRMA	−3.54	3.54	1.4384
E-IXH-PI-11.003	110890	6.4	HRMA	−10.61	10.61	12.1095
E-IXH-PI-11.005	110892	6.4	HRMA	−17.68	17.68	31.1065
E-IXH-PI-11.006	110893	6.4	HRMA	−21.21	21.21	44.7368
E-IXH-PI-22.004	111084	4.51	HRMA	0	−20	20.6847
E-IXH-PI-22.002	111085	4.51	HRMA	0	−10	5.6211
E-IXH-PI-21.001	111086	4.51	HRMA	−3.54	3.54	1.4384
E-IXH-PI-21.003	111087	4.51	HRMA	−10.61	10.61	12.1095
E-IXH-PI-21.005	111088	4.51	HRMA	−17.68	17.68	31.1065
E-IXH-PI-21.006	111089	4.51	HRMA	−21.21	21.21	44.7368

13.3.1 Off-Axis Images: Large Lobes

The off-axis images show two large approximately oval lobes; these are a facility effect resulting from the spherical aberration which is introduced by the finite source distance at XRCF. Symmetry considerations indicate that for an ideal perfectly aligned telescope, these lobes should be symmetric about a line containing the off-axis image and the optical axis. The observed large lobes are asymmetric and also tilted relative to each other; this is a consequence of the tilt-compensated decenter within the mirror pair. The lighter swaths through the image result from shadowing by support struts, predominantly those in the Central Aperture Plate.

The approximately concentric ripples in the large lobes result from the low-order mirror surface errors; these are also caustics, analogous to the pattern of bright lines on the bottom of a swimming pool caused by the ripples on the water surface. In this case they result from axial ripples on the mirror surface. The agreement between the location and shape of the ripples in the X-ray data as compared to the raytraces is an indication of the fidelity of the low-order mirror maps used in the raytrace. The ripples are more noticeable in the Shell 1 images; Figure 13.7 shows them at a different contrast setting.

The relative balance between the sizes of the lobes is sensitive to the axial position of the detector; at the best off-axis focus for the mirror pair, these lobes are comparable in size. The relative shape and orientation of the lobes depends on the direction of the decenter relative to the direction of the off-axis source (working in HRMA-centered coordinates). In addition to the offsets

Table 13.2: Phase 1 Off-Axis Images (Individual Shell)

TRW ID	RunID	Energy	Shell	pitch	yaw	defocus
E-IXH-PI-50.001	111757	1.486	6	0	−20	54.1046
E-IXH-PI-50.002	111758	1.486	4	0	−20	30.2079
E-IXH-PI-50.003	111759	1.486	3	0	−20	23.6882
E-IXH-PI-50.004	111760	1.486	1	0	−20	15.5253
E-IXH-PI-51.001	111761	1.486	6	−10.61	10.61	30.3917
E-IXH-PI-51.002	111762	1.486	4	−10.61	10.61	17.4109
E-IXH-PI-51.003	111763	1.486	3	−10.61	10.61	13.6771
E-IXH-PI-51.004	111764	1.486	1	−10.61	10.61	9.0284
E-IXH-PI-52.001	111765	1.486	6	16.42	17.68	85.0136
E-IXH-PI-52.002	111766	1.486	4	16.42	17.68	46.4008
E-IXH-PI-52.003	111767	1.486	3	16.42	17.68	36.0489
E-IXH-PI-52.004	111768	1.486	1	16.42	17.68	23.6816

in the large lobes, a relative P to H decenter produces a pincushion-shaped caustic at best (off-axis) focus; this is discussed further in §13.3.2.

Some of the XRCF single-shell off-axis images show obvious indentations in the large lobes. In some cases (e.g., Shells 3 and 4 at pitch $= 0'$, yaw $= -20'$, Shells 1 and 3 at pitch $= 16.42'$, yaw $= 17.68'$) this appears to be a result of vignetting by the shutter assembly; preliminary raytraces show that a shutter assembly decenter of about 2 mm appears to be consistent with these results. In other cases the indentations arise from the morphology of the off-axis images: Shells 1 and 6 at pitch $= 0'$, yaw $= -20'$ appears to be consistent with no additional vignetting by the shutter assembly.

A raytrace experiment was performed in which the relative direction between the off-axis source and the decenter direction was systematically varied. (The pitch and yaw of the shell were assumed fixed and the decenter direction varied.) The results are shown in Figure 13.4; a close-up of the pincushion core is shown in Figure 13.5. Note that the smaller of the large lobes and the orientation of the cuspy pincushion rotate oppositely to the change in decenter direction and at approximately half the rate that the decenter varies. The size of the pincushion also varies somewhat with relative angle between off-axis source direction and P to H mirror decenter direction. Note that the lobes and the pincushion core both show the expected bilateral symmetry when the decenter direction and the off-axis direction are parallel ($\phi = 0°$ and $\phi = 180°$.)

13.3.2 Off-Axis Images: Pincushion Caustics

The pincushion caustics are also a consequence of the tilt-compensated decenter in the optics. Raytrace studies show that the dimension of the pincushion scales inversely with the mirror pair nodal radius. The pincushion gets larger as the magnitude of the off-axis angle increases (for constant tilt-compensated decenter) and also gets larger as the magnitude of the tilt-compensated decenter increases (for constant source off-axis angle). For fixed magnitude of off-axis angle and

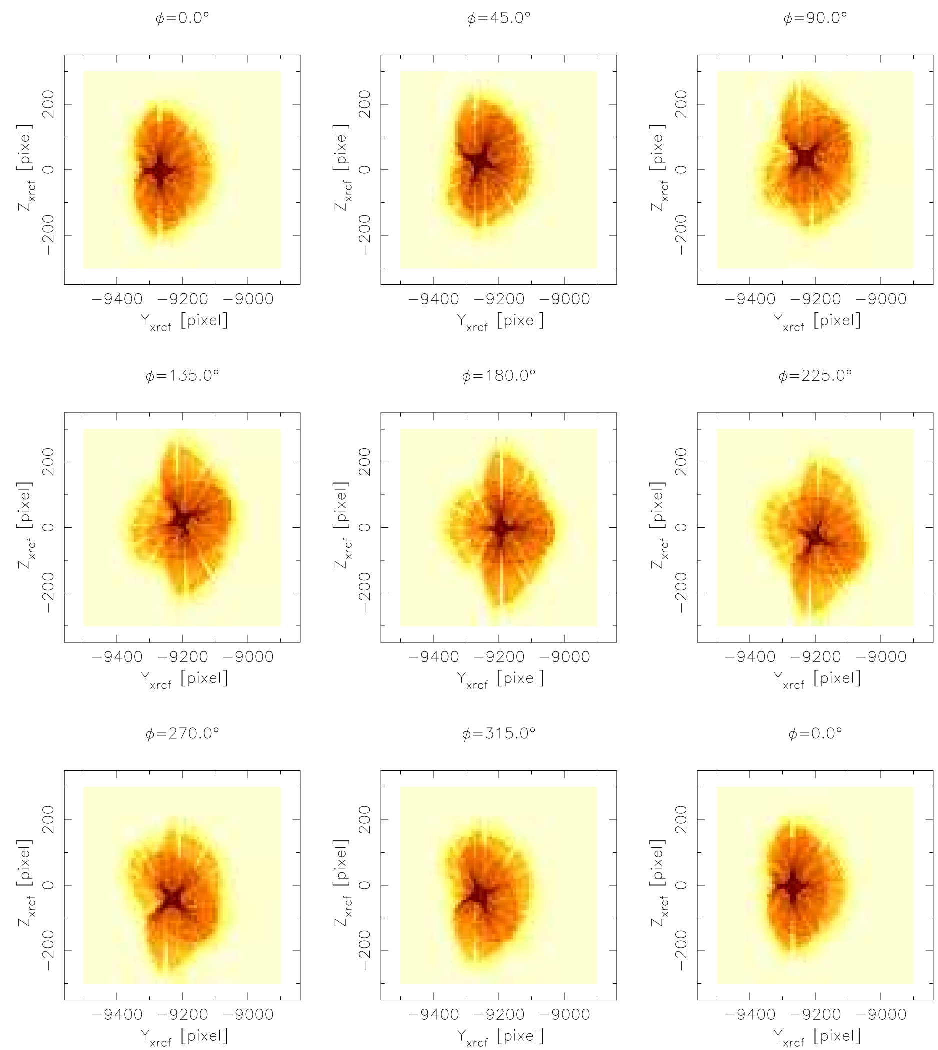

Figure 13.4: Variation of off-axis image with angle between source and decenter direction. Shell 3, pitch $= 16.42'$, yaw $= 17.68'$. Pixel width 6.43 μm; binned to 8×8 pixels. (Raytrace data; logarithmic stretch)

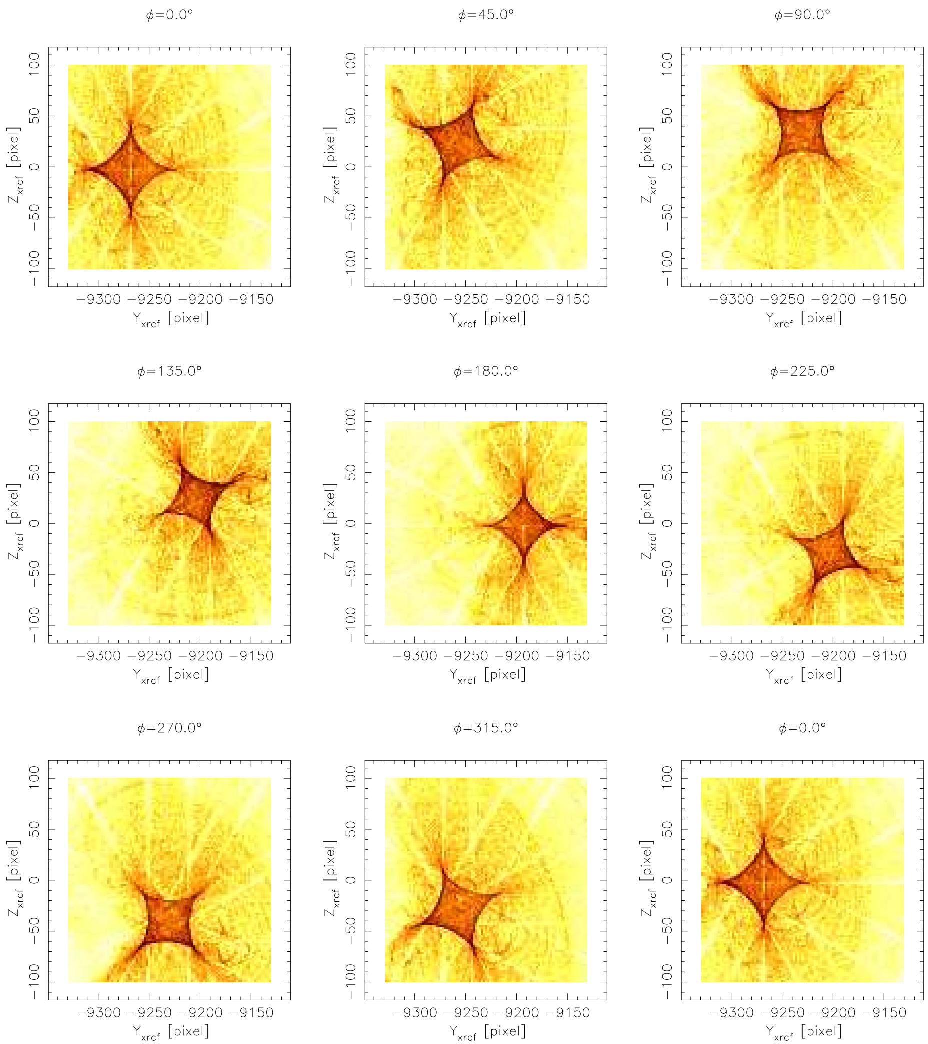

Figure 13.5: Variation of off-axis image with angle between source and decenter direction. Shell 3, pitch = $16.42'$, yaw = $17.68'$. Pixel width 6.43 μm; binned to 1×1 pixels. (Raytrace data; logarithmic stretch)

tilt-compensated decenter, the pincushion size and the orientation of the axes of the pincushion vary with relative angle between off-axis direction and the decenter direction. Symmetry considerations suggest that the pincushion should show full bilateral symmetry about the decenter direction when the decenter direction is parallel or anti-parallel to the off-axis direction, and this is seen in Figure 13.5 ($\phi = 0°$ and $\phi = 180°$ cases, where ϕ is the angle between the decenter direction and the projection onto the focal plane of the off-axis source direction); the corners of the pillbox are aligned with the decenter direction. Closer scrutiny of Figure 13.5 shows that the pincushion size varies systematically with angle between decenter direction (at fixed decenter magnitude) and (fixed) off-axis direction. The pincushion orientation changes by 90° as the ϕ changes by 180° so the pincushion rotates about half as rapidly as ϕ varies. Detailed measurements show that the factor of 1/2 is only approximate, but by symmetry, the pincushion rotation between $\phi = 0°$ and $\phi = 180°$ must be exactly 90° in the limit of otherwise ideal optics.

Raytracing also shows that the size and orientation of the pincushion is insensitive to the axial location of the detector; the basic structure of the pincushion is the same even with focal errors as large as several mm (though differences become readily apparent if the image is sufficiently out of focus that the pincushion unravels).

13.4 Measuring the Tilt-Compensated Decenter

Raytrace studies revealed an important feature of the tilt-compensated decenters: for constant off-axis angle and in the neighborhood of a given decenter value, the variation of the *pincushion size* with *decenter magnitude* and the variation of *pincushion orientation* with *decenter direction* are relatively uncoupled from each other. This means that once an initial estimate of the decenter parameters is obtained, the decenter magnitude and direction can be refined by using the sensitivities of pincushion size and orientation to decenter magnitude and direction to refine the estimate.

The above procedure was carried out for the single-shell pitch = $0'$, yaw = $-20'$ measurements. The approximate direction of the decenter was be assessed from the morphology of the large lobes; this also removes the $\pi/2$ angular ambiguity in the pincushion orientation (see Figure 13.4). Raytraces were used to provide an initial estimate for the magnitude and direction; the same initial values were assumed for all four shells. The relative sizes of the large lobes do depend sensitively on focal position and serve as an additional check that the images were taken at very nearly the best off-axis focus for the individual shell; examination of the X-ray data indicates that the individual shell images were taken near best focus.

The decenter magnitude and direction can be determined by measuring the pincushions in the X-ray data and simulation (on an expanded scale to make measurement easier). Figure 13.9 shows and expanded view of the the pincushion cores in the pitch= $0'$, yaw= $20'$ images, and Figure 13.10 shows the equivalent images based on raytraces using the mirror rigid-body model obtained in Chapter 14.

Figure 13.6 shows the measurement schematically. The width, w, of the pincushion along a slice through the narrow portion of the pincushion (midway up the box) was measured. In addition, the angle, θ between the Y axis and a line connecting opposing corners (at $\sim +45°$) was measured. These metrics were compared with those in raytraced images. Once reasonably good agreement was obtained, a raytrace study established the sensitivity of box width w to decenter magnitude and also the sensitivity of box orientation θ to decenter direction; it was found that for Shell 6 the pincushion width w varied with decenter magnitude as 123 pixels mm^{-1} of decenter (1 pixel= 6.43 μm); the sensitivity scales inversely with the mirror nodal radius. (Note that the sensitivities may depend on the approximate magnitude of the tilt-compensated decenter and its direction relative to the

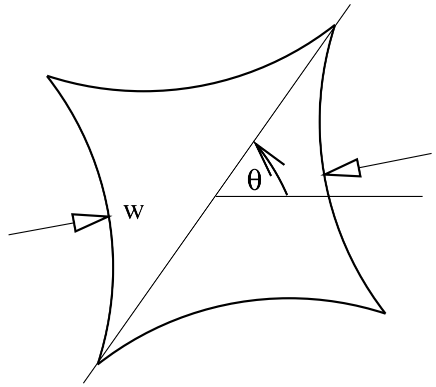

Figure 13.6: Schematic diagram of pincushion measurement. The width, w is measured across the narrow part of the pincushion. The orientation, θ, is measured using the diagonal of the pincushion.

off-axis source direction.)

As an illustration of the procedure, consider Figures 13.7 and 13.8 (Shell 1; pitch= $0'$, yaw= $-20'$). In Figure 13.7 a raytrace using the current best estimate for Shell 1 tilt-compensated decenter (upper left panel) is compared to the X-ray image (lower right panel). The effects of increasing (decreasing) the tilt-compensated decenter by 0.1 mm is shown in the lower left (upper right) panel; the change in pincushion size is clearly visible. Similarly, in Figure 13.7 the current best estimate for Shell 1 coma-free decenter+tilt (upper left panel) is compared to the X-ray image (lower right panel). The decenter is direction changed by $-24°$ (upper right) or $+24°$ (lower left); note the change in pincushion orientation. In this case it is also possible to see a darker bar across the pincushion at about 120° from about halfway across the bottom of the box; the position of this bar changes with pincushion orientation, and the agreement in bar position is quite good between the X-ray data and the current best raytrace model. (This bar is even more clearly visible in the upper left panels of Figures 13.9 and 13.10; a similar feature is seen in the upper right panel of Figure 13.10, but vignetting by the shutter assembly obscures that portion of the image in the corresponding X-ray data (upper right panel of Figure 13.9).)

Note that the X-ray image cores and the raytrace image cores differ in detail for at least two reasons: angle-dependent sensitivity of the HSI detector and vignetting by the quadrant shutter assembly; for example, note the vignetting evident in the bottom of the pincushion for Shell 3 and the top of the pincushion for Shell 4 in Figure 13.9. Nevertheless, the diagnostic features (pincushion size and orientation) are visible clearly enough to allow a good determination of decenter direction and magnitude. Where visible, agreement in the pincushion substructure between the X-ray data and the raytraces provides further support for the accuracy of the tilt-compensated decenter values.

The estimated relative decenters of the H mirrors relative to their mating P mirrors are given in Table 13.3. Note that these decenters are given in `SAOsac` raytrace coordinates (see §1.4); angle

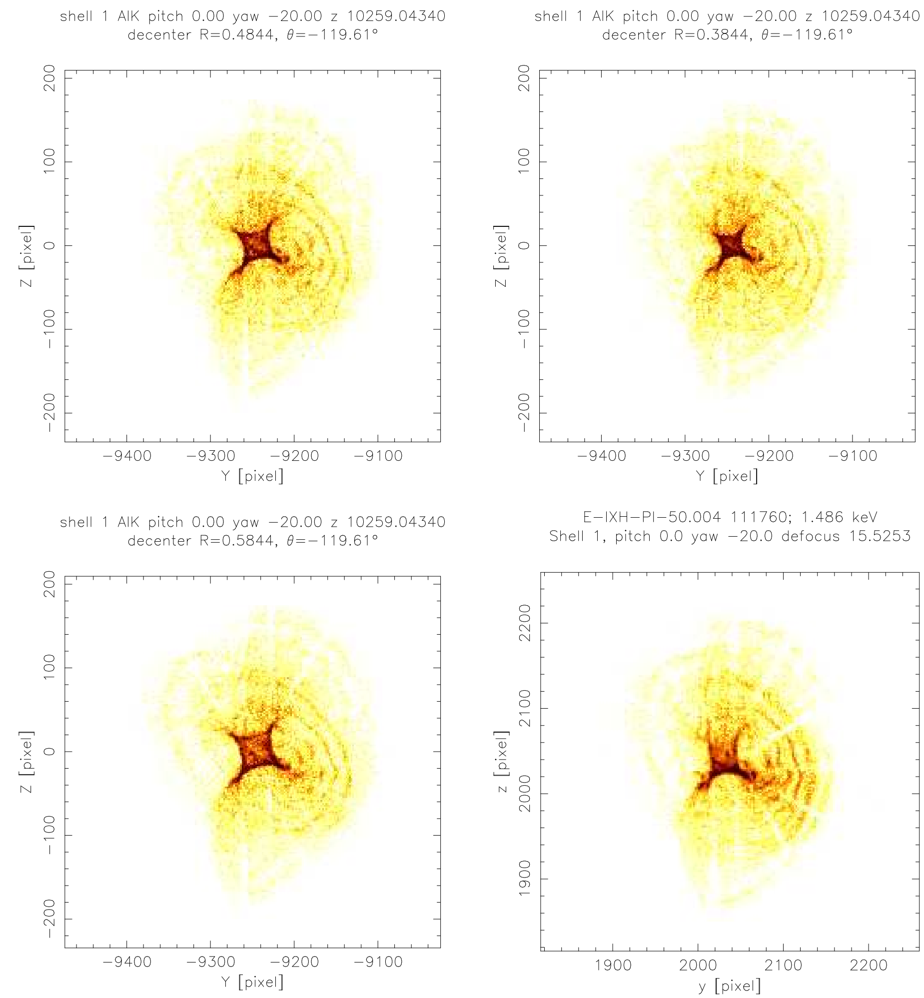

Figure 13.7: Off-axis images (Shell 1; pitch = $0'$, yaw = $-20'$). Top left: Current raytrace model. Top right: decenter magnitude $\Delta R_0 - 0.1$ mm. Bottom left: decenter magnitude $\Delta R_0 + 0.1$ mm. Bottom right: HSI image (X-ray data) (to same scale). Pixel width 6.43 μm; binned to 2×2 pixels. Logarithmic stretch.

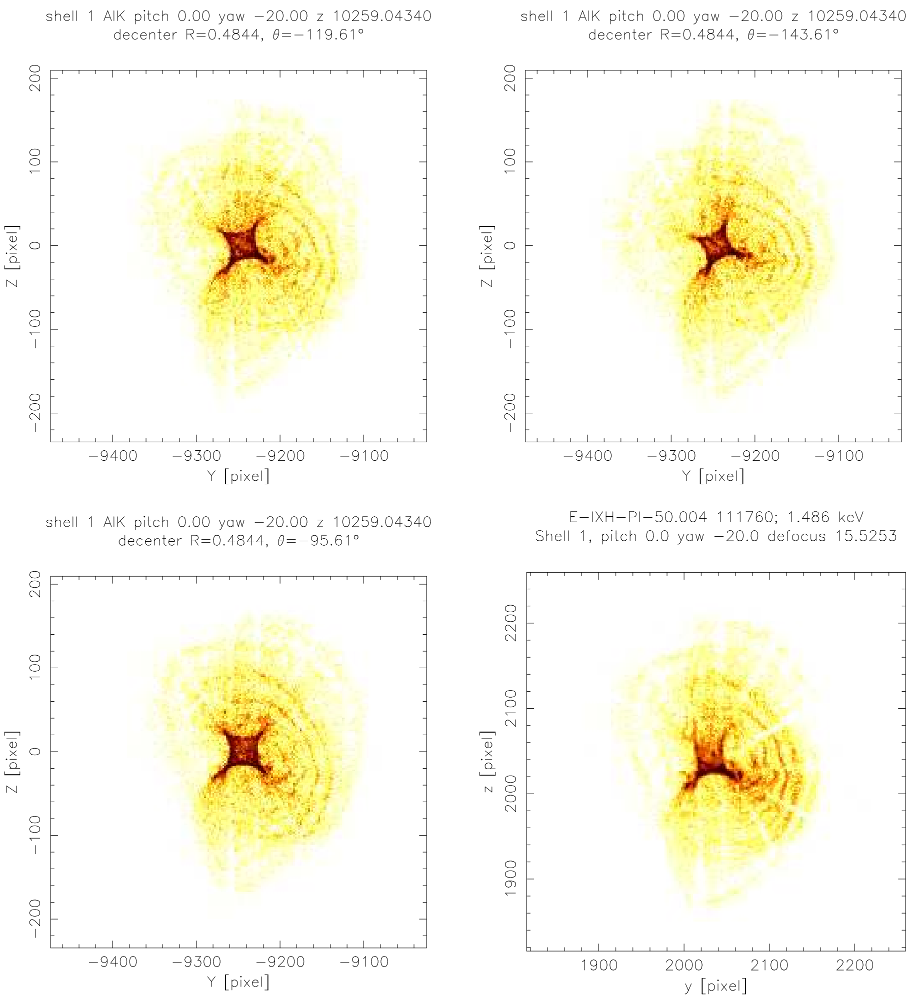

Figure 13.8: Off-axis images (Shell 1; pitch = $0'$, yaw = $-20'$). Top left: Current raytrace model. Top right: decenter direction $\Delta\phi_0 - 24°$. Bottom left: decenter direction $\Delta\phi_0 + 24°$. Bottom right: HSI image (X-ray data) (to same scale). Pixel width $6.43\,\mu$m; binned to 2×2 pixels. Logarithmic stretch.

13.4. Measuring the Tilt-Compensated Decenter

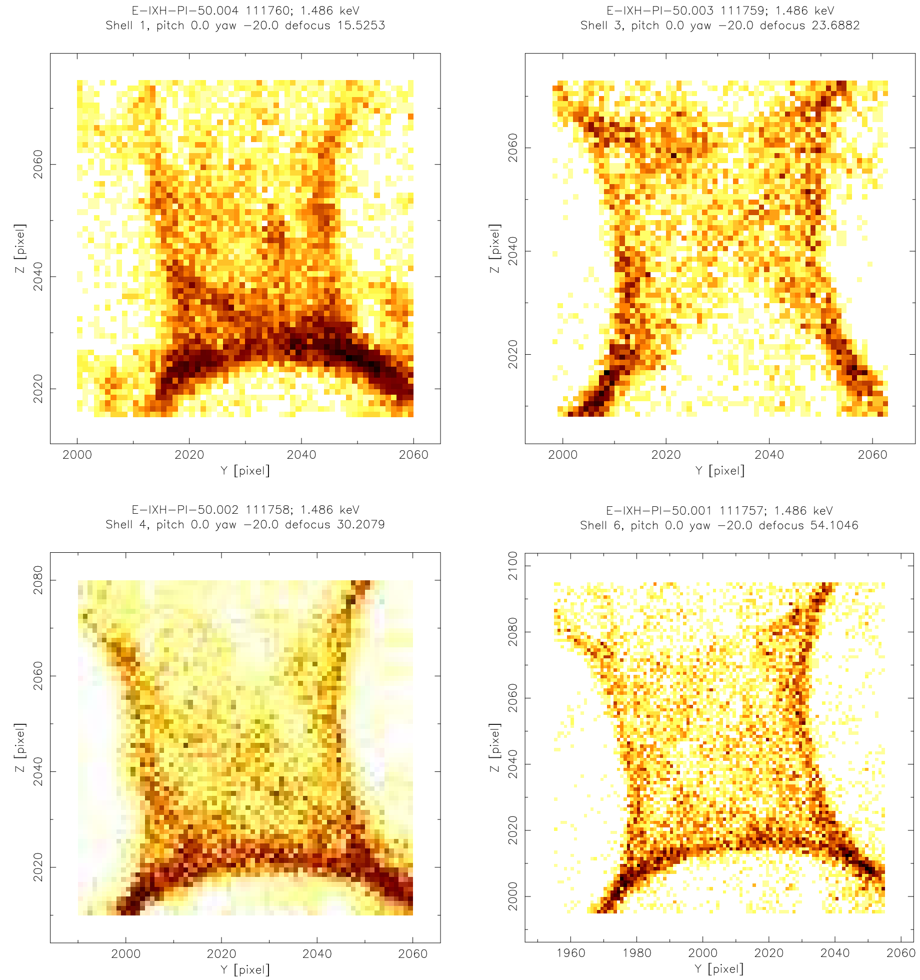

Figure 13.9: Core pincushions of off-axis images for individual shells; pitch = $0'$, yaw = $-20'$. Pixel width $6.43\,\mu$m; binned to 1×1 pixels. (X-ray data; logarithmic stretch)

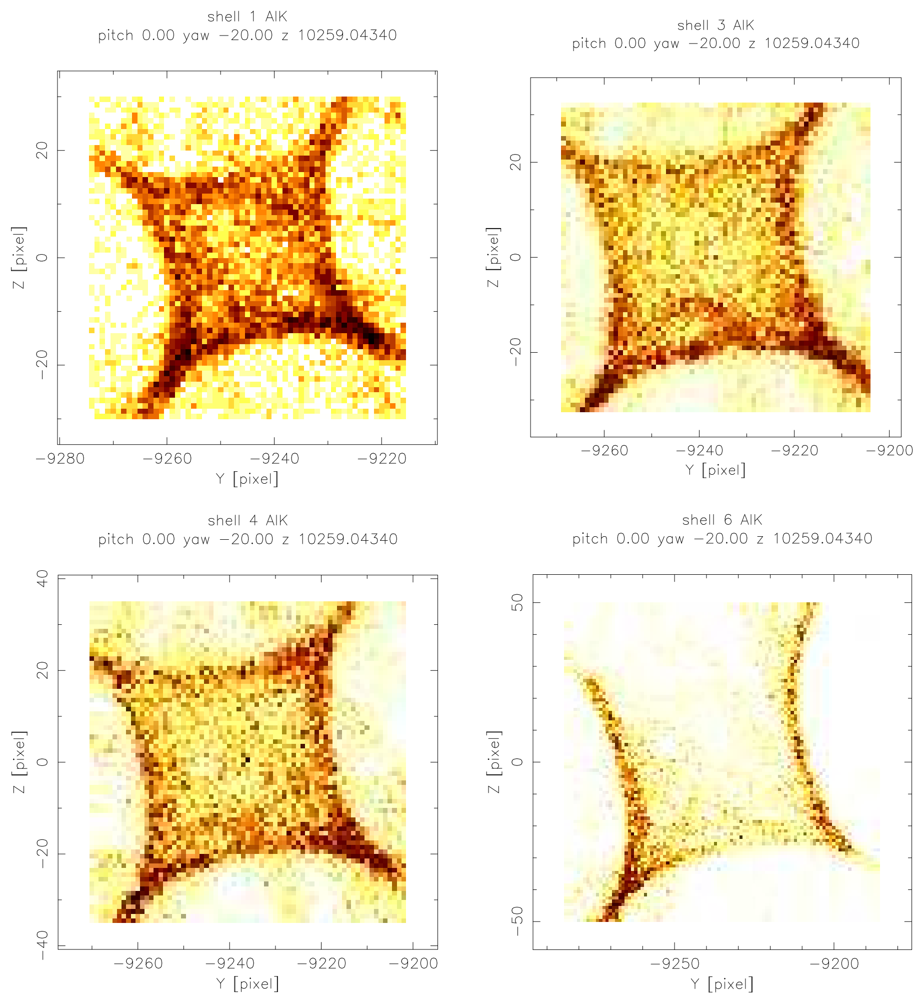

Figure 13.10: Core pincushions of off-axis images for individual shells based on current SAO raytrace model; pitch $= 0'$, yaw $= -20'$. Pixel width $6.43\,\mu$m; binned to 1×1 pixels. (Raytraced; logarithmic stretch)

Table 13.3: Measured Tilt-Compensated Decenters

	decenter†		decenter†	
mirror	magnitude (mm)	angle (deg)	Δx_0 (mm)	Δy_0 (mm)
h1	0.4844	−119.61	−0.2393	−0.4211
h3	0.5077	−109.61	−0.1704	−0.4782
h4	0.4562	−111.90	−0.1702	−0.4233
h6	0.4736	−114.42	−0.1958	−0.4312

†coma from decenter cancelled by compensating tilt

is measured from the `SAOsac` raytrace $+X$ axis with $+Y$ at $+90°$ (see Figure 1.8);

$$X_{SAOsac} = -Y_{XRCF} \tag{13.1}$$

$$Y_{SAOsac} = +Z_{XRCF} \tag{13.2}$$

$$Z_{SAOsac} = -X_{XRCF} \tag{13.3}$$

$$\tag{13.4}$$

Note that the actual body-centered decenter and tilt for each optic must also be consistent with optical measurements at EKC at the end of HRMA buildup. The construction of the mirror rigid-body database (based on the above tilt-compensated decenter and the X-ray and optical measurements of the alignment) is discussed in Chapter 14; the current mirror database is `/proj/axaf/simul/databases/mirror/EKCHDOS06.rdb`.

The current HRMA model (`trace-shell4` configuration file `xrcf_SAO1G+HDOS_HDOS-scat-970220_03`) was raytraced for each mirror pair and off-axis angle combination as listed in Table 13.2. The raytraces accumulated a total ray weight of about 100000 per image (comparable to the number of events in the X-ray images). The raytrace fractional weights were converted statistically into unit weights (`mxwldmn`) and blurred to the HSI resolution (`mcp` using the `/proj/axaf/simul/databases/detectors/hsi.par` specification file. The images *do not*, however, incorporate the angle-dependent HSI detector quantum efficiency, nor do they include the vignetting introduced by the quadrant shutter assembly at these large off-axis angles. The raytraces of the HRMA model are plotted in Figures 13.11, 13.12, and 13.13; these can be compared with the X-ray images in Figures 13.1, 13.2, and 13.3.

13.5 Future Directions

This chapter represents a preliminary attempt at extracting the tilt-compensated H to P decenters from the X-ray data. It is thought that the decenters are accurate to better than 10%. The current estimate is based on single-shell data at a single off-axis angle (pitch $= 0'$, yaw $= -20'$). Single-shell off-axis X-ray images were obtained in two other directions; inspection of the raytrace data in Figures 13.11 and 13.13 compared to the X-ray data in Figures 13.1 and 13.3 shows good qualitative agreement. (Some of the detailed differences between the images are caused by vignetting by the quad shutter assembly at these large off-axis angles.) The single-shell data taken

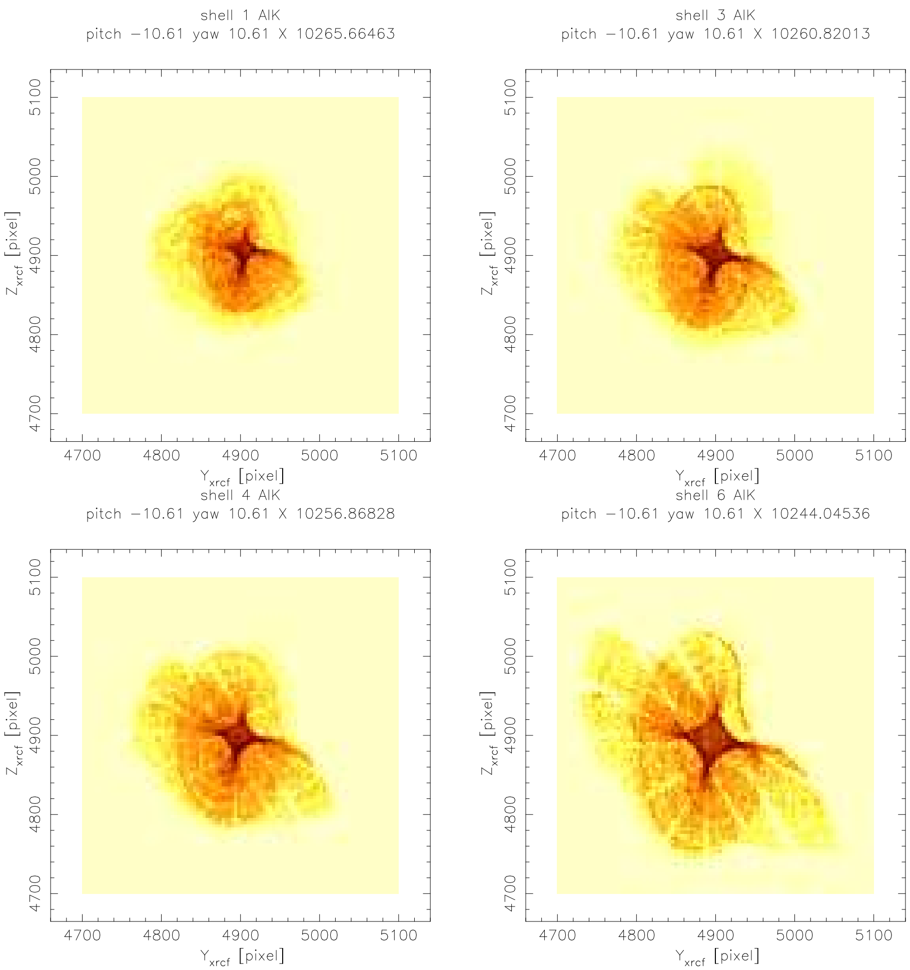

Figure 13.11: Off-axis images for individual shells; pitch = $-10.61'$, yaw = $10.61'$. Pixel width 6.43 μm; binned to 4×4 pixels. Two large overlapping lobes and a dense central pincushion can be seen; the light lanes are shadows of the CAP struts. The concentric ridges in the large lobes result from low-frequency surface errors on the mirrors. (Raytrace data; logarithmic stretch)

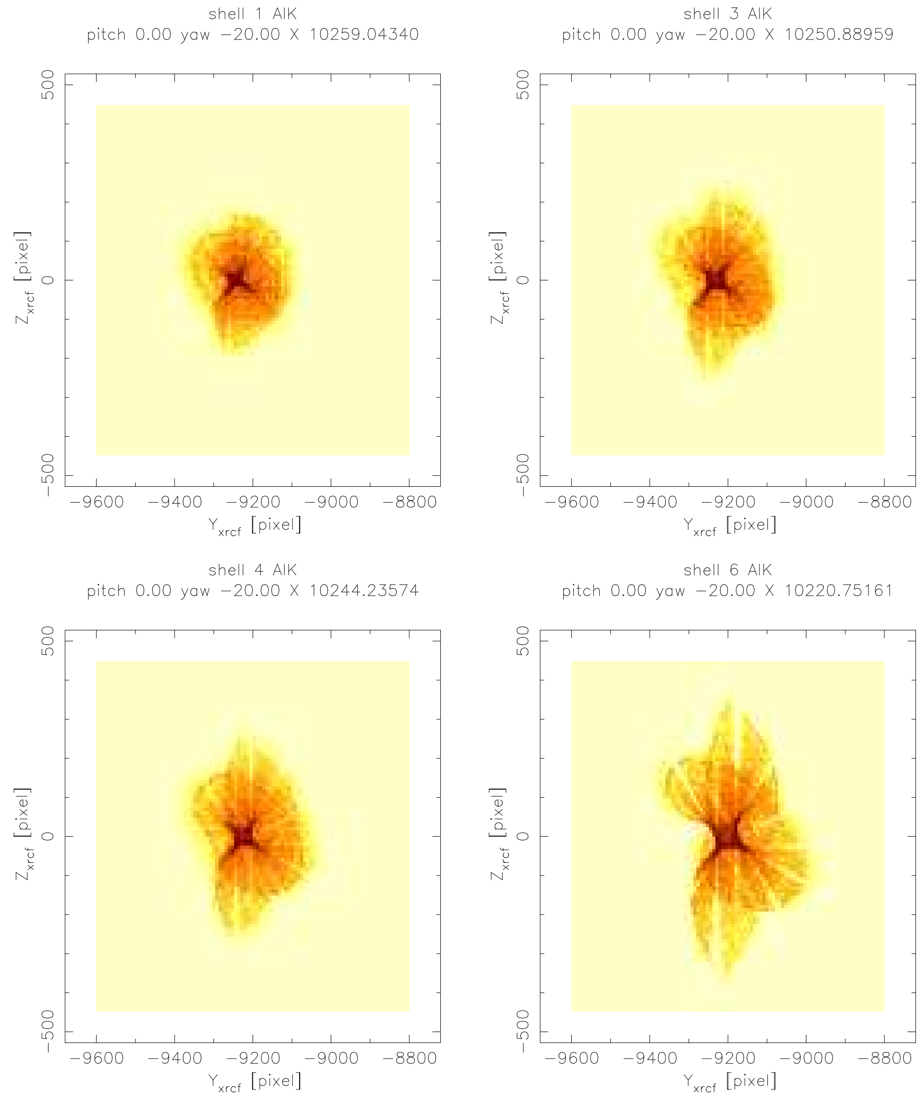

Figure 13.12: Off-axis images for individual shells; pitch = $0'$, yaw = $-20'$. Pixel width 6.43 μm; binned to 8×8 pixels. Two large overlapping lobes and a dense central pincushion can be seen; the light lanes are shadows of the CAP struts. The concentric ridges in the large lobes result from low-frequency surface errors on the mirrors. (Raytrace data; logarithmic stretch)

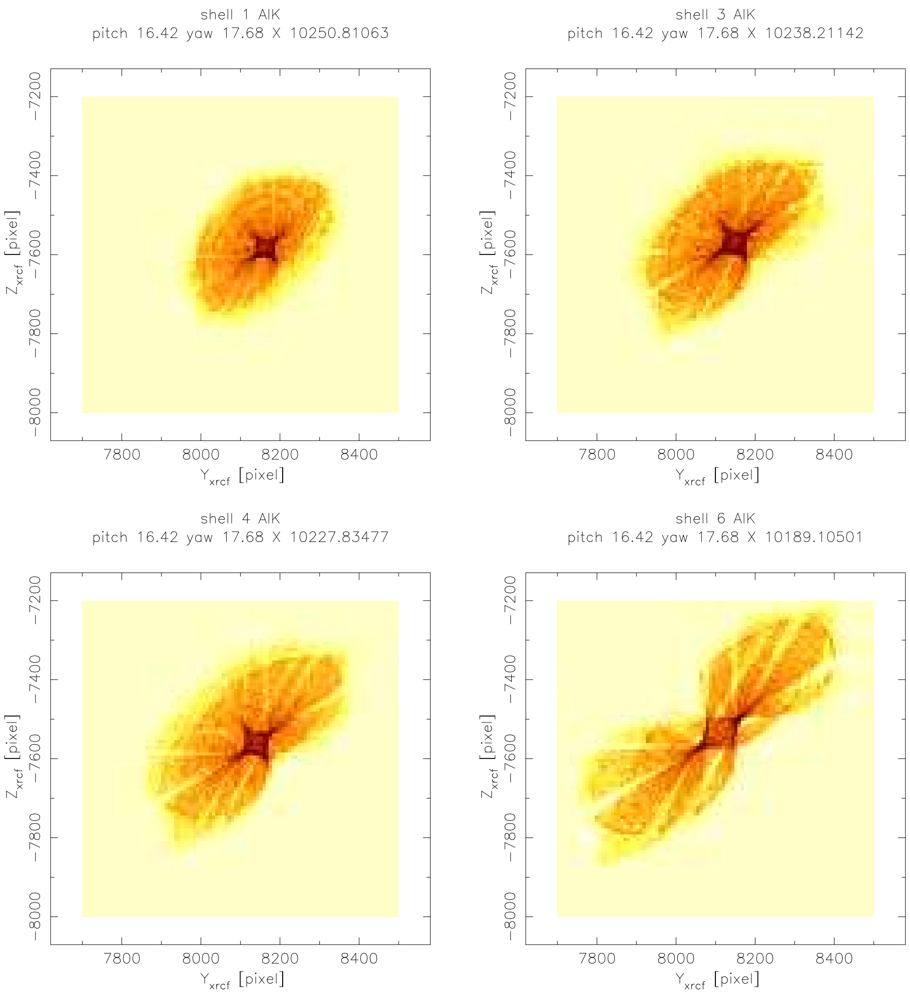

Figure 13.13: Off-axis images for individual shells; pitch = $16.42'$, yaw = $17.68'$. Pixel width $6.43\,\mu$m; binned to 8×8 pixels. Two large overlapping lobes and a dense central pincushion can be seen; the light lanes are shadows of the CAP struts. The concentric ridges in the large lobes result from low-frequency surface errors on the mirrors. (Raytrace data; logarithmic stretch)

at the other two off-axis angles can be used to provide additional estimates of the tilt-compensated decenters; this will produce a better estimate and allow an assessment of the measurement errors. The model can also be checked against the full-HRMA off-axis images at different energies obtained during Phase 1 of the XRCF testing.

Preliminary raytrace studies show that the HATS Fourier coefficients associated with rigid body alignment are insensitive to a tilt-compensated decenter. The effects may show up in the higher Fourier components but noise in the data may make it impractical to extract a value. Further preliminary studies indicate that a tilt-compensated decenter has little effect on the quadrant shutter focus estimators (of order $10\,\mu$m axially) but could produce a significant bias in the tilt estimates. The analysis in Chapter 11 compared against a model incorporating the estimated tilt-compensated decenter, so whatever bias the decenter introduces is also present in the modeling. Care must be taken, however, in attempting a breakdown into individual components until this bias is better understood.

The effects of the tilt-compensated decenter on the analysis and interpretation of the other calibration data needs to be investigated. Although the tilt-compensated decenter does not produce on-axis coma on-orbit, the finite source distance at XRCF produces an effective spherical aberration which may make the tilt-compensated decenter effects visible in images even on-axis: preliminary raytraces indicate that the on-axis blur circle should be asymmetric. The available on-axis data also needs to be checked to determine whether they are consistent with the measured tilt-compensated decenter values.

The single-shell off-axis images show signs of vignetting by the closed shutters for adjacent shells. It may be possible to ascertain the lateral decenter of the shutter assembly relative to the optical axis by making use of the full set of off-axis images for the individual shells Preliminary raytraces indicate a horizontal decenter by about 2 mm; a further study could refine the decenter of the shutter assembly. Because we have pure yaw cases but not pure pitch cases, it will be easier to constrain the Y_{XRCF} component than the Z_{XRCF} component of the shutter assembly decenter.

Finally, some of the images (single-shell and full HRMA) at large off-axis angles show single-reflection ghost images. Once the tilt-compensated decenters and other alignments of the HRMA are well determined, it may be possible to deduce something about the as-built X-ray baffle placement from the shapes of the off-axis images and the ghost images.

Chapter 14

Rigid-Body Misalignment Parameters

In this chapter the incorporation of the rigid-body misalignment parameters into the raytrace model is discussed. In §14.1 the extraction of mirror rigid body parameters from the HATS optical data is discussed; in particular we are concerned with the focal plane image lateral parfocalization ("focal plane decenters") and the residual tilts. Other rigid body parameters are axial parfocalization (discussed in Chapter 10) and relative P to H decenters (*tilt-compensated decenters* (discussed in Chapter 13). The axial parfocalization was accommodated in the models by placing the mirrors at the as-measured positions and making a slight adjustment to the mirror maps. The remaining rigid body parameters were treated by adjusting the lateral position and tilts of the individual mirror elements; the construction of this rigid body database is described in §14.2. The database is based upon HATS measurements of the lateral parfocalization and residual tilt, and the X-ray measurements of the tilt-compensated decenters (Chapter 13).

14.1 HATS Data

During HRMA buildup, the alignment state of the HRMA optics was assessed using the Eastman Kodak Company HATS system (HRMA Alignment Test System). In the HATS tower configuration the HRMA optics were supported vertically in an assembly and testing tower (H optics upper, P optics lower) suspended above an optical flat (the Autocollimating Flat, or ACF); the configuration is illustrated schematically in Figure 14.1. An aperture mask with 24 evenly spaced apertures for each test zone (*i.e.*, mirror shell) was placed above the ACF. The aperture mask also carried a Tilt Reference Indicator (TRI, consisting of a pair of autocollimators, one looking down at the ACF, and the other looking up at a flat mounted in the CAP) which monitored the parallelism between the CAP and the ACF. HATS includes a Centroid Detector Assembly (CDA) mounted on rails at the top of the tower; this was used to assess the alignment of the optics at the 20 m (folded path) P focus or at the 10 m system focus. The alignment of the HRMA was probed using a double-pass system in which a directable laser beam from the CDA source (S) was reflected off an H, a P, the ACF, the P and H again, finally reaching the CDA detector (D); the centroids of the returned beam and an internal reference beam were measured using a quad-cell detector.

For a given mirror pair, the HATS measures the double-pass centroids for a set of 24 apertures equally spaced in azimuth around the optic. The alignment test is basically a double-pass Hartmann test of the X-ray optics. The test laser acts as a pencil beam probing a single azimuth (about the optical axis). The alignment state (and some low-order deformations of the optics) can be assessed

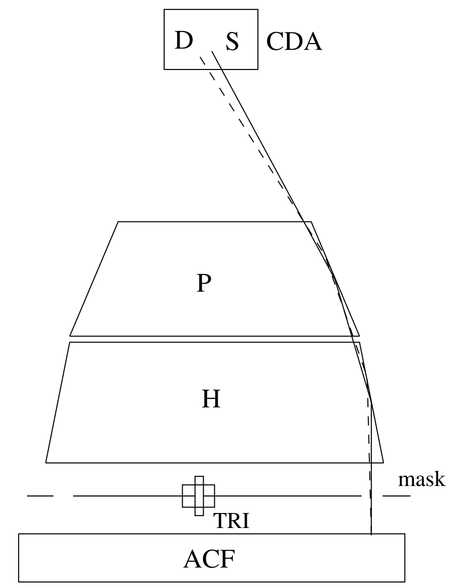

Figure 14.1: Schematic diagram of HATS double-pass configurations. A beam originates at source S, reflects from the H, the P, the Autocollimating Flat (ACF), the P and H again, and finally reaches detector D. The variation in the return beam centroid location with azimuth of the test beam provides information on mirror alignment.

by analyzing the variation in centroid location of the return beam as a function of the pointing azimuth. For example, if the CDA source/detector plane is in front of the HRMA focus (between the focus and the HRMA), the centroids will move along a defocus circle in phase with the beam azimuth (in-phase "1θ" variation). A relative tilt between the P and H, or a relative decenter between the optics produces coma which manifests as a "2θ" variation: the centroid position angle varies twice as quickly as the test beam azimuth varies. A lateral parfocalization error shows up as a relative displacement of the whole set of centroid positions; tilt and relative decenter can both change the lateral parfocalization.

These misalignment coefficients are clearly amenable to a Fourier analysis in which the appropriate low-order Fourier coefficients are interpreted in terms of misalignments. For a double-pass configuration containing both a P optic and its corresponding H optic, the coefficients relevant to rigid-body alignment are given in Table 14.1, in which Q_n is the Fourier coefficient of order n, and Re and Im indicate the real and imaginary components, respectively. The relations between the Fourier decomposition and HRMA alignment are described more fully in Lewis (1993).

Basically, Q_0 gives the displacement of the image in the focal plane, $Re(Q_1)$ gives the radius of the cone of rays (defocus circle, positive in front of the focal point, negative behind the focal point), and Q_2 provides the size and orientation of the 2θ coma circle. Because this is a double-pass experiment, the actual parfocalization and coma errors for a point source at infinity are a factor of two smaller than the Q_n coefficients. Although the interpretation of the HATS Q_0 and

Table 14.1: HATS Fourier Coefficients (ATP augmented data set)

Fourier Coefficient	Rigid Body Term
$Re(Q_0)$ and $Im(Q_0)$	lateral focus error
$Re(Q_1)$	axial focus error
$Re(Q_2)$ and $Im(Q_2)$	residual coma

Q_2 Fourier coefficients is straightforward, the interpretation of Q_1 is complicated by a number of axially symmetric biases including deformation of the CAP under load, curvature of the ACF, "dimples" induced by the mirror supports under 1g, and refraction by radial temperature gradients within the HRMA.

14.1.1 November 1996 HATS ATP (Augmented) Data Set

The final HATS test data (Acceptance Test Procedure, or ATP) were obtained on November 9 and 10, 1996. We augment the original 9 ATP tests with an additional 15 tests performed at that time to obtain an augmented ATP data set as indicated in Table 14.2. We evaluated the means and standard deviations of the Fourier coefficients for this augmented test sequence; the Fourier coefficients evaluated and averaged using the SAO-written `PV-WAVE` package `hats_plot`. The means and errors used for the following analysis were taken from the output file `/ceaxaf1/ekc/HATS_data/hrma_atp/AZMIS.avg`; the errors quoted are the standard deviations of the set of Fourier coefficients obtained for the 24 individual alignment tests in the augmented HATS ATP data set. The Fourier coefficients relevant to rigid-body mirror element alignment are given in Table 14.3.

Table 14.2: HATS ATP (Augmented) Data

11/09/1996	21:49:36.000†	11/10/1996	07:35:05.000
11/09/1996	22:39:14.000†	11/10/1996	08:19:18.000
11/09/1996	23:44:28.000	11/10/1996	09:03:20.000†
11/10/1996	00:28:20.000†	11/10/1996	09:48:05.000†
11/10/1996	01:12:16.000†	11/10/1996	10:32:04.000†
11/10/1996	01:56:05.000†	11/10/1996	11:16:26.000†
11/10/1996	03:10:53.000	11/10/1996	12:00:32.000†
11/10/1996	03:54:49.000	11/10/1996	12:44:35.000†
11/10/1996	04:38:47.000	11/10/1996	13:28:30.000†
11/10/1996	05:22:45.000	11/10/1996	14:12:29.000†
11/10/1996	06:06:47.000	11/10/1996	14:56:24.000†
11/10/1996	06:50:54.000	11/10/1996	15:40:26.000†

†not in original HATS ATP data set

As noted above, the interpretation of Q_1 is complicated by a number of axially symmetric biases; see Chapter 10 for further discussion of axial parfocalization. The raytrace model for the axial parfocalization was updated by correcting the axial placements of the mirrors and adjusting the cone angles in the mirror maps; consequently the axial parfocalization is not discussed further here (see Chapter 10).

Table 14.3: HATS Fourier Coefficients

		units	MP1	MP3	MP4	MP6
1	$Re(Q_0)$	(μm)	-11.49 ± 9.42	-0.18 ± 9.40	-1.31 ± 9.66	-3.78 ± 9.24
2	$Im(Q_0)$	(μm)	7.62 ± 8.89	13.43 ± 8.77	9.89 ± 9.00	4.89 ± 9.08
3	$Re(Q_1)$	(μm)	-24.65 ± 1.09	-11.98 ± 2.42	-30.67 ± 1.35	6.81 ± 1.94
4	$Re(Q_2)$	(μm)	-8.66 ± 0.35	6.26 ± 0.58	5.76 ± 0.27	29.68 ± 0.62
5	$Im(Q_2)$	(μm)	2.60 ± 0.30	-1.93 ± 0.59	-0.76 ± 0.38	-3.07 ± 0.44

The HATS test procedure yields only relative values for the parfocalization so $\langle Q_0 \rangle = [-5.48, 9.42]$, the R^2-weighted mean, was subtracted from Q_0; R is an effective radius for the mirror pair and was taken from Waldman (1995). The resulting Q_n values are given in Table 14.4.

Table 14.4: HATS Fourier Coefficients: r^2-weighted Q_0 removed

		units	MP1	MP3	MP4	MP6
1	$Re(Q_0)$	(μm)	-5.97 ± 9.42	5.30 ± 9.40	4.17 ± 9.66	1.69 ± 9.24
2	$Im(Q_0)$	(μm)	-1.71 ± 8.89	4.10 ± 8.77	0.57 ± 9.00	-4.43 ± 9.08
3	$Re(Q_1)$	(μm)	-24.65 ± 1.09	-11.98 ± 2.42	-30.67 ± 1.35	6.81 ± 1.94
4	$Re(Q_2)$	(μm)	-8.66 ± 0.35	6.26 ± 0.58	5.76 ± 0.27	29.68 ± 0.62
5	$Im(Q_2)$	(μm)	2.60 ± 0.30	-1.93 ± 0.59	-0.76 ± 0.38	-3.07 ± 0.44

Relative rigid body misalignments of the P to H optics in either decenter or tilt can cause a comatic image distortion in the focal plane. The coma circle diameter in the focal plane is related to a pure H relative decenter or a pure H relative tilt angle as:

	1″ H tilt	1 mm H decenter
Coma circle radius (″)	1	10
Coma circle radius (μm)	48.5	488

The breakdown between mirror element tilt and decenter is not uniquely determined by the coma as measured on-axis. Because both tilt and decenter introduce coma, the net coma can vanish for some combination movements; in particular, for combinations of H tilt + H decenter which are equivalent to a pure rotation about the H far focus, the comas introduced by the decenter and the tilt cancel each other leaving the net coma unchanged. We therefore factor the decenter and tilt into two components:

- coma; appears even on-axis
- tilt-compensated decenter; no on-axis coma, but an additional off-axis aberration appears (see Chapter 13).

We interpret the coma as a pure body-centered tilt of the H relative to its companion P optic. In the rest of this section, *tilt* refers to the corresponding component of on-axis coma expressed as a tilt of the H optic unless otherwise noted.

From the Q_0 and Q_2 coefficients it is straightforward to obtain the residual coma and lateral parfocalization:

Table 14.5:

$\Delta X_{DPSAOsac}$	$=$	$+\Delta X_{SAOsac}$	$=$	$+Re(Q_0)/2$
$\Delta Y_{DPSAOsac}$	$=$	$-\Delta Y_{SAOsac}$	$=$	$+Im(Q_0)/2$
$azmis_{DPSAOsac}$	$=$	$-azmis_{SAOsac}$	$=$	$-Re(Q_2)/(2F_H)$
$elmis_{DPSAOsac}$	$=$	$+elmis_{SAOsac}$	$=$	$+Im(Q_2)/(2F_H)$

where $F_H = 9607$ mm is an effective focal length for HATS measurements (Waldman, 1995); the extra factors of 2 arise because this is a double-pass measurement. The numerical values for the lateral parfocalization and residual tilts are given in Table 14.6.

Table 14.6: Summary: HRMA Lateral Parfocalization and On-Axis Coma (SAOsac coordinates)

		units	MP1	MP3	MP4	MP6
Lateral Parfocalization	δX	(μm)	−3.00	+2.65	+2.08	+0.84
Lateral Parfocalization	δY	(μm)	+0.86	−2.05	−0.28	−2.22
On-Axis Coma	*elmis*	($''$)	+0.02926	−0.02069	−0.00423	−0.03292
On-Axis Coma	*azmis*	($''$)	−0.09019	+0.06720	+0.06188	+0.31865

14.1.2 Conversion of HATS data to Rigid Body Coefficients

On-Axis Coma: Tilt and Decenter

The coma measures a combination of relative P to H tilt and P to H decenter. As noted above, we decompose the mirror decenters and tilts into two components: pure body-centered H tilt, and a (coma-free) tilt-compensated H decenter. We assign all of the measured on-axis coma to a pure body-centered tilt; the tilt-compensated decenter is incorporated into the model in §14.2. When a body-centered tilt is applied to the H optic, the lateral focus position also shifts and this affects the lateral parfocalization. We restore lateral parfocalization to the measured values by applying a decenter to the mirror pair as a whole. In terms of the HATS Fourier coefficients, the corrected mirror pair body-centered decenter is given by in Table 14.7 where

$$Q_0' = Q_0 - Q_2^\star$$

and $\star$ indicates complex conjugate.

From these adjusted Q_0' and Q_2 values we derive the body-centered HATS-based decenter values (δX, δY) and tilts (`elmis`, `azmis`), in the `SAOsac` double-pass raytrace coordinates (see Tables 14.7 and 14.8).

Table 14.7: Conversion to Rigid Body Misalignment

$\Delta X_{\mathrm{MP},DPSAOsac}$	$=$	$+\Delta X_{\mathrm{MP},SAOsac}$	$=$	$+Re(Q_0')/2$
$\Delta Y_{\mathrm{MP},DPSAOsac}$	$=$	$-\Delta Y_{\mathrm{MP},SAOsac}$	$=$	$+Im(Q_0')/2$
$azmis_{\mathrm{H},DPSAOsac}$	$=$	$-azmis_{\mathrm{H},SAOsac}$	$=$	$-Re(Q_2)/(2F_H)$
$elmis_{\mathrm{H},DPSAOsac}$	$=$	$+elmis_{\mathrm{H},SAOsac}$	$=$	$+Im(Q_2)/(2F_H)$

Table 14.8: Body-center rigid body coefficients (*double-pass* coordinate system)

Coefficient	units	MP1	MP3	MP4	MP6
$\delta X_{dp,P}$	(μm)	1.347	−0.482	−0.796	−13.995
$\delta Y_{dp,P}$	(μm)	0.446	1.087	−0.097	−3.748
$\mathrm{azmis}_{dp,P}$	($''$)	0.0	0.0	0.0	0.0
$\mathrm{elmis}_{dp,P}$	($''$)	0.0	0.0	0.0	0.0
$\delta X_{dp,H}$	(μm)	1.347	−0.482	−0.796	−13.995
$\delta Y_{dp,H}$	(μm)	0.446	1.087	−0.097	−3.748
$\mathrm{azmis}_{dp,H}$	($''$)	0.09019	−0.067200	−0.061875	−0.318647
$\mathrm{elmis}_{dp,H}$	($''$)	0.02926	−0.020686	−0.004233	−0.032918

These can be converted from double-pass `SAOsac` to standard `SAOsac` coordinates using the relations in §1.4; the results are given in Table 14.9.

Table 14.9: Body-center rigid body coefficients (standard `SAOsac` coordinate system)

Coefficient	units	MP1	MP3	MP4	MP6
δX_P	(μm)	1.347	−0.482	−0.796	−13.995
δY_P	(μm)	−0.446	−1.087	0.097	3.748
azmis_P	($''$)	0.0	0.0	0.0	0.0
elmis_P	($''$)	0.0	0.0	0.0	0.0
δX_H	(μm)	1.347	−0.482	−0.796	−13.995
δY_H	(μm)	−0.446	−1.087	0.097	3.748
azmis_H	($''$)	−0.09019	0.067200	0.061875	0.318647
elmis_H	($''$)	0.02926	−0.020686	−0.004233	−0.032918

14.2 Construction of the Mirror Rigid-Body Database

In this section we summarize the current rigid-body mirror database used as the basis for our raytrace models. We start with an ideal "OSAC"-style mirror prescription; the OSAC mirror conic is described by

$$r^2 = \rho_0^2 + 2Kz - Pz^2 \tag{14.1}$$

where r is the radius corresponding to location z along the axis; z is measured from the body center of the optic so ρ_0 is just the radius corresponding to the body center. The adopted mirror parameters, incorporating the effects of the end-cut, are given in Table 14.10 (Zhao, 1996).

Table 14.10: SAOsac mirror parameters, baseline optic prescription

Mirror	P (dimensionless)	K (mm)	ρ_0 (mm)
p1	0.0	−8.9333113530131421	606.86080963697918
p3	0.0	−5.7939624154424676	488.46244215611011
p4	0.0	−4.5165799273846270	431.26225933154404
p6	0.0	−2.4957050467401789	320.56977725634789
h1	−1.7797716637950735E-03	−26.0506034413416841	579.89015840093919
h3	−1.1532395834759916E-03	−16.875942397594130	466.64379784205380
h4	−8.9864417477996457E-04	−13.150318066441841	411.91935912458604
h6	−4.9625995845653374E-04	−7.2620248152618760	306.09851668776219

To this we apply the decenters and tilts implied by the HATS optical measurements (Table 14.9), and the as-measured optic axial positions (see Chapter 10) to obtain Table 14.11.

Table 14.11: SAOsac mirror parameters, decenters and tilts from ATP data; as-measured axial mirror positions

Mirror	X_0 (mm)	Y_0 (mm)	Z_0 (mm)	azmis ($''$)	elmis ($''$)
P1	0.001347	−0.000446	−426.5761	0.0	0.0
P3	−0.000482	−0.001087	−436.7098	0.0	0.0
P4	−0.000796	0.000097	−440.3572	0.0	0.0
P6	−0.013995	0.003748	−445.0821	0.0	0.0
H1	0.001347	−0.000446	481.0146	−0.09019	0.02926
H3	−0.000482	−0.001087	480.9282	0.067200	−0.020686
H4	−0.000796	0.000097	480.8279	0.061875	−0.004233
H6	−0.013995	0.003748	479.2152	0.318647	−0.032918

Recall that we are working in our standard SAOsac raytrace coordinate system so Z_0 is along the optical axis (positive *from* HRMA *towards* the detectors).

To this basic configuration we apply the optic-to-optic decenters as derived from the off-axis X-ray images (Chapter 13). The mirror (body-center) decenters must also be consistent with the optically determined (focal plane) decenters and coma. This was achieved as follows: A pure rigid body rotation of an H optic about its far focus preserves the coma in the focal plane. For ideal optics the distance from H body center to H far focus is 19668.11899 mm. Raytraces studies show that a tilt-compensated H decenter also shifts the focal plane centroid of the double-pass image by about 1.023902 times the magnitude of the relative H decenter; we can correct for this can be corrected by applying a compensating decenter of the mirror pair as a whole by an amount equal to $0.5 \times 1.023902 \times H_{\text{decenter}}$. (The extra factor of 0.5 results because of the double-pass nature of the HATS alignment test.) That is, if the H to P decenter component of a tilt-compensated decenter

of the H is $[\delta x_H, \delta y_H]$, the compensating tilt (in radians) is:

$$\delta\, elmis = -\frac{\delta y_H}{19668.11899}, \tag{14.2}$$

$$\delta\, azmis = -\frac{\delta x_H}{19668.11899} \tag{14.3}$$

and the compensating mirror *pair* decenter is $-0.5 \times 1.023902 \times [\delta x_H, \delta y_H]$.

In summary, the procedure for incorporating the P to H decenter is:

1. Start with the baseline ideal optics prescription (Table 14.10).
2. Apply a mirror decenter/tilt combination which reproduces the optical measurements of the focal plane decenter and coma, and as-measured optic spacing (Table 14.11.)
3. Apply relative decenters to the H optics (Table 13.3).
4. Apply a compensating tilt to each H optic such that the combined decenter (Table 13.3) plus tilt is equivalent to a pure rotation of the H body center about the H far focus.
5. Decenter to the mirror pair as a whole by −1.023902 times half of the H decenter from Table 13.3 to restore lateral parfocalization.

The resulting rigid-body parameters are given in Table 14.12.

Table 14.12: Rigid-Body Mirror Parameters (EKCHDOS06)

Mirror	X_0 (mm)	Y_0 (mm)	Z_0 (mm)	azmis ($''$)	elmis ($''$)
P1	0.1239	0.2151	−426.5761	0.0	0.0
P3	0.08675	0.2437	−436.7098	0.0	0.0
P4	0.08634	0.2168	−440.3572	0.0	0.0
P6	0.08625	0.2245	−445.0821	0.0	0.0
H1	−0.1154	−0.2060	481.0146	2.4194219	4.4454479
H3	−0.08365	−0.2345	480.9282	1.8542174	4.9943249
H4	−0.08386	−0.2065	480.8279	1.8468078	4.4350269
H6	−0.1096	−0.2067	479.2152	2.3720568	4.4891913

These rigid-body data were incorporated into an updated raytrace mirror database; the current mirror database is /proj/axaf/simul/databases/mirror/EKCHDOS06.rdb. As noted in Chapter 10, the axial parfocalization correction was incorporated into the mirror maps by adjusting the mirror cone angles. The current HRMA model (trace-shell4 configuration file, xrcf_SAO1G+HDOS_HDOS-scat-970220_03), incorporates the adjusted mirror maps.

The rigid-body configuration in Table 14.12 was converted into the SAOsac (double-pass) coordinate system using the transformations in Table 1.3 and raytraced in a double-pass configuration; the optics were assumed to be otherwise ideal. The Fourier coefficients relevant to focal plane decenter and residual coma were evaluated and compared to the HATS-derived values given in Table 14.4; the resulting values are listed in Table 14.13. The values agree to better than 0.4 μm; this is satisfactory agreement, well within the measurement uncertainties for Q_0 and comparable to the measurement uncertainties for Q_2 (Table 14.3).

14.3. Future Directions

Table 14.13: Fourier Coefficients: HATS *vs.* raytrace

mirror	units	data	MP1	MP3	MP4	MP6
$Re(Q_0)$	(μm)	ATP Data	−5.9709	5.2962	4.1713	1.6929
$Re(Q_0)$	(μm)	raytrace	−5.6195	5.2857	4.1754	1.6076
$Re(Q_0)$	(μm)	residual	−0.3514	0.0105	−0.0041	0.0853
$Im(Q_0)$	(μm)	ATP Data	−1.7083	4.1013	0.5668	−4.4305
$Im(Q_0)$	(μm)	raytrace	−1.7612	4.1548	0.2073	−4.4666
$Im(Q_0)$	(μm)	residual	0.0529	−0.0535	0.3595	0.0361
$Re(Q_2)$	(μm)	ATP Data	−8.6649	6.2598	5.7638	29.6826
$Re(Q_2)$	(μm)	raytrace	−8.3901	6.2643	5.7719	29.6405
$Re(Q_2)$	(μm)	residual	−2.0748	−0.0045	−0.0081	0.0421
$Im(Q_2)$	(μm)	ATP Data	2.6014	−1.9269	−0.7608	−3.0664
$Im(Q_2)$	(μm)	raytrace	2.7256	−1.9222	−0.3803	−3.0516
$Im(Q_2)$	(μm)	residual	−0.1242	−0.0047	−0.3805	−0.0148

14.3 Future Directions

This is a preliminary assessment of the mirror rigid-body orientation parameters. As our data reductions and analyses are refined, the improved estimates of axial parfocalization (Chapter 10) and tilt-compensated decenters (Chapter 13) will be incorporated into the model.

The analysis of the optical alignment data can also be improved: various double-pass raytrace analyses were based on optics which were ideal other than for the misalignments. Because raytraces indicate that Fourier decomposition is insensitive to details of the mirror map (other than the axial parfocalization, as noted above), this is not expected to change the estimates appreciably.

Preliminary raytrace investigations indicate that the tilt-compensated decenters do not significantly bias the HATS-based measurements of the coma or parfocalization. It is possible that the tilt-compensated decenters affect some of the higher-order HATS residuals, though.

Finally, an assessment of the lateral parfocalization at XRCF needs to be made. Measurement the lateral parfocalization in X-rays is complicated by several factors: tilts induced by 1g distortion of HRMA as supported in the horizontal XRCF configuration, maintaining stability and accuracy of absolute centroid positions over long timescales, and the large pinholes (10 μm or 20 μm). Although the X-ray measurements may not improve on the HATS values, the X-ray centroids will provide additional constraints on the 1g model. (In the optical HATS measurements the HRMA was supported vertically, so no appreciable 1g-induced tilts are introduced.)

Chapter 15

HRMA Ring Focus Shutter Test

15.1 Introduction

The HRMA ring focus shutter test was designed to measure the HRMA quadrant shutter positions. During the HRMA calibration in early January 1997, it was found that the throughput of the HRMA top and bottom quadrants were unequal; for Shell 6 it could differ by as much as 10%. An early suggestion was that the shutters were not positioned properly. For example, if the North or/and South shutters were blocking part of the bottom quadrant, the throughput asymmetry would occur. It could also be due to one shutter blocking a slice of neighboring shell,

There are four shutters for each mirror pair mounted behind the H shells. Named according to their positions, they are called T(op), B(ottom), N(orth) and S(outh) shutters. Each shutter is 92° wide to ensure a complete coverage when all four shutters are closed.

15.2 Measurements

The ring focus shutter tests were done when the HSI was at the ring focus position (65.2 mm defocus), with the C-K source and with either T & B shutters open or N & S shutters open for one shell only. The eight shutter test images were taken on 97/01/15 with C-K source immediately after the ring focus test 108944, which had all 16 shutters open. Image 108944 had an integration time of 1800 sec. The shutter tests had integration times ranging from 200 to 600 sec. Table 15.1 lists these eight shutter tests.

15.3 Data Analysis

Figures 15.1 and 15.2 show the shutter test images for Shell 1. There were four pairs of those images for the four shells. Each image pair was added together to make a full ring, which was then sliced into 360 sections, with 1° per sector. The intensity of each sector (counts/second/sector) was measured, using the IRAF package, and plotted as a function of azimuthal angle.

15.4 Results

Figures 15.3 – 15.6 illustrate the results of the ring focus shutter test. There are five panels in each figure:

Table 15.1: HRMA Ring Focus Shutter Test Data
Date: 97/01/15 Source: C-K Defocus: 65.2 mm

Run ID	TRW ID	Shell	Shutters open	Integration time
108945	D-IXH-RF-17.001	1	T + B	200 seconds
108946	D-IXH-RF-17.002	1	N + S	200 seconds
108947	D-IXH-RF-17.003	3	T + B	200 seconds
108948	D-IXH-RF-17.004	3	N + S	300 seconds
108949	D-IXH-RF-17.005	4	T + B	360 seconds
108951	D-IXH-RF-17.006	4	N + S	360 seconds
108953	D-IXH-RF-17.007	6	T + B	600 seconds
108954	D-IXH-RF-17.008	6	N + S	600 seconds

1. The top panel is the HSI intensity from run 108944 (C-K source, 1800 sec exposure time), which was taken with all the shutters open. The intensity variation is due to the quantum efficiency of the HSI which depends on the incident angle of the X-ray. There are intensity dips at 30° multiples. These are due to the supporting struts blocking the rays.

2. The second panel is the HSI intensity from the shutter tests. In addition to the intensity dips at 30° multiples, there are dips at ±45° and ±135°. These are due to the regions where the shutters overlapped. Since each shutter is designed to be 92° wide, each open quadrant should be 88° wide. The figures show that those dips are 2–3° wide as expected and that their positions are within 1–2° from expected.

3. The third panel is the ratio of the above two. The dips at ±45° and ±135° are still there as expected. There are also spikes (both positive and negative) at 30° multiples. Because the HSI moved between these tests, the gaps were not aligned exactly.

4. The fourth panel is the the third panel with the spikes and dips removed. It looks pretty flat.

5. The fifth panel shows the data from the fourth panel binned into 15° bins and fitted to a straight line. The straight line is the average ratio of the entire ring. The data fit to this straight line very well.

These figures answer the question of whether the shutters were mounted properly. As we can see, the ratios of the ring focus test and the shutter tests have a very constant (other than the spikes and dips) of ~ 3 (due to a different source intensity for run 108944 compared to the others). This tells us that the shutters were not blocking anything other than their assigned area. If there were any unwanted obstruction in the azimuthal direction, there would have been dips wider than 2–3° at the ±45° and ±135° locations. If there were any unwanted obstruction in the radial direction, the intensity ratio would have dropped below 3 in that quadrant.

15.5 Conclusion

Based on the HSI ring focus shutter test, all the shutters were mounted properly. They only obstruct rays in their assigned area when closed. The HRMA throughput asymmetry was thus not due to the shutters. (It was later determined that the throughput asymmetry was attributable to the decenters between the P shells and the H shells. See Chapter 13.)

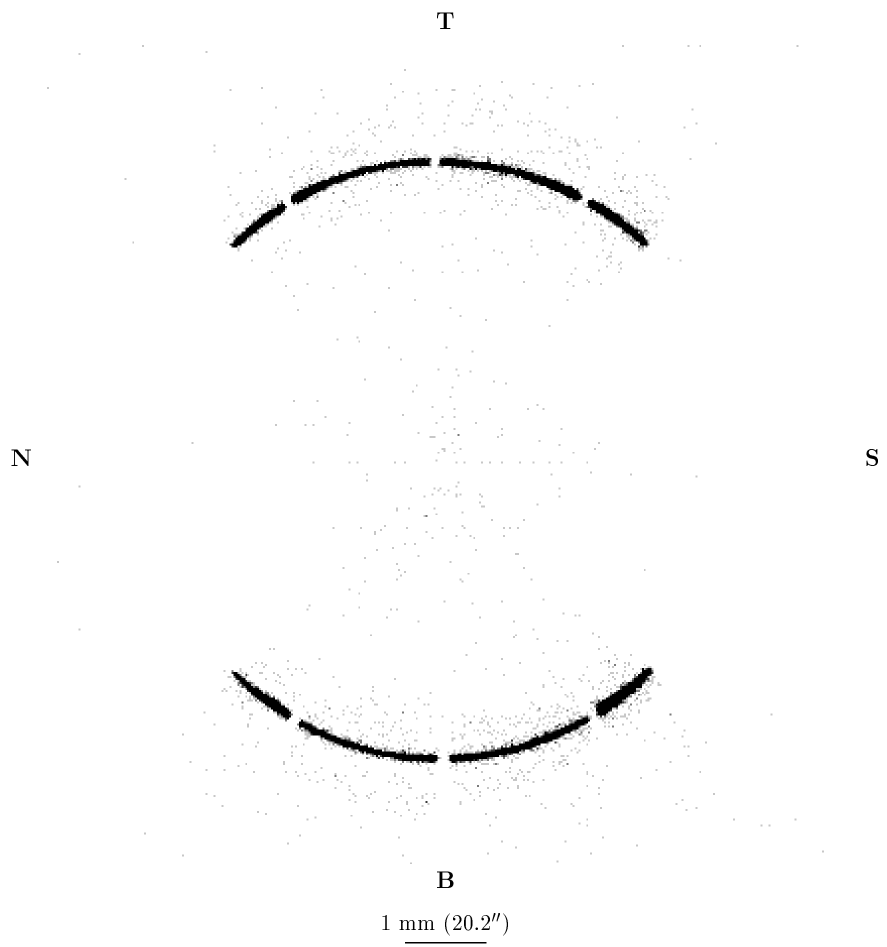

Figure 15.1: The HRMA ring focus shutter test image. Source: C-K; Defocus: 65.2 mm; Date: 97/01/15; Run ID: 108945; TRW ID: D-IXH-RF-17.001.

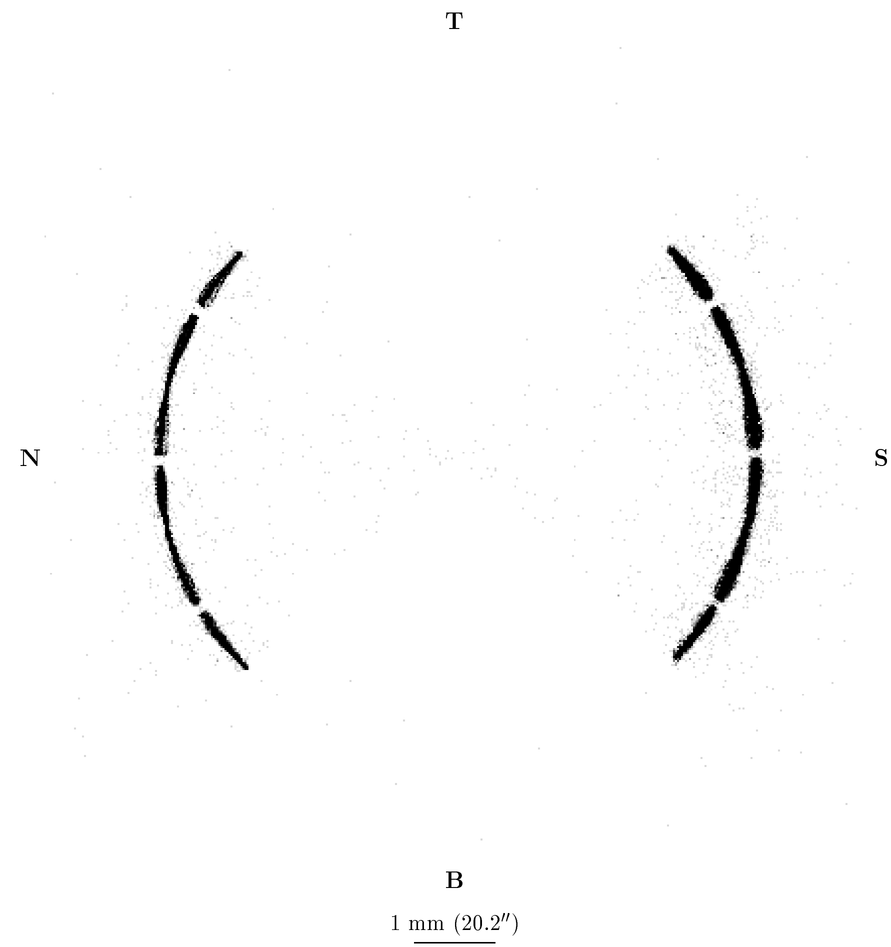

Figure 15.2: The HRMA ring focus shutter test image. Source: C-K; Defocus: 65.2 mm; Date: 97/01/15; Run ID: 108946; TRW ID: D-IXH-RF-17.002.

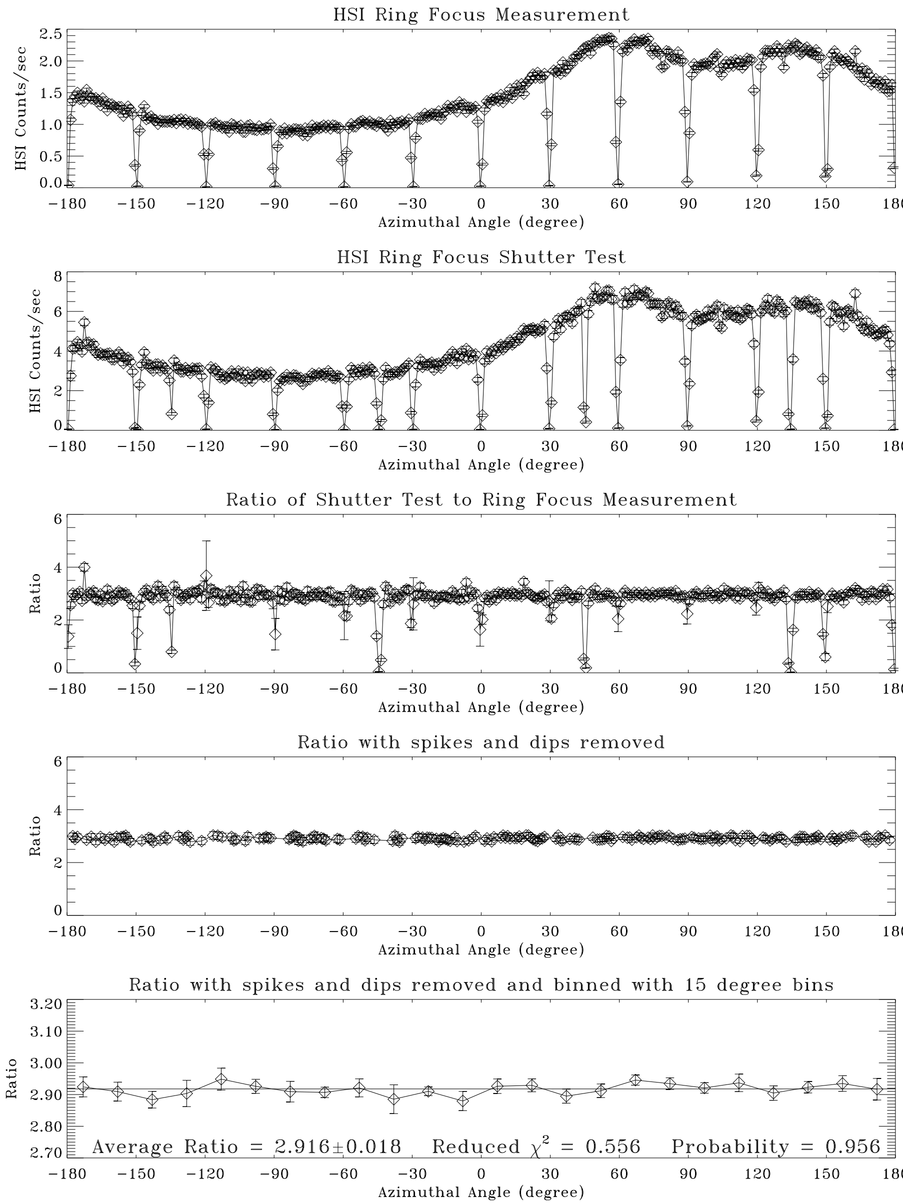

Figure 15.3: The HRMA ring focus shutter test. Ring 1

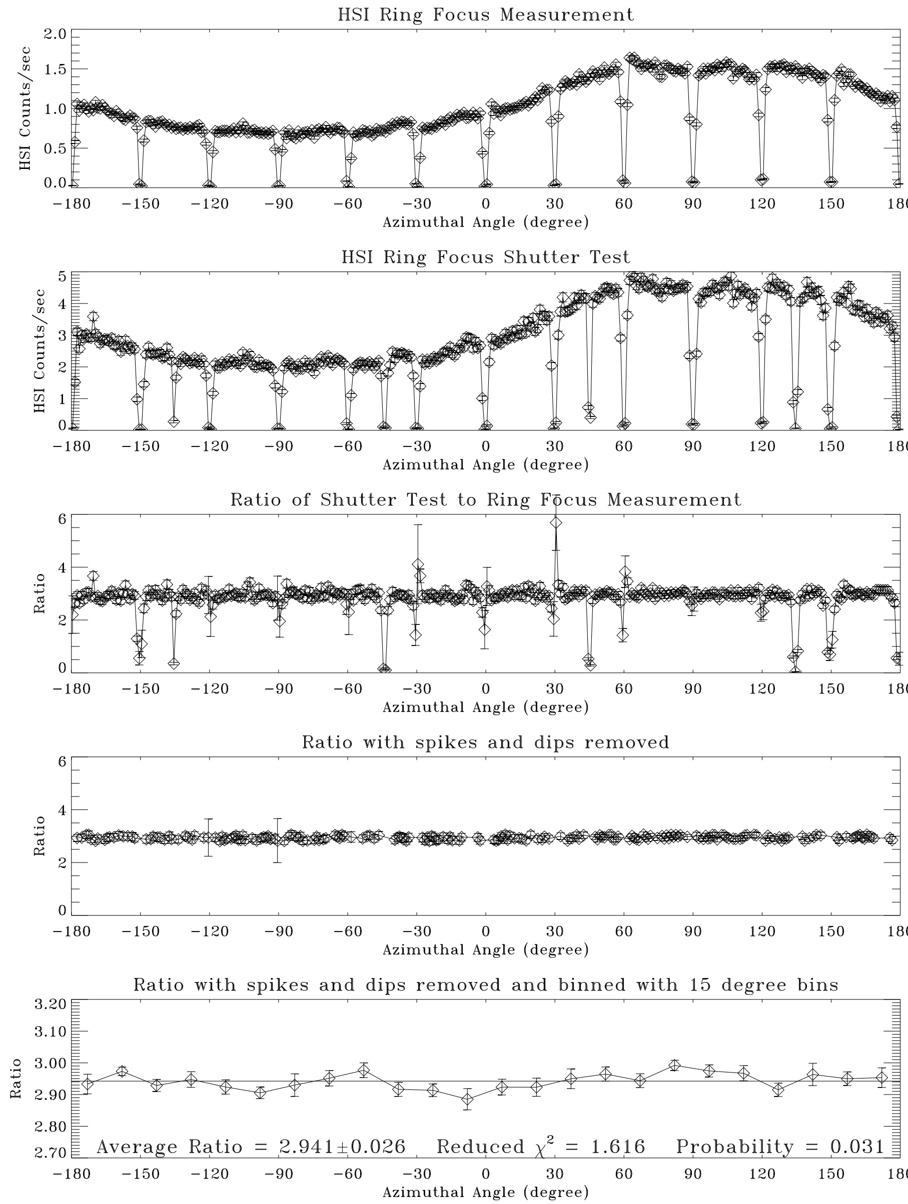

Figure 15.4: The HRMA ring focus shutter test. Ring 3

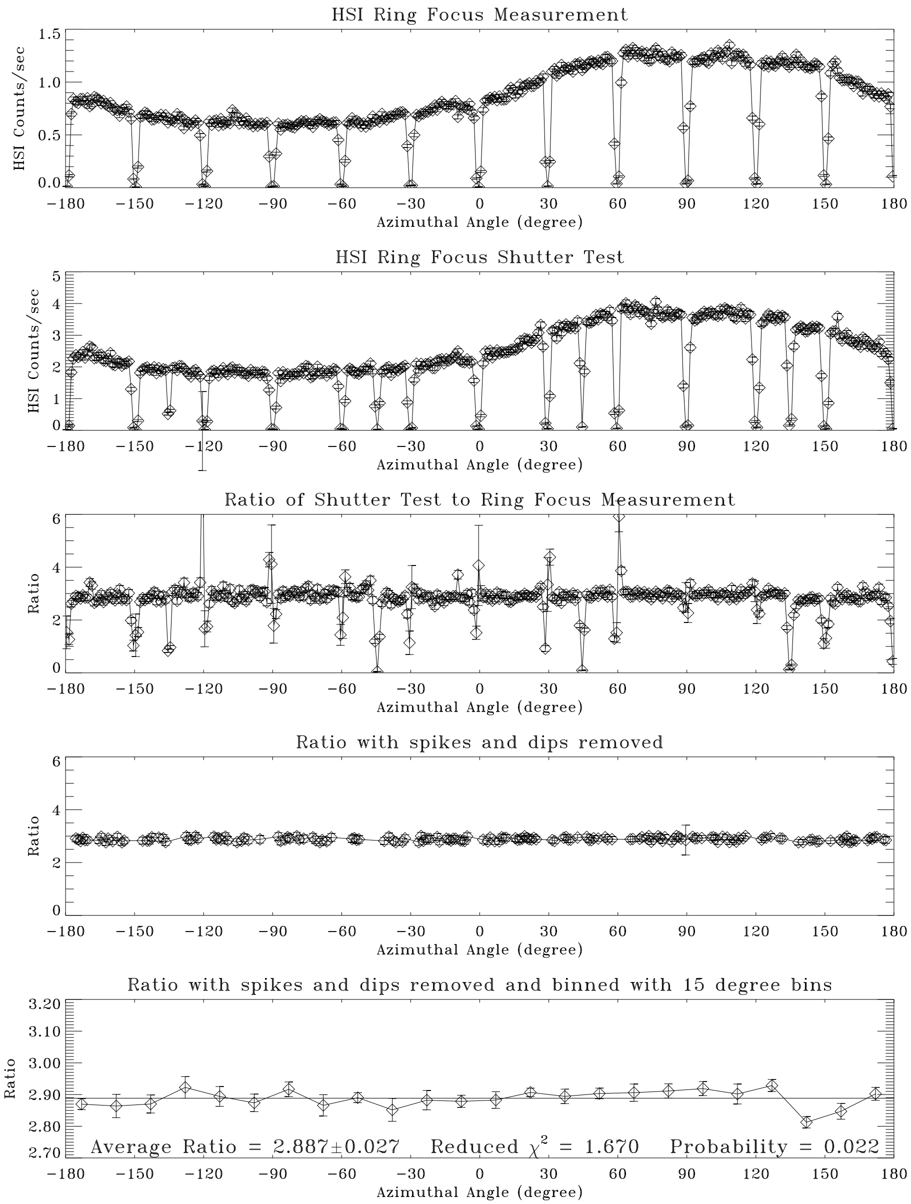

Figure 15.5: The HRMA ring focus shutter test. Ring 4

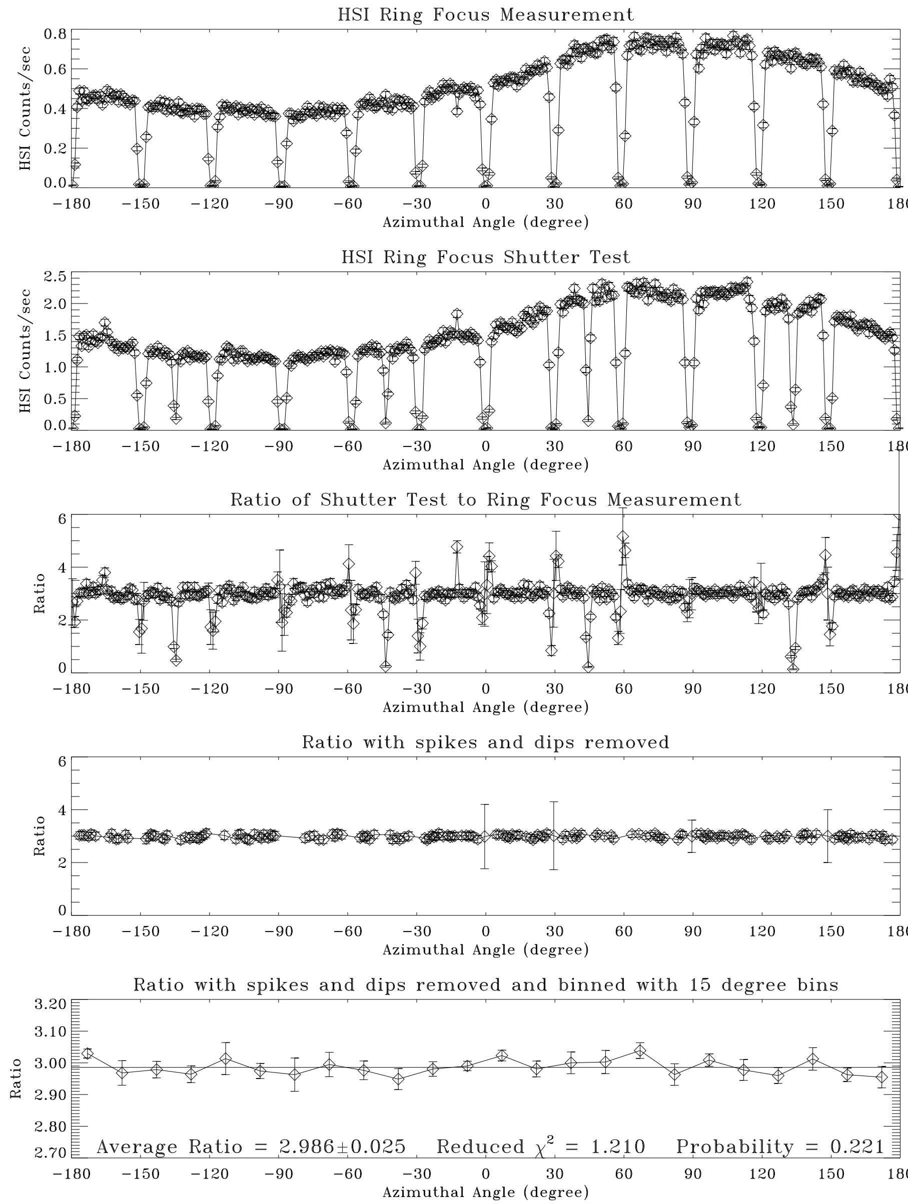

Figure 15.6: The HRMA ring focus shutter test. Ring 6

Chapter 16

Description of Data Organization

As described in Chapter 1, the Phase 1 XRCF tests were done with the HXDA equipment, which consists of the High Speed Imager (HSI), an imaging microchannel plate detector, seven Flow Proportional Counters (FPC), and two Solid State Detectors (SSD).

The data produced by these detectors is organized as follows. Each logical operation is tagged with a unique identifier, known as the runid. For each exposure, each operating spectral detector (FPC or SSD) produces a "pulse height analyzer" (`pha`) file. This is an RDB file, with a name of the form: `acq`<*runid*>`d`<*detector*>`i`<*iteration #*>`.pha` where <*runid*> is a six digit number, <*detector*> is a one-digit detector id, and <*iteration #*> is a one- to three-digit iteration number. For example: `acq123456d2i39.pha`.

In addition, for each logical operation, each detector generates a summary (`sum`) file. This is also an RDB table, with columns containing focal plane detector coordinates, counts and counting rates for the detector in question, summed over a region of interest in pulse-height space set at the measurement time. These files are suitable for many quick-look purposes. They have names of the form <*runid*>`d`<*detector*>`.sum` (e.g., `123456d2.sum`). There are also "scan" (`scn`) files, in which the counts rates in the sum files for the focal plane detector are divided by those of a single selected BND detector, producing normalized counting rates. These have names of the form <*runid*>`.scn`, e.g., `123456.scn`.

The `pha` file headers record the filename, the runid, the UT start time of the exposure (the IRIG time), the creation date of the file (in UT, measured by the local computer), the state of the shutters, the live and true times for the exposure (as measured by the MCB), the detector voltage, and various other less pertinent information. These entries are all automatically created by the HXDS software. The headers of the sum files have much information taken from the test plan at the time the test began, and can be quite informative as to the circumstances at test time, and the intentions of the test planners and conductors. Some of the data are manually entered, and must be checked against other sources.

The HSI produces two files for each exposure. One is a legal FITS file, which is logically a table of events detected, with raw coordinates and a pulse height for each. Its name has the form `hsi`<*runid*>`i`<*iteration #*>`.fits`, e.g., `hsi123456i2.fits`. The second file is the complete raw data stream. This file is generally compressed and written to tape shortly after it is taken, since it can be quite large. The name, in our example, would be `hsi123456i2.fits.rd.gz` (even though it is not a legal FITS file).

The data files for a given 24 hour period (from UT midnight to UT midnight) are gathered in a directory `data/`*date*, where *date* is the date in the format `YYMMDD`; for example `data/961228` holds

data from December 12, 1996 (UT). At XRCF, these data were all stored in the second floor control computers in the directory tree `/data/xrcfa/data`; there are several mirrors of this data structure in various places at SAO, for example `/data/asc13/data/xrcfa` and `/data/hxds3/phase1`.

In addition to the data files, various aspects of the system are logged either periodically, or when the state changes. This information is written to a series of log files, in a directory parallel to the above data directory tree, known as `logs`. In this directory, there are subdirectories for each type of log file, further subdivided by UT date. The information is then recorded in multi-column RDB tables with time tags, typically a few minutes' worth in each file, to keep file sizes small.

The types of log files are these:

- coord – HXDS Coordination level software log
- gat – HXDS Gas and Temperature information
- hsa – HRMA Shutter Assembly information
- rate – counting rates in the various HXDS detectors
- stg – positions of HXDS translation stages
- xss – X-ray Source System information

All of these data and log files are ingested into the ASC archive. In many cases, the names are changed, though the instrument data files contain their original names in a field in their headers, so the names can be restored if desired. The ASC archive also ingests other facility information, including a higher-frequency version of the XSS log; HRMA temperature information, etc.

Bibliography

Akima, H. (1978). *ACM Transactions on Mathematical Software*, 4(2):148.

Beckmann, P. and Spizzichino, A. (1963). *The Scattering of Electromagnetic Waves from Rough Surfaces*. Pergamon Press, Oxford.

Bevington, P. R. and Robinson, D. K. (1992). *Data Reduction and Error Analysis for the Physical Sciences*. McGraw-Hill Inc., New York, second edition.

Cash, W. (1979). Parameter estimation in astronomy through application of the likelihood ratio. *Astrophysical Journal*, 228:939.

Chappell, J. H. and Murray, S. S. (1989). Position modeling for the AXAF high resolution camera (HRC). In *SPIE Proceedings*, volume 1149, page 460, San Diego. SPIE.

Cohen, L. M. (April 1997). XRCF measurement & epoxy strain. Memorandum, Smithsonian Astrophysical Observatory.

Gaetz, T. J., Podgorski, W. A., Cohen, L. M., Freeman, M. D., Edgar, R. J., Jerius, D., Van Speybroeck, L., and Zhao, P. (1997). Focus and alignment of the AXAF optics. In *SPIE Proceedings*, volume 3113, San Diego. SPIE.

Graessle, D. E., Burek, A. J., Fitch, J. J., Harris, B., Schwartz, D. A., and Blake, R. L. (1997). Optical constant from synchrotron reflectance measurements of AXAF witness mirrors, 2-12 kev. In *SPIE Proceedings*, volume 3113, San Diego. SPIE.

Griner, D. B., Zissa, D. E., and Korsch, D. (September 1985). Test method for telescope using a point source at a finite distance. MSFC Center Director's Discretionary Fund Final Report, Project No. H20 Technical Memorandum TM-86523, NASA.

Henke, L., Gullikson, E. M., and Davis, J. C. (1993). X-ray interactions: photoabsorpion, scattering, transmission, and reflection at E=50–30,000 eV, Z=1–92. *Atomic Data and Nuclear Data Tables*, 54:181. Additional data were taken from `http://www-cxro.lbl.gov/optical_constants/`.

Jahoda, K. and McCammon, D. (1988). Proportional counters as low energy photon detectors. *Nuclear Insturmentation and Methods*, A272:800.

Lewis, T. S. (1993). AXAF HRMA alignment test analysis. Tech Note XKR93-1831CD, Eastman Kodak Company.

Nousek, J. A. and Shue, D. R. (1989). χ^2 and c statistic minimization for low count per bin data. *Astrophysical Journal*, 342:1207.

O'Dell, S. et al. (1992). In *SPIE Proceedings*, volume 1742, page 171. SPIE.

SAO (1997). HXDS operation instructions. Technical Report SP-SAO-4004, Smithsonian Astrophysical Observatory.

Texter, S. (1997). IAP encoder positions. Memo, TRW.

Tsiang, E. Y. (1997). JMKMOD: Models and software for the ground calibration of AXAF. Technical Report SAO-AXAF-DR-97-276, Smithsonian Astrophysical Observatory.

Waldman, M. (1995). ARM zone diameters for HATS software. Tech Note AXAF-95-0209-WALDMAN, Eastman Kodak Company.

Zhao, P. (1995). AXAF VETA-I mirror X-ray test results (cross check with the HDOS metrology data). Technical Report SAO-AXAF-DR-95-146, Smithsonian Astrophysical Observatory.

Zhao, P. (1996). OSAC parameters for AXAF mirrors – formulae and precisions (revised). Memorandum, Smithsonian Astrophysical Observatory.

Zhao, P., Freeman, M. D., Jerius, D., and Shao, Y. (1993). AXAF VETA-I mirror ring focus measurements. In *SPIE Proceedings*, volume 2011, page 59, San Diego. SPIE.

Zissa, D. E. and Korsch, D. (October 1986). Experimental evaluation of the ring focus test for X-ray telescope using AXAF's technology mirror assembly. MSFC Center Director's Discretionary Fund Final Report, Project No. H20 Technical Memorandum TM-86570, NASA.